

CONNECTING THE DOTS: INVESTIGATING PLANET FORMATION AND  
COMPOSITION THROUGH OBSERVATIONS OF CARBON AND OXYGEN  
SPECIES IN STARS, DISKS, AND PLANETS

by

Johanna Kavanagh Teske

---

A Dissertation Submitted to the Faculty of the  
DEPARTMENT OF ASTRONOMY  
In Partial Fulfillment of the Requirements  
For the Degree of  
DOCTOR OF PHILOSOPHY  
In the Graduate College  
THE UNIVERSITY OF ARIZONA

2014

THE UNIVERSITY OF ARIZONA  
GRADUATE COLLEGE

As members of the Dissertation Committee, we certify that we have read the dissertation prepared by Johanna Kavanagh Teske entitled “Connecting the Dots: Investigating Planet Formation and Composition Through Observations of Carbon and Oxygen Species in Disks, Stars, and Planets” and recommend that it be accepted as fulfilling the dissertation requirement for the Degree of Doctor of Philosophy.

\_\_\_\_\_  
Caitlin Griffith Date: 11 April 2014

\_\_\_\_\_  
Katia Cunha Date: 11 April 2014

\_\_\_\_\_  
Simon Schuler Date: 11 April 2014

\_\_\_\_\_  
Daniel Apai Date: 11 April 2014

\_\_\_\_\_  
George Rieke Date: 11 April 2014

Final approval and acceptance of this dissertation is contingent upon the candidate's submission of the final copies of the dissertation to the Graduate College.

I hereby certify that I have read this dissertation prepared under my direction and recommend that it be accepted as fulfilling the dissertation requirement.

\_\_\_\_\_  
Dissertation Director: Caitlin Griffith Date: 11 April 2014

## STATEMENT BY AUTHOR

This dissertation has been submitted in partial fulfillment of requirements for an advanced degree at The University of Arizona and is deposited in the University Library to be made available to borrowers under rules of the Library.

Brief quotations from this dissertation are allowable without special permission, provided that accurate acknowledgment of source is made. Requests for permission for extended quotation from or reproduction of this manuscript in whole or in part may be granted by the head of the major department or the Dean of the Graduate College when in his or her judgment the proposed use of the material is in the interests of scholarship. In all other instances, however, permission must be obtained from the author.

SIGNED: Johanna Kavanagh Teske

## ACKNOWLEDGMENTS

I would like to acknowledge the patience, dedication, and open-minded attitude of my second year project and thesis advisors, Joan Najita, Caitlin Griffith, Simon Schuler, and Katia Cunha. These individuals have given me multitudes of good advice, their time and energy (a lot of it!), and helped me become a better researcher and a better person. Thanks also to my other co-authors on these thesis papers, who contributed their time and expertise to make the science possible and understandable (and publishable): Dr. John Carr, Dr. Ilaria Pascucci, Dr. Daniel Apai, Dr. Thomas Henning, Jake Turner, Matthias Mallonn (formerly Mueller), and especially Dr. Verne Smith, who has been instrumental in observation gathering and interpretation, and has helped me shape my postdoctoral plans.

I would like to thank very much Dr. Don McCarthy, Dr. Edward Prather, Gina Brissenden, and Dr. Colin Wallace, who have helped foster my teaching and communication skills, and kept me engaged in thinking and excited about education and outreach.

I would like to acknowledge the National Science Foundation for funding my first three years of graduate school, and enabling me to work with whomever I wanted during this time. I was also supported during the summer by Dr. Griffith's NASA's Planetary Atmospheres Program grant, and during this last year by a NASA Keck PI grant.

In addition, my thesis was possible due to the data available in the Keck Observatory Archive (KOA), operated by the W. M. Keck Observatory and the NASA Exoplanet Science Institute (NExSci), under contract with the National Aeronautics and Space Administration, as well as data collected from the Subaru and Keck telescopes on Mauna Kea. For this I acknowledge the very significant cultural role and reverence that the summit of Mauna Kea has always had within the indigenous Hawaiian community. My thesis also used data collected with the STELLA robotic telescope in Tenerife, an AIP facility jointly operated by AIP and IAC, and the University of Arizona Kuiper 1.55 m telescope on Mount Bigelow. I thank the staff at all of these facilities, particularly the Kuiper Telescope, for their patience, and the University of Arizona, NOAO, and NASA TACs for awarding time for my thesis observations.

## DEDICATION

This thesis is dedicated to my dad, who took me to museums around the world, introduced me to *Contact*, and taught me that “doing the math” was cool; my first and second grade teacher Rick Stevens, who fostered in me the wonder of discovery and exploration; my middle school English teacher, Mrs. Ellen Flurry, who made sure I knew I could do whatever I put my mind to; my “PALTAG” teacher, Mrs. Susan Bucks, whose class and joie de vivre were my fuel through high school; my high school chemistry teacher, Mrs. Judy Iskowitz, who got me hooked on spectroscopy and understanding the physical universe; Dr. Monika Konaklieva, my college organic chemistry teacher, who let me do an extra credit project about PAHs that spurred my interest in astrochemistry; my college advisor, Dr. Nathan Harshman, who believed in me and was so passionate about his teaching; Dr. Jackie Milingo, my first REU advisor who introduced me to research and how think about constructing a research project; my friends in college and graduate school who suffered with me, believed in me, and made me laugh; and Dr. Alycia Weinberger, my undergraduate thesis advisor who jump-started my astronomy career, who has continued be a fantastic advisor and role model, and without whom I wouldn’t have made it into or through graduate school.

Finally, and most importantly, I dedicate this thesis to my mom, who has been my inspiration and my rock, kept me humble and sane, always eager to hear about my life and my work, an invaluable source of wisdom, and who believed in me when I didn’t believe in myself.

## TABLE OF CONTENTS

LIST OF FIGURES . . . . .	8
LIST OF TABLES . . . . .	10
ABSTRACT . . . . .	11
1 INTRODUCTION . . . . .	13
2 OVERVIEW OF STAR & PLANET FORMATION . . . . .	17
2.1 Stage 1: Stars . . . . .	17
2.1.1 Brief Outline of Stellar/Galactic Chemical Evolution . . . .	17
2.1.2 Measuring Stellar Composition . . . . .	21
2.2 Stage 2: Disks . . . . .	28
2.2.1 Observational Constraints of Disk Physical Processes and Composition . . . . .	31
2.3 Stage 3: Planetesimals . . . . .	36
2.4 Stage 4: Planets . . . . .	38
2.4.1 Observational Constraints on Exoplanet Compositions . . . .	41
2.5 Connecting the Dots – The Role of C and O . . . . .	45
2.5.1 Stage 0: Host Star Composition’s Role in Planet Formation .	45
2.5.2 Step 1: C and O in the Protoplanetary Disk . . . . .	47
2.5.3 Step 2: C and O in Planetesimals . . . . .	51
2.5.4 Step 3: C and O in Planets . . . . .	55
2.6 Last Word . . . . .	62
3 MEASURING ORGANIC MOLECULAR EMISSION IN DISKS WITH LOW RES- OLUTION <i>Spitzer</i> SPECTROSCOPY . . . . .	64
3.1 Introduction . . . . .	65
3.2 Data Sets . . . . .	67
3.3 Analysis and Results . . . . .	70
3.3.1 SH vs. SL Measurements . . . . .	70
3.3.2 Variation in HCN Feature Strength . . . . .	80
3.4 Discussion . . . . .	86
3.5 Summary & Conclusions . . . . .	90
4 OPTICAL OBSERVATIONS OF THE TRANSITING EXOPLANET GJ 1214B . .	92
4.1 Introduction . . . . .	93
4.2 Observations and Data Reduction . . . . .	96
4.3 Light Curve Analysis . . . . .	99
4.4 Discussion & Conclusions . . . . .	102

5	C/O RATIOS OF STARS WITH TRANSITING HOT JUPITER EXOPLANETS .	116
5.1	Introduction . . . . .	117
5.1.1	The Role of Carbon and Oxygen . . . . .	119
5.2	Observations and Data Reduction . . . . .	121
5.3	Derivation of Stellar Parameters and Abundances . . . . .	122
5.3.1	Stellar Abundances of Ni, C, and O . . . . .	125
5.3.2	Abundance Uncertainties . . . . .	129
5.4	Results and Discussion . . . . .	130
5.4.1	Comparison to Previous Studies of C and O in Exoplanet Host Stars . . . . .	131
5.4.2	Trends with $C/O_{\text{host star}}$ versus Planetary Parameters . . . .	137
5.4.3	Carbon and Oxygen in Specific Exoplanet Systems . . . . .	140
5.5	Summary . . . . .	154
6	CARBON AND OXYGEN ABUNDANCES IN THE HOT JUPITER EXOPLANET HOST STAR XO-2N AND ITS BINARY COMPANION . . . . .	169
6.1	Introduction . . . . .	170
6.2	Observations and Data Reduction . . . . .	172
6.3	Abundance Analysis and Results . . . . .	172
6.4	Discussion . . . . .	175
6.5	Conclusions . . . . .	179
7	CARBON AND OXYGEN ABUNDANCES IN COOL METAL-RICH EXOPLANET HOSTS: A CASE STUDY OF THE C/O RATIO OF 55 CANCRI . . . . .	183
7.1	Introduction . . . . .	184
7.2	Observations and Abundance Analysis . . . . .	186
7.2.1	Data . . . . .	186
7.2.2	Stellar Parameters . . . . .	187
7.2.3	Stellar Abundances . . . . .	189
7.3	Results & Discussion . . . . .	195
7.4	Conclusions . . . . .	202
8	CONCLUSIONS . . . . .	210
8.1	Summary . . . . .	210
8.2	Next Steps . . . . .	215
8.2.1	How is Planet Composition Related to Stellar Activity? . . .	216
8.2.2	More Transiting Giant Planet Host Stars . . . . .	218
8.2.3	Small Planet Host Stars . . . . .	221

## LIST OF FIGURES

2.1	Figure 11 from Bensby & Feltzing (2006), showing from their sample of nearby F and G dwarf stars (a and b) carbon and oxygen abundances relative to iron, and (c and d) carbon and iron abundances relative to oxygen. Thin and thick disk stars are indicated by open and filled circles, respectively, and a few thick disk stars from Nissen et al. (2002) are included as filled triangles in panels b and d. . . . .	21
3.1	Comparison of SH, smoothed SH, and SL Data for AA Tau . . . . .	68
3.2	Zoom in of Figure 3.1 around $14\ \mu\text{m}$ HCN feature . . . . .	73
3.3	Comparison SH, smoothed/resampled and SL HCN equivalent widths . . . . .	77
3.4	Comparison of stellar parameters and SL HCN flux . . . . .	85
4.1	Individual light curves of GJ 1214b for each date of observed transit I . . . . .	108
4.2	Individual light curves of GJ 1214b for each date of observed transit II . . . . .	109
4.3	Results of combined-night analyses compared to other published transit measurements of GJ 1214b . . . . .	110
4.4	Zoom out of Figure 4.3, including data covering a greater range in wavelength . . . . .	111
4.5	Variability in the out-of-transit (OoT) $g'$ -band data . . . . .	112
5.1	Sample spectra obtained with Subaru/HDS . . . . .	165
5.2	Spectrum synthesis fit to forbidden oxygen line at $6300.3\ \text{\AA}$ for HD 189733 . . . . .	166
5.3	Carbon and oxygen abundance versus iron abundance, comparing our results to literature values . . . . .	167
5.4	C/O versus iron abundance comparing our results to literature values . . . . .	168
5.5	Host star C/O ratio versus planetary $T_{\text{eq}}$ and $R_p$ . . . . .	168
6.1	spectrum synthesis fits to forbidden oxygen line at $6300.3\ \text{\AA}$ for XO-2N and XO-2S . . . . .	181
6.2	Carbon abundance, oxygen abundance, and C/O versus iron abundance for XO-2 system, comparing our results to literature values . . . . .	182
7.1	CN blend contribution to oxygen forbidden line at $6363\ \text{\AA}$ line; How measured $\log N(\text{O})_{55\text{Cnc}}$ changes with $\log N(\text{Ni})$ for 55 Cnc . . . . .	208



7.2	Carbon abundance, oxygen abundance, and C/O versus iron abundance for 55 Cnc, comparing our results to literature values . . . . .	209
8.1	Stellar iron abundance versus inferred planet heavy-element mass for Miller & Fortney (2011) sample . . . . .	223
8.2	Distribution of detected exoplanet radii . . . . .	224
8.3	Radius versus mass distribution for transiting planets with measured masses . . . . .	225
8.4	Comparison of (Meléndez et al. (2012) results to my reanalysis . . . . .	226

## LIST OF TABLES

1	Our T Tauri Sample . . . . .	71
2	HCN Short-Low Measurements . . . . .	75
3	HCN Short-High and Smoothed & Resampled Measurements . . .	76
4	Correlation Between SH and SL HCN Emission . . . . .	79
5	Correlations Between Stellar Parameters & SL HCN Emission . . .	80
1	Summary of Observations . . . . .	113
3	TAP Model Fitting Results . . . . .	115
5.1	Observing Log . . . . .	157
5.2	Observing Platform Details . . . . .	158
5.3	Derived Stellar Parameters . . . . .	159
5.4	Lines Measured, Equivalent Widths, and Abundances . . . . .	160
5.5	Oxygen Abundances Derived from Different Indicators . . . . .	161
5.6	Elemental Abundances and Ratios . . . . .	162
5.7	Abundance Sensitivities . . . . .	163
5.8	Comparison of Average C & O Measurements to Previous Work .	164
6.1	Lines Measured, Equivalent Widths, and Abundances . . . . .	180
6.2	Derived Stellar Parameters . . . . .	180
7.1	Derived Stellar Parameters and Elemental Abundances for 55 Cnc	204
7.2	Lines Measured, Equivalent Widths, and Abundances . . . . .	205
7.3	55 Cnc Carbon and Oxygen Abundances from Different Indicators	206
7.4	C/O Ratios of 55 Cnc Based on Different C and O Abundance In- dicators . . . . .	207

## ABSTRACT

What physical processes and sources of material contribute to exoplanet compositions? Specifically, what roles do the protoplanetary disk composition and structure, and host star abundances play in the different stages of planet formation? In this thesis, beginning with a brief literature review in Chapter 2, I trace oxygen and carbon species through these stages to inform how, when, and where planets form.

In Chapter 3 I describe a study of the molecular emission from the warm inner disks of T Tauri stars, where terrestrial planets likely form. I report moderate correlations between HCN emission strength and both stellar accretion rate (measured from UV or optical excess emission associated with accretion) and X-ray luminosity. These correlations point towards accretion related processes being an important source of disk atmosphere heating, and suggests that efficient  $\text{H}_2\text{O}$  formation and/or UV dissociation of  $\text{N}_2$  (both also associated with higher stellar accretion rates) may aid in the production of HCN. Studies following mine have further connected the abundance of HCN versus  $\text{H}_2\text{O}$  to the growth and migration of planetesimals in the disk, which helps control the formation of both giant and terrestrial planets.

I shift to an already-formed exoplanet in Chapter 4, where I present optical photometry of the best-observed transiting super-Earth GJ 1214b with the goal of constraining the short-wavelength slope of its transmission spectrum. Most previous observations suggested a flat spectrum from the near-IR to the optical, corresponding to a low-scale-height, high-molecular-weight atmosphere. My observations are in general agreement with these findings, keeping the “door open” for a  $\text{H}_2\text{O}$ -rich atmosphere for GJ 1214b, which other published  $g$ -band observa-

tions appeared to contradict.

Chapters 5-7 of my thesis focus on measuring stellar abundances, particularly C/O ratios, in transiting (mostly) hot Jupiter exoplanet host stars from high resolution optical spectroscopy. Host star abundances may indicate the precursor materials present in the disk and available for incorporation into planets. In hot Jupiters, the C/O ratio affects the partitioning of C in the major observable molecules, making C and O diagnostic of temperature structure and composition. I also demonstrate that extra caution is necessary in deriving carbon and oxygen abundances, especially for cool and metal-rich stars. Though exoplanetary C/O ratios are still uncertain, the more precise abundance analysis possible right now for their host stars can help constrain their formation environments and current compositions. I summarize my graduate school research in Chapter 8, and discuss the next steps I will take in my postdoctoral career.

## CHAPTER 1

## INTRODUCTION

Within the last 20 years, and particularly during the time I have been in graduate school, the search for and discovery of planets outside of our Solar System has accelerated dramatically, exposing the great diversity in the outcomes of planet formation and evolution within our Galaxy. The raw material for planet formation appears to be common – nearly every star within Taurus and Orion star-forming regions 1 Myr or less has a disk with enough mass to make a planetary system (Youdin & Kenyon 2013; Williams & Cieza 2011). From broad searches for radial velocity, microlensing, and transit planetary signatures, statistical estimates indicate that on average every star in our Galaxy hosts at least one planetary companion (e.g., Cassan et al. 2012; Batalha et al. 2013; Swift et al. 2013; Tuomi et al. 2014). Petigura, Howard, & Marcy (2013) predict, based on the independent analysis of *Kepler* photometry by, that one in five stars has an Earth-sized planet in the habitable zone (where a terrestrial mass planet can sustain liquid water on its surface [Huang 1959; Hart 1978; Kasting et al. 1993]). It is evident that the Solar System is by no means the typical exoplanetary system configuration, but only one of many possibilities. Out of the many different characteristics of exoplanetary systems that we can study in order to understand the origins of their observed diversity, I am most interested in chemical composition, as it is crucial for confirming habitability. In this thesis I focus on observationally constraining the atmospheric compositions of both exoplanets and their host stars.

The living mass on Earth is dominated (making up  $\sim 96\%$ ) by the most prevalent elements in the universe – hydrogen, oxygen, carbon, and nitrogen (Bergin 2013). Oxygen’s dominance originates from the high  $\text{H}_2\text{O}$  content in living or-

ganisms, while carbon is foundational to the chemistry and energy generation of life on our planet. The “holy grail” of exoplanet science would be to find an Earth-like, habitable planet, perhaps with a similar composition as our own. This discovery will rely heavily on determining what exoplanets are made of, through the study of the material from which they are formed and by collecting and interpreting spectra of their atmospheres. Water (as vapor and/or ice) is observed in many star and planet nurseries through the Galaxy (Cernicharo and Crovisier 2005; Boogert et al. 2008; Melnick 2009; Bergin & van Dishoeck 2012), throughout the Solar System in all the planets, the Moon, comets, Kuiper belt objects, the satellites of giants planets, some asteroids (e.g., Rivkin et al. 2002; Jewitt et al. 2007; Encrenaz 2008), and even in other galaxies (e.g., Shimonishi et al. 2010; Lis et al. 2011; Weiß et al. 2013). It acts as a coolant in gas that allows interstellar clouds to collapse to form stars, and facilitates the coagulation of small dust particles that grow to form planetesimals and planets. Water is an effective solvent due to its dipole nature, helps transport biological molecules throughout organisms, and promotes the decomposition of ATP, the critical medium of chemical energy transport within cells. Carbon, with its potential to share four bonds and bond readily with itself, is the main reservoir of electrons in diffuse interstellar clouds, helping to both heat and cool gas, and is found in >75% of interstellar molecules (Henning & Salama 1998). Carbon is also prominent in (carbonaceous) dust and on grain surfaces/within grains (Herbst & van Dishoeck 2009), comets (e.g., Delsemme 1991; Greenberg 1998) and its abundance relative to other elements helps characterize primitive meteorites. This thesis concentrates on the abundances of oxygen and carbon carrying molecules in exoplanets and the elements C and O in their host stars, as these are the third and fourth most abundant elements in the universe and make up readily observable features in both stars

and planets.

While solar-type stars have atmospheres composed mostly of atoms and their ions, and are characterized broadly by their masses and metallicities, cooler planets have atmospheres more rich with molecules whose observations can be more challenging to interpret. Planetary atmospheres serve as potential records of formation processes/conditions, accretion history, and geophysical modification. They can suffer intense (and often, in the case of hot Jupiter exoplanets, anisotropic) radiation from their host star(s), have steep temperature gradients and inversions, experience complex photochemistry and/or other disequilibrium processes, and host multi-component, time-varying clouds. And yet, all of these processes are active areas of study in exoplanet science and can be better understood with observations that are possible right now. In particular, the latter part of my thesis focuses the comparison of exoplanet compositions to their host stars can provide insight into formation conditions and evolutionary history.

The suite of exoplanets for which some aspects of their atmospheres may be characterized, either through primary or secondary eclipse, now spans a wide range of planet masses and temperatures, including highly irradiated “hot Jupiters” ( $T \sim 1300\text{--}3000$  K), warm but more widely separated gas giants ( $T \sim 500\text{--}1500$  K), smaller “hot Neptunes” ( $T \sim 700\text{--}1200$  K), and cooler “super-Earths” ( $T \sim 500$  K) that still possibly possess significantly massive gaseous atmospheres. Notably many exoplanets have no analogs in our Solar System, and thus present new problems to solve and opportunities to learn about planet formation; comparative studies can enhance our understanding of our own Solar System planets’ formation and evolution, and perhaps even the origins of life on Earth. Photometric and spectroscopic observations from either/both ground and space have been reported for  $\gtrsim 50$  transiting exoplanets and a handful of directly-imaged exoplan-

ets, and show signs of the molecules  $\text{H}_2\text{O}$  (detected frequently),  $\text{CO}$ ,  $\text{CO}_2$ ,  $\text{CH}_4$  (see Madhusudhan et al. 2014 and Tinetti et al. 2013 for a review of the extensive list of publications), which are predicted to dominate (e.g., Burrows & Sharp 1999; Lodders & Fegley 2002; Burrows, Budaj, & Hubeny 2008; Maudhusudhan & Seager 2009), as well as atomic K and Na (e.g., Charbonneau et al. 2002, Redfield et al. 2008; Colon et al. 2010), and (in a few cases) atmospheric escape of atomic species (e.g., Vidal-Madjar et al. 2003, 2004; Ben-Jaffel 2007, 2008; Lacavelier des Etangs et al. 2010, 2013; Fossati et al. 2010; Linsky et al. 2010). It is through dedicated observing campaigns like that for super-Earth GJ 1214b (e.g., Kreidberg et al. 2014), and other well-studied hot Jupiter systems like HD 189733b, HD 209458b, and WASP-12b, that enough data may be accumulated to infer with some level of confidence the atmospheric compositions of exoplanets.

In the following Chapter 2 I summarize how planet formation proceeds from the initial host star birth, through the build up of material through protoplanetary and debris disks, and the growth of both gas and terrestrial planets. In the instances/stages that overlap specifically with observations conducted for this thesis, I outline the physical processes responsible for the observed parameters and interpretation of them. Before the published Chapters begin, I connect the stages of planet formation through the role that carbon and oxygen species play in each stage, and how they can be traced through stages to inform how, when, and where planets form.



## CHAPTER 2

### OVERVIEW OF STAR & PLANET FORMATION

This Chapter is intended as only a broad literature review of star and planet formation. It is unpublished.

#### 2.1 Stage 1: Stars

##### 2.1.1 Brief Outline of Stellar/Galactic Chemical Evolution

The chemical components that eventually go into planets originate from the earliest phases of the stellar formation. Stars are born from low density, cold, giant molecular clouds that fragment, having collapsed or gathered by some dynamical event (Ballesterro-Paredes et al. 2007; Mac Low & Klessen 2004; Dobbs 2013), and condense into pre-stellar cores with densities high enough ( $\geq$  a few  $10^4 \text{ cm}^{-3}$ ) to shield molecules from destructive interstellar radiation (Bergin et al. 2004; Clark et al. 2012). At the low temperatures of pre-stellar cores, gas-phase species freeze onto sub-micron grains of dust, while H atoms on the grain surfaces can bond with other atoms and CO to form  $\text{H}_2\text{O}$ ,  $\text{H}_2\text{CO}$ ,  $\text{CH}_3\text{H}$ , and other hydrogenated species (Herbst & van Dishoeck 2009). Once gravity overwhelms the support from thermal pressure or magnetic fields, cores collapse further to form proto-stars (Larson 2003; McKee & Ostriker 2007). These growing stars are surrounded by disks of rotationally-supported gas that have too much angular momentum to fall directly onto the central object (Cassen & Moosman 1981; Terebey et al. 1984), and as gravitational energy is converted into radiation this envelope warms up. The formation of more complex molecular species is possible both on grain surfaces, where the warmer temperatures provide species with more mobility, and in the gas phase once the dust grain mantles sublime. Within  $\sim 0.5 \text{ Myr}$  (Evans

et al. 2009), the star is left with an exposed, volatile gas-rich protoplanetary disk that itself lasts only a few Myr (Williams & Cieza 2011), and is subject to violent outbursts from the star that can further vaporize grains and/or excite gas phase molecules.

Once stars ignite and begin fusion, they can take on the role of Galactic (or extra-galactic) “archeological” markers, helping to distinguish populations of stars that formed at different times and thus with different compositions. Only hydrogen, helium, and a bit of lithium were created during the Big Bang, with all other elements formed in stars (e.g., Burbidge et al. 1957; Meyer & Zinner 2006; Truran & Heger 2003). Thus stellar abundances and kinematic distributions can be studied to understand more broadly how star formation is/was different across the Galaxy and how the main components of the Galaxy (disk, bulge, halo) have changed through time. In particular, the chemical composition of a stellar atmosphere is generally assumed to be indicative of its formation environment. Late-type O, B, and A stars may be used to probe the present composition of the Galaxy, since their massive predecessors have already died (though in some cases these stars can be affected by diffusion or accretion). Later-type F and G stars span an age range matching that of the Galaxy and have convection zones deep enough to erase abundance changes induced by diffusion or accretion, but shallow enough that elements from the interior are brought to the surface (Nissen 2011); thus they are good stellar population tracers, as are K giants, which can be observed at greater distances (Nissen 2011).

On the main sequence, stars burn hydrogen into helium via the proton-proton chain and CNO cycle reactions, wherein the latter C, N, and O isotopes inherited from earlier stellar generations serve as catalysts. Once the core has burnt up its hydrogen, contraction sufficiently increases the temperature and density and

the star becomes a red giant, eventually igniting helium burning in the core. At this stage, convection brings the products of hydrogen burning to the surface, most notably  $^{13}\text{C}$ ,  $^{14}\text{N}$ , and  $^{17}\text{O}$  (Marty, Alexander, & Raymond 2012). The triple alpha process bridges the large mass gap between helium and carbon, and this efficient production of carbon, versus the less efficient production of oxygen via the addition of another helium atom, influences the presence of carbon versus oxygen in the universe (Henning & Salama 1998).

When the core helium is spent, the stars move along the asymptotic giant branch (AGB), and a hot central mass of carbon and oxygen builds below helium- and hydrogen-burning shells. In  $\sim 3\text{-}10 M_{\odot}$  stars, a deep convection zone can bring  $^{12}\text{C}$  from the helium burning region of the star out to the surface (a “second dredge up”). In  $\lesssim 4 M_{\odot}$  stars, this results in a rapid increase in the  $^{12}\text{C}/^{13}\text{C}$  and C/O ratios, and the envelope’s C/O ratio can exceed 1. For more massive stars ( $\sim 4\text{-}10 M_{\odot}$ ), “hot bottom burning” destroys much of the added  $^{12}\text{C}$ , keeping the  $^{12}\text{C}/^{13}\text{C}$  ratio low and  $\text{C/O} < 1$ . AGB stars are important precisely because they transport C and O material to the surface, and then lose these envelopes in massive stellar winds. Red giant stars whose photospheres become particularly carbon-rich (so-called classical carbon stars) are the largest producers of stardust or “smog” in the universe, which forms when the carbon atoms in their cool stellar winds stick together. The total production rate of carbon from these stars is  $\sim 0.002 M_{\odot}/\text{year}$  (Henning & Salama 1998).

For less massive stars, an inert white dwarf core is left behind at the end of their lives, mostly composed of  $^{12}\text{C}$  and  $^{16}\text{O}$ . If in a binary, a white dwarf can accrete enough mass from its companion to ignite carbon fusion and, unable to regulate pressure and temperature like a main sequence star due to degeneracy pressure, it explodes due to the immense energy release. As more massive  $\sim 10\text{-}$

$25 M_{\odot}$  stars leave the main sequence, they also experience convective dredge-ups that bring CNO cycle products to the surface, but not He-burnt material, so their C/O ratios remain  $<1$ . The internal structure of one of these massive stars prior to Type II SN explosion consists of concentric shells of more and more advanced nucleosynthetic processing. The two major products of Type II SN are still  $^{12}\text{C}$  and  $^{16}\text{O}$ , but further “burning” can occur during the explosion, producing elements even heavier than Fe. In the early history of the Galaxy, massive stars were the main chemical contributors; with time, intermediate mass stars have contributed more material to the Galaxy. These changes are observable by comparing products produced more prevalently by massive stars (e.g., O) to those produced more by low mass stars (e.g., C, Fe).

For instance, the flat trend between observations of  $[\text{C}/\text{Fe}]$  vs.  $[\text{Fe}/\text{H}]$  in stars is evidence that Galactic carbon enrichment likely happens on the same timescale as the enrichment of Fe from SNe Ia (Bensby & Feltzing 2006; see Figure 2.1). This is in contrast to the clear break and subsequent downturn in  $[\text{O}/\text{Fe}]$  vs.  $[\text{Fe}/\text{H}]$ , which indicates the importance of (early-formed) massive stars’ Type II SNe in Galactic oxygen enrichment. The distributions of  $[\text{C}/\text{O}]-[\text{O}/\text{H}]$  and  $[\text{Fe}/\text{O}]-[\text{O}/\text{H}]$  show a gradual increase with  $[\text{O}/\text{H}]$  in thin disk stars, but an initial flat trend followed by a sharp increase around  $[\text{O}/\text{H}]=0$  in thick disk stars. The resulting picture is that carbon enrichment at low metallicities (in the Galactic halo and metal-poor thick disk) is due to massive stars, but that with time, as more low and intermediate mass stars evolve, they dominate the carbon enrichment of the ISM as seen in thin disk stars and the metal-rich thick disk population (Bensby & Feltzing 2006; Fabbian et al. 2009; Carigi et al. 2005). I discuss these trends, and how my results on exoplanet host stars relate to them, further in Chapters 5-7.

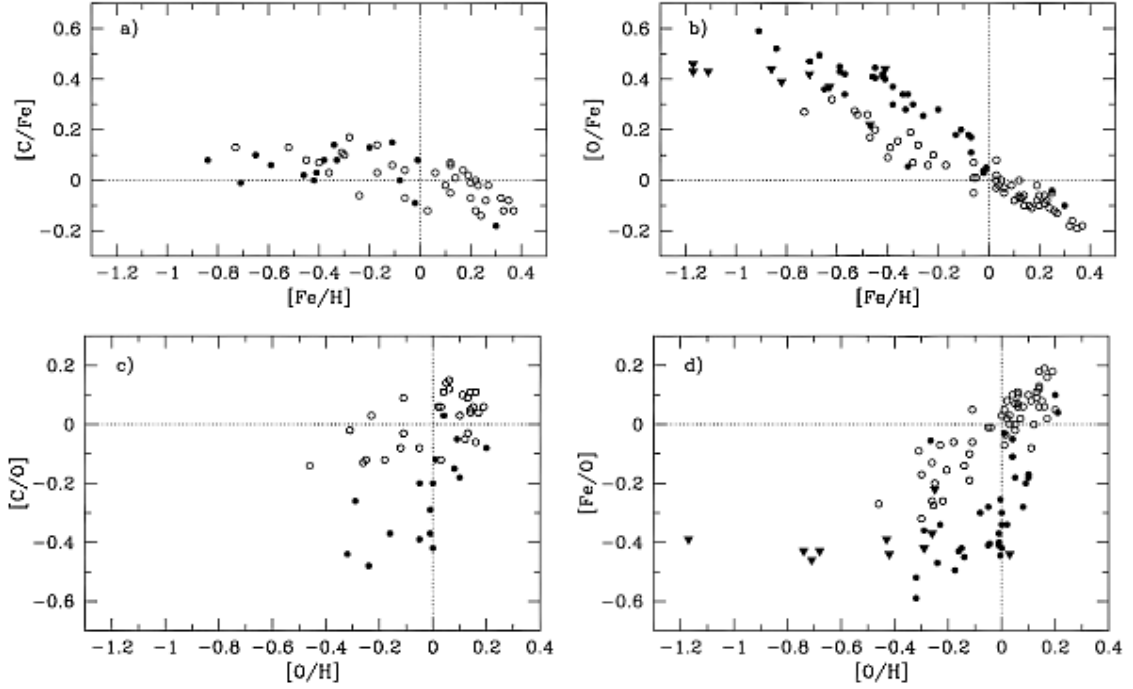


Figure 2.1 Figure 11 from Bensby & Feltzing (2006), showing from their sample of nearby F and G dwarf stars (a and b) carbon and oxygen abundances relative to iron, and (c and d) carbon and iron abundances relative to oxygen. Thin and thick disk stars are indicated by open and filled circles, respectively, and a few thick disk stars from Nissen et al. (2002) are included as filled triangles in panels b and d.

### 2.1.2 Measuring Stellar Composition

In order to study how stellar composition has changed through space and time, and, for this thesis, how stellar and planetary compositions compare, one may use high-resolution optical spectra of stars to probe their upper atmospheres (photospheres). One can measure the strength of elemental absorption lines (usually Fe, as described below), and combine these measurements with assumptions/simplifications about how the stellar atmosphere behaves to derive basic

parameters like temperature, pressure, metallicity, and turbulence. Once the physical environment of the star is established, the differences in absorption line strength and shape for many more elements can be connected to their relative abundances within the star, through additional equivalent width measurements of these elements' lines and/or comparing these elements' lines to synthesized stellar models that vary only one elemental abundance at a time.

The stellar atmosphere being analyzed can be approximated (following Gray 2005) as a plane-parallel homogenous (one-dimensional) slab, and assumed to be in local thermodynamic equilibrium (LTE), such that the distributions of atoms over all possible excitation and ionization states are governed by the Boltzmann equation

$$\frac{N_n}{N} = \frac{g_n}{u(T)} e^{-\chi_n/kT} \quad (2.1)$$

where  $k$  is Boltzmann's constant,  $N$  is all atoms of the same species,  $N_n$  is the number of atoms of that species per unit volume in level  $n$ ,  $g_n$  is the statistical weight,  $\chi_n$  is the excitation potential of level  $n$ , and  $u(T) = \sum g_i e^{-\chi_i/kT}$  (the partition function), and the Saha equation

$$\frac{N_1}{N_0} P_e = \frac{(2\pi m_e)^{3/2} (kT)^{5/2}}{h^3} \frac{2u_1(T)}{u_0(T)} e^{-I/kT} \quad (2.2)$$

where  $\frac{N_1}{N_0}$  is the ratio of ions to neutrals,  $\frac{u_1}{u_0}$  is the ratio of ionic to neutral partition functions,  $m_e$  is the electron mass,  $I$  is the ionization potential,  $h$  is Planck's constant, and  $P_e$  is the pressure of the free electrons in ionized gas,  $N_e kT$  (Gray 2005).

The stellar atmosphere's emergent flux, and thus the measured spectral line fluxes, are governed by the radiative transfer equation, describing how energy flows across an specific area element  $\Delta A$ , within a specific solid angle  $\Delta\omega$ , in a

time  $\Delta t$ , and a  $\Delta\nu$  spectral increment:

$$I_\nu = \frac{dE_\nu}{\cos\theta dA d\omega dt d\nu}$$

$$dI_\nu = \kappa_\nu \rho I_\nu ds + j_\nu \rho ds$$

(2.3)

where  $\kappa_\nu$  is the total absorption coefficient (including scattering),  $\rho$  is the mass density per unit volume, and  $j_\nu$  is the emission coefficient. Defining  $\ell_\nu$  as the pure absorption coefficient, the opacity is

$$d\tau_\nu = (\ell_\nu + \kappa_\nu) \rho dx$$

(2.4)

and the source function is

$$S_\nu = \frac{j_\nu^\ell + j_\nu^c}{\ell_\nu + \kappa_\nu}$$

(2.5)

where  $j_\nu^\ell$  is the line emission coefficient and  $j_\nu^c$  is the continuum emission coefficient. Equation 1.3 can then be written simply as

$$\frac{dI_\nu}{d\tau_\nu} = -I_\nu + S_\nu$$

(2.6)

In the case of LTE emission,

$$S_\nu = \frac{2h\nu^3}{c^2} \frac{1}{e^{h\nu/kT} - 1}$$

(2.7)

or  $S_\nu = B_\nu$ , in the case of black-body radiation. The flux is then

$$\mathfrak{F} = 2\pi \int_0^\pi I_\nu \cos(\theta) \sin(\theta) d\theta$$

(2.8)

where  $\theta$  is the angle between surface normal and the observer's line of sight. At the surface ( $\tau_\nu=0$ ),

$$\mathfrak{S}(0) = 2\pi \int_0^\infty S_\nu(\tau_\nu) E_2(\tau_\nu) d\tau_\nu \quad (2.9)$$

where  $E_2$  is an exponential integral (see Gray 2005, Chapter 7 for the full derivation).

To see how the resulting line profile is related to the derived quantities of the star (particularly abundance associated with the measured element's lines), the surface flux can be computed by assuming a temperature distribution is known as a function of  $\tau_0$ , a reference optical depth scale (usually 5000 Å) as:

$$\begin{aligned} \mathfrak{S}(0) &= 2\pi \int_0^\infty S_\nu(\tau_\nu) E_2(\tau_\nu) d\tau_\nu \\ &= 2\pi \int_0^\infty B_\nu(T) E_2(\tau_\nu) \frac{d\tau_\nu}{d\tau_0} d\tau_0 \\ &= 2\pi \int_0^\infty B_\nu(T) E_2(\tau_\nu) \frac{\ell_\nu + \kappa_\nu}{\kappa_0} \tau_0 \frac{d\log \tau_0}{\log e} d\tau_0 \end{aligned} \quad (2.10)$$

The opacity  $\tau_\nu$  is computed with ( $t_0$  is a dummy variable)

$$\tau_\nu(\tau_0) = \int_{-\infty}^{\log \tau_0} \frac{\ell_\nu + \kappa_\nu}{\kappa_0} t_0 \frac{d\log t_0}{\log e} \quad (2.11)$$

The continuous absorption coefficient is composed of the absorption from several physical process, including neutral hydrogen bound-free and free-free absorption, bound-free and free-free absorption by the  $H^-$  ion, and molecular hydrogen absorption, which must be reduced by the stimulated emission factor  $1 - e^{-h\nu/kT}$ , as well as absorption by helium and metals and electron scattering. The total absorption coefficient sums all of these contributions; it can then be written in  $\text{cm}^{-2}/\text{g}$  as



$$\kappa_\nu = \frac{\kappa_{total}}{\sum A_j \mu_j} \quad (2.12)$$

where  $\mu_j = 1.6606 \times 10^{-24} \text{ g} \times$  the element's atomic weight,  $A_j$  is the number abundance relative to H. The line absorption coefficient  $\ell_\nu$  is fully defined in Gray (2005) equations 11.38-11.55, but what is important is that there is a dependence of  $\ell_\nu$  on  $g_n A f$ , the statistical weight of the lower level  $\times$  abundance  $\times$  the oscillator strength. By measuring the equivalent width of a line,

$$W = \int_0^\infty \frac{\mathfrak{S}_\nu - \mathfrak{S}_c}{\mathfrak{S}_c} d\nu \quad (2.13)$$

where  $\mathfrak{S}_\nu$  is the surface flux and  $\mathfrak{S}_c$  is the continuum flux (without  $\ell_\nu$ ), with a known  $g_n$  and  $f$ , the abundance is the remaining variable to be determined. Following the derivation given in Gray (2005), eq. 16.1-16.4, the total flux for a line on the weak part of the curve of growth, divided by its  $\lambda$  as is customary to normalize effects of turbulences and thermal broadening, is

$$\log\left(\frac{W}{\lambda}\right) = \log C + \log A + \log g_n f \lambda - \theta_{\text{ex}} \chi - \log \kappa_\nu \quad (2.14)$$

where  $C$  is a constant defined in Gray (2005) equation 16.4 and  $\theta_{\text{ex}} = 5040/T$ . Thus, from a measurement of a photospheric line, with a known  $g_n f \lambda$  and  $\chi$  (excitation potential), and with a set (model-determined)  $\theta_{\text{ex}}$  and  $\kappa_\nu$ , curves of growth for the measured species can be generated by plotting the measured  $\log(W/\lambda)$  as a function of  $\log(w/\lambda) - \log A$ , calculated with equation 1.15 above as  $\log C + \log g_n f \lambda - \theta_{\text{ex}} \chi - \log \kappa_\nu$ . This is the formal approach adopted by the spectral analysis program MOOG (Snedden 1973) that I use in my stellar parameter and abundance determinations, which follows the specific formulation of Edmond (1969).

From the equations above, one can deduce that the spectral line shapes are sensitive to temperature (through  $N_j/N_E$ ,  $\kappa_\nu$ , and  $\theta_{\text{ex}}$ ) and surface gravity (through

$N_{r^{th} \text{ ionization stage}}/N_E$  and  $\kappa_\nu$ ). The microturbulence velocity parameter was introduced to account for the equivalent widths of saturated lines being greater than predicted by thermal+damping broadening models (and is related to  $\Delta\nu_D$ , see equation 11.45 in Gray 2005). To determine a star's physical parameters, one may use measured equivalent widths of a prevalent and multiply ionized species, usually Fe, to satisfy the necessary excitation balance (setting the temperature,  $T_{\text{eff}}$ ), ionization balance (setting the gravity,  $\log g$ ), and minimize the trend between  $\log N(\text{Fe I})$  and the observed reduced equivalent width (setting the microturbulence,  $\xi$ ).

Practically, first a stellar spectrum is normalized to a continuum value of  $\sim 1$  by fitting a multi-order polynomial. Then the equivalent widths (EWs) of weak (not saturated) Fe lines are measured by fitting them with a Gaussian profile, or if significant wings are present, a Voigt profile. The Fe I and Fe II EWs measured (and in some cases, additional species like Ti and/or Cr) are then used in the three ways mentioned above to determine the stellar atmosphere that best matches the environment that created the observed line strengths. The number of atoms at level  $i$  scales as (using the prescription of Takeda 2002)

$$\begin{aligned} n_i^I &\propto \epsilon T^{-3/2} n_e e^{(\chi_{ion} - \chi_i)/(kT)} \\ n_j^{II} &\propto \epsilon e^{-\chi_j/(kT)} \end{aligned} \quad (2.15)$$

where  $n_i^I$  is for neutral atoms,  $n_j^{II}$  is for ionized atoms,  $\epsilon$  is the Fe abundance,  $n_e$  the electron density,  $\chi_{ion}$  is the Fe ionization potential, and  $\chi_i$  is the excitation potential of level  $i$ . These relations can then be connected back to the line opacity

$\ell$  with

$$\begin{aligned}\ell_i^I &\propto \epsilon T_{eff}^{-3/2} g^{1/3} e^{(\chi_{ion}-\chi_i)/(kT_{eff})} \\ \ell_i^{II} &\propto \epsilon e^{-\chi_j/(kT_{eff})}\end{aligned}\tag{2.16}$$

assuming that the electron pressure scales as  $\propto g^{1/3}$  (e.g., Gray 2005, eq.9.20). As noted above, the line strength is actually determined by the ratio of the line opacity  $\ell$  to the continuum opacity  $\kappa$ . The main contribution to  $\kappa$  is  $H^-$  opacity, which scales with  $n_e$  similarly to  $\ell_i^I$  (e.g., Gray 2005, eq. 13.25), meaning in  $\ell^I/\kappa$  the  $g$ -dependence cancels while a new  $g^{-1/3}$  factor is introduced to  $\ell^{II}/\kappa$ . Thus,

$$\begin{aligned}\epsilon^I &\propto T_{eff}^{+3/2} e^{-(\chi_{ion}-\chi_i)/(kT_{eff})} \\ \epsilon^{II} &\propto e^{+\chi_j/(kT_{eff})} g^{+1/3}\end{aligned}\tag{2.17}$$

and we can see that the Fe abundances from Fe I lines increase with increasing  $T_{eff}$  but do not depend strongly on  $\log g$ , while those from Fe II lines decrease with increasing  $T_{eff}$  but increase with increasing  $\log g$ . Utilizing the Fe I relation,  $T_{eff}$  can be constrained by requiring that Fe I lines with different excitation potentials produce the same abundance. Utilizing the Fe II relation, and the condition of ionization equilibrium (abundances derived from Fe I should be equal to those derived from Fe II),  $\log g$  can be constrained. Additionally, since  $\xi$  preferentially affects the stronger lines, while weaker lines remain essentially  $\xi$ -independent,

this parameter is determined by requiring that abundances from Fe I lines show no dependence on their (reduced) equivalent widths ( $\log(EW/\lambda)$ ).

Because a variation in  $T_{eff}$  will change both Fe I and Fe II abundances ( $\log N(\text{Fe I})$  and  $\log N(\text{Fe II})$ ), changing  $T_{eff}$  could also change  $\log g$ ; none of the stellar parameters are completely independent. Hence, to determine the best atmospheric parameters ( $T_{eff}$ ,  $\log g$ ,  $\xi$ , and  $[\text{Fe}/\text{H}]$ ), an iterative scheme of testing how stellar model conditions affect the correlations between  $\log N(\text{Fe I})$  and  $\xi$ ,  $\log N(\text{Fe I})$  and  $(\log(EW/\lambda))$ , and how closely  $\log N(\text{Fe I})$  and  $\log N(\text{Fe II})$  match is implemented. This process is detailed further, and the error determination explained, in Chapters 5-7.

## 2.2 Stage 2: Disks

The next stage of stellar and planet formation, protoplanetary disk, is where many chemical properties and the initial architecture of the eventual planetary system are set. It is also during this stage that much of the mass of the star is built up from accretion of material through the disk (Najita et al. 2007). Disks evolve with time as gas disperses and particles mix and grow, changing their orbits with respect to the gas (Hughes & Armitage 2010). The condensation fronts of the most prevalent molecular species change as the temperature, pressure, and chemical structure of the disk changes, thereby affecting which species are in solid versus gas phase at specific locations within the disk. The lifetime of gas in the inner disk, limited by accretion onto the star, external radiation and photoevaporation, grain growth, etc., places an upper limit on the time available for giant planet formation (Zuckerman et al. 1995; Najita et al. 2007). The significant inward migration of large gas giant exoplanets from their likely formation distances (e.g., Ida & Lin 2004) indicates they must interact with a still-gas-rich disk.

Afterwards, residual gas left over in the inner terrestrial planet forming region may play an important role in defining the final masses, eccentricities, and compositions of smaller planets. Thus, disks have the potential to provide a window into the physical processes controlling both small and large planet formation.

Protoplanetary disks form as a result of angular momentum conservation during the rapid growth of a new star through gravitational collapse. Most of the material in the original envelope surrounding the star is rapidly funneled onto it, and after the initial collapse and embedded disk phases, so-called “class 0” and “class I”, lasting about 0.5 Myr (Evans et al. 2009), the remaining disk material is only a few % of the central stellar mass (Caselli & Ceccarelli 2012). While the disk gradually spreads out with time, far-UV photoevaporation restricts the outer edge of the disk, limiting viscous expansion to  $\sim$ several hundreds of AU (Gorti, Dullemond, & Hollenbach 2009). As the star continues to accrete disk material, solid particles can settle and grow in the more quiescent midplane of the disk, decreasing the observed scale height of the disk and thus the amount that is impinged upon by stellar radiation. This affects the observed slope of stellar spectral energy distributions (SEDs), and is a method for tracking disk evolution (described more below). In the inner disk, once the photoevaporation rate due to the stellar chromosphere exceeds the inward accretion rate, the inner disk drains of material in  $\lesssim 0.1$  Myr and forms an inner, few-AU-wide hole. This weakening of accretion marks the transition from a “classical T Tauri” phase to a “weak T Tauri” phase, and is followed by rapid disk dissipation. Results from large *Spitzer* Legacy observational programs have shown that  $\sim 80\%$  of young weak T Tauri stars have lost their disks of micron-sized dust (as probed by  $24\ \mu\text{m}$  flux); the entire disk disappears quickly after gas is no longer funneling onto the star (Padgett et al. 2006, Cieza et al. 2007, Wahhaj et al. 2010). In summary, the disk

evolves from opaque, to opaque with an inner hole, to optically thin/transparent on a timescale of  $\sim 10$  Myr (Mamajek et al. 2004; Sicilia-Aguilar et al. 2005; see also references in Williams & Cieza 2011).

It is on the classical T Tauri phase that Chapter 3 focuses, specifically the inner warm region of the disk where terrestrial planets likely form. For blackbody grains, a water condensation temperature of 180 K (at a pressure of  $10^{-4}$  bar) implies that the snow line – the transition region in the disk from water in the vapor to water in the gas phase – occurs at  $\sim 3$  AU, which is roughly where the asteroid belt is in our Solar System (Youdin & Kenyon 2013). It is within the  $\sim 1$ -5 AU region that the observations in Chapter 2 originate. Such NIR and MIR observations, particularly those of *Spitzer*-IRS, have shown that this region is rife with water and simple organic molecules in many (mostly T Tauri) disks (Carr & Najita 2008; Salyk et al. 2008; Pontoppidan et al., 2010; Salyk et al., 2011; Carr & Najita 2011). Interestingly, while the strength of  $\text{H}_2\text{O}$  lines seems relatively constant among most stars observed, the strength of organic species varies, as I discuss in the next section below and in Chapter 2.

Beyond the flared wall structure that was deduced from large far-IR excesses (Kenyon & Hartmann 1987) and confirmed by HST images (Burrows, Stapelfeldt, Watson, et al. 1996; Padgett, Brandner, et al. 1999), a so-called “photon-dominated region” (PDR) is exposed to stellar and interstellar UV radiation as well as X-ray radiation from the still very active central star. Below the PDR exists a warm molecular layer where photochemistry may still occur (Henning et al. 2010; Aresu et al. 2012), but where radical and ion species dominate gas compositions (Semenov 2011). Even further below, in the midplane of the disk, molecular freeze-out becomes relevant and larger dust grains with icy mantles can grow (Dullemond et al. 2007). It is these growing solid particles that will form the cores of

giant planets, and perhaps terrestrial planets.

### 2.2.1 Observational Constraints of Disk Physical Processes and Composition

Though gas is 99% of the total mass of the ISM, and also of protoplanetary disks at the beginning of their evolution, the detection of gas is difficult because it emits at very specific wavelengths, versus dust features that are identified through broad spectra bands, requiring high resolution spectroscopy. The majority of the opacity in disks is due to dust, and at wavelengths where dust emission is optically thick a gaseous line can only be distinguished if its excitation temperature differs from that of the dust (Williams & Cieza 2011). Recombination line emission and excess hot emission due to accretion of gas onto the central star indicate that indeed the gas is present, but determining its amount or physical conditions requires further observational diagnostics (Hartmann 2009).

Here I focus on the warm inner disk, as this is the topic of Chapter 3. Though this region is too small to be spatially resolved, high spectral resolution observations distinguish the different velocities of gas at different distances away from the host star (Najita et al. 2007). Molecules are abundant in the gas phase at the warm temperatures ( $\sim 100\text{--}5000\text{ K}$ ) and high densities ( $\gtrsim 10^{21}\text{ cm}^{-2}$  column density) within  $\lesssim 5\text{ AU}$ , and can be observed in emission or absorption if the temperature in the disk increases or decreases with height (Calvet et al. 1991; Malbet & Bertout 1991). When the gas is optically thick, the observed spectral features probe only the upper atmosphere of the disk, analogous to the upper atmospheres of stars probed by the observations detailed in the first section. Optically thin regions can arise from dust sublimation (e.g., Carr 1989) or grain coagulation, or if there is a decrease in the actual column density of the gas in the disk, e.g., from a giant planet forming a gap in the disk or when the gas in the disk is dissipating (in late stages of disk evolution). As opposed to the majority of stellar

spectral features, which are dominated by atoms, the molecular spectra of inner disks are more complex. Electronic transitions ( $\Delta E \sim 1$  eV) are generally observed in the UV from diffuse, low density molecular gas in absorption, but can arise in disks as emission features, too. Vibrational modes of lower energy ( $\sim 0.01$ -1 eV) are observed in warm dense regions like the inner disk; emission can occur in vibrating and rotating molecules via ro-vibrational transitions. Lower energy rotation modes are detected at millimeter and submillimeter wavelengths, while higher energy rotational states trace higher temperatures and densities at shorter wavelengths. (Bergin 2013) Thus, emission and absorption of molecular gas in the disk can give us information about a range of different inner disk environments.

The strength of molecular emission varies due to chemical abundance changes and also excitation, so the “retrieval” of volatile abundances – inverting line fluxes and profiles to fundamental physical parameters – is model-dependent and usually iterative (Pontoppidan et al. 2014). One analysis approach is SED fitting, using the whole spectral energy distribution across multiple wavelengths (1-1000  $\mu\text{m}$ ), usually composed of many broad-band photometric observations. Assuming some dust distribution/composition, structural models for the disk are fit, providing the backbone for the fractional abundance structure of the molecular gas (e.g., Zhang et al. 2013; Bergin et al. 2013). Alternatively, the global disk physical structure can be constrained by fixing input elemental abundances in a thermo-chemical model, solving the detailed radiative transfer and chemistry simultaneously, to calculate line fluxes and seeing if they match the data (e.g., Aikawa et al. 2002; Thi et al. 2010; Woitke et al. 2011; Tilling et al. 2012). Both approaches rely on assumptions and result in degeneracies and uncertainties, so that absolute abundances derived from disk observations are still only good to



$\sim$  an order of magnitude (Pontoppidan et al. 2014). In Chapter 3, I take a very simplified approach of only measuring relative strengths of molecular emission features across disks, and comparing these “indices” to different disk properties deduced from other observations (e.g., stellar accretion rate, X-ray luminosity, spectral type) to look for trends that might reveal the cause of the molecular emission.

There are a few prominent molecules, in terms of what has been observed and what we have learned from these observations, that arise from the inner regions of protoplanetary disks. CO is essentially ubiquitous (Brown et al. 2013), abundant over a wide range of temperatures from where it condenses on to grains ( $\sim 20$  K) through where it thermally dissociates ( $\sim 4000$  K at inner disk densities). Hence the CO molecule, readily detected in ro-vibrational lines (Najita et al. 2003; Blake & Boogert 2005), probes the disk from cool outer regions ( $> 100$  AU) to the innermost disk radii. CO overtone transitions ( $\Delta\nu=2$ ,  $\lambda=2.3 \mu\text{m}$ ), requiring  $T \geq 2000\text{K}$  and densities  $> 10^{10} \text{ cm}^{-3}$ , were the emission lines first associated with the gaseous inner disk (Scoville et al. 1983; Carr 1989; Calvet et al. 1991). Broad velocity profiles ( $> 100 \text{ km s}^{-1}$ ) indicate that CO overtone emission extends from very close to the star,  $\sim 0.05$  AU, out towards  $\sim 0.3$  AU in low mass (Chandler et al. 1993; Najita et al. 2000) or even out to  $\sim 3$  AU in high mass stars (Blum et al. 2004; Bik and Thi 2004). Though CO overtone emission is detected in only a small fraction of disks, these sources often show large near-infrared excesses indicating an optically thick disk, implying that the CO gas emission arises from a vertical temperature inversion in the upper disk atmosphere (that has lower continuum opacity) (Najita et al. 2003). The source of the heating could include UV (Calvet et al. 1991; DAlessio et al. 1998) or X-ray (Glassgold et al. 2004) radiation from the star, turbulent heating within the disk atmosphere perturbed by a stellar wind

flowing over the disk surface (Carr et al. 1993), and/or disk accretion dissipating turbulence (Glassgold et al. 2004). Evidence based on distinguishing intrinsic versus (macroscopic) rotational line broadening in CO overtone emission suggests that turbulence is key in heating disk atmospheres (Carr et al. 2004, Najita et al. 1996; Hartmann et al. 2004). Besides stellar wind generating turbulence over the disk surface, the magnetorotational instability (MRI; Balbus & Hawley 1991) or baroclinic instability (Klahr & Bodenheimer 2003) may induce turbulent angular momentum transport in disks.

The  $\Delta\nu=1$  fundamental CO transitions around  $4.6\ \mu\text{m}$  are found in a larger number of disks because of the lower temperature (1000-1500 K) and column density ( $\sim 10^{18}\ \text{cm}^{-2}$ ) requirements for excitation. Emission lines from multiple vibration state transitions are typically detected, making the CO fundamental lines a powerful diagnostic of temperature and column density, as well as the excitation mechanism (based on the relative strengths of different transitions) (Najita et al. 2007). The measured fundamental transition line profiles are broad ( $\sim 50\text{-}100\ \text{km s}^{-1}$ ) and only have one peak, versus the double-peaked CO overtone emission, suggesting an origin from  $\lesssim 0.1\ \text{AU}$  out to  $1\text{-}2\ \text{AU}$  in disks around low mass stars (Najita et al. 2003). In fact, for T Tauri systems for which the inclination is known, the measured velocity of the CO emission can be converted into an inner radius, with typical values  $\sim 0.04$  (Najita et al. 2003). This is a smaller radius than interferometry or SED interpretation indicates for dust, consistent with the gaseous disk extending inward farther than the dust component. Interestingly, the number distribution of close-in extrasolar planets has a peak around  $\sim 0.04\text{-}0.05\ \text{AU}$  (Wright et al. 2011), and drops off significantly at smaller radii, roughly consistent with the edge of the inner gaseous disk stopping the inward orbital migration of planets (Lin et al. 1996).

Of interest from an astrobiological perspective is the presence of water and organics in disks. The *Spitzer* IRS instrument has contributed greatly to the detection of these molecules and the understanding of their prevalence and varying strengths in inner protoplanetary disks. Prior to its launch, water was detected in only a few stars that also showed CO overtone emission (Carr et al. 2004; Najita et al. 2000; Thi and Bik 2005). The seminal work of Carr & Najita (2008) reported a wealth of molecular lines in the mid-infrared (10-20  $\mu\text{m}$ ) spectrum of the classical T Tauri star AA Tau, dominated by pure rotational lines of  $\text{H}_2\text{O}$  but showing lines and bands of OH, HCN,  $\text{C}_2\text{H}_2$ , and  $\text{CO}_2$ . Two more disks were soon shown to also have strong water emission, as traced by ro-vibrational transitions near 3  $\mu\text{m}$  (Salyk et al. 2008), and Pontoppidan et al. (2010) detected water, along with emission from OH,  $\text{CO}_2$ , and organics in about half of  $\sim 50$  disks around low mass stars. Pascucci et al. (2009) surveyed over 60 disks around  $\lesssim 1 M_\odot$  stars and found HCN emission in up to 30% and  $\text{C}_2\text{H}_2$  emission in up to 10% of their sample. The excitation temperatures of these detections imply a location of  $\sim 1\text{-}5$  AU, and likely result from gas phase chemistry sustained by sublimation of icy grain mantles, brought there by vertical and radial transport, in the warm region above the disk midplane (Williams & Cieza 2011). Most of the oxygen in the inner disks is carried by water (38%) and CO (30%), while carbon seems to be slightly underabundant (by  $\sim 40\%$ ), sequestered in some refractory species as in the ISM (Salyk et al. 2011; Pontoppidan et al. 2014). In the last section of this introduction, and in Chapter 3, I elaborate on how the strength of water and organic molecules varies with disk properties, and the implications for the composition of forming planets.

### 2.3 Stage 3: Planetesimals

Once the opaque protoplanetary disk disappears, many pre-main and main sequence stars sustain a dusty disk of 1-10  $\mu\text{m}$  grains (Wyatt 2008); these disks appear to be made of material similar in composition to the material of comets and so-called “zodiacal light” of our Solar System (Youdin & Kenyon 2012). These grains coagulate and grow into larger bodies called planetesimals, which serve as the building blocks of planets, comets, and asteroids; the process of planetesimal growth likely preserves at least some previous chemical history initiated in the previous disk stage (Caselli & Ceccarelli 2012). Thus the cores of giant, and terrestrial, planets are influenced by the composition and dynamics/transport of proto-planetary bodies. For instance, it is generally accepted that giant planet core formation must have at least begun beyond the snow line, as more solid material was available there to be accreted.

The steps between grain growth and planetesimal formation have been extensively studied and many different mechanisms have been proposed to explain how solid bodies can grow larger than  $\sim$ meter-sized (see Youdin & Kenyon 2013 references). Particles that are  $\sim$ centimeter-sized are too small for gravity to be effective at growing them via collisions, yet too big for electrostatic forces to cause them to stick together (Morbidelli et al. 2012). Small grains also drift toward the star via gas drag (Widenschilling 1997), and at the relative velocities of several meters per second, particles are expected to break up. As the drift speed is maximum for meter-sized bodies, the problem is referred to as the meter-sized barrier (Blum & Wurm 2008). Furthermore, Mars- to Earth-mass bodies are more efficient at scattering planetesimals rather than accreting them, and giant planet cores are not formed fast enough (within the lifetime of the gaseous disk) in standard evolution models (e.g., Thommes et al. 2003).

As this is not the subject of any of the work presented in this thesis, I will take at face-value that, since we see large debris in disks and we see evidence of dust coagulation in our own Solar System, this step must occur. I will also focus on the core accretion method of planet formation, versus the quite-possible but perhaps less-prevalent (for planets) method of gravitational instability (e.g., Safronov 1969; Goldreich & Ward 1973; Youdin & Shu 2002), in which clumps of gas undergo run-away local contraction. The general picture of core accretion is that sub-micron sized dust grains settle and agglomerate to millimeter or centimeter sized rocks, and possibly even larger “boulders”, by low-velocity collisions (e.g., Blum & Wurm 2008), after which they are concentrated by some process into large-enough clumps to become gravitationally bound (e.g., Chiang & Youdin 2010 and references therein). The largest planetesimals can rapidly increase their collisional cross section and undergo runaway accretion (Safronov & Zvjagina 1969; Greenberg et al. 1978; Wetherill & Stewart 1993). As the orbits of near-by, still-small planetesimals are excited by the growing embryos, accretion by the embryo slows. At this point, a population of  $\sim$ lunar- to Mars-mass embryos may exist in the inner disk (terrestrial planet region), and  $\sim$ Earth-mass embryos may exist in the outer disk (giant planet region) (Kokubo & Ida 2002). The growth of giant planet cores from Mars- to Earth-sized embryos is also poorly understood, but thin gas envelopes around the embryos that enhance their cross section (Inaba & Ikoma 2003), back-reactions from planetesimal scattering (Fernandez & Ip 1984; Kirsh et al 2009), and/or convergent type 1 migration (linear perturbations in the disk caused by small mass object; Paardekooper et al. 2011; Lyra et al. 2010) have been proposed to bridge this growth gap. If/when a giant planet’s accreted gaseous envelope reaches a mass comparable to its core mass ( $\geq 5\text{--}10 M_{\text{Earth}}$ ), gas accretion accelerates and the planet becomes a gas giant

within  $\sim 10^5$  years (Ikoma et al. 2000; Mizuno 1980; Helled et al. 2014). If growth is halted before a significant amount of gas mass is accreted from the surrounding nebula, a super-Earth or Neptune-type planet can result (Turrini, Nelson, & Barbieri 2014).

As a gas giant planet gorges itself with the surrounding disk gas that remains, it clears a gap that eventually halts its accretion and sets its final mass. This gap cuts off gas exterior to the planet from interacting with gas interior to it, and as the disk viscously evolves most of the gas is dragged inward to the star, taking the planet with it (type 2 migration; Lin & Papaloizou 1986). At this point, remaining embryos slowly grow by collisions with planetesimals, until the local surface density of planetesimals and embryos is similar, at which point giant embryo-embryo impacts can occur (Wetherill 1985; Kenyon & Bromley 2006). Gravitational scattering by fully-grown planets sweeps the remaining small planetesimals into the star, into a planet, or outward into space (Marty, Alexander, & Raymond 2012). One important caveat in this process relevant to resulting planet compositions is that planetesimal formation does not necessarily start at the same time in every region of the disk, and (in some growth scenarios) can occur sporadically, so that a smooth radial gradient in chemical composition corresponding to condensation temperature is probably too simplistic (Morbidelli et al. 2012). The non-static nature of solid material in the disk and the implications for planet chemistry will be discussed further in the last section of this introduction.

## 2.4 Stage 4: Planets

The last phase of planet formation is dominated by the less-massive “leftovers” impacting and dynamically interacting with the newly-formed planets. The orbital configurations of most discovered exoplanetary systems (albeit with obser-

vation biases) demonstrate the strong effects of migration, likely due to the exchange of angular momentum with the disk (e.g., Lin et al. 1996; Papaloizou et al. 2007 and references therein), interactions with remaining planetesimals (Hahn & Malhotra 1999), and/or 3-body interactions with stellar companions (Fabrycky & Tremaine 2007). Because big, gas giant planets must form fast in order to accrete their mass before the disk dissipates, they are influential players in the dynamical dance among young planets and can excite the orbits of smaller, including terrestrial-sized, bodies.

Within our own Solar System, radiometric dating of the lunar surface and lunar debris found on Earth indicate that the Moon (and thus Earth, and likely other inner planets) was subject to a significant increase in impacts about 4 billion years ago. Known as the “late heavy bombardment” due to its occurrence over half a billion years after the Solar System formation, this influx of impacts has been explained by a period of planet-planet scattering that rearranged their orbital configuration (Tsiganis et al. 2005; Gomes et al. 2005; Morbidelli et al. 2007; Levison et al. 2011). The “Nice” model proposes that after the gas in the Solar System protoplanetary disk dissipated, small angular momentum transfers between the outer gas/ice planets and a mass of planetesimals in a trans-Neptunian disk moved Saturn, Uranus, and Neptune outward and Jupiter inward. Once Jupiter and Saturn cross their 1:2 mean motion resonance, Jupiter shifts Saturn outward, which destabilizes the orbits of Neptune and Uranus. These planets run into the trans-Neptunian planetesimal population and scatter them into the inner Solar System, causing the Late Heavy Bombardment. The Nice Model accounts for other observed Solar System properties, like Jupiter’s Trojans, the asteroid belt, outer system satellites, and the Kuiper belt.

There have been updates to the Nice model since it was first put forth, but

the basic idea is the same. However, the Nice model predicts certain Solar System properties that are not observed, including a much-too-massive Mars (by  $\times 5$ -10). Hansen (2009) suggested that the distribution of material in the disk was not smooth during the gas giant planets' dynamical evolution, and that if the terrestrial planets instead derived from embryos covering 0.7-1 AU, a smaller Mars is produced, as well as the correct (observed) sizes of Mercury, Venus, and Earth. To explain the break in the disk surface density at 1 AU, Walsh et al. (2011, 2012) introduced an inward-then-outward migration of Jupiter just after its formation in a still relatively-gas-rich stage via type 2 migration. As Saturn started to build up its gas mass, it was drawn inward by Jupiter until the planets were in a 3:2 mean motion resonance, at which point they switched their direction of migration and moved outward until the disappearance of the gas in the Solar protoplanetary disk left them at their current orbits (Masset & Snellgrove 2001; Morbidelli & Crida 2007; Pierens & Nelson 2008; Pierens & Raymond 2011). If Jupiter “tacked”, or changed direction, at  $\sim 1.5$  AU, then the inner disk of embryos feeding terrestrial planet formation would naturally have an edge around 1 AU. The “Grand Tack” explanation is able to account for the observed composition/distribution of the asteroid belt, and can also account for the delivery of “C-type” bodies containing volatiles to Earth.

The terrestrial planets themselves were formed from the accretion of the rocky planetesimals in the inner Solar System, and followed an evolutionary path distinct from gas giants – their atmospheres likely resulted mostly from outgassing and external bombardment, and internal differentiation of solid material led to a molten core-viscous mantle-thin upper crust structure (van Dishoek et al. 2014). The small amount of residual gas may have helped circularize the terrestrial planet orbits (e.g., Kominami & Ida 2002) and transported inward icy water-



and/or carbon- containing solids that formed in the colder outreaches of the Solar System (Ciesla & Lauretta 2005; Bond et al. 2010; Lee et al. 2010). Though I have focused here on the Solar System planet formation, these processes can be generalized to exoplanetary systems, as well, as evidenced by the observed orbital configurations and mass distributions.

## 2.4.1 Observational Constraints on Exoplanet Compositions

As this thesis focuses on transiting exoplanets, I will highlight the concepts behind measuring a transiting planet’s absorption and emission spectra. I will not detail here the extensive observations of many exoplanets – what planets have been observed during primary/secondary eclipse, at what wavelengths, by which groups, etc. The reader may refer to the most recent by Tinetti et al. (2014), Burrows (2014), and Madhusudhan et al. (2014) for details on specific planetary systems and what is (or is not) known about exoplanetary atmosphere compositions. Instead, this thesis focuses on observations of one super-Earth exoplanet, GJ 1214b, with the goal of constraining the short wavelength slope of its atmospheric transmission spectrum (Chapter 4). Additionally, the compositional information that is possible to derive from hot Jupiter spectra, and how this compares to the compositions of their host stars, motivates Chapters 5 and 6.

### 2.4.1.1 Transmission or Primary Transit

As a transiting planet passes between its host star and the observer, the star’s flux is diminished by an amount corresponding to the ratio of the stellar and planetary areas. The transmission spectrum of the planet represents the star light that passes through the planet’s atmosphere, attenuated by the absorption of molecular or atomic species. The transit depth measured at a particular wavelength (assuming insignificant internal heat from the planet itself) is then (Brown 2001)

$$A = \frac{\pi R_P^2}{\pi R_S^2} + \int_{R_p}^{\infty} \frac{2\pi R(1 - T(R))dR}{\pi R_S^2} \quad (2.18)$$

where  $R_P$  is the radius of the planet (at a specific pressure) where the planet goes from opaque to transparent,  $R_S$  is the star's radius,  $R$  is the distance from the center of the planet (including the transparent atmosphere), and  $T(R)$  is the transmitted light through the planet's atmosphere, which depends on the composition (and thus scale height,  $kT/\mu g$ ) of the atmosphere. (See Griffith 2014, §3 for a concise approximation of  $T(R)$ .)

Transmission observations from both space and ground, interpreted using atmospheric models based on the above formulation, have detected absorption of ions and radicals likely escaping the atmospheres of giant planets (e.g., Vidal-Madjar et al. 2003, 2004; Ben-Jaffel 2007, 2008; Linsky et al. 2010; Lecavelier des Etangs et al. 2010, 2012; Fossati et al. 2010), alkali metals like sodium and potassium (Charbonneau et al. 2002; Redfield et al. 2008; Snellen et al. 2008; Wood et al. 2011; Colon et al. 2010; Sing et al. 2011), and water vapor (e.g., Barman 2007; 2008; Beaulieu et al. 2010; Charbonneau et al. 2008; Grillmair et al. 2008; Knutson et al. 2008; Madhusudhan & Seager 2009; Tinetti et al. 2010). Other molecular species expected to be dominant in planetary atmospheres – CO, CO<sub>2</sub>, CH<sub>4</sub> – are more difficult to detect. Recent transmission observations suggest that a fraction, perhaps large, of hot planets have their atmospheres obscured by hazes or clouds of yet-unknown composition (e.g., Deming et al. 2013; Mandell et al. 2013; Wilkins et al. 2014; Ranjan et al. 2014).

In Chapter 4, I discuss observations of the first super-Earth to be spectroscopically characterized, GJ 1214b (Charbonneau et al. 2009). Multiple ground- and space-based campaigns have focused on this planet, because it is a rare case of a small planet atmosphere that can be probed (due to its host star being an

M dwarf, creating a favorable planet-to-star flux ratio). While the debate over whether this exoplanet's atmosphere is hydrogen or water dominated raged for several years, HST/WFC3 observations published this year reached unprecedented precision (30 parts per million) with twelve transits between 1.1-1.7  $\mu\text{m}$ , ruling out a cloud-free model with compositions dominated by  $\text{H}_2\text{O}$ ,  $\text{CH}_4$ ,  $\text{CO}$ ,  $\text{N}$ , or  $\text{CO}_2$  at greater than the  $5\sigma$  confidence level (Kreidberg et al. 2014). The authors find that the atmosphere of GJ 1214b must have clouds to be consistent with their observed flat spectrum. They perform a Bayesian analysis to constrain the cloud-top pressure to  $<10^{-2}$  mbar for a solar mean molecular composition and  $<10^{-1}$  mbar for a water-rich composition.  $\text{ZnS}$  or  $\text{KCl}$  could form in the relatively cool atmosphere of GJ 1214b, but would form at high pressures (deeper than 10 mbar for a  $50\times$  solar metallicity), requiring transport up from their originating altitude to explain the observed spectrum. Perhaps the most likely explanation for GJ 1214b's flat spectrum is photochemically-produced hydrocarbons in the upper atmospheres, similar to the haze on Titan (Miller-Ricci Kempton et al. 2012; Morley et al. 2013).

#### 2.4.1.2 Emission or Secondary Transit

When a planet is eclipsed by its host star, the difference between the summed light of the planet+star and that of the star alone equates to the planet's emitted light from its dayside. Emission spectra are sensitive to the dayside composition and the vertical pressure-temperature profile, which controls whether spectral features are seen as emission or absorption.

The flux emitted and/or reflected from a planet can be equated to the stellar radiation it absorbs,

$$4\pi R_P^2 F_P = (1 - A_B) F_S \frac{R_S^2}{a^2} \pi R_P^2 \quad (2.19)$$

where  $R_P$  is the planet's radius,  $R_S$  is the star's radius,  $F_P$  is the flux from the

surface of the planet, and  $F_S$  is the flux from the surface of the star,  $a$  is the planet's semimajor axis (distance between the star and the planet), and the factor  $(1-A_B)$  is the amount of the stellar energy absorbed by the planet ( $A_B$  is the Bond albedo, the fraction of incident stellar radiation scattered back into space). This equation can be rearranged to represent the observed quantity, the planet/star flux ratio (which in reality is observed at a specific wavelength or frequency),

$$\frac{R_p^2}{R_*^2} \frac{F_p}{F_*} = \left(\frac{R_p}{a}\right)^2 \frac{f}{4} (1 - A_B) \quad (2.20)$$

Almost all secondary eclipse measurements have been photometric, suggesting that molecular features can potentially be distinguished, but that the results of retrieving the atmospheric parameters (e.g., Madhusudhan & Seager 2009; Swain et al. 2009ab) are poorly constrained. Infrared ( $\gtrsim 1 \mu\text{m}$ ) emission spectra of exoplanets, many taken with *Spitzer*, indicate that the presence of  $\text{H}_2\text{O}$ ,  $\text{CO}$ ,  $\text{CO}_2$ , and  $\text{CH}_4$  can explain most features present in hot Jupiters. However, many observations from both ground and space still suffer significant systematic errors that are often comparable to or larger than the astrophysical signal due to the planet. Beyond overcoming the observational uncertainties, matching observations to atmospheric models is degenerate for both transmission (e.g., between the molecular abundances and the assumed  $R_p$ ) and emission spectra (between the molecular abundances and the vertical thermal profile) (Griffith 2014). Different atmospheric modeling approaches – assuming or not assuming radiative-convective equilibrium, including or not including disequilibrium processes, including or not including more than the four standard molecules – with varying numbers of free parameters populate the field of exoplanet atmosphere interpretation. However, it is clear from just the exoplanets whose atmospheres have any observations that there is significant diversity in their temperatures and compositions. It is in the cause/causes of this diversity that I am most interested.

## 2.5 Connecting the Dots – The Role of C and O

### 2.5.1 Stage 0: Host Star Composition's Role in Planet Formation

At this point, the most robust connection between star composition and the properties of resulting planets is the so-called “planet-metallicity” correlation – stars hosting large, close-in (hot Jupiter) planets are more metal-rich (often, but not always, parameterized by the solar-normalized iron abundance,  $[\text{Fe}/\text{H}]$ ) than stars without detected gas giant planets (Buchhave et al. 2012; Santos et al. 2004; Fischer & Valenti 2005; Sousa et al. 2011; Ghezzi et al. 2010; Everett et al. 2013). This is consistent with the theories of planet formation, in that more solid material facilitates faster growth of planets, giving enough time for them to build up large cores and accrete the gas that remains in the protoplanetary disk (Morbidei et al. 2012). “Metals” thus appear important for forming Jupiter-sized exoplanets, but the host star metallicity-planet occurrence trend is weaker for Neptune-sized planets (e.g., Ghezzi et al. 2010) and does not hold for terrestrial-sized planets (Buchhave et al. 2012; Everett et al. 2013). The question arises as to whether  $[\text{Fe}/\text{H}]$  a good predictor of giant planets because it represents the total available metal content, or because Fe is a uniquely important core-forming material? Other, less robust enhancements in C, Si, Mg, Al, Ni, and Ti (Bodagheer et al. 2003; Robinson et al. 2006; Adibekyan et al. 2012ab) in Jupiter and/or Neptune hosting stars versus stars without detected planets hint at potential patterns indicative of planet formation (e.g., Adibekyan et al. 2012a).

Silicon, with a condensation temperature ( $T_c$ ) comparable to Fe (Lodders 2003), is an important contributor to dust in planet-forming regions a principle component of rocky-type planets (Robinson et al. 2006). Doubling Fe, Si, and O in solar protoplanetary disk models increases the solid surface density by 13%, 7.1%, and 58%, respectively (Robinson et al. 2006). Thus, besides Fe, Si and O are the most

significant solid mass contributors – O primarily through  $\text{H}_2\text{O}$  ice accreted beyond the snow line, and Si through silica/silicates in small grains (Brugamyer et al. 2011). Interestingly, controlling for  $[\text{Fe}/\text{H}]$ , Brugamyer et al. (2011) find a difference in  $[\text{Si}/\text{Fe}]$  between host stars and stars without known planets, but no difference in  $[\text{O}/\text{Fe}]$ . Si and O are both  $\alpha$ -elements, and the Si/O ratio is  $\sim$ constant among metal-rich stars, so  $[\text{Si}/\text{Fe}]$  should trace  $[\text{O}/\text{Fe}]$  (Robinson et al. 2006). Stellar photospheres may instead be tracing species important for grain nucleation (Si) rather than icy mantle growth (O), and refractories like Si may be the limiting reagents for planet formation. Silicon may thus be more important than Fe and O for terrestrial planet formation.

As described above, oxygen and carbon are of particular interest in both star and planet formation. The measurement of O and C in stars, especially with respect to Fe, serves as a fundamental diagnostic of the chemical enrichment history of the Galaxy, and the abundance of C relative to O incorporated into exoplanets can be similarly indicative of current structure and evolutionary history. Carbon is a volatile, like O, but can contribute mass both to grain nuclei – universally up to 20% of C is likely in refractory grains (Henning & Salama 1998) – and to icy mantles – simulations of ice giants Uranus and Neptune show they required solid  $\text{CH}_4$  in their feeding zones to grow to their present sizes (Dodson-Robinson et al. 2010). Thus C may be another chemical compass for planet formation.

Another, not-yet-confirmed, connection between host star composition and exoplanet composition/type derives from our own Solar System. Using high-precision chemical abundance analyses of “solar twins” that have stellar properties almost identical to that of the Sun, studies have found that the Sun is deficient (by  $\sim 20\%$ ) in refractory elements ( $T_c \geq 900$  K) relative to volatile elements when compared to most ( $\sim 85\%$ ) solar twins stars (Meléndez et al. 2009, 2012;

Ramírez et al. 2009, 2010). This could be a signature of terrestrial planet formation, with the “missing” refractory elements from the Sun’s photosphere incorporated into rocky planets (Meléndez et al. 2009; Gustafsson et al. 2010; Chambers 2010). The amount of missing material in our Sun amounts to that needed to form the terrestrial planets (Meléndez et al. 2009, Gustafsson et al. 2010; Chambers 2010), and the abundance patterns in meteorites mirror this solar abundance anomaly (Alexander et al. 2001; Ciesla 2008). However, subsequent studies of solar analogs with/without planets indicate that their abundance patterns may not be so different, or indistinguishable from Galactic chemical evolution (González Hernández et al. 2010, 2013; Schuler et al. 2011). New evidence indicates that in Jupiter/Neptune host stars that are metal-rich or warmer than the Sun (with less massive convective envelopes), the depletion signature may depend on the stellar convective envelope size at the time of planet formation, and thus the timescale of disk dispersal around different types of stars (Ramírez et al. 2014).

Measuring host star abundances is thus a potentially powerful tool for diagnosing the initial conditions of planet formation. In Chapters 5-7 I explore this idea for hot Jupiter exoplanetary systems, and for one super-Earth exoplanetary system. However, as I discuss below, there are additional factors to consider in the planet-building process, in particular how the composition of the different reservoirs of material available for incorporation into planets change throughout its evolution. In the following sections I summarize how observations of carbon and oxygen species (and the ratio of carbon to oxygen ratio) trace the stages of planet formation.

### 2.5.2 Step 1: C and O in the Protoplanetary Disk

Key to determining what material is available for planet formation, both in gas and solid state, is the location of condensation fronts within the disk at various

distances from the star. These fronts change substantially with time as the disk temperature changes in response to the evolving stellar radiation (e.g., Kennedy & Keynon 2008) and internal disk heating (e.g., Lissauer 1987). Young  $\sim$  solar-mass stars' high accretion rates can drive the snow line ( $\text{H}_2\text{O}$  condensation front) out to or past 5 AU, but during the time that giant planets accrete most of their mass, the disk accretion rate drops and decreases viscous heating, enabling the snow line to move to  $\sim 1$  AU. As the disk clears and the inner regions become optically thin, the snow line can again be pushed out when the previously-shielded midplane of the disk is directly exposed to stellar flux (Garaud & Lin 2007; Zhang et al. 2013).

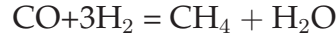
In a typical, mid-life protoplanetary disk around a solar type star (e.g., with a power-law temperature profile  $T_0 \times (\frac{r}{1\text{AU}})^{-q}$ , with  $T_0=200$  K and  $q=0.62$ ; Andrews & Williams 2007), the  $\text{H}_2\text{O}$ ,  $\text{CO}_2$ , and CO condensation fronts occur around  $\sim 2$ , 10, and 40 AU (e.g., Öberg et al. 2011). Interior to the  $\text{H}_2\text{O}$  iceline (at  $\sim 120$ -150 K), carbon and silicate grains are still in condensed form, and the gas-phase C/O ratio is slightly above solar ( $\sim 0.6$ , with solar  $\sim 0.5$ ) due to the slightly higher abundance of O relative to C in refractory species (Turrini Nelson, & Barbieri 2014). Between the  $\text{H}_2\text{O}$  and  $\text{CO}_2$  condensation fronts, oxygen is removed in the condensation of water, resulting in a higher  $\text{C}/\text{O}_{\text{gas}}$  ( $\sim 0.8$ ) and a lower  $\text{C}/\text{O}_{\text{solid}}$  ( $\sim 0.25$ ) (Öberg et al. 2011). After  $\text{CO}_2$  freezes out (at  $\sim 50$  K), the  $\text{C}/\text{O}_{\text{gas}}$  ratio is further enhanced to  $\sim 1$ , and the  $\text{C}/\text{O}_{\text{solid}}$  ratio also increases slightly (to  $\sim 0.3$ ). Thus, given the likely location of giant exoplanet formation (as opposed to their currently-observed close-in orbits), most simplified scenarios of atmosphere-interior decoupling and accretion of only locally-produced solids and gas lead to a super-solar C/O ratio in the exoplanet.

In the previous sections I reviewed how *Spitzer*-IRS has detected water va-



por in the inner regions of many disks, helping confirm the picture of high water abundance at a few AU. Within more than an order-of-magnitude uncertainty, abundance ratios of  $\text{H}_2\text{O}/\text{CO} \sim 1\text{-}10$  have been inferred for emitting radii within a few AU, with the water abundance on order of  $10^{-4}$  (with respect to hydrogen) (Salyk et al. 2011; Mandell et al. 2012). At larger radii, out to 100 AU, *Herschel*-PACS has detected far-infrared lines from water (Rivi re-Marichalar et al. 2012; Meeus et al. 2012; Fedele et al. 2012, 2013) suggesting an upper-limit  $\text{H}_2\text{O}$  abundance of  $10^{-5}$ , but the  $\text{H}_2\text{O}/\text{CO}$  ratio is also still very uncertain (van Dishoek et al. 2014). Beyond 100 AU, *Herschel*-HIFI has only made two detections of water ground rotational transitions (557 and 1113 GHz), one of which is a Herbig Ae star. The detection of cold gaseous water in the T Tauri star (TW Hydra) implies an abundance  $\sim 10^{-7}$  in the intermediate disk layers (Hogerheijde et al. 2011); the bulk of oxygen is likely on icy grains in the disk midplane.

However, the condensation of water may be subject to the effects of nonequilibrium carbon chemistry via

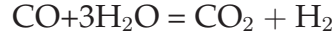


which under equilibrium conditions will favor CO as the major carbon-carrying gas at high temperatures but will switch to  $\text{CH}_4$  gas at lower temperatures ( $\sim 650$  K at  $10^{-4}$  bar; Lodders 2003). If methane formation is kinetically inhibited (as is expected, e.g., Lewis & Prinn 1980), graphite precipitation can occur via



at 626 K (versus the  $\text{CH}_4$  production below  $\sim 650$  K and then condensation at 41 K in the equilibrium case). Due to graphite’s increasing thermodynamic activity with decreasing temperature, CO and  $\text{CO}_2$  gas abundances drop with decreasing

temperature (Lodders 2003). Note that the above reaction excludes water, whose condensation temperature remains the same (182 K). If instead  $\text{CH}_4$  and graphite formation are inhibited, CO remains the stable gas because the above reactions cannot proceed, and CO can react with water via



At 650 K, water is still present as a gas to react with CO, but with decreasing temperature, the  $\text{CO}_2$  abundance increases at the price of decreasing CO and  $\text{H}_2\text{O}$  gas, lowering the water vapor pressure and thus its condensation temperature to 121 K (Lodders 2003).

Recently, variations in the inner disk C/O ratio were measured in a range of protoplanetary disk *Spitzer*-IRS observations using the proxy ratio of HCN to  $\text{H}_2\text{O}$  strength (Carr & Najita 2011; Najita et al. 2013). The HCN/ $\text{H}_2\text{O}$  ratio was found to increase with submillimeter-measured disk mass, suggesting that higher mass disks more readily form larger, non-migrating bodies that trap water (and oxygen) beyond the snow line and outside the region reflecting the HCN/ $\text{H}_2\text{O}$  ratio variation. In this scenario, then, the composition of the upper layers of warm inner disk gas is a diagnostic of the radial transport of solids in the mid-plane, and thus perhaps planet formation timescales. Variation in the strength of  $\text{C}_2\text{H}_2/\text{HCN}$  has also been observed between disks around high and low mass stars (varying with spectral type; Pascucci et al. 2009). Brown dwarf disks show a higher  $\text{C}_2\text{H}_2/\text{HCN}$  than T Tauri disks (Pascucci et al. 2009), with  $\text{C}_2\text{H}_2 \sim 7\times$  more abundant, and also a depletion in  $\text{H}_2\text{O}$  vapor in comparison to other simple organics. A possible explanation is that brown dwarf disk atmospheres have higher C/O ratios, which enhances the  $\text{C}_2\text{H}_2/\text{HCN}$  and HCN/ $\text{H}_2\text{O}$  molecular ratios. This could be explained by more non-migrating icy planetesimals causing

the higher C/O ratios, since brown dwarf disks are thought to proceed through the stages of planet formation faster than T Tauri disks (Pinilla et al. 2012, 2013; Pascucci et al. 2014 and references therein). With higher C/O ratios in the terrestrial planet forming region, brown dwarf disks may produce more carbon-rich rocky planets.

An important caveat to remember is that the regions probed by these molecules may not be the same, and thus may be subject to different environmental conditions. Also, the observations interpreted as varying C/O trace only the warm disk surface, whereas the overall disk composition may be different. How the composition of the host star is related to the composition of its disk, at different radii and scale heights, and the timescale of disk dissipation are still open questions (and ones I hope to continue to address in my postdoctoral position). For instance, the effect of metallicity (the initial gas-to-dust) on the content in protoplanetary disk evolution is an active area of research, especially with the observed planet-metallicity correlation. The differences between metallicities of weak T Tauri and classical T Tauri stars in Taurus and Orion appear to be minor (D’Orazi et al. 2009), although Yasui et al. (2009) found that the fraction of disks with warm inner gas (not cleared out) is smaller in low-metallicity clusters. The median disk lifetime in low-metallicity clusters is also substantially shorter than in the solar neighborhood, from which Yasui et al. (2010) inferred a disk lifetime-metallicity dependence.

### 2.5.3 Step 2: C and O in Planetesimals

One of the most well established trends in star and planet formation, the planet-metallicity correlation, is almost always based on  $[\text{Fe}/\text{H}]_{\text{star}}$  representing metallicity and, as a proxy, the amount of solid material available for incorporation into planets. However, condensed volatiles represent at least  $2\times$  the mass available

for planetesimal formation, and as much as  $3\text{--}4\times$ , at the radii beyond the main condensation fronts described above (Pontoppidan et al. 2014). The increase in solid mass beyond each respective snow line affects the growth of planets on all scales, and may actually catalyze planetesimal formation via a mechanism like the streaming instability, which requires high surface densities (Youdin & Shu 2002; Johansen et al. 2007).

Specifically, oxygen-bearing water mantles on dust particles may aid in efficient sticking at higher collision velocities than grains without water. Simulations show that silicate grains break up at collision velocities  $\sim 10\times$  lower than icy grains (Wada et al. 2009), and icy grains could also melt and re-freeze quickly in high energy impacts (Wettlaufer 2010). In the often described “cold finger effect”, hot water can diffuse outward towards its snowline and condense again just outside this transition, increasing the solid density here by a factor of 2-4, which could help facilitate planet formation (Stevenson & Lunine 1988). Most water ice in the solar nebula likely ended up in the giant planets, as they formed outside the  $\sim 2.7$  AU snow line predicted at the end of the gas-rich disk phase (Hayashi 1981) (although the snow line likely moved inward from a larger distance during earlier times in the disk; Kennedy & Kenyon 2008). As I will discuss in the next section, the amount of water in the Solar System planets is still an open question, though the *Juno* probe will soon give a better estimate of the oxygen content of Jupiter. Studying the compositions of stars with respect to their planets in hotter exo-systems where  $\text{H}_2\text{O}$  will exist as a gas in the observable atmosphere is a promising avenue for exploring more the role of  $\text{H}_2\text{O}$  in gas planet formation.

The dominant condensible carbon-bearing species in disks are CO and  $\text{CH}_4$  (Dodson-Robinson et al. 2009), although carbon-rich dust may be another, potentially important, source of solid carbon for planet formation. Pollack et al. (1994)

estimate, based on observations, theory, and lab experiments, that in molecular cloud cores and protoplanetary disks, 50-70% of carbon is present in a refractory phase, compared to 1-2% in ice and 15-35% in gas. A few debris disks have been found to host atomic carbon in the gas phase (Roberge et al. 2013; Donaldson et al. 2013; Redfield 2007; Roberge et al. 2006; Brandeker et al. 2013; Cataldi et al. 2014), which is unexpected as such a late stage of disk evolution, and points towards an origin in dust destruction of some kind (Fernández et al. 2006; Beust & Valiron 2007, Chen et al. 2007; Czechowski & Mann 2007). In these cases, the composition of the debris going into planets may thus be studied by observing the residual gas, and different gas production mechanisms can be constrained (e.g., evaporation close to the star, photon-stimulated desorption, collisional vaporization). Polycyclic aromatic hydrocarbons (PAHs) are abundant through the ISM (e.g., Tielens 2008), likely formed in the ejecta of carbon stars as “soot” (Frenklach & Feigelson 1989; Chercheneff et al. 1991), and potentially important to pre-biotic chemistry as the starting point for the growth of more complex organics, amino acids, and nucleotides (Cronin & Chang 1993; Hudgin, Bauschlincher, & Allamandola 2005). PAHs have also been observed in protoplanetary disks (Bouwman et al. 2008; Geers et al. 2007; Boersma et al. 2008), and when they react with atomic H they can form  $C_2H_2$  at amounts comparable to those observed in inner disks of T Tauri stars (e.g.,  $C_2H_2/CO \sim 0.02$ ; Carr & Najita 2008). Kress et al. (2010) highlighted that PAHs are likely the most abundant carbon-bearing compound in the terrestrial planet forming region of disks ( $\leq 2$  AU). In addition, Lodders (2004) proposed, based on the (perhaps anomalously) low O abundance measure by the *Galileo* and the high C abundance measured in all outer gas giants (Niemann et al. 1998; Courin et al. 1984; Baines et al. 1995), that Jupiter was formed from abundant carbonaceous matter around the “tar line” at the time

of its main growth period. The solid surface density was dominated by carbon rather than oxygen (water) with the snow line positioned farther out. This is another suggestion that will be tested with *Juno* measurements of Jupiter's  $\text{H}_2\text{O}$  abundance.

It is again important to acknowledge that the compositions of gas and dust in protoplanetary disks are not uniform or static, and evolve with time as the gas dissipates, and different parts of the disk are exposed to viscous and/or stellar heating. The condensation fronts move inward with time (Sasselov & Lecar 2000; Ciesla & Cuzzi 2006; Dodson-Robinson et al. 2009), with exact positioning depending on the detailed temperature-pressure profile of the disk. Solid particles migrate radially due to drag forces and pressure, and due to perturbations by larger forming clumps/proto-planets. Interestingly, super-Earth, Neptune, and Jupiter sized exoplanets likely have different formation and migration histories that may be constrained based on their chemical compositions. While I have not gone into detail about an alternative mechanism for planet formation, gravitational instability (GI), the final compositions of different types of exoplanets can shed light on its prevalence. In a simplistic picture, gas giants formed quickly ( $\sim 10^3$  years; Baruteau et al. 2011; Zhu et al. 2012) via GI will reflect the bulk disk composition because grain growth does not have enough time to proceed between formation and migration (Turrini, Nelson, & Barbieri 2014). Core-accretion-formed planets can display a range of abundance ratios depending on the relative movement and timescale of accretion of gas and solid components. Building up a population of exoplanets for which we have accurate star and planet compositions is one path towards a better understanding of different planet formation mechanism(s) and what controls these mechanisms.

### 2.5.4 Step 3: C and O in Planets

The growing number and diversity of exoplanets has revolutionized the conception of a planetary system, what is common or expected, and what is possible as a result of planet formation in terms of mass, radius, inclination, eccentricity, variability, atmospheric chemistry, etc. However, I think it is still useful to examine what we know about the composition of planets in our Solar System, since these are in principle the objects we can best study.

#### 2.5.4.1 Carbon and Oxygen in Earth and Jupiter

The mass of water in Earth's crust (including the atmosphere and oceans in this definition) is just  $2.8 \times 10^{-4} M_{Earth}$  (Lee, Evans, & Bergin 2005). The mass of water in the mantle today is an open question; new evidence suggests that a mass of water exceeding the mass of Earth's ocean water may reside just in the lower transition zone of Earth's interior (Pearson et al. 2014). More water may have existed in the primitive Earth if it was lost during differentiation or impacts (van Dishoeck et al. 2014). However, the million dollar question is, how did Earth get wet? As described above, the condensation front of water was farther out than the formation location (at the time of formation) of the terrestrial planets, so the local environment was water-poor. Several scenarios are possible, but a key piece of evidence is that the deuterium to hydrogen (D/H) ratio in Earth's oceans is  $\sim 6\times$  higher than the solar nebular D/H ratio, as derived from Jupiter and Saturn's D/H ratios and present-day solar  $^3\text{He}/^4\text{He}$  and  $^4\text{He}/\text{H}$  ratios (e.g., Lauretta & McSween 2006). Comets may have similar D/H ratios to the terrestrial ratio (e.g., comet 103P/Hartley 2, Hartogh et al. 2011), but the D/H ratios of the six measured comets are  $\sim 2\times$  higher than Earth's D/H ratio. Additionally, the probability of comets hitting Earth is small (Morbidelli et al. 2000) – the mass of comets delivered to Earth would only have accounted for  $\sim 10\%$  of Earth's crustal

water (Morbidelli et al. 2012). The best match to Earth's D/H ratio comes in carbonaceous chondrites, which have D/H ratios almost identical to Earth. This suggests that water was delivered to Earth from primitive planetesimals from the outer asteroid belt, and simulations have shown that up to 10% of Earth may have been formed from such planetesimals (e.g., Morbidelli et al. 2000; Raymond et al. 2009). In fact, Earth likely had two atmospheres: first, a hydrogen-rich, proto-atmosphere that grew from what Earth captured from its local environment but that was lost to hydrodynamic escape (Porcelli & Pepin 2003; Zahnle et al. 2007; Holland, Cassidy, & Ballentine 2009), and second, an atmosphere created by outgassing and incorporating the material from impacts (Morbidelli et al. 2012; Halliday 2013).

The opposite scenario applies to Earth's carbon, which is about three orders of magnitude less (relative to silicon) than what was available in the feeding zone of Earth (as represented by the Sun) (Lee et al. 2010). Again, we do not know the amount of carbon sequestered in Earth's core, but including estimates of this amount still results in a significant carbon deficit (Allegre et al. 2001). This suggests that something destroyed the refractory carbon prior to the formation of Earth, or at least kept primordial carbon grains from going into rocks, but not in comets, which have near-solar carbon abundances (Bockele-Morvan et al. 1998, 2008; Mumma & Charnley 2012). In simulations of terrestrial planet formation, assuming that ~15% of Earth was formed from delivered bodies from beyond 2.5 AU, the same source of Earth's water can also account for the carbon abundance estimated for Earth (O'Brien et al. 2006). This explanation is bolstered by the isotopic ratios of the noble gases in Earth's atmosphere, which are consistent with a mixture of 90% chondritic and 10% solar material (Marty 2012; Alexander et al. 2012). Of note is the observation in polluted white dwarfs that C/Fe and



C/Si abundance ratios are well below solar and consistent with asteroidal material that is carbon-poor (Jura 2008; Gansicke et al. 2012; Farihi et al. 2013) – Earth’s missing carbon may be a common occurrence in terrestrial planet formation.

Jupiter’s elemental abundances have been derived from remote spectra and from the *Galileo* probe, and while carbon was measured in slight excess versus solar (enhanced by  $\times 4 \pm 2$ ; Owen & Encrenaz 2006), oxygen showed a significant depletion. The abundance of gaseous water in Jupiter’s atmosphere (which has little CO) gives only a lower limit to the oxygen abundance, since the troposphere is a cold trap where water can freeze out and thus remain undetected. The idea is that *Galileo* was injected into a “hot spot” in Jupiter’s atmosphere that was transparent down to the troposphere, and that the oxygen depletion is thus not an accurate representation of Jupiter’s overall atmosphere (which is expected to have an oxygen abundance 3-10 $\times$ solar deep in the interior, Encrenaz 2008; Mousis et al. 2009). Lodders (2004) postulated that maybe Jupiter actually did form in an oxygen-poor environment; the “Grand Tack” model of Jupiter and Saturn’s formation hypothesizes that Jupiter may have moved within 1.5 AU, where it could have accreted refractory materials rich in carbon. *Juno* will measure the water at high pressures via a microwave radiometer (Janssen et al. 2005) and at higher levels in the atmosphere via the Jovian Infrared Auroral Mapper (Adriani et al. 2008), providing a definitive answer as to whether water (and oxygen) is above or below the solar abundance.

#### 2.5.4.2 Carbon and Oxygen in Exoplanets

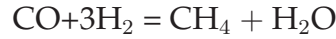
I summarized above how the composition of disks in which planets form can change with time and therefore influence the planets that result. While the envelopes of gas giant exoplanets are typically considered to be mostly H and He, the small fraction that is “metallic” could be stellar, substellar, or super-stellar in

chemical composition, depending on how and from where gas and solids are incorporated into the planet. For instance, if planetesimals are broken up as they sink to the core of a giant planet, the planetary envelope might be enriched in heavy elements compared to the gas in the disk (Helled et al. 2014). In fact, how enriched the envelope is from incoming planetesimals may actually influence the gas accretion. Hori & Ikoma (2011) found that the critical core mass needed to initiate rapid gas accretion is reduced when the envelope is polluted, leading to increased formation timescales of gas giant planets with small cores and enriched envelopes. The composition of accreted bodies depends on the distance away from the star – between 1-3 AU, the composition is  $\sim 70\%$  Si and  $30\%$  Fe (e.g., mostly refractory); between 3-4 AU volatiles play a role, with  $\sim 85\%$  Si,  $5\%$  C,  $9\%$   $\text{H}_2\text{O}$ ; once the water snowline is crossed out past 4 AU, the composition is  $\sim 70\%$   $\text{H}_2\text{O}$  (which may still trap silicates and other metals),  $26\%$  C,  $1\%$  N, and  $1\%$  other elements (Turrini, Nelson & Barbieri 2014). Accretion of solid material with abundances different than solar (like Earth and Jupiter above) can thus be reflected in abundance ratios of planetary atmospheres. Accretion of objects does not halt after the final stages of planet formation, however, and also has the potential to alter the observed atmosphere, though likely only temporarily. When comet Shoemaker-Levy 9 hit Jupiter, metals and silicates were seen in its atmosphere, but were gone within a matter of months (Taylor et al. 2004).

The upper atmospheres of gas-rich planets, once accretion has stopped and they are “mature”, are cool enough to form monatomic and molecular gases more complex (or at least in greater relative abundance) than what is possible in stars like the Sun. Water is expected to be a dominant component at all temperatures, whereas at the nominal  $\sim 1$  bar, CO will dominate at  $T \gtrsim 1300$  K and  $\text{CH}_4$  will dominate at cooler temperatures. Observations support water’s ubiquity in (mostly

transiting) hot Jupiter atmospheres (Barman 2007; Tinetti et al. 2007; Grillmair et al. 2008; Beaulieu et al. 2010; Swain et al. 2008; Crouzet et al. 2012; Deming et al. 2013; Birkby et al. 2013) and the presence of carbon-bearing species (CO, CO<sub>2</sub>, and CH<sub>4</sub>) (Swain et al. 2008, 2009ab; Tinetti et al. 2010a; Snellen et al. 2010; Brogi et al. 2012; de Kok et al. 2013), but in both cases the relative abundances are still not well constrained (e.g., Madhusudhan & Seager, 2009; Lee et al. 2012; Line et al. 2012, 2014).

The ratio of carbon to oxygen is a key parameter for the chemical composition and evolution of gas giant planets as it controls the balance of the most abundant molecular species. At the nominal pressure and temperature of 1 bar and 2000 K, in a solar C/O ( $\sim 0.5$ ) environment, the reaction



favors the production of CO, which acts as the dominant carbon carrier and shares the available oxygen with H<sub>2</sub>O. At  $T \lesssim 1200$ , CH<sub>4</sub> becomes the dominant carbon carrier, and H<sub>2</sub>O is the dominant oxygen carrier. However, if the C/O ratio is  $\gtrsim 0.8$ , there is less oxygen available, and at high temperatures ( $T \geq 1200$ ) where CO dominates, the H<sub>2</sub>O abundance (assuming  $P = 1$  bar) can drop by up to three orders of magnitude (depending on  $T$ ) as compared to the solar case, and the excess carbon is present as CH<sub>4</sub> (and likely other hydrocarbons) (Kuchner & Seager 2005; Madhusudhan et al. 2011; Madhusudhan 2012; Fortney et al. 2011; Moses et al. 2011, 2013). The large changes in the abundances carbon and oxygen species in hot ( $T \geq 1200$  K) Jupiter atmospheres induced by changes in the C/O ratio result in potentially observable changes in their observed atmospheres. The C/O ratio can also (1) be influenced by non-equilibrium processes like vertical transport (affecting pressures  $\sim 1\text{--}10^{-4}$  bar) and photochemistry (at

pressures  $\lesssim 10^{-6}$  bar, but possibly affecting observable pressures), when the time scales for transport of gaseous species are shorter than the chemical kinetics time scales (e.g., Visscher & Moses 2011); and (2) influence the observability of disequilibrium chemistry products, particularly in cooler ( $T \lesssim 1200$  K) planets (e.g., Moses et al. 2013).

In Chapters 5 and 6, I go into more detail about the different observed and modeled atmospheric chemistries of transiting hot Jupiter planets, how the hot Jupiter atmospheric abundances compare to their host star C/O ratios, and what implications these comparisons have for constraining planet formation scenarios.

As an example, we can consider WASP-12b (Hebb et al. 2009), an extremely irradiated hot Jupiter with an equilibrium temperature of  $\sim 2600$  K and short period ( $\sim 1.09$  days), which makes it one of the best-observed exoplanets. Madhusudhan et al. (2011) compared a grid of model predictions, using the atmospheric parameterization of Madhusudhan & Seager (2009), to multi-wavelength photometric observations across  $0.9\text{--}8\ \mu\text{m}$  and derived a best-fit carbon-rich composition ( $\text{C/O} \geq 1$ ) with under-abundant  $\text{H}_2\text{O}$  and overabundant  $\text{CH}_4$  ( $2 \times 10^{-5}$ – $1 \times 10^{-3}$ ). This finding was confirmed by Madhusudhan (2012) with additional data. If true, the planet is significantly enhanced in carbon above its host star, with  $\text{C/O} = 0.48 \pm 0.08$  (detailed in Chapter 5), but has a substellar C/H ( $\text{C/H} \sim 6 \times 10^{-4}$  based on the previously [Fe/H] measured in WASP-12, but see Chapter 5 for an update to this metallicity). Öberg et al. 2011, based on simple models of a solar-type protoplanetary disk, reported that a high C/O and low C/H are consistent only with an atmosphere formed predominantly from gas accretion outside the water snowline, between the CO and  $\text{CO}_2$  snowlines. Ali-Dib et al. (2014) recently constructed a more realistic protoplanetary disk model including gas drag, sublimation, vapor diffusion, and condensation and coagulation, and found that

CO gas is depleted more gradually than H<sub>2</sub>O gas within the snow line. This longer time period of CO gas in the disk, coupled with its condensation front at a larger distance, gives CO gas more time to travel before condensing and makes it the dominant C and O bearing species beyond the snow line. The authors note that in their calculations, C/O will never exactly be 1 due to residual water vapor slightly decreasing the ratio, and that CO will still be depleted with respect to the initial stellar abundance, leading to a substellar C/H in WASP-12b. All of the attention paid to WASP-12b may be in vain, however, due to the recently discovered close M-dwarf stellar companion (Bergfors et al. 2011; Crossfield et al. 2012). Accounting for the dilution of the reported eclipse depths due to the companion, WASP-12b's emission spectrum is best fit with a featureless blackbody at 3000 K (Crossfield et al. 2012).

Terrestrial, rocky planets likely form in different conditions and at later times compared to gas giant planets when there is little gas left (e.g., Nagasawa et al. 2007), though residual gas may influence their atmospheric composition (e.g., transport water or carbon-rich solids to the inner disk, e.g., Ciesla & Lauretta 2005; Ciesla & Cuzzi 2006; Bond et al. 2010; Lee et al. 2010) and help circularize their orbits (Kominami & Ida 2002). In rocky planets,  $C/O \geq 0.8$  results in compositions dominated by SiC and graphite, with cores of iron and iron-peak elements. Since graphite is less dense than SiC, a pure carbon layer on top of a differentiated planet, versus the silicate composition of the Earth's crust, is expected (Kuchner & Seager 2005). In cold C planets, carbonaceous compounds that would be react to form CO in more oxidizing atmospheres could rain down onto the surface, forming oceans of tar (Kuchner & Seager 2005). Carbon-rich interiors also influence geophysical processes – both C and SiC have thermal conductivities over two orders of magnitude higher than Earth-like silicates and oxides (Goldberg et al.

2001), which, in addition to less  $\text{H}_2\text{O}$  in a C-rich environment, may decrease the probability of plate tectonics (Valencia et al. 2007; Korenaga 2010; Unterborn et al. 2013). Throughout much of Earth’s mantle, carbon is likely in diamond form (Dasgupta & Hirschmann 2010), although the high viscosity and thermal conductivity of diamond has little impact in Earth’s case because it is relatively carbon-poor. A “diamond”-rich planet would have a drastically different dynamics and thermal evolution versus a silicate-rich Earth-like composition, due to diamond’s 2-, 3-, and 5-orders of magnitude larger than bulk silicate lattice thermal conductivity (Osako & Ito 1991; Panero & Jeanloz 2001), radiative thermal conductivity (Keppeler et al. 2008), and viscosity (Unterborn et al. 2013), respectively. And yet, compared to solar-composition, a C-rich system would have a larger inner zone of refractory C solids and less  $\text{H}_2\text{O}$  ice farther out, concentrating more solid mass in the inner disk (Bond et al. 2010). Thus, C-rich systems may be more efficient at producing small planets, but their habitability may be reduced. At this point, observational constraints on rocky-planet compositions are limited to either measuring their host star abundances and assuming similarity (whether exact or some ratio or relation) or measuring their mass and radius and inferring a density and thus their bulk composition.

## 2.6 Last Word

This chapter has given a broad overview of the “story” of planet formation, how the different steps in this process are observed, and the important role that carbon and oxygen (and their carriers) play in the evolution and composition of stars, disks, and planets. The next Chapters are ordered semi-chronologically, starting with my second-year project detailing the interpretation of observed emission from HCN gas in the warm inner disks around T Tauri stars (Chapter 3),

moving on to observational constraints on the composition of the best-observed super-Earth GJ 1214b based on optical transmission photometry (Chapter 4), and finishing with several Chapters (5-7) focused on the relationship between host star C/O ratios and their (mature) planets' compositions, and how this comparison may illuminate planet formation histories. In the conclusion of my thesis, I discuss future directions for my research.

## CHAPTER 3

MEASURING ORGANIC MOLECULAR EMISSION IN DISKS WITH LOW  
RESOLUTION *Spitzer* SPECTROSCOPY

We explore the extent to which *Spitzer* IRS spectra taken at low spectral resolution can be used in quantitative studies of organic molecular emission from disks surrounding low mass young stars. We use *Spitzer* IRS spectra taken in both the high and low resolution modules for the same sources to investigate whether it is possible to define line indices that can measure trends in the strength of the molecular features in low resolution data. We find that trends in HCN emission strength seen in the high resolution data can be recovered in low resolution data. In examining the factors that influence the HCN emission strength, we find that the low resolution HCN flux is modestly correlated with stellar accretion rate and X-ray luminosity. Correlations of this kind are perhaps expected based on recent observational and theoretical studies of inner disk atmospheres. Our results demonstrate the potential of using the large number of low resolution disk spectra that reside in the *Spitzer* archive to study the factors that influence the strength of molecular emission from disks. Such studies would complement results for the much smaller number of circumstellar disks that have been observed at high resolution with IRS. A verison of this chapter originally appeared as a published paper in the *Astrophysical Journal* (Teske et al. 2011). All of the work described below was carried out by me, with much help from my advisor at the time, Joan Najita, and very helpful commentary and edits from the co-authors of the published paper, John Carr, Ilaria Pascucci, Daniel Apai, and Thomas Henning.



### 3.1 Introduction

Circumstellar disks composed of gas and dust are ubiquitous around forming stars and are the birthplace of planets. Since habitable planets are expected to form in warm inner disks ( $< 3\text{--}4$  AU for sun-like stars), studying this region is especially relevant to understanding the origin and evolution of habitable planetary systems and their diverse properties. Interest in the origin of stars and planets has lead to numerous studies of the gaseous components of disks at large ( $> 20$  AU) radial distances (e.g., Dutrey et al. 1996, 1998, 2007; Kastner et al. 1997; Guilloteau & Dutrey 1998; Thi et al. 2004; Semenov et al. 2005; Qi et al. 2008) as well as warmer, solid components within  $\sim 10$  AU of the star (e.g., Natta et al. 2007; Henning & Meeus 2009; Apai & Lauretta 2010).

Observations of the warm gas within the inner disk are also necessary to fully understand the structure and dynamics affecting disk evolution and planet formation (see Carr 2005; Najita et al. 2007a; Millan-Gabet et al. 2007; Carmona 2010 for recent reviews). When such gas is viewed in emission from disks around T Tauri stars (TTS), which are optically thick in the continuum at small disk radii ( $< 10$  AU), the emission likely originates in a temperature inversion region at the disk surface. The very inner regions of the gaseous disk ( $< 0.3$  AU) have been studied previously using molecular transitions such as CO overtone emission (e.g., Carr et al. 1993; Chandler et al. 1993; Najita et al. 1996, 2000, 2009; Blum et al. 2004; Thi et al. 2005; Thi & Bik 2005; Berthoud et al. 2007) and ro-vibrational  $\text{H}_2\text{O}$  emission (e.g., Carr et al. 2004; Najita et al. 2000, 2009; Thi & Bik 2005). Observations of CO fundamental emission (e.g., Carr et al. 2001; Najita et al. 2003, 2008; Blake & Boogert 2004; Brittain et al. 2007; Salyk et al. 2007, 2009; Pontoppidan et al. 2008) and UV transitions of  $\text{H}_2$  (e.g., Valenti et al. 2000; Ardila & Basri 2000; Herczeg et al. 2002, 2006; Bergin et al. 2004) have been used to probe larger

disk radii (out to  $\sim 1\text{--}2$  AU).

More recently, observations of T Tauri disks made with the high resolution ( $R \sim 700$ ) modules of the Infrared Spectrograph (IRS) on board the *Spitzer Space Telescope* (Houck et al. 2004) have revealed that simple organic molecules (HCN,  $\text{C}_2\text{H}_2$ ,  $\text{CO}_2$ ) and water (Lahuis et al. 2006; Carr & Najita 2008; Salyk et al. 2008) are present in the warm inner disk region ( $\lesssim 5$  AU). IRS observations indicate that mid-infrared molecular emission is common among TTS (Pontoppidan et al. 2010; Carr & Najita 2011; see also Pascucci et al. 2009 in the context of low resolution IRS data) and can be used to probe the thermal and chemical structure of the inner gaseous disk (see Figure 3.1).

With the cryogen of the *Spitzer Space Telescope* depleted, it is no longer possible to obtain more sensitive, mid-infrared spectroscopy of protoplanetary disks, making the *Spitzer* archive the primary source of new information on warm disk chemistry. However, with most of the data in the archive taken in low-resolution mode, the question emerges: How much information regarding molecular emission features can be extracted from the low-resolution observations? Pascucci et al. (2009) previously explored this question, showing that molecular emission could be detected in low resolution IRS spectra of dozens TTS and lower-mass stars and brown dwarfs. They found that HCN emission at  $14\text{ }\mu\text{m}$  was almost always brighter than  $\text{C}_2\text{H}_2$  emission at  $13.7\text{ }\mu\text{m}$  among T Tauri stars, while only  $\text{C}_2\text{H}_2$  and no HCN was detected for lower mass stars and brown dwarfs. This led them to propose that there are differences in the relative abundance of molecular species as a function of stellar mass.

Here we build upon the work of Pascucci et al. (2009) by investigating the extent to which we can extract quantitative information from low resolution *Spitzer* IRS spectra of inner T Tauri disks. To do this, we compare the molecular emission

strength in a sample of high resolution IRS spectra of T Tauri stars with similar measurements of the same sources made in the low resolution mode of IRS. If quantitative trends in the strength of molecular emission features can be recovered from low resolution spectra, the archival *Spitzer* IRS data could be used to study the strength of molecular features in disks. Since, as we discuss below, a variety of physical and chemical processes can potentially affect the molecular emission strength, spectra of large samples of sources, such as those available in the *Spitzer* archive, are a valuable asset for demographic studies that seek to identify the dominant processes influencing the molecular emission from disks. In §2 we describe the data sets used in this paper. In §3 we present our method of analysis and our results. The latter are explored further in §4.

### 3.2 Data Sets

For our comparison of high and low resolution data, we examined a small set of *Spitzer* IRS spectra of T Tauri stars in the Taurus-Auriga star-forming region. The higher resolution data were taken with IRS in the short-high mode (SH, 10–19  $\mu\text{m}$ ,  $R \sim 700$ ), and the lower resolution data were taken in the short-low mode (SL, 5.2–14  $\mu\text{m}$ ,  $R \sim 100$ ). Our SH data set was selected from classical T Tauri stars that were observed as part of the Cycle 2 GO Program 20363 (Carr & Najita 2008, 2011). From 11 sources in that program, we selected a sample of “normal” T Tauri stars, i.e, sources with stellar accretion rates  $\lesssim 10^{-7} \text{ M}_{\odot} \text{ yr}^{-1}$ , to avoid the influence of highly energetic accretion processes (e.g., jets) on the spectrum. We also excluded close binary stars (the closest companion separation in our sample is 0.88”) since tidal interactions between the disk and binary can disrupt or truncate the inner disk region ( $< 5 \text{ AU}$ ). The resulting 8 sources display mid-infrared colors that are typical of “normal” TTS. That is, they have colors

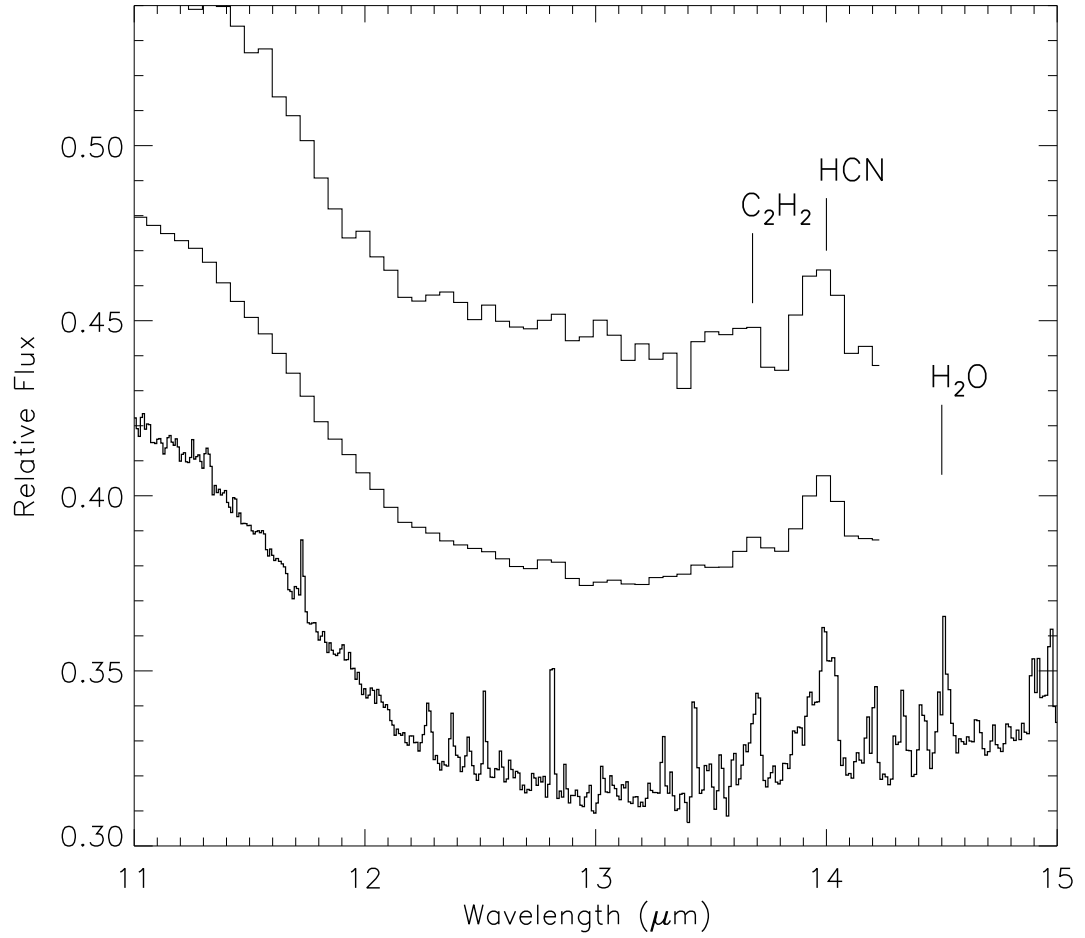


Figure 3.1 The 11–15  $\mu\text{m}$  spectrum of AA Tau as observed in the SH ( $R \sim 700$ , bottom) and SL ( $R \sim 100$ , top) modes. The middle spectrum is the SH spectrum smoothed to the resolution of the SL data and rebinned to the pixel sampling of the SL data. Several prominent molecular features are marked with vertical lines. The high resolution data reveal a rich emission spectrum that is common among TTS. We show that trends in HCN emission strength in high resolution spectra can be recovered from lower resolution data.

that are unlike those of transition objects. Specifically, as described in Furlan et al. (2006), our sample has  $n_{6-13}$  between  $-1.0$  and  $-0.01$ , and  $n_{13-25}$  between  $-0.40$  and  $0.17$ , where  $n_{6-13}$  and  $n_{13-25}$  are the  $6-13\ \mu\text{m}$  and  $13-25\ \mu\text{m}$  colors, respectively.

To compare with the 8 SH spectra, we examined SL spectra of the same objects, originally observed as part of the *Spitzer* GO Program 2 (P.I. Houck). We used the reduced SL spectra from Pascucci et al. (2009). The observations were originally published as part of a larger data set by Furlan et al. (2006) using an alternative reduction procedure that they detail. Since the molecular emission features were not the focus of the latter study, those spectra were not as reliable in the  $13-15\ \mu\text{m}$  region.

In order to determine the processes that might influence the strength of any observed molecular emission, we also examined SL spectra of an additional 10 sources from the Pascucci et al. (2009) sample that have stellar properties similar to those of the SH sample: accretion rates within an order of magnitude of the typical T Tauri rate  $10^{-8}\ \text{M}_{\odot}\text{yr}^{-1}$  (Hartmann et al. 1998), an absence of close companions, and normal mid-infrared colors. While the full sample of 18 SL sources is relatively uniform in infrared spectral shape, binarity, and spectral type, it exhibits more variety in stellar accretion rate and X-ray luminosity (see Table 1). The stellar accretion rates in Table 1 are from Hartmann et al. (1998) and Najita et al. (2007b). Najita et al. adopted stellar accretion rates from several literature sources and placed them on the same scale as Hartmann et al., providing a set of comparable, consistent values. The X-ray luminosities are from the recent reanalysis of Güdel et al. (2010) of *XMM-Newton* and *Chandra* observations of a large number of T Tauri stars. The X-ray luminosities are for the  $0.3-10\ \text{keV}$  range and have been corrected for line-of-sight absorption (Güdel et al. 2010). We also

assume a distance of 140 pc. The properties of our full sample are described in Table 1.

### 3.3 Analysis and Results

#### 3.3.1 SH vs. SL Measurements

As described in §1, Pascucci et al. (2009) previously showed that the  $14\ \mu\text{m}$  HCN feature is almost always brighter than the  $13.7\ \mu\text{m}$   $\text{C}_2\text{H}_2$  feature in T Tauri spectra, making it typically the most apparent feature at low spectral resolution. Thus, while we investigated the possibility of detecting the emission from several molecules (HCN,  $\text{C}_2\text{H}_2$ ,  $\text{H}_2\text{O}$ ) in the SL data, we chose to focus in this paper on HCN due to its greater detectability in our sample.

To estimate the strength of the HCN feature, we defined a feature index based on the structure seen in existing SH spectra and synthetic disk emission models (e.g., Carr & Najita 2008) to avoid contamination from neighboring molecular features. We selected the wavelengths  $13.885\ \mu\text{m}$  and  $14.062\ \mu\text{m}$  to define the boundaries of the HCN feature. To estimate the underlying continuum, we found the average flux density in two neighboring regions,  $13.776\text{--}13.808\ \mu\text{m}$  and  $14.090\text{--}14.126\ \mu\text{m}$ , assigned these values to the midpoint of each region, and performed a linear fit to these two midpoints. We subtracted the continuum estimate from the spectrum and summed the resulting spectrum within the wavelength boundaries of the feature to obtain the feature flux. The equivalent width of the feature was calculated in a corresponding way. These values are reported in Tables 2 & 3. In the SH spectra, the continuum regions each span three pixels and the HCN feature spans fifteen pixels, while in the SL spectra the continuum regions each span less than one pixel and the HCN feature spans three pixels (see Figure 3.2).

Table 1. Our T Tauri Sample

Object	Spectral Type <sup>a</sup>	$\log(\dot{M}_*/M_{\odot}\text{yr}^{-1})^c$	$\log(L_X/\text{erg s}^{-1})^e$	IRS Mode
AA Tau	K7	−8.48	30.01	SH, SL
BP Tau	K7	−7.54	30.16	SH, SL
CW Tau	K3	−7.61	...	SL
CX Tau	M2.5	−8.97	...	SL
CY Tau	M1	−8.12	...	SL
DK Tau	K7	−7.42	29.93	SH, SL
DN Tau	M0	−8.46	30.03	SL
DO Tau	M0	−6.85	29.37	SH, SL
DP Tau	M0.5	−7.88	28.99	SL
DS Tau	K5	−7.89	...	SL
FZ Tau	M0 <sup>b</sup>	−7.32	...	SL
GI Tau	K6	−8.02 <sup>d</sup>	29.82	SH, SL
GK Tau	K7	−8.19	30.09	SH, SL
HN Tau	K5	−8.89 <sup>d</sup>	29.50	SL
IP Tau	M0	−9.10	...	SL
IQ Tau	M0.5	−7.55	29.50	SL
RW Aur	K3	−7.12	30.21	SH, SL
UY Aur	K7	−7.18	29.60	SH, SL

References. — (a) Kenyon & Hartmann (1995), unless otherwise noted; (b) Hartigan et al. (1994); (c) Najita et al. (2007b), unless otherwise noted; (d) Hartmann et al. (1998); (e) Güdel et al. (2010), corrected for line-of-sight absorption and assuming a distance of 140 pc

The errors on the SH spectra are described in Carr & Najita (2011). They are derived from the average RMS pixel variation around  $14\ \mu\text{m}$ . To estimate the errors on the SL spectra, we performed a linear fit to the continuum over  $\sim 15$  pixels between  $13\ \mu\text{m}$  and  $14.2\ \mu\text{m}$ , excluding the regions around HCN ( $13.885\ \mu\text{m} - 14.062\ \mu\text{m}$ ) and  $\text{C}_2\text{H}_2$  ( $13.609\ \mu\text{m} - 13.736\ \mu\text{m}$ ), and used the standard deviation of the difference between the observed spectrum and the fit as a measure of the pixel-to-pixel noise. We quote this measurement as our  $1\sigma$  errors in Table 2. These errors are generally smaller than those reported by Pascucci et al. (2009), who adopted an error for each pixel based on the difference in flux observed in a small number (2) of nod positions.<sup>1</sup>

In Table 2 we show the SL fluxes, equivalent widths, and errors determined using the feature and continuum regions defined above. Objects for which we have SH data are listed in Table 3 along with their flux and equivalent width measurements.

To understand any difference between these two data sets, we first smoothed the SH spectra to the approximate resolution of the SL spectra ( $R \sim 100$ ) by convolving with a Gaussian profile and rebinned to match the SL pixel sampling. As these two data sets are “contemporaneous” (they are the same data), comparing them avoids any complications arising from time variability in the mid-infrared emission spectrum. We find that the fluxes and equivalent widths of the smoothed/resampled data are on average  $\sim 50\%$  of those measured for the

---

<sup>1</sup>This latter error estimate can be affected by flux differences in the two beam positions if the object is not equally centered in the slit in each beam position. Some of the spectra appeared to suffer from this effect as the estimated errors were often larger than the pixel-to-pixel differences in the final spectrum (e.g., CW Tau, CY Tau, DN Tau, GI Tau, GK Tau, IP Tau). While our errors are generally smaller than the Pascucci et al. (2009) errors, our adopted errors may still overestimate the true error. That is because our approach assumes that the true spectrum is featureless in the region used to estimate the pixel-to-pixel variation (i.e., in the regions around the HCN and  $\text{C}_2\text{H}_2$  features), whereas the spectra may in fact have a rich spectrum of weaker emission features (Fig. 3.1). We return to this issue below.



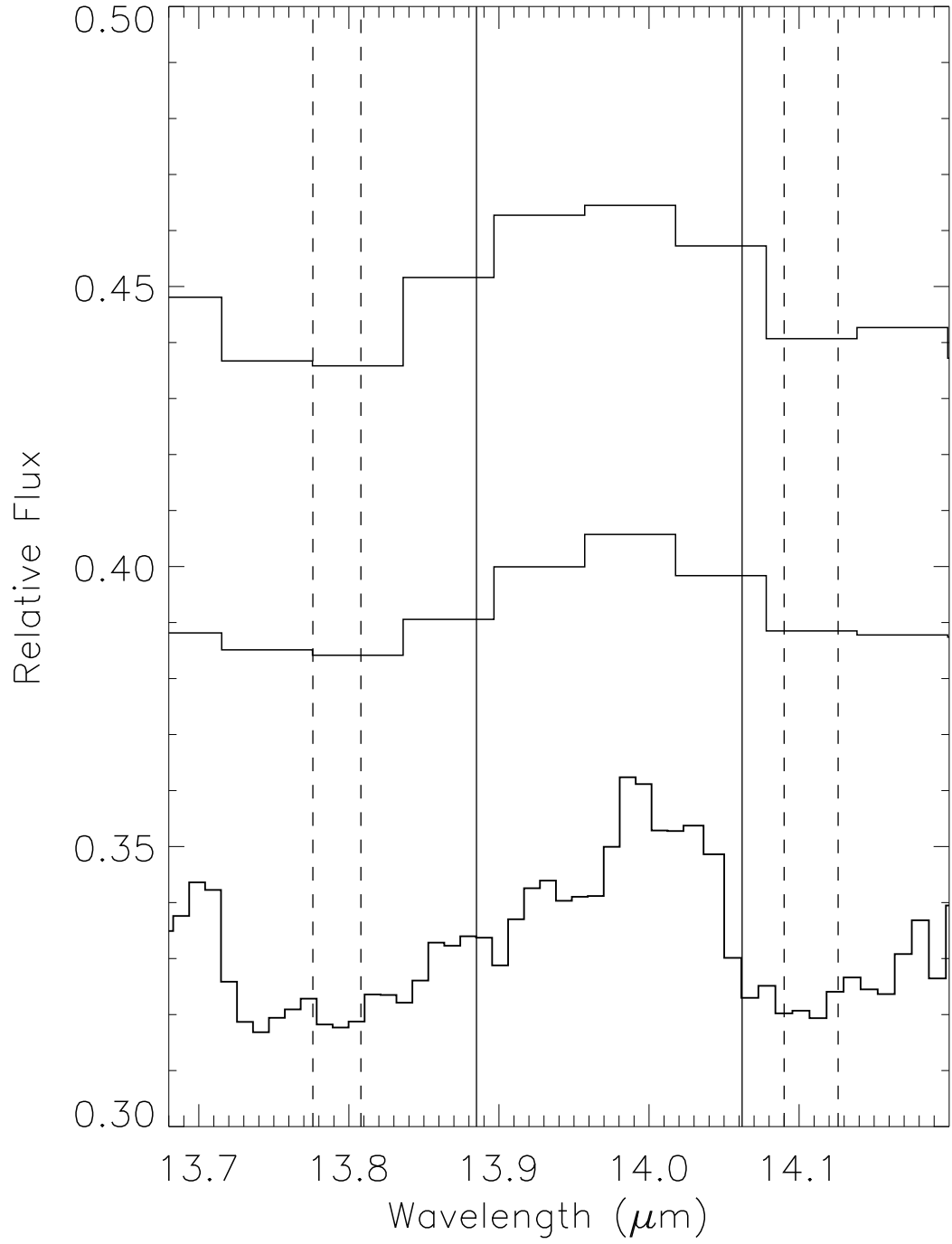


Figure 3.2 Spectrum of AA Tau comparing SH (bottom), smoothed and resampled (middle), and SL (top) data in the region around the 14  $\mu\text{m}$  HCN feature. The dotted vertical lines indicate the left and right continuum regions, and the vertical lines define the HCN feature, as listed in §3.

SH data (Fig. 3.3a). The lower values for the smoothed/resampled data are the result of the neighboring line emission from water and other features (Fig. 3.1; Carr & Najita 2008, 2011; Pontoppidan et al. 2010), which blends into a pseudo-continuum at lower spectral resolution, diluting the HCN flux and equivalent width. Because the neighboring line emission can vary from source to source in both shape and strength relative to HCN (stronger or weaker neighboring emission lines), there is dispersion about the  $\sim 50\%$  average value.

We would expect that the effect of the lower spectral resolution would lead to a similar difference between the SH measurements and those made on the real SL data. An additional factor in comparing the SH data with the (non-contemporaneous) SL data is the possibility of time variability in the HCN and/or non-HCN line emission spectrum, which would increase the dispersion beyond that arising from the lower resolution alone. This is indeed the case. The comparison of the SL equivalent widths shows more dispersion than the smoothed/resampled data when compared against the SH data (Fig. 3.3b). Figure 3.3c shows that the lower average equivalent width of the smoothed/resampled data does indeed capture the trend of the reduction in the SL equivalent width. Similar results are found for the HCN fluxes of the SH, smoothed/resampled, and SL data sets.

The HCN equivalent width and flux measurements from the SH and SL data are well correlated (Figure 3.3 and Table 4). To assess the significance of the apparent trends, we use two correlation coefficients, Kendall's rank correlation coefficient,  $\tau_{Kendall}$ , and Pearson's linear correlation coefficient,  $r$ . The former,  $\tau_{Kendall}$ , is a non-parametric statistic that measures the degree of correlation between two variables; values close to unity signify a tighter correlation, while values close to 0 signify no correlation. Our calculated  $\tau_{Kendall}$ -values are all  $\geq 0.59$ . The two-sided  $P$  values that correspond to  $\tau_{Kendall}$ ,  $P_{\tau}$ , represent the confidence lev-

Table 2. HCN Short-Low Measurements

Object	SL HCN Flux (mJy- $\mu$ m)	SL HCN EW ( $10^{-3}$ $\mu$ m)
AA Tau	$4.00 \pm 0.66$	$10.6 \pm 1.77$
BP Tau	$2.43 \pm 0.34$	$5.77 \pm 0.81$
CW Tau	$3.17 \pm 0.77$	$4.15 \pm 1.02$
CX Tau	$-0.178 \pm 0.53$	$-1.16 \pm 3.35$
CY Tau	$-0.170 \pm 0.54$	$-1.47 \pm 4.60$
DK Tau	$1.75 \pm 0.70$	$1.96 \pm 0.78$
DN Tau	$2.20 \pm 0.39$	$7.04 \pm 1.28$
DO Tau	$1.87 \pm 1.27$	$1.19 \pm 0.81$
DP Tau	$0.608 \pm 0.66$	$1.03 \pm 1.11$
DS Tau	$2.33 \pm 0.23$	$9.65 \pm 0.99$
FZ Tau	$4.37 \pm 1.38$	$4.93 \pm 1.58$
GI Tau	$2.99 \pm 0.62$	$4.09 \pm 0.85$
GK Tau	$-1.13 \pm 0.77$	$-1.37 \pm 0.93$
HN Tau	$0.783 \pm 0.59$	$0.992 \pm 0.75$
IP Tau	$-0.964 \pm 0.69$	$-5.26 \pm 3.75$
IQ Tau	$2.02 \pm 0.62$	$6.07 \pm 1.90$
RW Aur	$5.51 \pm 1.34$	$4.32 \pm 1.06$
UY Aur	$2.62 \pm 1.30$	$0.871 \pm 0.43$

Table 3. HCN Short-High and Smoothed &amp; Resampled Measurements

Object	SH HCN Flux (mJy- $\mu$ m)	SH HCN EW ( $10^{-3}$ $\mu$ m)	SM+RS HCN Flux (mJy- $\mu$ m)	SM+RS HCN EW ( $10^{-3}$ $\mu$ m)
AA Tau	$4.43 \pm 0.08$	$13.9 \pm 0.25$	$2.52 \pm 0.06$	$7.72 \pm 0.18$
BP Tau	$4.31 \pm 0.08$	$11.6 \pm 0.21$	$2.35 \pm 0.06$	$6.21 \pm 0.15$
DK Tau	$5.01 \pm 0.15$	$6.59 \pm 0.19$	$2.20 \pm 0.10$	$2.86 \pm 0.13$
DO Tau	$1.32 \pm 0.25$	$0.653 \pm 0.12$	$-0.676 \pm 0.12$	$-0.333 \pm 0.09$
GI Tau	$4.69 \pm 0.12$	$6.18 \pm 0.15$	$2.47 \pm 0.08$	$3.22 \pm 0.11$
GK Tau	$0.850 \pm 0.15$	$1.07 \pm 0.15$	$0.104 \pm 0.09$	$0.130 \pm 0.11$
RW Aur	$9.36 \pm 0.25$	$6.32 \pm 0.17$	$3.97 \pm 0.18$	$2.64 \pm 0.12$
UY Aur	$5.95 \pm 0.34$	$2.24 \pm 0.12$	$1.56 \pm 0.24$	$0.58 \pm 0.09$

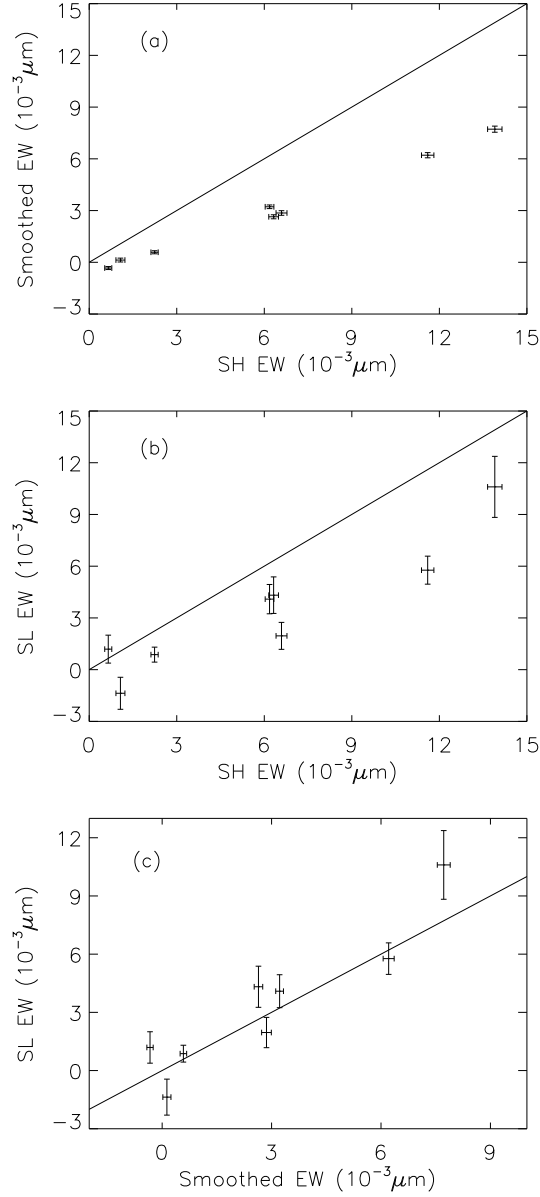


Figure 3.3 The comparison SH, smoothed/resampled and SL HCN equivalent widths (Tables 2 and 3). A unity line is shown for reference in each plot.

els of the coefficient – a smaller  $P$  value indicates a lower probability of a false conclusion. Pearson's  $r$ -value measures how closely two parameters fit a linear relationship (assuming the parameter distributions are normal). The closer  $|r|$  is

to unity, the more linear the relationship. Our calculated  $r$ -values are all  $\geq 0.80$ , signifying a near-linear correlation. We also calculate  $p_{rand}$  (as a %), the probability that our measurements are randomly distributed (and thus uncorrelated). The calculated  $p_{rand}$  values,  $\sim 1.8\%$  and  $7.0\%$  for the equivalent width and flux relations, respectively, indicate that it is highly unlikely that our measurements are randomly distributed. These statistics for the above trends are shown in Table 4. As we suspect and the figures indicate, the trends we find are statistically significant.

To summarize, while the SL measurements do not recover the HCN flux of the SH spectra, our results suggest that studies using SL spectra can recover quantitative trends in molecular emission strength seen in higher resolution observations. The SL HCN measurements may therefore track the SH HCN measurements well enough to reveal interesting trends when compared with other T Tauri properties. We explore this possibility in the next section.

Although we refer to our SL measurements as “fluxes” and “equivalent widths”, it is more useful to think of these quantities as *line* indices. The index can be positive (e.g., if there is HCN emission) or negative. The latter could occur either if there is either true absorption (e.g., as in IRS 46; Lahuis et al. 2006) or emission from other features in the “continuum” regions that are used to define the index.

In addition to the HCN emission feature, we also attempted a similar analysis for  $C_2H_2$  ( $\sim 13.7 \mu m$ ) and an  $H_2O$  feature at  $\sim 12.4 \mu m$ . We were unable to recover with the SL data emission strength trends seen in the SH data for these features, probably because they are weaker than HCN in spectra of T Tauri stars (Pascucci et al. 2009). We note that greater success may be possible with data analysis techniques more sophisticated than those used here. We also note that when we performed the same analysis using the Furlan et al. (2006) reduction of

Table 4. Correlation Between SH and SL HCN Emission

Parameters	n <sup>a</sup>	r <sup>b</sup>	$\tau_{Kendall}$ <sup>c</sup>	P <sub><math>\tau</math></sub> <sup>d</sup>	p <sub>rand</sub> (%) <sup>e</sup>
SH vs. SL EW	8	0.904	0.714	0.019	1.77
SH vs. SL Flux	8	0.797	0.590	0.108	7.01
Smoothed vs. SL EW	8	0.908	0.714	0.019	1.64

<sup>a</sup>The number of objects used for calculation of the statistic.

<sup>b</sup>Pearson's  $r$  linear correlation coefficient, a measure of how closely two variables fit a linear relationship.  $|r|$  values closer to 1 indicate better correlation.

<sup>c</sup>Kendall's  $\tau$  rank statistic, a measure of the degree of correlation between two parameters that does not assume normally distributed data. The closer  $|\tau|$  is to 1, the better the correlation.

<sup>d</sup>Two-sided  $P$  value, the probability (assuming no correlation) of obtaining a result at least as extreme as the result that is actually observed. The lower the  $P$  value, the higher the probability of correlation..

<sup>e</sup>Probability of getting  $r$  from a random distribution of size  $n$ .

Table 5. Correlations Between Stellar Parameters &amp; SL HCN Emission

Parameters	Points Rejected	$n^a$	$r^b$	$\tau_{Kendall}^c$	$P_\tau^d$	$p_{rand} (\%)^e$	$\chi^2$	$q$
$\log \dot{M}_*/M_\odot \text{yr}^{-1}$ vs. SL Flux – initial fit	none	18	0.534	0.386	0.028	8.42	1.17	0.280
$\log(\dot{M}_*/M_\odot \text{yr}^{-1})$ vs. SL Flux – final fit	2	16	0.655	0.567	0.178	2.87	0.753	0.721
$\log(L_X/\text{erg s}^{-1})$ vs. SL Flux – initial fit	none	12	0.403	0.382	0.099	34.19	1.37	0.186
$\log(L_X/\text{erg s}^{-1})$ vs. SL Flux – final fit	1	11	0.648	0.587	0.016	9.80	0.676	0.731
Spectral Type vs. SL Flux – initial fit	none	18	−0.541	−0.405	0.028	7.26	3.34	0.00
Spectral Type vs. SL Flux – final fit	1	17	−0.564	−0.485	0.010	6.19	3.12	0.00
Spectral Type vs. $\log(L_X/\text{erg s}^{-1})$	none	12	−0.464	−0.355	0.150	26.34	1.33	0.205
Spectral Type vs. $\log(\dot{M}_*/M_\odot \text{yr}^{-1})$	none	18	−0.269	−0.154	0.417	52.36	1.48	0.096
$\log(L_X/\text{erg s}^{-1})$ vs. $\log(\dot{M}_*/M_\odot \text{yr}^{-1})$	none	12	−0.084	0.015	1.00	67.47	1.62	0.095

Note. — See description of parameters in Table 4 and in text.

the SL data we did not find a significant correlation between SL and SH emission strengths, demonstrating that the specific data reduction procedure for the SL data can influence the ability to recover trends in SH data.

### 3.3.2 Variation in HCN Feature Strength

In our sample of SL spectra, the HCN flux varies from non-detections (below  $\sim 1$  mJy- $\mu\text{m}$ ) to over 5 mJy- $\mu\text{m}$ , and the HCN equivalent width varies over approximately an order of magnitude (see Table 2). What causes the strength of the HCN feature to differ in these systems? Although the sources have many similar properties (e.g., they have similar stellar masses and spectral types), the stellar accretion rate ( $\dot{M}_*$ ) and X-ray luminosity ( $L_X$ ) do vary across the sample, as may other physical properties not described here. To investigate whether stellar accretion rate and X-ray luminosity play a role in determining the HCN emission strength, we compared the HCN fluxes of the sources in the SL sample with their values of  $\dot{M}_*$  and  $L_X$  from the literature (Table 1).



In Figure 3.4, panels (a), (b), and (c) plot SL HCN flux against stellar accretion rate, stellar X-ray luminosity, and spectral type, respectively. Panels (d), (e), and (f) plot these three quantities – accretion rate, X-ray luminosity, and spectral type – against each other. The distribution of points suggests possible trends between SL HCN flux and the quantities in Fig. 3.4a, b, c, although these trends, if they exist, are not extremely tight. The lack of a tight correlation is perhaps not surprising since many physical and chemical processes (e.g., heating that is unrelated to accretion, chemical synthesis, photodestruction, excitation conditions) can potentially affect the strength of any given molecular emission feature. As a result, outliers in any trend are to be expected, e.g., if some systems have managed to synthesize more or less HCN. We therefore employed the following simple rejection scheme when examining our data for possible trends: we performed a weighted linear fit, including uncertainties in both the x- and y-directions, to all of the data in Fig. 3.4a, b, and c and iteratively rejected the top one to two outliers, all of which were above  $3.3\sigma$ . The outliers are plotted as open triangles in Fig. 3.4, and a summary of the fit statistics is given in Table 5. Table 5 also reports the reduced  $\chi^2$  of the linear fit and  $q$ , the probability that a correct model would give a  $\chi^2$  value equal to or larger than the observed  $\chi^2$ .

In the case of Fig. 3.4a, where we plot SL HCN flux versus stellar accretion rate, the Pearson’s  $r$ -value associated with all of the data points shown is 0.53 and the  $\tau_{Kendall}$  value is 0.39 (see Table 5). Rejection of the top two outliers at  $3.6\sigma$  and  $3.8\sigma$  (open symbols) resulted in a Pearson’s  $r$ -value associated with the remaining data points of 0.66 and the  $\tau_{Kendall}$  value of 0.57 (see also Table 5), suggesting a potential positive correlation between stellar accretion rate and HCN flux.

Even with outlier rejection, there is still significant scatter, which is perhaps to

be expected, as discussed above. In addition, the difficulty in determining precise veiling and bolometric corrections likely introduces systematic uncertainty in stellar accretion rate measurements, as discussed by Hartigan et al. (1991) and Gullbring et al. (1998). These authors also note that time variability, as a result of intrinsic fluctuation in the accretion rate or the modulation of a nonaxisymmetric magnetosphere, can contribute to the uncertainty; they suggest a cumulative uncertainty of  $\sim 3$  in stellar accretion rate (Hartigan et al. 1991; Gullbring et al. 1998). We represent this uncertainty by the horizontal bar in the lower left corner of Fig. 3.4a.

For Fig. 3.4b, which shows SL HCN flux versus stellar X-ray luminosity, the associated Pearson's  $r$ -value for all of the data points is 0.40 and the  $\tau_{Kendall}$  value is 0.38 (see Table 5). Rejection of the top outlier at  $3.3\sigma$  (open symbol) resulted in a Pearson's  $r$ -value associated with the remaining data points of 0.65 and the  $\tau_{Kendall}$  value of 0.59 (see also Table 5), suggesting a potential positive correlation between stellar X-ray luminosity and HCN flux. The larger  $p_{rand}$  and  $P_\tau$  for these data (compared to those shown in Fig. 3.4a or 4c; see Table 5) are partly a result of the smaller sample size  $n$  (12 versus 18 objects). Some of the scatter in this plot is likely the result of variability in  $L_X$ . Güdel et al. (2010) note that the range of uncertainty in X-ray flux determination is dominated by variability on various time scales, and (apart from singular flares) is typically characterized by flux variations within a factor of two from low to high levels. We represent this uncertainty by the horizontal error bar in the lower left corner Fig. 3.4b.

Fig. 3.4c shows SL HCN flux versus stellar spectral type. The associated Pearson's  $r$ -value for all of the data points is  $-0.54$  and the  $\tau_{Kendall}$  value is  $-0.41$  (see Table 5). Rejection of the top outlier  $3.5\sigma$  (open symbol) resulted in a Pearson's  $r$ -value associated with the remaining data points of  $-0.56$  and the  $\tau_{Kendall}$  value of

−0.49 (see also Table 5). An estimated spectral type error of 0.5 subclass is much smaller than the dispersion of the points. While the statistics suggest a possible negative correlation between spectral type and HCN flux, it seems unlikely that spectral type (and therefore stellar temperature) directly affects the HCN flux from the disk; while the HCN flux in our sample varies over almost an order of magnitude, the range of spectral types we studied is relatively narrow, spanning  $\sim 1400$  K in temperature.

Fig. 3.4d may shed some light on this issue. It shows that within our sample, X-ray luminosity decreases on average with later spectral type. The associated Pearson’s  $r$ -value for all the objects plotted is −0.46, and the  $\tau_{Kendall}$  value is −0.36 (see Table 5). This modest correlation in our sample is also supported by larger samples of pre-main sequence stars (e.g., Winston et al. 2010; Preibisch et al. 2005); our examination of those data show a similar decrease in X-ray luminosity with later spectral type. This trend between X-ray luminosity and spectral type could be explained as a consequence of the rough proportionality between  $L_X$  and  $L_*$  in pre-main sequence stars, with  $L_X/L_* \sim 10^{-4} - 10^{-3}$  (Telleschi et al. 2007; Preibisch et al. 2005). Among stars in Myr-old populations such as those in our sample,  $L_*$  also decreases with later spectral type (Stelzer & Neuhäuser 2001; Preibisch et al. 2005; Winston et al. 2010), so  $L_X$  would also be expected to decrease with later spectral type in our sample. Thus, the trend in Fig. 3.4c may not reflect a fundamental relationship between HCN flux and spectral type, but instead results from the two underlying relations between  $L_X$  and HCN flux (Fig. 3.4b) and  $L_X$  decreasing with later spectral type (Fig. 3.4d).

Another possibility is that the luminosity associated with accretion ( $L_{acc}$ ) is decreasing with later spectral type and this is what drives the trend of HCN flux with spectral type. The average accretion rate is known to decrease with decreas-

ing mass (later spectral type), but the spread at any given mass is  $\sim$  two orders of magnitude (Muzerolle et al. 2005). In Fig. 3.4e, we plot stellar accretion rate versus spectral type. There is no strong correlation (see Table 5) within the narrow range of spectral type of our sample, consistent with Muzerolle et al. (2005). In Fig. 3.4f, we plot the stellar X-ray luminosity versus the stellar accretion rate. The comparison also shows no correlation (see Table 5).

Because our data set is small (and our analysis methods explorative), larger samples of IRS spectra are needed to confirm that any trends exist and test whether any of the fits proposed are reasonable representations of the trend. Our sample is artificially sparse at high accretion rates due to the difficulty in measuring HCN emission from low resolution spectra of high-accretion sources; their enhanced continuum flux reduces the contrast of emission features above the continuum. Thus it would be useful to expand the sample to include more sources covering the same range of stellar accretion rates as well as a larger range of accretion rates. If HCN flux and stellar accretion rate are correlated, we would expect that sources with accretion rates  $< 10^{-9} \text{ M}_{\odot} \text{ yr}^{-1}$  would have low to undetectable HCN fluxes. Similarly, we would expect that sources with X-ray luminosities below  $\sim 6.3 \times 10^{28} \text{ erg s}^{-1}$  would not show detectable HCN, and that sources with X-ray luminosities above  $\sim 2.5 \times 10^{30} \text{ erg s}^{-1}$  might continue to show enhanced HCN emission with increasing X-ray flux.

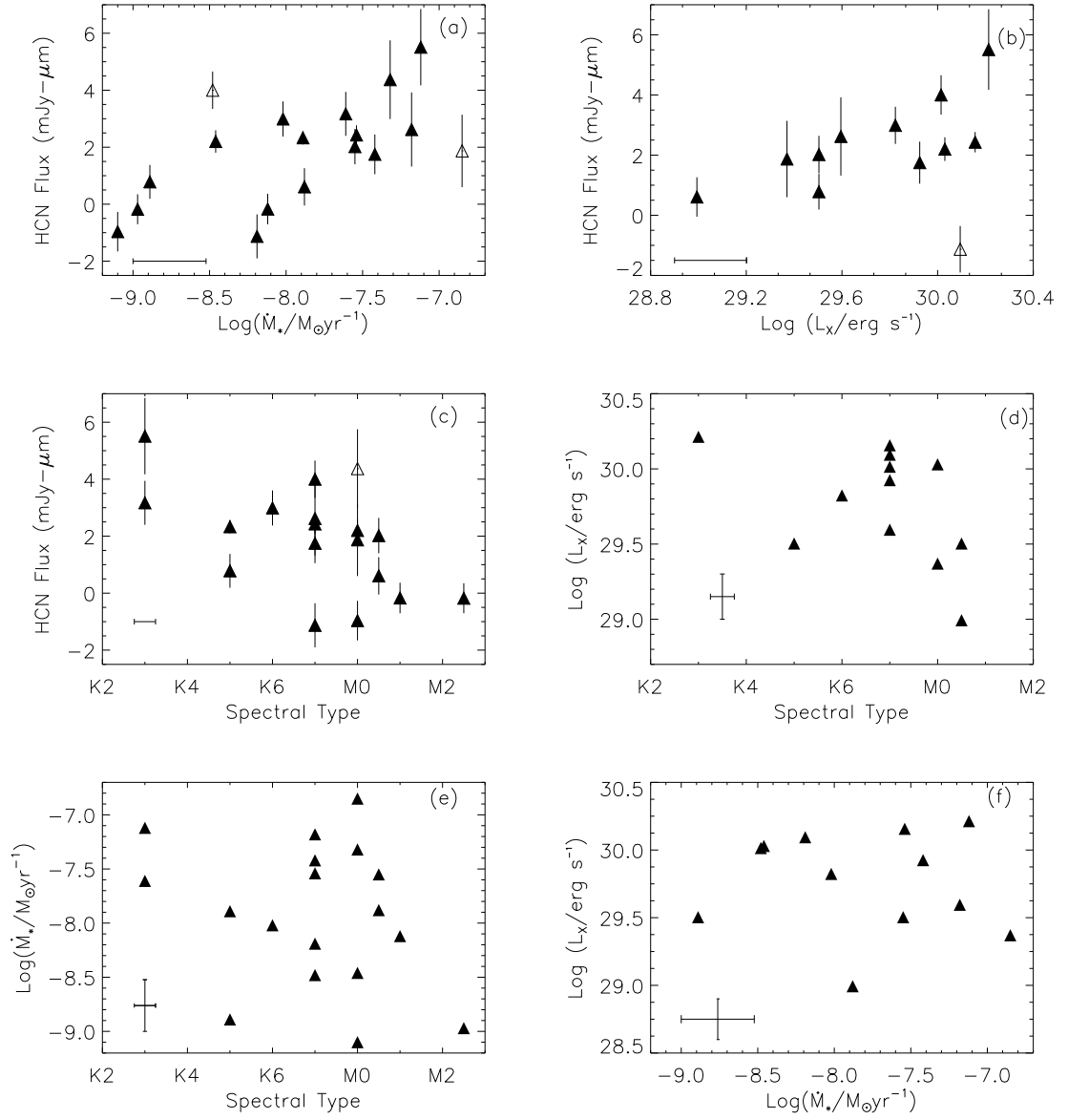


Figure 3.4 The comparison of stellar parameters and SL HCN flux. Open triangles designate outliers identified by iterative rejection. (a) SL HCN flux versus stellar accretion rate ( $\dot{M}_*$ ). (b) SL HCN flux versus stellar X-ray luminosity ( $L_X$ ). (c) SL HCN flux versus spectral type. (d)  $L_X$  versus spectral type. (e)  $\dot{M}_*$  versus spectral type. (f)  $L_X$  versus  $\dot{M}_*$ .

### 3.4 Discussion

We find that SH and SL measurements of the  $14\ \mu\text{m}$  HCN feature are correlated in our small sample of T Tauri stars. Our results support the work of Pascucci et al. (2009), who used these SL spectra as part of their larger sample to deduce the differences between gaseous disks surrounding T Tauri stars and those surrounding lower mass stars and brown dwarfs. That study showed a prominent difference in the relative detection rates of HCN and  $\text{C}_2\text{H}_2$  between the two samples, with HCN detected more commonly in TTS than in the lower mass objects. The median spectra they created of samples of T Tauri stars and the lower mass objects showed that the flux ratio of HCN to  $\text{C}_2\text{H}_2$  is  $\sim 3$  for T Tauri stars and much lower,  $\sim 0.2$ , for the lower mass objects. Our results show that such comparisons can be extended to comparisons of HCN feature fluxes in the spectra of individual objects.

We also find potential trends between the SL HCN flux index and stellar accretion rate, X-ray luminosity, and stellar spectral type. With respect to the potential trend with stellar accretion rate, a similar relation between CO fundamental emission and stellar accretion rate has been reported in TTS and Herbig Ae-Be stars (Najita et al. 2003; Brittain et al. 2007). These authors suggest that a correlation between CO emission and accretion rate would be expected if accretion-related processes heat the disk atmosphere. In a related study of transition objects, Salyk et al. (2009) report that the sources in their sample that show inner-disk CO fundamental emission have higher accretion rates. The sources that display CO fundamental emission also display  $\text{Pf}\beta$  emission, which is moderately correlated with the accretion diagnostic  $\text{H}\alpha$ . Accretion-related processes could strengthen the HCN emission by enhancing the temperature, and/or the HCN abundance, in the disk atmosphere.

The effect of accretion-related heating on disk molecular emission has been studied by Glassgold et al. (2004, 2009). They proposed two sources of mechanical heating in the disk atmosphere: viscous accretion, possibly generated by the magnetorotational instability (MRI; Stone et al. 2000), and stellar wind interaction with the disk surface (Glassgold et al. 2004). Glassgold et al. (2009) invoked mechanical heating, due to one or both of these sources, in addition to the formation of  $\text{H}_2$  on warm grains, to explain the large column densities of warm  $\text{H}_2\text{O}$  that are observed in emission in disk atmospheres. Glassgold et al. (2009) determined that these processes can increase the thickness of the warm water column to the extent reported by Carr & Najita (2008) and Salyk et al. (2008). If mechanical heating does affect the thermal-chemical structure of disk atmospheres in this way, and if higher accretion rates and higher rates of mechanical heating derive from the same physical mechanism, we would expect to see a correlation between accretion rate and  $\text{H}_2\text{O}$  feature strength. Accretion rate may play a similar role in enhancing HCN emission strength, i.e. by increasing the column density of warm HCN in the disk atmosphere.

There may be an additional chemical connection between  $\text{H}_2\text{O}$  and HCN emission, with efficient water formation possibly leading to an enhanced HCN abundance. As described by Lahuis & van Dishoeck (2000), efficient  $\text{H}_2\text{O}$  formation will drive most of the available oxygen into  $\text{H}_2\text{O}$ , resulting in a lower abundance of gaseous  $\text{O}_2$ . Since  $\text{O}_2$  would otherwise react with atomic carbon, the lack of  $\text{O}_2$  could lead to an enhanced atomic C abundance and in turn a larger HCN abundance (e.g., via the reaction scheme described by Agundez et al. 2008). Perhaps for this reason, hot cores that are found to have the highest gas phase  $\text{H}_2\text{O}$  abundances are also those with the highest HCN abundances (e.g., van Dishoeck 1998; Lahuis & van Dishoeck 2000). Thus accretion-related mechanical heating

in disks may enhance disk HCN emission both thermally, by producing a deeper temperature inversion at the disk surface, and chemically, by enhancing the HCN abundance as a consequence of efficient water formation. Detailed modeling is needed to explore these possibilities.

Increased UV irradiation produced by higher stellar accretion may also enhance the HCN abundance. Using Agúndez et al. (2008) as a guide, Pascucci et al. (2009) argued that the HCN abundance in disk atmospheres may be limited by the availability of atomic nitrogen and that the atomic nitrogen abundance depends primarily on the dissociation of  $N_2$  via UV-dissociation. Thus, HCN would be brighter for sources with more energetic UV flux (i.e., higher accretion rate), while  $C_2H_2$  (not requiring nitrogen to form) would not vary. This may explain their finding that T Tauri stars have stronger HCN emission relative to  $C_2H_2$  than lower mass stars and brown dwarfs, as these lower mass objects would have lower photospheric UV emission and lower accretion rates than TTS. The range in stellar accretion rate among T Tauri stars may induce a range in their HCN abundances for similar reasons.

Another factor that may play a role in setting the HCN flux from the disk is X-ray irradiation, based on Fig. 3.4b. The effect of X-ray irradiation on the thermal-chemical structure of disks has been investigated previously by Glassgold et al. (2004, 2009), although they did not specifically study HCN. X-ray irradiation may enhance the abundance of molecular ions and radicals that lead to enhanced HCN emission. Further modeling is needed to investigate the relative roles of X-ray and UV irradiation in this context.

We find a possible trend of HCN flux decreasing with stellar spectral type (Fig. 3.4c). While this is in the spirit of the trend found by Pascucci et al. (2009), it is unlikely that stellar spectral type itself (i.e., stellar temperature) is affecting



the HCN flux for this small sample of TTS. The other two processes we examined, stellar accretion rate and stellar X-ray flux (and/or other processes not yet identified) are likely to have a more direct influence on the HCN flux. Stellar accretion rate is not well correlated with spectral type (see Fig. 3.4e) and the TTS in our sample span a small mass range, so the resulting accretion luminosity seems unlikely to be correlated over the range of spectral types that we studied. In comparison,  $L_X$  shows a possible correlation with spectral type (Fig. 3.4d), so it may be responsible for the moderate correlation of HCN flux with spectral type.

Several of the objects in our sample (plotted as open triangles in Fig. 3.4a, b, and c) appear to deviate from the possible trends we identify here. The dispersion we observe could arise from differences in disk structure (e.g., flaring) and composition that may originate from the natal environment as well as the dynamic processing that occurs within the disk lifetime. This makes the objects that deviate from our observed trends not only expected, but of particular interest. For example, while variations in stellar accretion rate are typically factors of  $\sim 2$  or less (Hartigan et al. 1991), stellar accretion rates of some individual sources may vary up to an order of magnitude on timescales of  $\sim 1$  yr (Alencar & Batalha 2002). This could induce a significant shift for some objects in our plots. Variability in the stellar accretion rate could also affect the time-averaged disk chemistry. Similar considerations might apply for stellar X-ray variability.

Another potential cause of dispersion is a different or additional heating source. The strength of the UV irradiation striking the disk may depend on the absorption along the line-of-sight, e.g., in a magnetosphere or an intervening wind (e.g., Alexander et al. 2004; Ercolano et al. 2008, 2009; Gorti & Hollenbach 2008, 2009). This could influence the temperature and chemical processing of the disk atmosphere, as might radial transport or vertical mixing between the upper layer and

regions closer to the disk midplane (e.g., Bergin et al. 2007; Turner et al. 2006; Semenov et al. 2006; Willacy et al. 2006).

Dust sedimentation can also increase the line-to-continuum contrast of molecular emission (Glassgold et al. 2004; Dullemond et al. 2007), and such emission is more commonly detected in more highly settled disks (Salyk et al. 2011). The properties and distribution of grains are known to vary widely over disk age and structure (e.g., Watson et al. 2009). If molecular formation (e.g.,  $\text{H}_2$ ) on grains influences disk chemical synthesis, variations in grain properties may lead to variations in observable molecular features (Glassgold et al. 2009). In the panels of Figure 3.4, there are several outlying points whose HCN flux index is enhanced or depleted relative to the rest of the points. These might be ideal systems in which to look for additional chemical peculiarity or heating mechanisms that could be affecting the molecular emission strength.

The trends described here require a larger sample to confirm. In tandem, it may be possible to expand the wavelength range we analyze by considering observations from *Spitzer* IRS modules that cover a wider wavelength range (i.e., Long-High,  $20\ \mu\text{m}$ – $40\ \mu\text{m}$ ) and more molecular species. Additional high resolution data would also help verify the technique of using SL spectra to recover real trends.

### 3.5 Summary & Conclusions

Our goal was to investigate the extent to which lower resolution *Spitzer* IRS data can be used to recover quantitative molecular emission trends seen in higher resolution *Spitzer* IRS data. We have shown that a simple prescription for measuring the strength of the  $14\ \mu\text{m}$  HCN emission feature, when applied to low resolution *Spitzer* data, can recover trends in HCN emission strength that are seen in high

resolution *Spitzer* data. Additionally, we report possible correlations between HCN flux and stellar accretion rate, and HCN flux and stellar X-ray luminosity, that may originate from accretion-driven mechanical heating and/or photochemistry at work in the inner disk atmosphere. While qualitative comparisons of the presence of line emission were possible and successful earlier (e.g., Pascucci et al. 2009), our results demonstrate that quantitative comparisons of the line intensities can also be carried out.

What controls the presence and strength of organic molecular features such as HCN in the planet-forming regions around young stars? One challenge in addressing this question is the large number of physical and chemical processes that can potentially affect the molecular emission strength, as discussed in §4. Our methods and results show that the large number of low resolution disk spectra that reside in the *Spitzer* archive could be used in future demographic studies to attempt to identify the relevant processes.

## CHAPTER 4

## OPTICAL OBSERVATIONS OF THE TRANSITING EXOPLANET GJ 1214B

We observed nine primary transits of the super-Earth exoplanet GJ 1214b in several optical photometric bands from March to August 2012, with the goal of constraining the short-wavelength slope of the spectrum of GJ 1214b. Our observations were conducted on the Kuiper 1.55 m telescope in Arizona and the STELLA-I robotic 1.2 m telescope in Tenerife, Spain. From the derived light curves we extracted transit depths in  $R$  ( $0.65 \mu\text{m}$ ),  $V$  ( $0.55 \mu\text{m}$ ), and  $g'$  ( $0.475 \mu\text{m}$ ) bands. Most previous observations of this exoplanet suggest a flat spectrum varying little with wavelength from the near-infrared to the optical, corresponding to a low-scale-height, high-molecular-weight atmosphere. However, a handful of observations around  $K_s$  band ( $\sim 2.15 \mu\text{m}$ ) and  $g$ -band ( $\sim 0.46 \mu\text{m}$ ) are inconsistent with this scenario and suggest a variation on a hydrogen- or water-dominated atmosphere that also contains a haze layer of small particles. In particular, the  $g$ -band observations of de Mooij et al. (2012), consistent with Rayleigh scattering, limit the potential atmosphere compositions of GJ 1214b due to the increasing slope at optical wavelengths (Howe & Burrows 2012). We find that our results overlap within errors the short-wavelength observations of de Mooij et al. (2012), but are also consistent with a spectral slope of zero in GJ 1214b in the optical wavelength region. Our observations thus allow for a larger suite of possible atmosphere compositions, including those with a high-molecular-weight and/or hazes. A version of this chapter originally appeared as a published paper in the Monthly Notices of the Royal Astronomical Society (Teske et al. 2013c). I conducted the Kuiper Telescope observations described here, as well as those data reduction and analysis. The STELLA-I observations, data reduction and analysis,

and the stellar variability study were conducted by co-author M. Meller (now M. Mallonn). Throughout the whole project, for all components (observing, reduction, analysis, interpretation), I worked closely with J. Turner and M. Meller. C. Griffith provided the atmospheric models of GJ 1214b.

#### 4.1 Introduction

Since the detection of the ‘super-Earth’ transiting extrasolar planet GJ 1214b (Charbonneau et al. 2009), its composition has been a topic of interest and debate. Discovered by the MEarth program, GJ 1214b has a radius ( $2.85 \pm 0.20 R_{\oplus}$ ; Harpsøe et al. 2013) and mass ( $6.26 \pm 0.86 M_{\oplus}$ ; Harpsøe et al. 2013) only slightly larger than that of the Earth, and transits a near by (13 pc) M star ( $0.216 \pm 0.012 R_{\odot}$ ; Harpsøe et al. 2013) with an orbital period of 1.5804 days and a semi-major axis of 0.0197 AU (Harpsøe et al. 2013). This causes a planet-to-star flux ratio comparable to that of a Jupiter-sized planet orbiting the Sun, and makes it one of only a handful of ‘super-Earth’ atmospheres that currently can be investigated with transit spectroscopy (Charbonneau et al. 2009). GJ 1214b represents a unique opportunity to study a planetary object unlike those in our Solar System, yet potentially similar to a large fraction of currently-detected exoplanets, many of which are smaller than Jupiter-sized (Borucki et al. 2012; Muirhead et al. 2012; Borucki et al. 2010; Howard et al. 2010).

The mass and radius of GJ 1214b imply a low density of  $1.87 \pm 0.40 \text{ g cm}^{-3}$  ( $\sim 0.35 \rho_{\text{Earth}}$ ; Rogers & Seager 2010) and suggest that GJ 1214b cannot be composed of rock and water ice alone, but likely has a significant gaseous atmosphere (Bean, Miller-Ricci Kempton & Homeier 2010; Miller-Ricci & Fortney 2010; Kundurthy et al. 2011). Models of its interior structure indicate GJ 1214b’s composition is most likely either (i) a mini-Neptune made of mainly solid rock and

ice with a significant hydrogen-dominated atmosphere accreted from its protoplanetary nebula, (ii) a world composed mainly of water ice with a secondary water vapor envelope formed by sublimation, or (iii) an object composed of purely rocky material with a hydrogen-dominated atmosphere formed by outgassing (Rogers & Seager 2010). A determination of the current composition of GJ 1214b will shed light on this planet's formation history, and thus potentially that of other super-Earth planets. If GJ 1214b's atmosphere is largely hydrogen, it likely formed from the accretion of proto-solar nebular gas or from the outgassing of significant amounts of hydrogen during the planet's cooling and solidification (Miller-Ricci Kempton, Zahnle & Fortney 2012). However, if instead the atmosphere is water-rich, then GJ 1214b could have formed from ice-rich material farther out in the protoplanetary disk before migrating inwards towards the star. Alternatively or in addition, the planet could have accreted less hydrogen-dominated nebular gas in the first place, or lost by atmospheric escape any hydrogen-rich gas that it did accrete (Rogers & Seager 2010).

Transmission photometry and spectroscopy indicate the bulk composition of GJ 1214b by measuring the attenuation of stellar light as it passes through the limb of the exoplanet's atmosphere. The modulation in the spectrum with wavelength increases with the atmosphere's scale height, which is inversely proportional to the atmosphere's molecular weight. The modulation in GJ 1214b's spectrum thus distinguishes between its possible compositions, since models (i) and (iii) (listed above) will have a large scale height and show prominent spectral features from absorption by molecular hydrogen, whereas model (ii) will have relatively small spectral features and scale height.

Several studies using transmission observations to determine GJ 1214b's atmospheric scale height and composition have been published. From the optical

( $\sim 0.6 \mu\text{m}$ ) through the near-infrared ( $4.5 \mu\text{m}$ ), most measurements indicate no significant spectral modulation with wavelength in the atmosphere of GJ 1214b (Bean et al. 2010; Bean et al. 2011; Crossfield, Barman & Hansen 2011; Désert et al. 2011; Berta et al. 2012; Narita et al. 2012; Fraine et al. 2013). Taken together, these observations suggest that GJ 1214b has a small scale height, and favors model (ii) above, in which the exoplanet’s atmosphere is dominated by water rather than hydrogen. However, there are hints of deviation (albeit with less statistical significance) from the flat-spectrum model in  $K_s$ -band ( $2.15 \mu\text{m}$ ; Croll et al. 2011; de Mooij et al. 2012),  $g$ -band ( $0.46 \mu\text{m}$ ; de Mooij et al. 2012), and  $R$ -band ( $0.65 \mu\text{m}$ ; Murgas et al. 2012). Including these latter observations requires modification of the water-world explanation. Collectively, the observations may alternatively be explained by a hydrogen-dominated atmosphere with an opacity source causing the muted spectral features (Miller-Ricci Kempton et al. 2012; Howe & Burrows 2012). The increase in the radius-ratio observed at short wavelengths is roughly consistent with Rayleigh scattering in an atmosphere with a relatively high scale height.

The goal of this paper is to constrain the transmission spectrum of GJ 1214b in the optical wavelength bands ( $\lesssim 0.70 \mu\text{m}$ ) in order to study the short-wavelength slope and the scattering regime in GJ 1214b’s atmosphere. If the short-wavelength data are indicative of a Rayleigh scattering power law, this indicates a relatively high scale height atmosphere, and scattering particles that are much smaller than the wavelength of light. A shallower slope in the short-wavelength data would indicate a particle-size closer to the Mie scattering regime,  $\sim 1 \mu\text{m}$ , or a small scale height atmosphere.

In Section 2 we give an overview of our observations and data reduction procedures. We discuss our transit light curve analysis in Section 3 and the implica-

tions of our results in Section 4.

## 4.2 Observations and Data Reduction

Our *R*- and *V*-band observations of the transit of GJ 1214b were conducted between March and June 2012 at the Steward Observatory 1.55 meter Kuiper Telescope on Mt. Bigelow near Tucson, Arizona using the Mont4k CCD. The Mont4k CCD contains a  $4096^2$  pixel sensor with a field of view (FOV) of  $9.7' \times 9.7'$ . We used  $3 \times 3$  binning to achieve a resolution of  $0.43''/\text{pixel}$ , and a  $3072 \times 1024$  pixel subframe with a field-of-view (FOV) of  $7.28' \times 2.43'$  to shorten read-out time to roughly 10 seconds. Our observations were taken with the Harris V (473-686 nm; FWHM 88 nm), and Harris R (550-900 nm; FWHM 138 nm) photometric band filters, and we did not defocus the telescope (GJ 1214A is not bright enough to saturate the detector with our short integration times). To ensure accurate time-keeping, an on-board clock was automatically synchronized with GPS every few seconds throughout the observational period. Due to excellent autoguiding, there was no more than a 4.4 pixels ( $\sim 1.9''$ ) drift in the *x* position and 2.1 pixels ( $\sim 0.9''$ ) in the *y* position of GJ 1214A in all our data sets for the Kuiper 1.55 m telescope (with averages of  $0.03''$  in the *x* position and  $0.06''$  in the *y* position). Our Kuiper 1.55 m observations are summarized in Table 1.

All *g'*-band (401-550 nm; FWHM 153 nm) transit observations were taken between May and August 2012 with STELLA-I, a fully robotic 1.2 m telescope in Tenerife, Spain (Strassmeier et al. 2010). Its wide field imager WiFSIP hosts a  $4096^2$  15-micrometre pixel back-illuminated CCD. It images a FOV of  $22' \times 22'$  with a scale of  $0.322''/\text{pixel}$ . Because of a sufficiently high density of suitable comparison stars in the field of GJ 1214A we applied a CCD window of  $2000^2$  pixels, reducing the field of view to about  $11' \times 11'$ . We did not defocus the tele-



scope because there was no danger of saturation of GJ 1214A due to its faintness at blue wavelengths. Each transit observation lasted  $\sim 3$  hours covering a sufficient amount of out-of-transit baseline before and after the rather short transit of  $\sim 53$  minutes. The robotic telescope took 98 exposures per run with 90 s exposure time and 20 s overhead resulting in a cadence of about 110 seconds. Our STELLA-I 1.2 m observations are summarized in Table 1.

Using standard IRAF<sup>1</sup> reduction procedures, each of our Kuiper 1.55 m images were bias-subtracted and flat-fielded. Turner et al. (2013) determined that using different numbers of flat-field images (flats) in the reduction of Kuiper Telescope/Monk4k data did not significantly reduce the noise in the resulting images. Thus, to save time, we used 10 flats in all sequential observations and reductions, as well as 10 bias frames taken during each observing run.

To produce the light curves from the Kuiper 1.55 m data, we performed aperture photometry (using the task PHOT in the IRAF DAOPHOT package) by measuring the flux from our target star as well as the flux from several (usually between 5-10) companion stars within an aperture radius that varied based on the star and the observing night conditions. For the analysis of each night's observations we used a constant sky annulus (with a width of 20 pixels), which was chosen to always start at a radius greater (by at least 7 pixels) than the target aperture; no stray light from the star was included. Considering several different combinations of reference stars and aperture radii, we picked the combination that produced the lowest RMS in the out-of-transit data points. To check that our derived transit depth from the Kuiper 1.55 m data was not dependent on the chosen aperture radius, we also tested several different aperture radii and found that

---

<sup>1</sup>IRAF is distributed by the National Optical Astronomy Observatory, which is operated by the Association of Universities for Research in Astronomy, Inc., under cooperative agreement with the National Science Foundation.

the resulting change in transit depth was not significant based on our derived uncertainties, which are a factor of  $\sim 2$  larger. A synthetic light curve was produced by averaging the light curves from our reference stars, and the final light curves of GJ 1214b were normalised by dividing by this synthetic light curve. The light curves for all of our data are shown in Figures 4.1 and 4.2 with  $1\sigma$  errors on each point converted from magnitude errors provided by the IRAF reduction. The out-of-transit baseline in all transits achieved a photometric RMS between 2-4 mmag ( $\sim 2.5\times$  the photon noise limit), which is typical for the Mont4k on the 1.55 meter Kuiper telescope for high S/N transit photometry (Turner et al. 2013; Dittmann et al. 2009a, 2009b, 2010, 2012; Scuderi et al. 2010).

For the STELLA-I 1.2 m WiFSIP data, we developed a photometry data reduction pipeline that is based on ESO MIDAS routines to subtract a bias using the overscan regions and a 2-d bias structure using a masterbias. The robotic system cycles through all filters of WiFSIP to take twilight flat-fields resulting in a time difference between science data and appropriate flat-field observations of less than 3 days. One master flat-field based on  $\sim 20$  flat-field exposures was used for flat-field correction. We performed aperture photometry using the publicly available software SExtractor<sup>2</sup> (Bertin & Arnouts 1996), which supplies several options for aperture photometry; we tested the estimation of fixed aperture magnitudes and automatic aperture magnitudes in our pipeline. For both options several aperture widths were tested to minimize the scatter of the out-of-transit data, and we consistently find an automatic aperture to yield the lowest RMS value. Again, to check that our derived transit depth from the STELLA-I 1.2 m WiFSIP data was not dependent on the chosen aperture radius, we also tested several different aperture radii and found that the resulting change in transit depth was

---

<sup>2</sup><http://www.astromatic.net/software/sextractor>

not significant based on our derived uncertainties. It should be mentioned that this option does not use a constant aperture shape over the field of view nor the same aperture shape and width throughout the exposure time series. It computes an elliptical aperture for every exposure and object by second order moments of its light distribution (see also Law et al. 2013; Matute et al. 2012; Polishook et al. 2012). Several widths of the ‘rectangular annulus’ used for local background estimation by SExtractor were tested in order to minimize the out-of-transit scatter. The same criterium was also used in the pipeline to search automatically for the best combination of comparison stars. We always started with the 25 brightest stars in the field and found 4 to 7 calibration stars to give the optimal solution. The light curves for all of our data are shown in Figures 4.1 and 4.2 with  $1\sigma$  errors on each point converted from magnitude errors provided by the SExtractor reduction. The RMS value of the out-of-transit STELLA-I data is in most cases  $\sim 1.2\times$  higher than the theoretical limit estimated from the photon noise of object and background and the read-out noise.

### 4.3 Light Curve Analysis

The light curve depth is a measurement of the effective area of light from the primary star that is blocked by the occulting planet ( $(\frac{R_p}{R_s})^2$ ). The effective size of the planet depends on the opacity of the atmosphere, and thus the atmosphere’s spectral features and composition. To derive the light curve depths, we used two different publicly available modeling software packages – the Transit Analysis Package<sup>3</sup> (TAP; Gazak et al. 2012) and JKTEBOP<sup>4</sup> (Southworth et al. 2004a, 2004b; Southworth 2008) – that simulate the shape of the light curves, considering the planet’s orbit and the limb darkening of the star. TAP utilizes Bayesian

---

<sup>3</sup><http://ifa.hawaii.edu/users/zgazak/IfA/TAP.html>

<sup>4</sup><http://www.astro.keele.ac.uk/jkt/codes/jktebop.html>

probability distributions with Markov Chain Monte Carlo (MCMC) techniques and a Gibbs sampler to fit transit light curves using the Mandel & Agol (2002) model and uses a wavelet likelihood function to more robustly estimate parameter uncertainties (Carter & Winn 2009). JKTEBOP was originally developed from the EBOP program written for eclipsing binary star systems (Etzel 1981; Popper & Etzel 1981) and uses the Levenberg-Marquadt Monte Carlo (LMMC) technique to compute errors, although there are additional error computation options (Southworth et al. 2004a, 2004b; Southworth 2010; Hoyer et al. 2011).

We modeled each transit individually with TAP, after normalizing the out-of-transit data to one, using five MCMC chains with lengths of 100,000 links each. (We note that TAP does not take into account the  $1\sigma$  individual-point errors as input.) The Gelman-Rubin statistic (Gelman & Rubin 1992) was used to ensure chain convergence, as outlined in Ford 2006. We also combined the data from the same bands into one simultaneous TAP analysis for each band in order to increase our sampling and precision; all of our TAP results are listed in Table 3. During the analysis, the inclination ( $i$ ), scaled semi-major axis ( $\frac{a}{R_S}$ ), eccentricity ( $e$ ), argument of periastron ( $\omega$ ), quadratic limb darkening coefficients ( $\mu_1$  and  $\mu_2$ ), and the orbital period ( $P_b$ ) of the planet were fixed to the values listed in Table 2. The time of mid-transit ( $T_c$ ) and planet-to-star radius ratio ( $\frac{R_p}{R_S}$ ) were left as free parameters. In addition, white and red noise were left as free parameters, as were the airmass fitting parameters (slope and y-intercept). The linear ( $\mu_1$ ) and quadratic ( $\mu_2$ ) limb darkening coefficients in each respective band were taken from Claret (1998) using approximations of the stellar parameters of GJ 1214 ( $T_{eff}=3000$ ,  $\log g=5.0$ ). See Table 2 for the limb darkening coefficients used for each band.

We also performed a similar analysis of our data with JKTEBOP in order to check our TAP results against a different transit analysis package. We obtained re-

sults consistent with those from TAP, although with slightly smaller errors ( $\sim 1.5$ - $3\times$  smaller). Both JKTEBOP and TAP have been shown to produce similar results in the study of another transiting exoplanet, WASP-5b (Hoyer, Rojo & López-Morales 2012). Hoyer et al. (2012) found that, in its default mode, JKTEBOP can underestimate the errors in the fitted parameters because it lacks multi-parameter uncertainty estimation and does not account for red noise. By including the wavelet decomposition likelihood function (see Carter & Winn 2009), TAP allows parameters that measure photometric scatter (uncorrelated white noise and time-correlated red noise) to evolve as free parameters in the transit fitting; the TAP method will recover the traditional  $\chi^2$  fitting statistic in the case of no red noise and the white noise fixed to the characteristic measurement error (Johnson et al. 2011). Hoyer et al. (2011) also found that if the parameter space does not have local minima, the LMMC (JKTEBOP) and MCMC (TAP) algorithms are equivalent, but that LMMC minimization can get trapped in such minima, and that the LMMC results can be biased toward their initial input values. We find similar results as Hoyer et al. (2012) in that the errors derived from our TAP analysis are slightly greater than the errors derived from our JKTEBOP analysis. We choose to use our TAP results throughout the rest of the paper due to their more conservative errors.

In the June 18 light curve, there appears to be a feature in the middle of the transit that could affect the TAP analysis and our measurement of  $\frac{R_p}{R_s}$ . We tested how the model would change by just excluding these potentially-anomalous data points and performing our light curve fitting without them. We do indeed find slightly larger  $\frac{R_p}{R_s}$  values for the transit of June 18, which in turn slightly increases our combined-night  $\frac{R_p}{R_s}$  value in  $g'$ -band (by  $\sim 0.0014$ ). However, within errors, these values are consistent with the values we derive using all of the data points;

to avoid any bias due to attempts to fit out these points, we report here the values derived using all of the data.

Our TAP analysis results are summarized in Table 3, and a comparison of our results and  $\frac{R_p}{R_s}$  values from the literature is shown in Figures 4.3 and 4.4.

#### 4.4 Discussion & Conclusions

Our derived  $\frac{R_p}{R_s}$  values match those in the literature (see Figure 4.3). Our analysis adopts the same values for the period, inclination ( $i$ ),  $\frac{a}{R_s}$ , eccentricity, and omega (see Table 2) used by Bean et al. (2010) and Bean et al. (2011), making our results directly comparable to theirs. These values were also used by de Mooij et al. (2012), except for the period, for which de Mooij et al. (2012) used 1.5804048346 days rather than Bean et al. (2011)'s 1.58040481 days. Bean et al. (2011) allowed the limb darkening coefficients to be free parameters in their fitting analysis, using as priors the theoretical values that they computed based on PHOENIX models of GJ 1214A with stellar parameters  $T_{eff} = 3026$  K,  $[M/H] = 0.0$ , and  $\log g = 5.0$ . Neither the theoretical priors nor the resulting fitted values for the limb-darkening coefficients are discussed in Bean et al. (2011), so we cannot compare our limb-darkening coefficients directly. We did use the limb darkening coefficient values from various Claret sources (see Table 2) corresponding to stellar parameters very similar to Bean et al. (2011):  $T_{eff} = 3000$  K,  $[M/H] = 0.0$ , and  $\log g = 5.0$ . De Mooij et al. (2012) used a four-parameter limb-darkening law, so our coefficients are also not directly comparable, although de Mooij et al. (2012) do use the same stellar parameter values ( $T_{eff} = 3026$  K,  $[M/H] = 0.0$ , and  $\log g = 5.0$ ) and Claret (2000; 2004) as sources for their non-linear limb-darkening coefficients.

GJ 1214A is known to have star-spot-induced variability (Charbonneau et al. 2009; Berta et al. 2011), and stellar activity can have an observable effect on

the transmission spectrum of a transiting planet from star-spots that are occulted or not occulted by the planet (Pont et al. 2008; Agol et al. 2010; Sing et al. 2011). If a planet passes in front of a star-spot, fully or partially masking it on the stellar surface, the observed flux will increase in proportion to the dimming effect of the star-spot on the total flux of the star, causing one to underestimate the true size of the planet, and decreasing  $\frac{R_p}{R_s}$ . If the star spot is not occulted by the planet, the transit depth will appear greater, since the planet will pass over a region that is on average brighter than the entire star; this will reduce the effective stellar radius and increase  $\frac{R_p}{R_s}$  (these effects are parameterized in Sing et al. 2011). De Mooij et al. (2012) found from their out-of-transit monitoring observations of GJ 1214A that the corrections in their  $\frac{R_p}{R_s}$  observations in  $r$ -band and  $K_s$ -band due to the possibility of occulted star-spots were 0.0011 and 0.0003, respectively. These authors also calculated the influence of different base levels of unocculted spots on the transmission spectrum observations of GJ 1214b, and found that for a spot-covering fraction of 10%, the change in their  $\frac{R_p}{R_s}$  values was -0.0007 in  $g$ -band and  $\sim$ -0.00065 in  $r$ -band (the authors shifted their values such that the  $i$ -band radius ratio remained the unaltered baseline value, to compare to non-corrected results more easily). Due to the errors in our derived  $\frac{R_p}{R_s}$  values, the level of star-spot-induced variations calculated by de Mooij et al. (2012) is not distinguishable with our data.

We also performed our own check calculations for possible star-spot corrections, using our  $g'$ -band out-of-transit data, i.e., data taken on the same nights as (and acting as the baseline for) the transit data. This check allows us to directly probe the host star variability in  $g'$ -band, our ‘bluest’ band and thus the one most affected by spots. We took the out-of-transit data from each night, calibrated using the same comparison stars, found the mean relative out-of-transit flux, and

normalised it to the brightest epoch (August 6; see Figure 4.5), which we assume to be the epoch with the lowest spot coverage. Between the dimmest (June 10) and brightest (August 6) epochs, there was a change of  $\sim 3\%$  in the flux of the star, translating to a transit depth that is deeper by  $1/0.97$ , or  $\sim 1.03$ , due to star-spots. To ensure that the observed change in flux of GJ 1214A was not due to systematic error, we performed the same analysis on three of the closest (in angular separation) reference stars and found that their flux varied by  $<1\%$  over the time period of our  $g'$ -band observations. Thus we assume that the  $\sim 3\%$  variability of GJ 1214A's flux is real, and that this change in host star flux is due to dark spots; we do not consider bright plage or faculae regions. Note that a dark region that is unocculted will make the transit appear deeper than it really is. Applying this star-spot correction to the June 10 transit results in a transit depth correction of  $(0.1196)^2 \times 0.03 = 0.00043$ , or an  $\frac{R_p}{R_s}$  correction of 0.0018 (using our TAP-analysis values for June 10; see Table 3). According to our data, this is the *greatest* magnitude of correction that could affect our  $\frac{R_p}{R_s}$  values, and it is markedly less than our TAP-based  $\frac{R_p}{R_s}$  errors on June 10 of  $^{+0.0064}_{-0.0068}$ . Since June 10 was the dimmest epoch, on the other  $g'$ -band nights the potential star-spot corrections are even smaller, and for  $V$ - and  $R$ -bands we can assume a lower flux variation due to the lower flux contrast between spots and the surrounding stellar surface at redder wavelengths. So, while the variability of GJ 1214A should be taken into account when evaluating transit observations taken over multiple epochs, we confirm that the resulting difference in  $\frac{R_p}{R_s}$  that could be induced by star-spots is well within our error bars and thus not distinguishable with our observations.

We find agreement within errors between our data, based on five nights of observations, and the large  $g'$ -band planet radius found by de Mooij et al. (2012), which was based on only one night of observing. However, our combined  $g'$ -



band observations (last line in Table 3) show that the  $g'$ -band planet radius could actually be smaller ( $\sim 0.7\sigma$  shallower) than that found by de Mooij et al. (2012). Taken with the low  $V$ -band  $\frac{R_p}{R_s}$  value that we find (where  $V$ -band spans 473-686  $\mu\text{m}$ ; FWHM 88  $\mu\text{m}$ ), our results suggest that the planet-to-star radius ratio does not increase significantly at shorter wavelengths; within our TAP-analysis-derived errors, the spectrum of GJ 1214b is consistent with zero slope (flat) from  $\sim 400$ -800 nm (see Figures 4.3 and 4.4).

Current transmission observations of GJ 1214b are somewhat contradictory at optical and  $K$ -band wavelengths, which complicates studies of its composition. While most high signal-to-noise observations indicate a featureless, flat spectrum across the optical and near-infrared (Berta et al. 2012; Bean et al. 2010; Bean et al. 2011; Désert et al. 2011; Narita et al. 2012), the measurements of Croll et al. (2011) (in  $K_s$ -band), de Mooij et al. (2012) ( $g$ -band and  $K_s$ -band), and Murgas et al. (2012) (around  $R$ -band) indicate potential variation in transit depth with wavelength. Yet there are a few constraints that persist, considering the two end-member models, one that is hydrogen-based and another that is water-(or heavy gas) based, that have been proposed to explain the structure of GJ 1214b's atmosphere. The observed spectral features of GJ 1214b are sufficiently muted such that, if it did have an  $\text{H}_2$  rich atmosphere, the prominent spectral features of water would need to be reduced by adding large sized ( $>1$  micron) particulates (Bean et al. 2010; Croll et al. 2011; Berta et al. 2012; Howe & Burrows 2012) and/or reducing the water abundance to one lower than that expected in a solar elemental abundance atmosphere (de Mooij et al. 2012; Howe & Burrows 2012). Alternatively the variations on a water-rich atmosphere proposed for GJ 1214b have muted features as a result of the atmosphere's larger mean molecular mass and thus smaller scale height. These models match most of the spectra except the

high absorption measured in *K*-band (Croll et al. 2011; de Mooij et al. 2012) and arguably in *g*-band (de Mooij et al. 2012).

Here we investigate one of the largest differences between the H<sub>2</sub>O-based and H<sub>2</sub>-based atmospheres – their spectral signatures at optical wavelengths. To illustrate the disparity in the spectra predicted for these two end-member atmospheric structures, we calculate spectra of an H<sub>2</sub> and an H<sub>2</sub>O atmosphere, consistent with prior studies. Transit depths  $(\frac{R_p}{R_s})^2$  were calculated with a numerical model that sums the contributions of the primary star’s transmission through the limb of the extrasolar planet. The absorption of light is derived along tangent lines at pressures that extend from  $10^{-7}$  bars to 10 bars. Since there is no evidence so far of the presence of methane or ammonia, as would be expected in a thermochemical equilibrium atmosphere at the temperatures in GJ 1214b’s atmosphere (Miller-Ricci Kempton et al. 2012), we include the spectroscopic absorption due to water only, which is calculated using the absorption coefficients of Freedman, Marley & Lodders (2008), and assuming a constant mixing ratio, as expected for the pressure levels we are probing (below the  $10^{-5}$  bar level) (Miller-Ricci Kempton et al. 2012). The H<sub>2</sub>-based model shown in Figures 4.3 and 4.4 assumes a water abundance of  $3.5 \times 10^{-5}$  and a cloud of brightly scattering particles (with real and imaginary indices of refraction of 1.65 and  $10^{-4}$ ) below 1 mbar, which represents one solution that mutes the water features. This particular model, one of many degenerate solutions, is compared to that of a non-cloudy water atmosphere to illustrate the different slopes between 0.3-0.9  $\mu\text{m}$  that result primarily from the different atmospheric scale heights. The H<sub>2</sub>-based atmosphere has a spectrum that demonstrates the increase in opacity due to Rayleigh scattering, which is suggested by the observations of de Mooij et al. (2012). The H<sub>2</sub>O-based atmosphere is excluded by the observations of de Mooij et al. (2012), because the small scale

height of the model depresses the  $0.46\ \mu\text{m}$  radius below that measured.

Our measurements are consistent with prior studies; we measure a  $g'$ -band radius that agrees with de Mooij et al. (2012), but allows for a greater number of solutions that include an  $\text{H}_2\text{O}$ -based atmosphere. We have recorded the first  $V$ -band observations of GJ 1214b (centered at  $0.55\ \mu\text{m}$ ). These data point to a lower absorption more consistent with an  $\text{H}_2\text{O}$ -rich atmosphere or a mixture of  $\text{H}_2$  and water; that is, an intermediate atmospheric structure. Such an atmosphere might be expected because any  $\text{H}_2\text{O}$ -rich atmosphere would necessarily produce hydrogen through photochemistry. We measure an  $R$ -band radius that is also consistent with either a  $\text{H}_2$  or an intermediate water and  $\text{H}_2$ -based atmosphere. Taken together, our observations can be best interpreted with an atmosphere that is partly  $\text{H}_2$  and partly water based. However, additional observations are needed from ground-based and space-based platforms to establish the optical continuum of GJ 1214b.

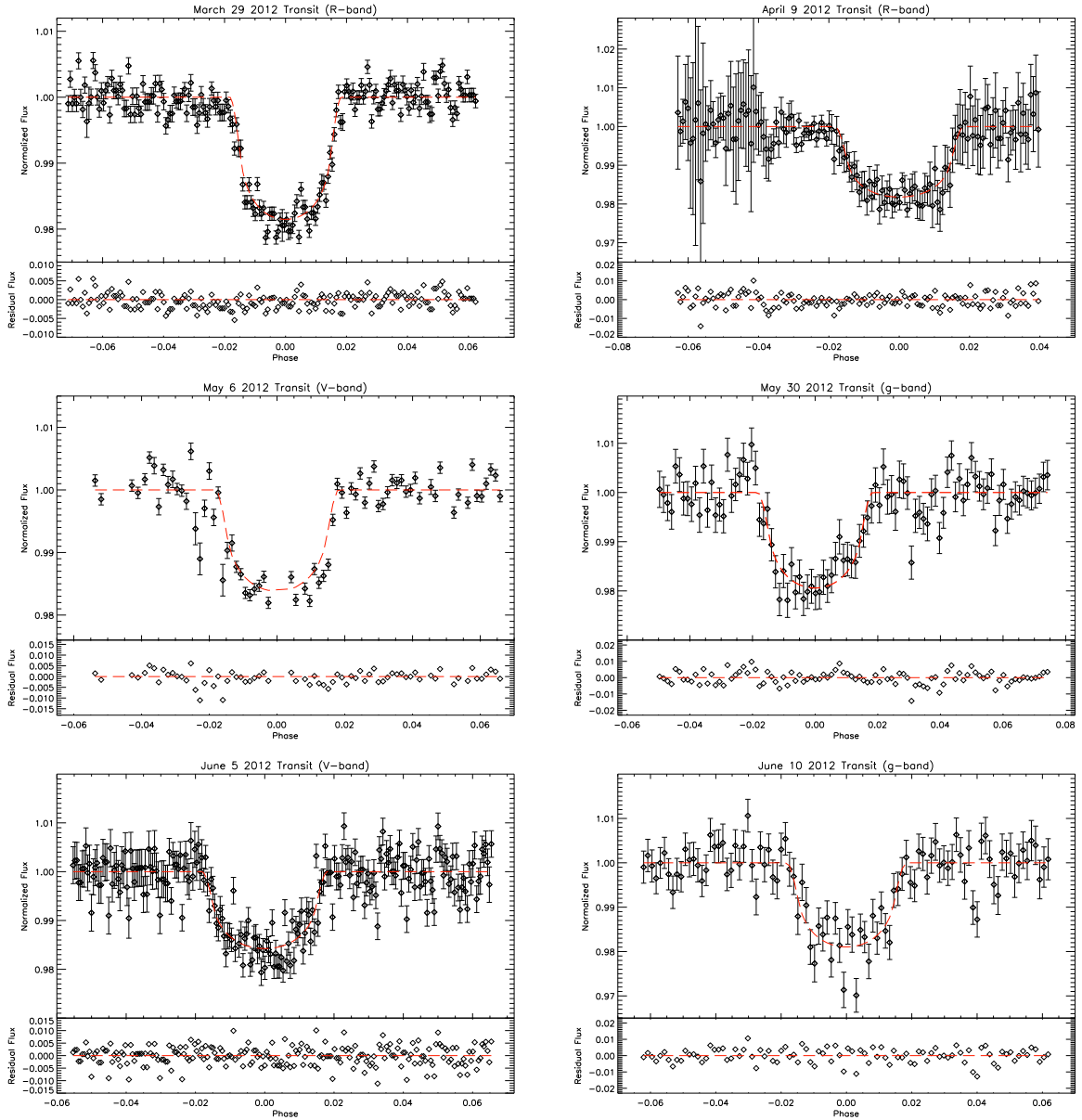


Figure 4.1 Individual light curves of GJ 1214b for each date of observed transit (UTC), shown in chronological order (L-R; top-bottom). The data have all been normalised to one, and the linear trend derived from the TAP analysis removed. Overplotted with a red dashed line are the TAP analysis fits to the data. The residuals from the TAP analyses are shown in the lower panels of each plot. The  $1\sigma$  error bars plotted on each point are based on the IRAF or SExtractor reduction and were not included in the TAP analysis fits.

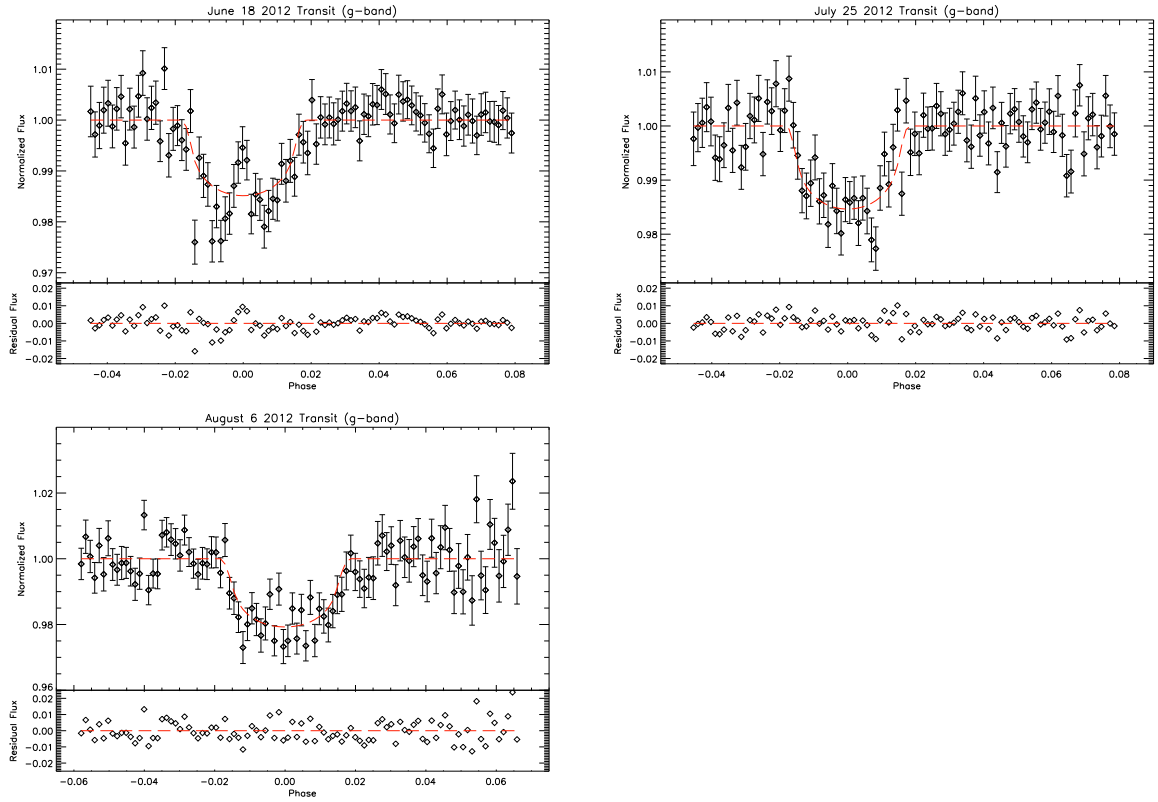


Figure 4.2 Individual light curves of GJ 1214b for each date of observed transit (UTC), shown in chronological order (L-R; top-bottom). The data have all been normalised to one, and the linear trend derived from the TAP analysis removed. Overplotted with a red dashed line are the TAP analysis fits to the data. The residuals from the TAP analyses are shown in the lower panels of each plot. The  $1\sigma$  error bars plotted on each point are based on the IRAF or SExtractor reduction and were not included in the TAP analysis fits.

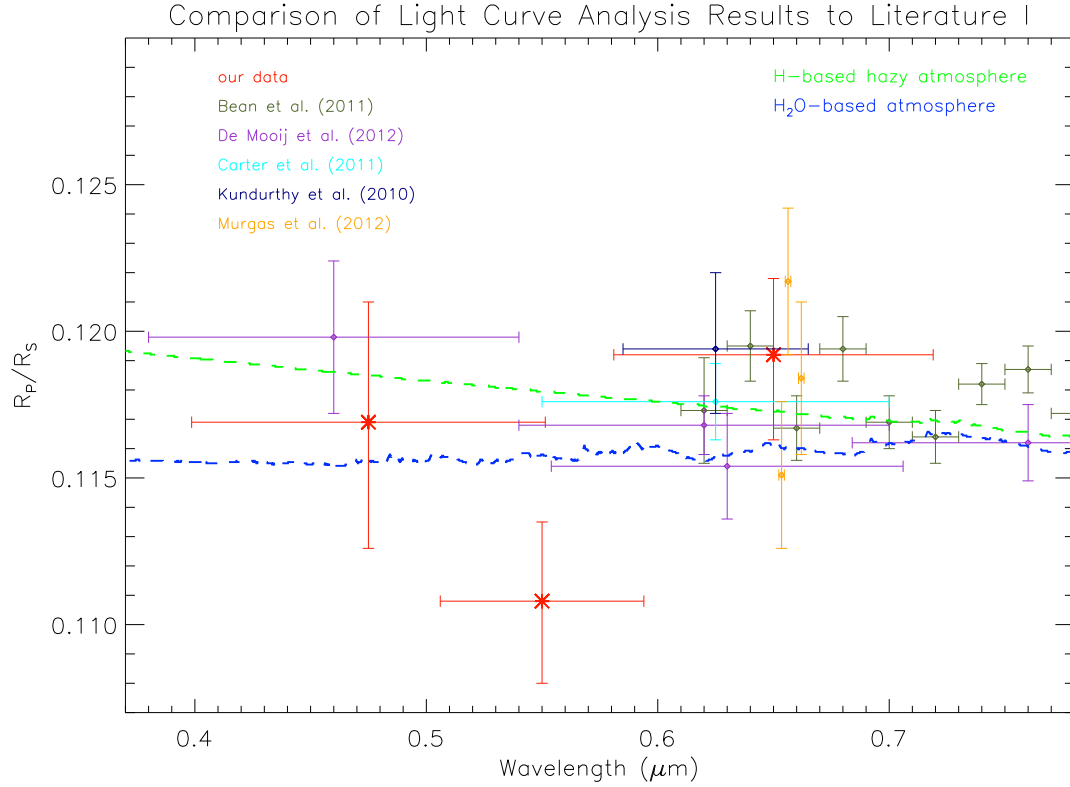


Figure 4.3 The results of our combined-night analyses (the last three rows in Table 3), as compared to other published transit measurements of GJ 1214b. Our results are bolded in red; the band-pass error bars on our measurements represent the FWHM of each filter. We overplot two examples of end-member models that are consistent with different selections of the existing data: a hydrogen-based and hazy atmosphere with a solar abundance of water (green) and a water-based atmosphere (blue). The former displays a greater modulation in the spectral features as a result of the higher scale height of the H<sub>2</sub>-based atmosphere.

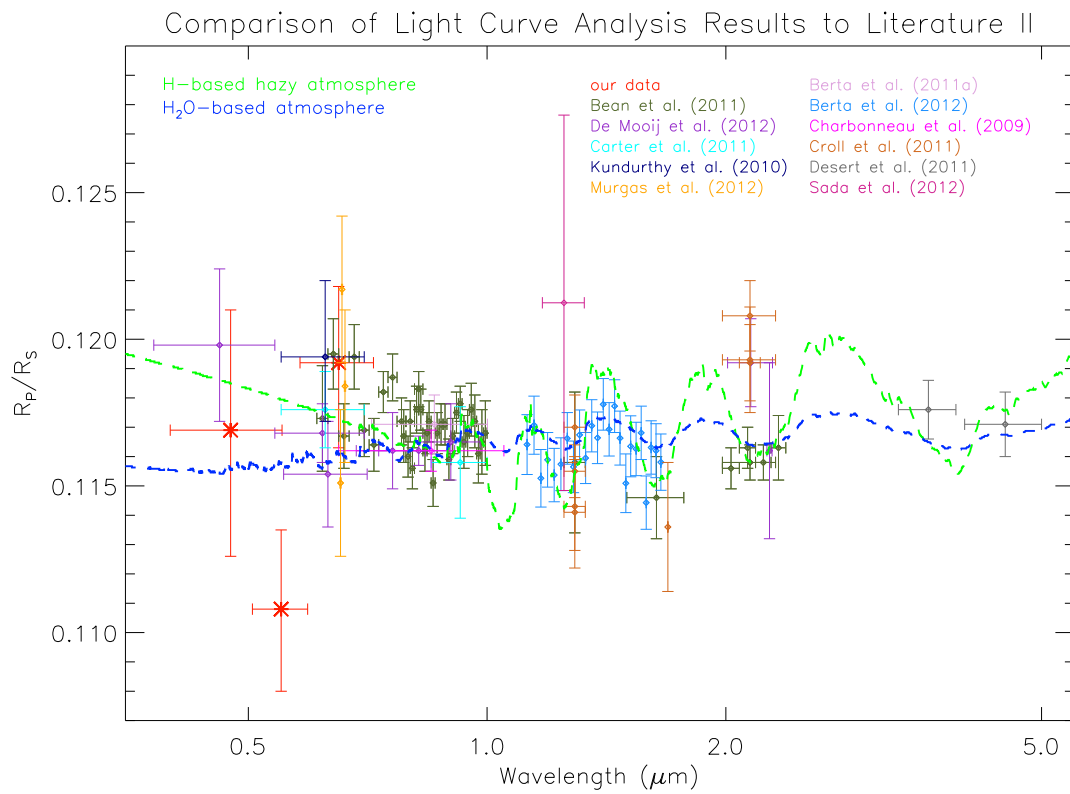


Figure 4.4 The same as Figure 4.3, but now including data covering a greater range in wavelength. See caption of Figure 4.3 for details.

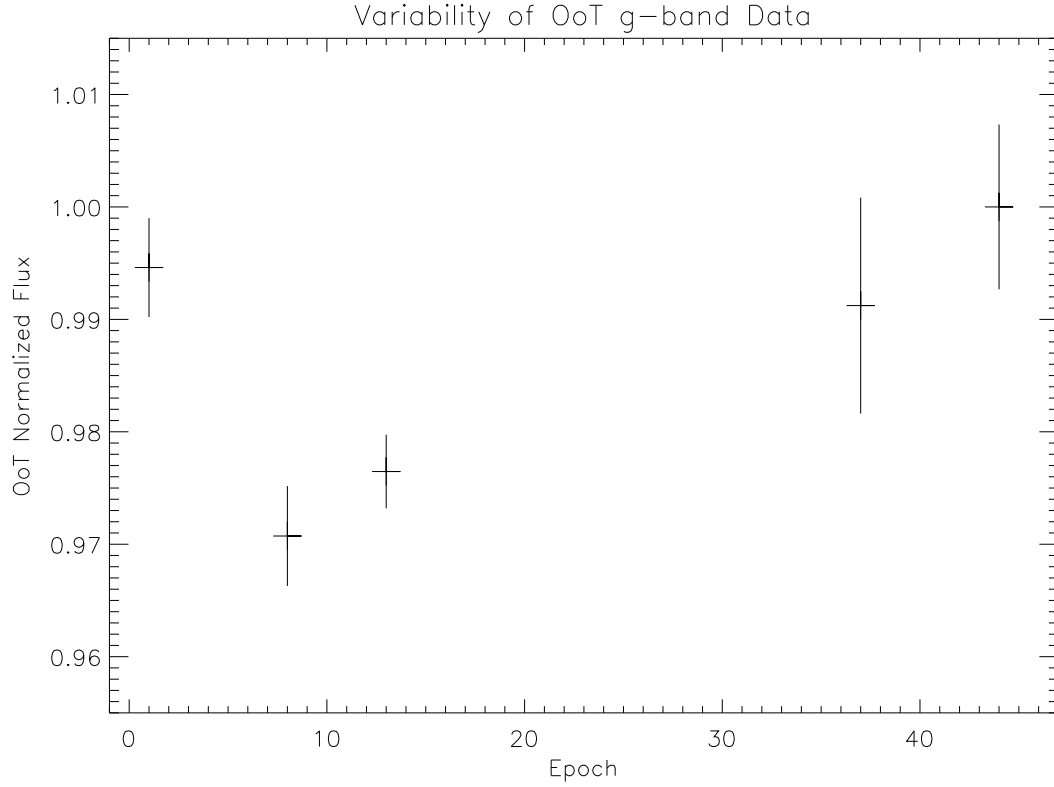


Figure 4.5 The variability in the out-of-transit (OoT)  $g'$ -band data from our observations. The x-axis represents the normalised epoch at which the data were observed, with the first  $g'$ -band epoch set to one. The out-of-transit data from each night were calibrated using the same set of comparison stars; then we found the mean out-of-transit flux level of each night and normalised all the data by dividing through the highest mean value, corresponding to the time at which the stellar surface was least spotted. The greatest difference is between epochs 8 (June 10) and 44 (August 6),  $\sim 3\%$ . The error bars represent the standard deviation of the out-of-transit flux for each night



Table 1. Summary of Observations

Observing Night (UTC)	Filter	Telescope	Start-Stop (UTC)	Int. Time (s)	In-Transit/Total Frames	Seeing (arsec)	Out of Transit RMS (mmag)
March 28-29 2012	Harris R	Kuiper 1.55 m	08:04-11:23	50	54/204	1.5-2.6	2.05
April 8-9 2012	Harris R	Kuiper 1.55 m	10:25-11:04	50	51/156	1.2-2.0	4.21
May 5-6 2012	Harris V	Kuiper 1.55 m	06:47-09:41	100	23/73	1.8-2.6	2.97
May 29-30 2012	Sloan $g'$	STELLA .2 m	23:52-02:51	90	29/98	1.09-1.24	4.11
June 4-5 2012	Harris V	Kuiper 1.55 m	07:30-10:20	30	69/235	1.0-1.9	3.97
June 9-10 2012	Sloan $g'$	STELLA 1.2 m	01:03-04:02	90	29/98	1.09-1.48	4.14
June 17-18 2012	Sloan $g'$	STELLA 1.2 m	23:05-02:04	90	29/98	1.09-1.17	3.22
July 25-26 2012	Sloan $g'$	STELLA 1.2 m	21:27-00:27	90	28/98	1.09-1.32	4.02
August 5-6 2012	Sloan $g'$	STELLA 1.2 m	22:40-01:40	90	29/98	1.14-2.37	5.50 (for airmass<2)

Note. — Column 8 gives the Out-of-Transit root-mean-squared (RMS) relative flux.

Table 2. Fixed Model Values for TAP

Period	1.58040481	Bean et al. 2011
Inclination	88.94	Bean et al. 2011
$a/R_S$	14.9749	Bean et al. 2011
Eccentricity	0.0	
Omega	0.0	
Harris V limb darkening coefficients	0.6406, 0.2955	Claret 1998
Harris R limb darkening coefficients	0.5392, 0.3485	Claret 1998
Sloan $g'$ limb darkening coefficients	0.6528, 0.2978	Claret 2004

Table 3. TAP Model Fitting Results

Transit Date (UTC)	Filter	Midtransit Time (BJD)	$R_p/R_S$	Airmass slope	Airmass y-intercept	Red Noise
March 29	Harris R	2456015.91453 <sup>+0.00037</sup> <sub>-0.00035</sub>	0.1203 <sup>+0.0027</sup> <sub>-0.0030</sub>	-0.0098 <sup>+0.0094</sup> <sub>-0.010</sub>	1.0005 <sup>+0.00089</sup> <sub>-0.00084</sub>	0.0073 <sup>+0.0032</sup> <sub>-0.0026</sub>
April 9	Harris R	2456026.97465 <sup>+0.00050</sup> <sub>-0.00051</sub>	0.1192 <sup>+0.0037</sup> <sub>-0.0040</sub>	-0.0340 <sup>+0.018</sup> <sub>-0.018</sub>	1.0002 <sup>+0.0012</sup> <sub>-0.0011</sub>	0.0072 <sup>+0.0055</sup> <sub>-0.0047</sub>
May 6	Harris V	2456053.84203 <sup>+0.00063</sup> <sub>-0.00064</sub>	0.1108 <sup>+0.0069</sup> <sub>-0.0088</sub>	-0.0240 <sup>+0.021</sup> <sub>-0.023</sub>	1.0011 <sup>+0.0018</sup> <sub>-0.0016</sub>	0.0098 <sup>+0.0054</sup> <sub>-0.0046</sub>
May 30	Sloan $g'$	2456077.54970 <sup>+0.0011</sup> <sub>-0.0012</sub>	0.1210 <sup>+0.0096</sup> <sub>-0.011</sub>	0.0070 <sup>+0.031</sup> <sub>-0.030</sub>	0.9995 <sup>+0.0025</sup> <sub>-0.0026</sub>	0.0171 <sup>+0.0067</sup> <sub>-0.0058</sub>
June 5	Harris V	2456083.87044 <sup>+0.00058</sup> <sub>-0.00058</sub>	0.1093 <sup>+0.0049</sup> <sub>-0.0050</sub>	-0.0660 <sup>+0.015</sup> <sub>-0.015</sub>	1.0015 <sup>+0.0012</sup> <sub>-0.0012</sub>	0.0083 <sup>+0.0061</sup> <sub>-0.0052</sub>
June 10	Sloan $g'$	2456088.51112 <sup>+0.00093</sup> <sub>-0.00083</sub>	0.1197 <sup>+0.0068</sup> <sub>-0.0070</sub>	0.0040 <sup>+0.025</sup> <sub>-0.023</sub>	0.9995 <sup>+0.0018</sup> <sub>-0.0019</sub>	0.0084 <sup>+0.0077</sup> <sub>-0.0056</sub>
June 18	Sloan $g'$	2456096.50120 <sup>+0.0014</sup> <sub>-0.0015</sub>	0.1058 <sup>+0.0096</sup> <sub>-0.012</sub>	0.0310 <sup>+0.031</sup> <sub>-0.031</sub>	0.9966 <sup>+0.0026</sup> <sub>-0.0027</sub>	0.0166 <sup>+0.0073</sup> <sub>-0.0071</sub>
July 25	Sloan $g'$	2456134.44320 <sup>+0.0010</sup> <sub>-0.0011</sub>	0.1077 <sup>+0.0078</sup> <sub>-0.0082</sub>	0.0000 <sup>+0.025</sup> <sub>-0.024</sub>	0.9995 <sup>+0.0020</sup> <sub>-0.0020</sub>	0.0090 <sup>+0.0085</sup> <sub>-0.0059</sub>
August 6	Sloan $g'$	2456145.50590 <sup>+0.0012</sup> <sub>-0.0014</sub>	0.1250 <sup>+0.012</sup> <sub>-0.018</sub>	0.1110 <sup>+0.043</sup> <sub>-0.047</sub>	0.9932 <sup>+0.0038</sup> <sub>-0.0035</sub>	0.022 <sup>+0.014</sup> <sub>-0.012</sub>
2 nights	Harris R	—	0.1192 <sup>+0.0026</sup> <sub>-0.0029</sub>	0.0000 <sup>+0.011</sup> <sub>-0.011</sub>	1.0000 <sup>+0.00093</sup> <sub>-0.00091</sub>	0.0104 <sup>+0.0034</sup> <sub>-0.0032</sub>
2 nights	Harris V	—	0.1108 <sup>+0.0027</sup> <sub>-0.0028</sub>	0.0019 <sup>+0.0089</sup> <sub>-0.0089</sub>	0.9998 <sup>+0.00068</sup> <sub>-0.00067</sub>	0.0043 <sup>+0.0042</sup> <sub>-0.0030</sub>
5 nights	Sloan $g'$	—	0.1169 <sup>+0.0041</sup> <sub>-0.0043</sub>	0.030 <sup>+0.013</sup> <sub>-0.012</sub>	0.9974 <sup>+0.0011</sup> <sub>-0.0012</sub>	0.0092 <sup>+0.0072</sup> <sub>-0.0060</sub>

## CHAPTER 5

## C/O RATIOS OF STARS WITH TRANSITING HOT JUPITER EXOPLANETS

The relative abundances of carbon and oxygen have long been recognized as fundamental diagnostics of stellar chemical evolution. Now, the growing number of exoplanet observations enable estimation of these elements in exoplanetary atmospheres. In hot Jupiters, the C/O ratio affects the partitioning of carbon in the major observable molecules, making these elements diagnostic of temperature structure and composition. Here we present measurements of carbon and oxygen abundances in 16 stars that host transiting hot Jupiter exoplanets, and compare our C/O ratios to those measured in larger samples of host stars, as well as those estimated for the corresponding exoplanet atmospheres. With standard stellar abundance analysis we derive stellar parameters as well as [C/H] and [O/H] from multiple abundance indicators, including synthesis fitting of the [O I] 6300 Å line and NLTE corrections for the O I triplet. Our results, in agreement with recent suggestions, indicate that previously-measured exoplanet host star C/O ratios may have been overestimated. The mean transiting exoplanet host star C/O ratio from this sample is 0.54 ( $C/O_{\odot}=0.54$ ), versus previously-measured  $C/O_{\text{host star}}$  means of  $\sim 0.65\text{--}0.75$ . We also observe the increase in C/O with [Fe/H] expected for all stars based on Galactic chemical evolution; a linear fit to our results falls slightly below that of other exoplanet host stars studies but has a similar slope. Though the C/O ratios of even the most-observed exoplanets are still uncertain, the more precise abundance analysis possible right now for their host stars can help constrain these planets' formation environments and current compositions. A version of this chapter is scheduled to appear as a published paper in the *Astrophysical Journal* (Teske et al. 2014). Most of the

observations were conducted by me at the Subaru Telescope and at the Keck Telescope; I also used observations collected by Verne Smith and Katia Cunha from Keck/HIRES and HIRES archive observations. I performed all of reductions, measurements, and the stellar parameter and abundance determinations, with careful help in checking these results from Simon Schuler, Katia Cunha, and Verne Smith. I wrote the text with much help in editing from the co-authors.

## 5.1 Introduction

To date, the most statistically significant trend in host star abundances pertains to metallicity. Stars hosting giant, close-in planets have higher metallicities (measured as  $[\text{Fe}/\text{H}]^1$ ) than stars without detected giant planets (e.g., Gonzalez 1998; Gonzalez et al. 2001; Santos et al. 2004; Fischer & Valenti 2005; Ghezzi et al. 2010). Statistical studies of dwarf stars hosting planets indicate a metallicity enhancement of  $\sim 0.15$  dex for stars with giant planets and a 99.9994% probability that stars with/without giant planets are drawn from different parent populations (Buchhave et al. 2012; Ghezzi et al. 2010). However, the host star metallicity trend is weaker for Neptune-sized planets – the difference in the mean  $[\text{Fe}/\text{H}]$  of Jovian-mass hosts versus Neptunian-mass hosts is  $\sim 0.10$  dex, with the Neptune-mass hosts showing lower  $[\text{Fe}/\text{H}]$  values (e.g., Ghezzi et al. 2010). Smaller planet ( $R_P \leq 4 R_\oplus$ ) host stars from the *Kepler* sample show no metallicity enhancement, and have a flatter distribution of metallicities, though roughly peaked at solar. These smaller planet host stars have a probability between 0.98 and 0.9996 of originating from a different parent population as larger planet host stars from *Kepler* (Buchhave et al. 2012; Everett et al. 2013).

Looking beyond the correlation between planet size and stellar metallicity,

---

<sup>1</sup> $[\text{X}/\text{H}] = \log N(\text{X}) - \log N(\text{X})_\odot$ , where  $\log N(\text{X}) = \log N(\text{X}/\text{H}) + 12$

several studies have searched for other trends between planet parameters and host star abundances indicative of planet formation conditions. Meléndez et al. (2009) find through abundance analyses of 11 solar “twins” that the Sun is deficient by  $\sim 20\%$  in refractory elements, which have condensation temperatures  $T_c \gtrsim 900$  K, relative to volatile elements when compared to other solar twins. This trend of decreasing refractory elemental abundances as a function of  $T_c$  is suggested to be a signature of terrestrial planet formation – the “missing” refractory elements from the stellar photosphere are incorporated into rocky planets (Meléndez et al. 2009). However, subsequent studies of similar precision measurements of solar analogs (González Hernández et al. 2010; González Hernández et al. 2013) and stars with planets (Schuler et al. 2011a & 2011b) across a range of  $T_c$  show that the abundance patterns of stars with and without planets are not significantly different, or may be indistinguishable from Galactic chemical evolution effects. New evidence from Jupiter- and Neptune-sized planet host stars that are more metal-rich, or warmer than the Sun and have less massive convective envelopes, indicates that the depletion signature may depend on the stellar convective envelope size at the time of planet formation, and thus the timescale of disk dispersal around different types of stars (Ramírez et al. 2014)

The growing number of transiting and directly-imaged exoplanet observations enable estimates of elemental and molecular abundances in the atmospheres of the planets themselves. The *Hubble Space Telescope* and *Spitzer Space Telescope*, aided by multiple ground-based facilities, have detected the most abundant molecules ( $\text{H}_2\text{O}$ ,  $\text{CO}$ ,  $\text{CH}_4$ ,  $\text{CO}_2$ ) in the atmospheres of several of the brightest transiting planets (e.g., Tinetti et al. 2007; Swain et al. 2008, 2009ab; Snellen et al. 2010; Beaulieu et al. 2010). Ground-based observatories have made similar strides in studying the molecular properties of a handful of directly imaged self-luminous

exoplanets (e.g., Marois et al. 2008; Barman et al. 2011ab; Skemer et al. 2012, 2013; Konopacky et al. 2013; Janson et al. 2013). The differences and trends between the elemental compositions of host star and exoplanet atmospheres provide clues about the formation and evolution processes of planetary systems.

### 5.1.1 The Role of Carbon and Oxygen

Carbon and oxygen are important players in the composition of stars and planets, as the third and fourth most abundant elements in the universe. The measurement of C and O in stars, especially with respect to iron, which is produced in both Type Ia and Type II supernovae, serves as a fundamental diagnostic of the chemical enrichment history of the Galaxy. The impact of massive stars' Type II supernovae, and thus the major oxygen contributor, lessens with time and increasing metallicity as the influence of low- and intermediate-mass stars' carbon contribution grows. Measuring C and O in exoplanets is diagnostic of current atmospheric composition and temperature structure: the atmospheric C/O ratio<sup>2</sup> affects the molecular composition, and hence observed spectral signatures, through thermochemical equilibrium partitioning of carbon in CO, CH<sub>4</sub>, and CO<sub>2</sub>.

The C/O ratio can also reflect where in the protoplanetary disk a planet formed, as well as subsequent migration and evolution (e.g., Stevenson & Lunine 1988; Gaidos 2000; Ciesla & Cuzzi 2006; Öberg et al. 2011). Theories of planet formation describe how close-in giant planets form in the outer protoplanetary disk, where icy planetesimals coalesce into a core, which accretes gas and migrates inwards (e.g., Pollack et al. 1996; Owen et al. 1999; Ida & Lin 2004b). The main molecular reservoirs of C and O have different condensation temperatures ( $T_c$ ), so their relative amounts vary at different temperatures and disk radii, as do the amounts

---

<sup>2</sup>The C/O ratio – the ratio of carbon atom to oxygen atoms – is calculated in stellar abundance analysis as  $C/O = N_C/N_O = 10^{\log N(C)} / 10^{\log N(O)}$ .

of these molecules in gas or solid form (Öberg et al. 2011). Gas and grains also move differently in the disk with time, as grains grow and decouple from the gas, sequestering solid material beyond the “ice” lines of different molecules (e.g., Ciesla & Cuzzi 2006; Öberg et al. 2011). The C/O ratio of a planet therefore does not necessarily reflect the protoplanetary-disk-averaged C/O ratio, and instead may point towards localized concentrations/depletions of carbon- and oxygen-bearing molecules (Ciesla & Cuzzi 2006; Öberg et al. 2011; Najita et al. 2013).

Many groups have performed stellar abundance analyses of exoplanet host stars in order to determine their physical parameters ( $T_{\text{eff}}$ ,  $\log g$ ,  $[\text{Fe}/\text{H}]$ ) and chemical abundances, to further study the trends discussed above (e.g., Delgado Mena et al. 2010; Petigura & Marcy 2011; Brugamyer et al. 2011; Schuler et al. 2011ab; Nissen 2013). However, only a few transiting exoplanet host stars have published abundances other than  $[\text{Fe}/\text{H}]$  or the more generic  $[\text{M}/\text{H}]$  (e.g., HD 209458, Schuler et al. 2011a; WASP-12, Petigura & Marcy 2011; 55 Cnc, Bond et al. 2010 & Teske et al. 2013b; XO-2, Teske et al. 2013a).

Here we add to the small sample of transiting exoplanet host stars with measured abundances beyond  $[\text{Fe}/\text{H}]$ , and the handful with measured C/O ratios. We report on sixteen transiting hot Jupiters hosts to investigate the extent to which we can relate host star compositions to those of their planets, and search for carbon-rich planet formation environments. The sample presented here contains the host stars of some of the most-observed exoplanets whose atmospheres can and are being modeled to constrain their C/O ratios (e.g., Madhusudhan 2012; Moses et al. 2013; Line et al. 2013). This work provides a step toward comparing specific host star and exoplanet atmospheres to search for the chemical effects of exoplanet formation.



## 5.2 Observations and Data Reduction

Our target list was chosen to include some of the best-studied hot Jupiter’s host stars that are observable from the northern hemisphere, and to include a range of planet radii, masses, and orbital periods. All but three of the planetary hosts in this sample have at least the 3.6  $\mu\text{m}$ , 4.5  $\mu\text{m}$ , 5.8  $\mu\text{m}$ , and 8.0  $\mu\text{m}$  diagnostic measurements of secondary eclipse depth from the *Spitzer* Infrared Array Camera (IRAC) (Fazio et al. 2004). These data cover wavelengths with features of  $\text{CH}_4$ ,  $\text{CO}$ ,  $\text{CO}_2$ , and  $\text{H}_2\text{O}$ , which are the most abundant oxygen and carbon molecules in hot Jupiter atmospheres. These measurements, in addition to *HST* and ground-based observations, are analyzed to infer the carbon and oxygen content in exoplanets (Moses et al. 2011, 2013; Lee et al. 2012; Madhusudhan 2012; Line et al. 2013), motivating our choice to target these host stars for C/O measurements. The planet orbiting HD 80606 has only 8.0  $\mu\text{m}$  photometry, and the planets orbiting HAT-P-16 and WASP-32 have only 3.6  $\mu\text{m}$  and 4.5  $\mu\text{m}$  photometry, and CoRoT-2’s planet is missing 5.8  $\mu\text{m}$  photometry. We include these systems to increase the planet mass range in this sample to include members of the 2.8% of transiting planets with masses  $M \times \sin i > 3 M_J$  – HD 80606b is  $3.94 \pm 0.11 M_J$  (Pont et al. 2009), HAT-P-16b is  $4.19 \pm 0.09 M_J$  (Buchhave et al. 2010), and WASP-32b is  $3.60 \pm 0.07 M_J$  (Maxted et al. 2010), and CoRoT-2b is  $3.47 \pm 0.22 M_J$  (Gillon et al. 2010).

There are three sources of observations for this project: the High Dispersion Spectrograph (HDS; Noguchi et al. 2002) on the 8.2-m Subaru Telescope at Mauna Kea Observatory, the High Resolution Echelle Spectrometer (HIRES; Vogt et al. 1994) at the Keck I Telescope, and the Keck/HIRES archive. All observations are logged in Table 5.1, and the platform configurations are detailed in Table 5.2. To facilitate a differential abundance analysis of these stars with respect to the

Sun (as indicated by the bracket notation), spectra of the Sun as reflected moonlight were taken at Subaru/HDS, and as reflected light from Vesta at Keck/HIRES (PID N014Hr; PI Marcy).

The HDS raw data were overscan-corrected, bias-subtracted, scattered-light subtracted, flat-fielded, extracted, and wavelength calibrated using standard techniques within the IRAF<sup>3</sup> software package using five bias frames, 20 flat fields, and thorium argon (ThAr) comparison lamp frames. All HIRES data were subject to a similar reduction procedure within the MAKEE pipeline<sup>4</sup> using corresponding bias ( $\sim 3$ ), flat ( $\sim 30$ ), ThAr, and trace star frames. Multiple exposures of single targets were then summed in IRAF.

We also obtained Keck/HIRES archive spectra of four targets that we originally observed with Subaru/HDS. The Subaru/HDS spectra were contaminated by atmospheric emission around the [O I] 6300 Å line, preventing a secure measurement of [O/H]; the O I triplet at  $\sim 7775$  Å was outside the Subaru/HDS wavelength coverage. Thus the Keck/HIRES archival data were used to verify the carbon abundance derived from the Subaru/HDS data, and to measure the oxygen abundance as described below. The four targets for which we obtained archival data are HAT-P-7 (PID A285Hr; PI Bakos; August 2008), TrES-3 (PID C290Hr; PI Herczeg; June 2008), HD 189733 (PID A259Hr; PI Winn; August 2006), and HD 149026 (PID N59H; PI Marcy; June 2005).

### 5.3 Derivation of Stellar Parameters and Abundances

We determine stellar parameters ( $T_{\text{eff}}$ ,  $\log g$ , microturbulence [ $\xi$ ]) and elemental abundances of Fe, C, Ni, and O following the procedures in Schuler et al. (2011a)

---

<sup>3</sup>IRAF is distributed by the National Optical Astronomy Observatory, which is operated by the Association of Universities for Research in Astronomy, Inc., under cooperative agreement with the National Science Foundation.

<sup>4</sup>[www.astro.caltech.edu/~tb/makee/](http://www.astro.caltech.edu/~tb/makee/)

and Teske et al. (2013a). Briefly, the strength and shape of absorption lines in stellar spectra depend on the formation environment (temperature, electron pressure) and the number and excitation state of absorbers themselves and thus their atomic constants. Thus one uses measurements from abundant, unblended lines in multiple ionization states – typically Fe – to determine the stellar environment in which the observed line strengths form, in an iterative manner. The “best” stellar model parameters – effective temperature, microturbulent velocity,  $\log g$ , and  $[\text{Fe}/\text{H}]$  – results from fulfilling excitation equilibrium such that the  $[\text{Fe}/\text{H}]$  values derived from the Fe I lines do not show any correlation with the lower excitation potential of the lines ( $\chi$ ), ionization equilibrium such that averaged abundances from Fe I and Fe II lines are equal, and ensuring that Fe I lines of all different equivalent widths yield consistent abundances.

Specifically, the Fe lines in this analysis are the same as in Teske et al. (2013ab). The final Fe line list contains 56 Fe I and 10 Fe II lines, although not every Fe line is measureable in every star in the sample. Lower excitation potentials and transition probabilities for the Fe lines are from the Vienna Atomic Line Database (VALD; Piskunov et al. 1995; Kupka et al. 1999; Ryabchikova et al. 1997).

Abundances of Fe, C, and Ni are derived from equivalent width (EW) measurements of spectral lines in each target individually (sample Subaru/HDS spectra are shown in Fig. 5.1). The EW measurements are performed with the goal of mitigating errors of the fit – we use a Gaussian profile to fit most lines, though some strong lines ( $\text{EW} \geq 90 \text{ m}\text{\AA}$ ) are fit with a Voigt profile to account for the broader wings of the line at the continuum, and some weaker lines are fit with a Simpson’s Rule approximation. The lines of the host stars are fit with either the one-dimensional spectrum analysis package SPECTRE (Fitzpatrick & Sneden 1987) or the ‘splot’ task in IRAF. The solar spectra corresponding to each target

used to derive differential abundances were fit with the same package as the target, e.g., where we use EW measurements from SPECTRE, we use corresponding EW measurements from SPECTRE of the Sun in our analysis. The abundances are then determined with an updated version of the local thermodynamic equilibrium (LTE) spectral analysis code MOOG (Snedden 1973), with model atmospheres interpolated from the Kurucz ATLAS9 grids<sup>5</sup>. For oxygen, we use the spectral synthesis method of matching a set of trial synthetic spectra to the observed spectrum derive the abundance from the blended [O I] line at  $\lambda = 6300.3 \text{ \AA}$  (see Fig. 6.1).

Initial values of  $T_{\text{eff}}$ ,  $\log g$ ,  $\xi$ , and  $[\text{Fe}/\text{H}]$  from the literature serve as our starting values in the iterative process of meeting the criteria outlined above. Prior to this iterative scheme, for each target's EW measurements we ensure no correlation between  $\chi$  and the EWs of the Fe I lines analyzed, as unique solutions for  $T_{\text{eff}}$  and  $\xi$  are only possible if there is no such initial correlation. The  $\log N(\text{Fe})$  values for the Sun are determined from the solar spectrum with a solar Kurucz model with  $T_{\text{eff}}=5777$ ,  $\log g=4.4$   $[\text{Fe}/\text{H}]=0.00$ , and  $\xi=1.38$ , and  $\log N(\text{Fe})$  values of the target stars are normalized to solar values on a line-by-line basis. The final  $[\text{Fe}/\text{H}]$  results from averaging the abundances derived from the individual Fe I and Fe II lines.

Uncertainties in the derived stellar parameters are calculated as detailed in Teske et al. (2013a) (Chapter 7). In Table 7.1 we list the final derived stellar parameters and their  $1\sigma$  uncertainties for each target, as well as the derived  $[\text{Fe I}/\text{H}]$  and  $[\text{Fe II}/\text{H}]$ , the number of lines used in our analysis, and the uncertainty in the mean ( $\sigma_{\mu}$ <sup>6</sup>).

---

<sup>5</sup>See <http://kurucz.harvard.edu/grids.html>

<sup>6</sup> $\sigma_{\mu} = \sigma / \sqrt{N - 1}$ , where  $\sigma$  is the standard deviation of the derived abundances and  $N$  is the number of lines used to derive the abundance.

### 5.3.1 Stellar Abundances of Ni, C, and O

A similar procedure as that used for the Fe lines is used to identify and select lines for Ni and C, with the same line lists as Teske et al. (2013ab), which include 5 lines for carbon and 20 lines for nickel, though not every line was measureable in every star in our sample. The C and Ni abundances are determined through standard EW analysis procedures with MOOG and the adopted stellar model for each target. The wavelength,  $\chi$ ,  $\log gf$ , measured EW, and resulting abundances for the carbon lines are listed in Table 7.2 for a sample of the targets. All lines parameters, equivalent widths, and resulting abundances are available in the full online version of Table 7.2.

We favor the two bluest C I lines (5052 Å and 5380 Å) in our analysis because they arise from the lowest energy levels considered here and have negligible non-LTE (NLTE) corrections ( $\leq 0.05$ ; Asplund et al. 2005; Takeda & Honda 2005; Caffau et al. 2010). The  $\log N(\text{C})_{\odot}$  values we derive with our EW measurements are a good match (within  $\leq 0.03$  dex) to the  $\log N(\text{C})_{\odot}$  values derived by Caffau et al. (2010) from these lines using 3D hydrodynamical simulations of the Sun. The remaining three C I lines arise from higher energy levels, potentially making them more susceptible to NLTE effects (Asplund 2005), although Asplund et al. (2005) find NLTE corrections for these lines in the Sun are comparable to those for the bluer C I lines. In cases where we find discrepant (larger) carbon abundances from the redder C I lines, we base our  $[\text{C}/\text{H}]$  measurement on the two bluest C I lines.

In HAT-P-7, TrES-3, HD 149026, and HD 189733,  $[\text{O}/\text{H}]$  is not measurable with the Subaru/HDS data because the  $[\text{O I}]$  6300 Å is contaminated by atmospheric emission and the wavelength coverage ends blueward of the O I triplet. The oxygen abundances of these four targets are instead measured from Keck/HIRES

archive data (detailed below). In these cases the stellar parameters and  $[\text{Ni}/\text{H}]$  derived from the Subaru/HDS data are carried through the analysis, but  $[\text{C}/\text{H}]$  is remeasured in the Keck/HIRES data so that the C/O ratio originates completely from one data source. In all four cases the  $[\text{C}/\text{H}]_{\text{HIRES}}$  value is equal to the  $[\text{C}/\text{H}]_{\text{HDS}}$  value within errors, with the differences all  $\leq 0.04$  dex, giving confidence to this method.

#### 5.3.1.1 Oxygen

The oxygen abundances of the targets in our sample are determined from two indicators, the forbidden  $[\text{O I}]$  line at  $\lambda = 6300.3 \text{ \AA}$  and the O I triplet at 7771-7775  $\text{\AA}$ , depending on what data are available. For seven of the thirteen (including XO-2S) targets, the oxygen abundance is derived solely from the Subaru/HDS data and the  $[\text{O I}]$  line, which is well-described by LTE (e.g., Takeda 2003). We adopt the Storey & Zeippen (2000)  $\log gf = -9.717$  value, based on their forbidden transition probability calculations including both relativistically-corrected magnetic dipole and electric quadrupole contributions. However, the 6300.3  $\text{\AA}$  feature is blended with a Ni I line composed of two isotopic components, with  $\log gf(^{60}\text{Ni}) = -2.695$  and  $\log gf(^{58}\text{Ni}) = -2.275$  (Johansson et al. 2003; Bensby et al. 2004). In the Sun, nickel accounts for  $\sim 30\text{-}40\%$  of the  $[\text{O I}]$  absorption line depth (Caffau et al. 2008; 2013). Therefore, in determining  $[\text{O}/\text{H}]$  from this line, we account for the nickel component by measuring  $[\text{Ni}/\text{H}]$  directly from each target's spectrum as described above and appropriately scaling the strength of the blend component due to nickel. We also test for potential blending in the 6300.3  $\text{\AA}$   $[\text{O I}]$  line with another, much weaker, CN line (Davis & Phillips 1963; Sneden & Lambert 1982) by fixing the carbon abundance to our measured  $[\text{C}/\text{H}]$  value and remeasuring the 6300  $\text{\AA}$  line oxygen abundance. Except in the cases of XO-2N and XO-2S (Teske et al. 2013b), our resulting oxygen abundances do not

change significantly ( $\leq 0.02 \log N(\text{O})$ ) by fixing the carbon abundance.

The free parameters in our synthesis fits are the continuum normalization, wavelength shift, line broadening, and oxygen abundance; we use our measured Ni and C abundances for each star, and N scaled from solar based on the measured  $[\text{Fe}/\text{H}]$  of each star. We also checked our synthesis results with the “blends” driver in MOOG, which accounts for contributions from additional lines to the primary element with a user-provided line list including these blending lines and corresponding blending species abundances. In Table 7.2 we list the measured EWs serving as input for our check with the “blends” driver and absolute abundances as determined from synthesis fitting of the  $[\text{O I}]$  line for a sample of the targets.

For the spectra in which the Subaru/HDS  $[\text{O I}]$  6300.3 Å is tellurically contaminated (HAT-P-7, TrES-3, HD 149026, and HD 189733) the even weaker  $[\text{O I}]$  6363.79 Å line is not distinguishable from noise, and the O I triplet at 7771-7775 Å is not covered. However, the public data retrieved from the Keck/HIRES archive do include the triplet at 7771-7775 Å and, in some cases, also display clean (not tellurically contaminated)  $[\text{O I}]$  6300 Å lines. In TrES-3, the data beyond  $\sim 7050$  Å are contaminated due to saturated ThAr lamp calibrations; fortunately in this case the  $[\text{O I}]$  6300 Å is measurable in the Keck/HIRES data. We also obtained our own Keck/HIRES data for HAT-P-1, HAT-P-16, and WASP-32, and use the  $[\text{O I}]$  6300 Å and O I triplet lines to derive oxygen abundances for these targets, as well as the stellar parameters and the  $[\text{C}/\text{H}]$  and  $[\text{Ni}/\text{H}]$  values.

In solar-type stars, the O I triplet lines at 7771.94 Å ( $\chi=9.15$  eV,  $\log gf=0.369$ ; Hibbert et al. 1991), 7774 Å ( $\chi=9.15$  eV,  $\log gf=0.223$ ; Hibbert et al. 1991), and 7775.4 Å ( $\chi=9.15$  eV,  $\log gf=0.001$ ; Hibbert et al. 1991) are prominent and suffer less from blending with other lines, and are therefore conducive to direct EW

measurement (Table 7.2). These lines are known to suffer from NLTE effects, detailed in Kiselman (1993; 2001) and Gratton et al. (1999), and several groups have derived NLTE corrections from statistical equilibrium calculations for varying stellar parameters. For comparison, as in Teske et al. (2013a), we apply NLTE corrections to the triplet abundances from three sources: Takeda (2003), Ramírez et al. (2007), and Fabbian et al. (2009) (Table 5.5). The differences in methodology applied by each of these sources to determine NLTE corrections is detailed in Teske et al. (2013a), who also note that the NLTE corrections from different sources give overlapping results.

The validity of using such NLTE corrections for cool ( $T_{\text{eff}} \lesssim 5400$  K) stars is questionable, as discussed in Teske et al. (2013a). They ultimately choose not to include the NLTE-corrected O I triplet abundances for the cool, metal-rich star 55 Cnc, instead relying on the averaged [O I] 6363.79 Å and LTE O I triplet abundances. In the spectra presented here, which are of lower S/N than the 55 Cnc data presented in Teske et al. (2013a), the [O I] 6363.79 Å line is not detected. Thus, in the case of stars with  $T_{\text{eff}} \lesssim 5400$  K and for which we have Keck/HIRES data with wavelength coverage including the O I triplet, we adopt the average of the [O I] 6300 Å and LTE O I triplet abundances. For warmer stars in which both the [O I] 6300 Å and O I triplet lines are measurable, we adopt the average of the [O I] 6300 Å and the three NLTE-corrected O I triplet abundances. In all cases the [O I] 6300 Å- and O I triplet-derived (whether LTE or NLTE) abundances match within the uncertainties.

Table 5.6 lists the final averaged [O/H] values for each target, along with [C/H] and the resulting C/O ratio. These C/O ratios are calculated with the prescription  $\log N_{\text{target}}(\text{O}) = \text{derived } [\text{O}/\text{H}]_{\text{target}} + \log N_{\odot}(\text{O})$  and  $\log N_{\text{target}}(\text{C}) = \text{derived } [\text{C}/\text{H}]_{\text{target}} + \log N_{\odot}(\text{C})$  where  $\log N_{\odot}(\text{O}) = 8.66$  and  $\log N_{\odot}(\text{C}) = 8.39$  (solar values from Asplund et al. 2005).



This table also shows the measured  $[\text{Ni}/\text{H}]$  abundances for each target, which are used in the derivation of  $[\text{O}/\text{H}]$  from the  $[\text{O I}]$  6300 Å line as described above.

### 5.3.2 Abundance Uncertainties

The uncertainties in the derived elemental abundances include the errors in the adopted stellar parameters ( $T_{\text{eff}}$ ,  $\log g$ , and  $\xi$ ) and the dispersion in the abundances derived from different absorption lines for the element, as the final adopted abundance is an average of these lines. To determine the uncertainty due to the stellar parameters, the sensitivity of the abundance to each parameter was calculated for changes of  $\pm 150$  K in  $T_{\text{eff}}$ ,  $\pm 0.25$  dex in  $\log g$ , and  $\pm 0.30 \text{ km s}^{-1}$  in  $\xi$ . These calculated abundance sensitivities for two targets, WASP-12 and HAT-P-1, are shown as an example in Table 5.7. The final uncertainty due to each parameter is then the product of this sensitivity and the corresponding scaled parameter uncertainty, as described in Teske et al. 2013a. The dispersion in the abundances derived from different lines is parameterized with the uncertainty in the mean,  $\sigma_{\mu}$ , for the abundances derived from the averaging of multiple lines. Then the total internal uncertainty for each abundance ( $\sigma_{\text{tot}}$ ) is the quadratic sum of the individual parameter uncertainties and  $\sigma_{\mu}$ .

In the case of the O I triplet, the error on  $[\text{O}/\text{H}]_{\text{NLTE}}$  was calculated separately for each of the applied NLTE corrections, but as these errors are smaller than the error derived from the LTE measurement, the LTE errors are conservatively adopted. In the cases of more than one measurable oxygen abundance indicator, the errors associated with  $[\text{O}/\text{H}]$  reported in Table 5.6 are the errors from each oxygen abundance indicator ( $[\text{O I}]$  6300 Å and LTE O I triplet) added in quadrature, unless otherwise noted. Similarly, the C/O ratio errors are the errors of  $[\text{C}/\text{H}]$  and  $[\text{O}/\text{H}]$  combined in quadrature.

## 5.4 Results and Discussion

Our final adopted stellar parameters and their  $1\sigma$  uncertainties for each target are listed in Table 7.1, and the adopted elemental abundances and their  $1\sigma$  uncertainties for each target are listed in Table 5.6. We compared our results to those of the catalog of Stars With ExoplanETs (SWEET-Cat), described in Santos et al. (2013), and those determined by Torres et al. (2012; T12). These two references are comparable to ours in their analysis methods and samples (transiting exoplanet host stars). SWEET-Cat compiles sets of atmospheric parameters previously published in the literature and, whenever possible, derived using the same uniform methodology of Santos et al. (2004). The main sources of stellar parameters in SWEET-Cat for the targets in our sample are Santos et al. (2004), Ammler-von Eiff et al. (2009), and Mortier et al. (2013). SWEET-Cat reports  $T_{\text{eff}}$ ,  $[\text{Fe}/\text{H}]$ , and  $\log g$  for all of the targets in our sample of stars, and  $\xi$  for ten of the targets.

T12 compared the resulting  $T_{\text{eff}}$  and  $[\text{Fe}/\text{H}]$  from three different stellar analysis programs. They include stellar parameter classification (SPC; Buchhave et al. 2012), Spectroscopy Made Easy (SME; Valenti & Piskunov 1996), and MOOG, the latter of which we employ here. They also determine  $\log g$  values, but do not report them, and  $v \sin i$  values, which we do not determine in our work. T12 report final “averaged”  $T_{\text{eff}}$  and  $[\text{Fe}/\text{H}]$  values from all attempted analysis methods for thirteen of the stars in our sample, though MOOG-derived  $T_{\text{eff}}$  and  $[\text{Fe}/\text{H}]$  values are included in that average for only ten of the stars in our sample.

In all cases our derived  $[\text{Fe}/\text{H}]$  values are consistent with those of SWEET-Cat and T12-average, within uncertainties. The median  $\Delta[\text{Fe}/\text{H}]$  (as in  $|\text{ours} - \text{theirs}|$ ) values are 0.08 and 0.02 for SWEET-Cat and T12-average, respectively. The  $T_{\text{eff}}$  and  $\log g$  values reported here also overlap within uncertainties the val-

ues reported in T12-average and those in SWEET-Cat in almost every case. The median  $\Delta \log g$  for SWEET-Cat is 0.17, and the median  $\Delta T_{\text{eff}}$  for SWEET-Cat and T12-average are 55 K and 41 K, respectively. In the two cases where  $T_{\text{eff}}$  does not overlap SWEET-Cat our values are cooler by 54 K (WASP-12) and 202 K (WASP-32). Two other sources (Brown et al. 2012; Maxted et al. 2010) report a very similar  $T_{\text{eff}}$  for WASP-32 as the (cooler) value derived here, and the results of Torres et al. (2012) for WASP-12 agree well with our  $T_{\text{eff}}$ . In the three cases where  $\log g$  does not overlap SWEET-Cat or T12-average our values differ by  $\leq 0.04$  dex.

#### 5.4.1 Comparison to Previous Studies of C and O in Exoplanet Host Stars

This study focuses on transiting exoplanet host star elemental abundances, particularly their C/O ratios. No previous study of which we are aware has uniformly derived [C/H], [O/H], and C/O values for these stars. However, several studies have examined C/O ratios in non-transiting exoplanet host stars versus stars not known to host planets. [Any star designated as a “non-host” has the potential to harbor a smaller (undetected) planet; indeed, it may be the case that most stars have one or more small planets (e.g., Cassan et al. 2012).] Here we compare our results to these other host star C/O studies.

Bond et al. (2006) measure [C/H] in 136 G-type stars, 20 of which are exoplanet hosts, and Bond et al. (2008) measure [O/H] ratios in 118 F- and G-type stars, 27 of which are known exoplanet hosts. Line lists are not explicitly given for the measured C lines in Bond et al. (2006); Bond et al. (2008) use the high-excitation O I triplet at  $\lambda = 7771.9, 7774.2, \text{ and } 7775.4 \text{ \AA}$ . Bond et al. (2010) also compiled C/O ratios derived from measurements in Ecuivillon et al. (2004) and (2006). Ecuivillon et al. (2004) measures [C/H] from the two lowest excitation lines of carbon (5052.17 and 5380.34  $\text{\AA}$ ), and Ecuivillon et al. (2006) measures [O/H] from the forbidden [O I] line at 6300.3  $\text{\AA}$ , the high-excitation O I triplet at

$\lambda = 7774 \text{ \AA}$ , and a set of 5 near-UV OH lines around  $3100 \text{ \AA}$ . Both of the Ecuivillon studies and the Bond studies implement an analysis method similar to that performed here, with the spectral synthesis code MOOG and a grid of Kurucz (1993) ATLAS9 model atmospheres, although these studies do not derive the host star parameters ( $T_{\text{eff}}$ ,  $\log g$ ,  $\xi$ , and  $[\text{Fe}/\text{H}]$ ), only specific elemental abundance ratios. In the host star sample reported in Bond et al. (2010), 35% have  $\text{C}/\text{O} > 0.8$  (they did not specifically report any non-host stars); Bond et al. (2008) find 8% of host stars and 5% of non-host stars in their sample to have  $\text{C}/\text{O} > 0.8$ .

Following the Bond et al. investigation, two larger studies of the  $\text{C}/\text{O}$  ratios of non-host stars versus host stars were conducted. Delgado Mena et al. (2010) measure carbon and oxygen in 100 host stars, along with 270 non-host stars, using the C I lines at  $5052.17 \text{ \AA}$  and  $5380.34 \text{ \AA}$  and the [O I] forbidden line at  $6300.3 \text{ \AA}$ . They measure equivalent widths with the ARES program<sup>7</sup> (Sousa et al. 2007), and used MOOG and Kurucz ATLAS9 model atmospheres (Kurucz 1996) for abundance analysis. Delgado Mena et al. (2010) find 34% of their measured host stars have  $\text{C}/\text{O} > 0.8$ , while in their non-host sample the fraction of stars with  $\text{C}/\text{O} > 0.8$  is 20%. Petigura & Marcy (2011) find carbon and oxygen abundances for 704 and 604 stars, respectively, but only 457 have reliable measurements for both elements that can be used to determine  $\text{C}/\text{O}$  ratios, 99 of which are exoplanet hosts. These authors measure the  $6587 \text{ \AA}$  C I line for carbon and the [O I] line at  $6300.3 \text{ \AA}$  for oxygen, and use the SME code with Kurucz (1992) stellar atmospheres for their abundance analysis. Petigura & Marcy (2011) find 34% of host stars in their sample have  $\text{C}/\text{O} > 0.8$ , versus 27% of non-host stars in their sample with  $\text{C}/\text{O} > 0.8$ .

The goal of this paper is to investigate and constrain values of stellar host  $\text{C}/\text{O}$  ratios in systems with observed transiting giant planets, since transit spec-

---

<sup>7</sup>The ARES code can be downloaded at <http://www.astro.up.pt/sousasag/ares/>.

troscopy potentially allows for determinations of the corresponding planetary C/O ratios. This goal is driven partially by the recent suggestion by Fortney (2012) that the C/O ratios of both host- and non-host stars in the studies noted above have been overestimated due to errors in the derived C/O ratios and the observed apparent frequency of carbon dwarf stars implied by these studies.

Nissen (2013) recently rederived the carbon and oxygen abundances for 33 of Delgado Mena et al. (2010)'s host stars that have additional ESO 2.2m FEROS spectra covering the O I triplet at 7774 Å, which was not originally used by Delgado Mena. He implements a differential analysis with respect to the Sun, with equivalent widths of C and O measured in IRAF with Gaussian profiles and abundances derived by matching the observed equivalent widths with those measured in plane parallel MARCS atmosphere models (Gustafsson et al. 2008) having the same stellar parameters as those published by Delgado Mena et al. (2010). Accounting for NLTE effects on the triplet line strengths by using the Fabbian et al. (2009) corrections, Nissen (2013) finds differences from Delgado Mena et al. (2010) in the derived oxygen abundances. This results in both a tighter correlation between [Fe/H] and C/O (Nissen finds  $C/O = 0.56 + 0.54[Fe/H]$  with an rms dispersion  $\sigma(C/O) = 0.06$ ), as well as a much smaller fraction of host stars with  $C/O > 0.8$  (only 1 out of 33).

The tight trend of increasing C/O with [Fe/H], e.g., Nissen (2013; as noted above), is indicative of the importance of overall Galactic chemical evolution in setting the fraction of dwarf stars that might be carbon rich. The increase in C/O with metallicity points to the importance of low- and intermediate-mass star carbon nucleosynthesis at later, more metal-rich times. The influence of high-mass star Type II supernovae, the major oxygen contributors, is diluted with time as low- and intermediate-mass stars become more important, thus C/O increases.

The fraction of “carbon-rich” ( $C/O \geq 0.8$ ) planet-hosting stars is thus expected to increase with increasing metallicity in the disk, with the Nissen trend indicating metallicities greater than  $[Fe/H] \sim 0.4$  might begin to have significant fractions of carbon-rich dwarf stars. All of the planet-hosting stellar samples discussed here have very few, if any, stars at these metallicities or higher.

This paper differs from the studies listed above because 1) the sample here is much smaller, being limited to only hosts of transiting exoplanets, and 2) only one non-host star is included (the binary companion XO-2S). In Figure 5.3 the host star abundances derived here, shown with red filled circles with error bars, for  $[C/H]$  and  $[O/H]$  versus  $[Fe/H]$  are compared to the results of the large samples of Delgado Mena et al. (2010), shown as gray asterisks for host stars and open squares for non-host stars, and Nissen (2013), shown as blue asterisks. All three studies define similar behaviors of  $[C/H]$  and  $[O/H]$  as a function of  $[Fe/H]$ , with the carbon exhibiting larger slopes with iron relative to oxygen; this illustrates the increasing importance of carbon production from low- and intermediate-mass stars relative to massive stars with increasing chemical maturity.

The slopes of the trends in Figure 5.3 are all quite similar, with the Nissen (2013) trend exhibiting the smallest scatter about a linear fit. Using the results of this paper, linear trends are fit to both  $[C/H]$  and  $[O/H]$  versus  $[Fe/H]$  with the following results:  $[C/H] = 0.95[Fe/H] - 0.05$  and  $[O/H] = 0.56[Fe/H] + 0.01$ . Excluding the apparently carbon-rich outlier HD 189733, these fits are  $[C/H] = 1.02[Fe/H] - 0.08$  and  $[O/H] = 0.56[Fe/H] + 0.01$ ; we refer to these fits without HD 189733 throughout the rest of the paper. Quantitatively, the C versus Fe slope is about twice as large (in dex) as that for O versus Fe based on the linear fits to the abundances derived here. The relation for carbon passes 0.08 dex below solar (i.e., at  $[Fe/H], [C/H] = 0, 0$ ) while passing close to solar for oxygen, offset by only

+0.01 dex.

Because of these even rather small offsets ( $\sim 0.05$ - $0.1$  dex), the C/O ratios as a function of [Fe/H] might fall below solar as defined by our results for this particular sample of stars: an offset of  $-0.05$  to  $-0.1$  dex in [C/O] would correspond to an offset of  $0.1$  to  $0.2$  lower in a linear value of C/O. This does not necessarily correspond to simply errors in the analysis, but may reflect both fitting linear relations to our results, which are probably only approximate descriptions of the real Galactic disk relation, as well as there not being a universal trend of [C or O]/H versus [Fe/H]. The offsets here most probably reflect both uncertainties in the analysis (already discussed in Section 3.2) and intrinsic scatter in real Galactic disk populations that will map onto the sample of stars analyzed here.

Figure 5.4 illustrates values of C/O versus [Fe/H] from this study, along with those values from Delgado Mena et al. (2010) and Nissen (2013). All three studies find a clear increase in C/O versus [Fe/H], which represents the signature of Galactic chemical evolution, as discussed previously. The relation in C/O in this work falls somewhat below those of the other two studies, but all three exhibit similar slopes. This similarity is born out by a quantitative comparison of C/O versus [Fe/H] between Nissen (2013) and this study. Nissen derived a linear fit of  $C/O = 0.54[Fe/H] + 0.56$ , while the same fit to the results here find  $C/O = 0.53[Fe/H] + 0.45$ . The adopted solar value in this study of  $C/O = 0.54$  is larger by  $0.09$  than the value defined by the best-fit linear relation defined by our sample of stars and our results. Including the outlier HD 189733 in our linear fit results in  $C/O = 0.43[Fe/H] + 0.49$ , corresponding to a C/O ratio  $0.05$  smaller than the solar value of  $0.54$ ; including this outlier increases the scatter around the fit from  $0.04$  to  $0.1$ . A linear difference of  $0.09$  corresponds to  $0.08$  dex for the solar-relative [C/O], which is comparable to the respective offsets of  $-0.08$  dex and  $+0.01$  dex in

the  $[C/H]$  and  $[O/H]$  relations.

Another way of investigating the inherent scatter within our results is to remove the linear best-fit from the values of  $C/O$  and look at the scatter about the fitted relation. When this is done the median residual scatter in  $C/O$  is  $\pm 0.04$ , or  $0.03$  dex in  $[C/O]$ . This comparison of  $C/O$  versus  $[Fe/H]$  trends between Nissen (2013) and this study indicates that the derived slopes are very similar, but there remain small offsets in zero-point  $C/O$  of  $\sim 0.10 - 0.15$  caused by a combination of differences in (presumably) the stellar samples, the adopted solar  $C/O$  ratios ( $0.58$  for Nissen and  $0.54$  for this study), as well as the abundance analysis, e.g., much of the offset is due to somewhat smaller values of  $[C/H]$  at our lower metallicity range.

The mean and standard deviation of the  $[C/H]$ ,  $[O/H]$ , and  $C/O$  distributions from this study, as well as those from all the previous studies of host star carbon and oxygen abundances mentioned above, are listed in Table 5.8. The mean  $[C/H]$  of the transiting exoplanet hosts in this paper is less than the mean  $[C/H]_{\text{host}}$  from the previous works,  $0.14$  in the five previous studies versus  $0.08$  found here. The mean  $[O/H]$  value found in our sample is the same as the mean  $[O/H]_{\text{host}}$  from previous studies,  $0.07$ . However, the standard deviations of  $[C/H]_{\text{transiting}}$  and  $[O/H]_{\text{transiting}}$  from this paper are large,  $0.20$  and  $0.13$ , respectively, so any differences in our mean  $[C/H]$  and  $[O/H]$  values are to be viewed with caution. The mean  $C/O$  ratio of the transiting exoplanet host stars in our sample is  $0.54$ , with a standard deviation of  $0.15$ , versus the mean from the previous papers of  $0.71$  with a standard deviation of  $0.07$ . Therefore, the sample of carbon and oxygen abundance ratios for transiting exoplanet host stars presented here, while marginally consistent, are on average lower than those measured by other groups for non-transiting exoplanet host stars. Our measurements are more



in line with the suggestions by Fortney (2012) and Nissen (2013) that prior studies overestimated C/O ratios; the mean  $C/O_{\text{hosts}}$  of Nissen is  $0.63 \pm 0.12$ .

However, as noted by Fortney (2012), each previous study scales their C/O ratios based on different  $\log N(C)_{\odot}$  and  $\log N(O)_{\odot}$  values. Delgado Mena et al. (2010) list  $\log N(C)_{\odot}$  and  $\log N(O)_{\odot}$  as 8.56 and 8.74, respectively, resulting in  $C/O_{\odot} = 0.66$ . These are also the values listed in Ecuivillion et al. (2004) and (2006), the quoted sources of Bond et al. (2010). Petigura & Marcy (2011) list  $\log N(C)_{\odot}$  and  $\log N(O)_{\odot}$  as 8.50 and 8.70, respectively, resulting in  $C/O_{\odot} = 0.63$ . Nissen (2013)'s  $C/O_{\odot} = 10^{8.43} / 10^{8.665} = 0.58$ . Figure 5.4 illustrates the different  $C/O_{\odot}$  from Delgado Mena et al. (2010) and Nissen (2013). Accounting for the difference in  $\log N(C)_{\odot}$  and  $\log N(O)_{\odot}$  decreases the average C/O ratios from the other sources (from top to bottom) in Table 5.8 by  $\sim 0.15$ ,  $\sim 0.13$ ,  $\sim 0.11$ , and  $\sim 0.05$ , closer to the average C/O ratio we derive for our sample. Figure 5.4's right panel shows the C/O ratios of Delgado Mena et al. (2010) and Nissen (2013) along with those derived in this work, all on the same scale, illustrating how using different solar C and O absolute abundances changes the resulting C/O ratios. This underscores the caution, as mentioned in Fortney (2012) and Nissen (2013), required when directly comparing C/O ratios derived from different groups.

We now focus on the C/O ratios in each studied system to investigate possible links between host star C/O ratios with planetary and system properties.

#### 5.4.2 Trends with $C/O_{\text{host star}}$ versus Planetary Parameters

Presently there are two major observed trends relating stellar chemical composition to the presence of planets – hot Jupiter exoplanets are more often found around intrinsically higher-metallicity stars (e.g., Fischer & Valenti 2005), and the fraction of stars with giant planets increases with stellar mass (e.g., Johnson et al. 2010; Ghezzi et al. 2010; Gaidos et al. 2013). Measuring potential host stars'

chemical abundance distributions may develop into a powerful tool for inferring the presence, or even specific type (size, orbit, composition), of exoplanets around different types of stars. This technique is of increasing importance in the context of large surveys that are discovering exoplanets, and targeted studies of unusual or potentially-habitable exoplanets.

In this study we explore whether the stellar C/O ratio has predictive power with respect to hot Jupiter properties, particularly the exoplanetary atmosphere compositions. Characteristic observations of the atmospheres of the exoplanets in this sample – the *Spitzer*/IRAC 3.6, 4.5, 5., and 8.0  $\mu\text{m}$  secondary eclipse fluxes – as well as their physical properties like mass, radius, semi-major orbital axis, period, and equilibrium temperature were gathered from the NASA Exoplanet Archive<sup>8</sup> and compared to host star C/O ratios. By eye it appears that planet radius and planet equilibrium temperature may decrease with increasing  $\text{C/O}_{\text{host star}}$  (Fig.5.5), but these trends are dominated by one or two points and, once these points are removed, no significant trends with planet parameters are found. We also find weak negative correlations between each system’s  $\text{C/O}_{\text{host star}}$  and planetary *Spitzer*/IRAC secondary eclipse fluxes (e.g.,  $r \sim -0.4$  to  $-0.6$ ), but these correlations are not statistically significant ( $p > 0.05$ ).

This lack of trends between  $\text{C/O}_{\text{host star}}$  and planetary properties is perhaps not surprising. The hot Jupiter host stars in this sample were chosen based on the amount of observational data that exists for their planets, and thus how “characterizable” their planets’ atmospheres are, with the goal of directly comparing star and planet C/O ratios. No planetary or stellar parameters serve as “control variables” in this study, and our sample is actually diverse in both respects. The host stars span  $5100 \lesssim T_{\text{eff}} \lesssim 6470 \text{ K}$ ,  $-0.21 \lesssim [\text{Fe}/\text{H}] \lesssim 0.44$ , and spectral types F6 through

---

<sup>8</sup><http://exoplanetarchive.ipac.caltech.edu/>

K1. The planets in our sample range in mass from  $\sim 0.5\text{--}4.2 M_J$ , in period from  $\sim 1.09\text{--}111$  days (with the second longest being 4.5 days), in density from  $\sim 0.2\text{--}8 \text{ g cm}^{-3}$  (with the second most-dense being  $3.4 \text{ g cm}^{-3}$ ), and in equilibrium temperature from  $\sim 400\text{--}2500 \text{ K}$ . That we do not find a significant correlation between  $C/O_{\text{host star}}$  and any of these planetary parameters implies that (1) our sample may yet be too small to reveal distinct trends, and/or (2) the influence of the host star C/O ratio is a more complex function of multiple parameters of the planet and/or its formation history.

While (1) is possible, (2) also seems likely and could result in the C/O ratio comparison between stars and planets serving a more interesting function. In protoplanetary disks, the relative ratios of carbon and oxygen can change as a compared to those in the parent star due to different temperature condensation fronts, and/or the movement of gas and grains in the disk (Stevenson & Lunine 1988; Lodders 2010; Ciesla & Cuzzi 2006; Öberg et al. 2011). In particular, the enhancement or depletion of water and thus oxygen is sensitive to the size and migration of icy solids in the disk, so the C/O ratios of the inner and outer disk regions evolve with time and depend on both initial conditions and the efficiency with which solids grow to large sizes (Ciesla & Cuzzi 2006; Najita et al. 2013). Overall, the final  $C/O_{\text{planet}}$  does not necessarily reflect the  $C/O_{\text{disk-average}}$ , and depends on the location and timescale of formation, how much of the atmosphere is accreted from gas versus solids, and how isolated the atmosphere is from mixing with core materials (Ciesla & Cuzzi 2006; Öberg et al. 2011). In our own solar system gas giant planets, oxygen is not well constrained because water, the major oxygen carrier, condenses deeper down in their cool ( $T \leq 125 \text{ K}$ ) atmospheres, out of the observable range of remote spectra (Madhusudhan 2012). However, carbon is known to be enhanced above solar by factors of  $\sim 2\text{--}6$ ,  $6\text{--}11$ ,  $18\text{--}50$ , and  $28\text{--}63$

in Jupiter, Saturn, Uranus, and Neptune, respectively (Wong et al. 2008 and references therein). Thus, though the composition of the host star provides a good estimate of the system C/O ratio and the natal molecular cloud environment, differences between the host star and planetary C/O ratios may be common, and may be used to probe where and when in the disk the planet formed.

A third possibility is that the host star C/O ratio has no connection to the formation of planets and is not a useful metric for distinguishing planet types. However, theoretical results (e.g., Johnson et al. 2012; Ali-Dib et al. 2014) demonstrating the influence of the host star C/O ratio on the composition of protoplanetary disk, and recent observations (e.g., Najita et al. 2013; Favre et al. 2013) indicating that disks themselves likely have a range of C/O ratios which are related to other planet formation parameters (mass of the disk, grain growth and composition, etc.), suggest that C/O ratios of host stars do play a role, at some stage, in planet formation.

### 5.4.3 Carbon and Oxygen in Specific Exoplanet Systems

A small fraction of exoplanets, mostly hot Jupiters orbiting very close to their host stars, have been observed and analyzed with spectroscopy and photometry in the optical and near-infrared during primary transit (e.g., Madhusudhan & Seager 2009; Swain et al. 2008, 2013; Moses et al. 2011; Mandell et al. 2013) and/or secondary eclipse (e.g., Charbonneau et al. 2005, 2008; Knutson et al. 2008; Madhusudhan et al. 2011; Crossfield et al. 2012). Direct imaging of exoplanets in wider orbits (e.g., Marois et al. 2008 & 2010; Lagrange et al. 2009; Bailey et al. 2014) has also opened up for study a new population of self-luminous planets in Jovian-type orbits.

As discussed in the introduction, a gas giant planet's C/O ratio has important implications for its composition. At the temperatures and pressures charac-

teristic of such atmospheres, a high C/O ratio ( $\gtrsim 0.8$ ) can significantly alter the temperature and chemistry structure by depleting the dominant opacity source  $\text{H}_2\text{O}$  and introducing new sources that are C-rich like  $\text{CH}_4$ ,  $\text{HCN}$ , and/or other hydrocarbons. In thermochemical equilibrium,  $\text{C/O} > 1$  causes O to be confined mostly to CO, depleting  $\text{H}_2\text{O}$  and enhancing  $\text{CH}_4$  versus what is expected in solar-abundance atmospheres ( $\text{C/O}_\odot = 0.55 \pm 0.10$ ; Asplund et al. 2009; Caffau et al. 2011), which have abundant  $\text{H}_2\text{O}$  and CO (Madhusudhan 2012; Moses et al. 2013). In carbon-rich atmospheres, the temperature controls how depleted the  $\text{H}_2\text{O}$  is compared to solar and the partitioning of carbon between  $\text{CH}_4$  and CO, which in turn influences the oxygen balance between CO and  $\text{H}_2\text{O}$  (Madhusudhan 2012).

With the ability to constrain exoplanet atmosphere compositions (e.g., Madhusudhan 2012; Lee et al. 2012; Moses et al. 2013; Konopacky et al. 2013; Line et al. 2013), a logical next step towards determining the host star's influence on exoplanet formation is the direct comparison of the abundance ratios of star/planet pairs.

#### 5.4.3.1 WASP-12

For WASP-12b, one of the brightest transiting exoplanets, the comparison between host star and planet composition has already begun (Madhusudhan et al. 2011; Madhusudhan 2012; Petigura & Marcy 2011; Crossfield et al. 2012; Swain et al. 2013; Copperwheat et al. 2013; Sing et al. 2013). The host star is found in this work to have  $[\text{Fe}/\text{H}] = 0.06 \pm 0.08$  and  $\text{C/O} = 0.48 \pm 0.08$ . We note that this metallicity differs significantly from the  $[\text{M}/\text{H}] = 0.30^{+0.05}_{-0.10}$  reported by Hebb et al. (2009) in the WASP-12b discovery paper, based on spectral synthesis of four regions including the Mg b triplet at 5160-5190 Å, Na I D doublet at 5850-5950 Å, 6000-6210 Å, and  $\text{H}\alpha$  at 6520-6600 Å, following the procedure of Valenti & Fischer (2005).

Coupling their atmospheric modeling and retrieval methods to published sec-

ondary eclipse photometry and spectroscopy spanning  $0.9\ \mu\text{m}$  to  $8\ \mu\text{m}$ , Madhusudhan et al. (2011) and Madhusudhan (2012) suggest that WASP-12b's atmosphere has a C/O ratio  $\geq 1$ . Their best fit describes an atmosphere abundant in CO, depleted in  $\text{H}_2\text{O}$ , and enhanced in  $\text{CH}_4$ , each by greater than two orders of magnitude compared to the authors' solar-abundance, chemical-equilibrium models. However, this high C/O<sub>planet</sub> ratio for WASP-12b's atmosphere is ruled out at the  $>3\sigma$  level with new observations at  $2.315\ \mu\text{m}$  and reanalysis of previous observations accounting for the recently detected close M-dwarf stellar companion (Bergfors et al. 2011; Crossfield et al. 2012). Including the dilution of the reported transit and eclipse depths due to the M-dwarf, the dayside spectrum of WASP-12b is best explained by a featureless 3000 K blackbody (Crossfield et al. 2012). Subsequent data (Sing et al. 2013) do not detect metal hydrides MgH, CrH, and TiH or any Ti-bearing molecules, which were previously suggested as indicative of high-C/O ratio scenarios (Madhusudhan 2012; Swain et al. 2013).

A C/O $<1$  composition for WASP-12b is also consistent with the study of Line et al. (2013), who use a systematic temperature and abundance retrieval analysis, combining differential evolution MCMC with an optimal-estimation-based prior, to rule out strong temperature inversion in WASP-12b's atmosphere and thus the presence of TiO causing such an inversion. Accounting for the M dwarf companion, these authors determine a best-fit C/O ratio for WASP-12b of 0.59 ( $\chi^2_{\text{best}}/N=2.45$ , with a 68% confidence interval of 0.54-0.95), suggesting that a high C/O ratio is not the explanation for WASP-12b's lack of atmospheric temperature inversion. If WASP-12b's C/O ratio really is super-solar and significantly different than its host star ( $0.48\pm0.08$ ), this suggests that some other mechanism influenced the composition of the exoplanet during its formation/evolution. Öberg et al. (2011) note that the high C/O and substellar C/H reported by Madhusud-

han et al. (2011) are only consistent with an atmosphere formed predominantly from gas accretion outside the water snowline. With our updated metallicity measurement, C/H in WASP-12 decreases to  $\sim 5 \times 10^{-4}$ , exactly in the middle of the C/H distribution spanned for the planet in Madhusudhan et al. (2011)'s best-fitting ( $\chi^2 < 7$ ) models. Thus, by these models, the planet's C/H is just as likely to be substellar as super-stellar. More data, particularly around  $3 \mu\text{m}$  (see Line et al. 2013, Figure 1), can help further constrain WASP-12b's C/O ratio and enable a more meaningful comparison between planet and host star. We note that the very recent HST/WFC3 transit spectra of WASP-12b from  $1.1\text{--}1.7 \mu\text{m}$  reported by Mandell et al. (2013) are fit equally well by oxygen- and carbon-rich models of Madhusudhan et al. (2011).

#### 5.4.3.2 XO-1

The hot Jupiter XO-1b's (McCullough et al. 2006) four *Spitzer*/IRAC photometric secondary eclipse observations have been explained with a solar-composition, thermally-inverted model (Machalek et al. 2008). However, it is also possible to fit the observations with a non-inverted (Tinetti et al. 2010), potentially carbon-rich atmosphere model (Madhusudhan 2012), which may include disequilibrium chemistry like photochemistry and/or transport-induced quenching (Moses et al. 2013). As the favored  $\text{C/O} \geq 1$  models are heavily dependent on the  $5.8 \mu\text{m}$  photometric point, new observations are necessary to confirm the carbon-rich nature of XO-1b's atmosphere. Here we find in the XO-1 host star  $[\text{Fe}/\text{H}] = -0.11 \pm 0.06$ , with  $[\text{C}/\text{H}] = -0.19 \pm 0.04$  and  $[\text{O}/\text{H}] = -0.09 \pm 0.05$ , resulting in  $\text{C/O} = 0.43 \pm 0.07$ .

#### 5.4.3.3 TrES-2 and TrES-3

TrES-2b and TrES-3b were among the first transiting hot Jupiter exoplanets discovered (O'Donovan et al. 2006; O'Donovan et al. 2007). Both fall under the highly-irradiation “pM” class predicted to have temperature inversions in their upper atmospheres (Fortney et al. 2008). Secondary eclipses of TrES-2b and TrES-3b were observed with the CFHT Wide-field Infrared Camera 2.15  $\mu\text{m}$  filter, (Croll et al. 2010a; 2010b), in *Spitzer*/IRAC’s four near-IR bands (O'Donovan et al. 2010; Fressin et al. 2010, respectively). Radiative transfer analyses of Line et al. (2014) use the CFHT and *Spitzer* data indicate a range of temperature-pressure profiles are too cool for TiO and VO to be in the gas phase, which suggests that these species do not cause thermal inversions. Line et al. (2014) find that the data provide minimal constraints on the abundances of  $\text{H}_2\text{O}$ ,  $\text{CO}_2$ , CO, and  $\text{CH}_4$ , and thus TrES-2b’s atmospheric C/O ratio. Their best fit ( $\chi^2_{\text{best}}/N=0.60$ ) is 0.20, but their 68% confidence interval spans 0.021-8.25. Interestingly, the C/O ratio of TrES-2 that we derive,  $0.41 \pm 0.05$ , has the lowest error in our sample and also the second-lowest C/O ratio value in our sample. Hence, if TrES-2b accreted much of its gas from a reservoir similar in composition to its host star, and its atmosphere remained mostly isolated from its interior, it may also have a sub-solar atmospheric C/O ratio.

For TrES-3b, radiative transfer analyses of the infrared photometry indicate that  $\text{H}_2\text{O}$  is well determined with an abundance near  $10^{-4}$ , and  $\text{CH}_4$  has an upper limit of  $\sim 10^{-6}$  (Line et al. 2014).  $\text{CO}_2$  shows a weak upper limit  $\sim 10^{-4}$ , derived from the 2.1  $\mu\text{m}$   $\text{CO}_2$  band wings within the  $K$  band measurement, while CO is unconstrained due to the large uncertainty in the *Spitzer* 4.5  $\mu\text{m}$  data point, combined with the fact that no other molecular absorption features of CO are probed by the current data (Line et al. 2014). Line et al. (2014) infer that  $\text{C/O} > 1$  in TrES-3b



due to the relatively high-confidence limit on  $\text{H}_2\text{O}$  and the small upper limit on  $\text{CH}_4$ . However, the data provide no constraints on the CO abundance, which is expected to be the major carbon carrier in an atmosphere as hot as TrES-3b. Their best fit ( $\chi^2_{\text{best}}/N=0.067$ ) C/O ratio for TrES-3b is 0.22, with a 68% confidence interval of 0-0.97. The very recently published HST/WFC3 secondary eclipse observations of TrES-3b are poorly fit with a solar-composition model ( $\chi^2/N = 3.04$ ), whereas the WFC3 data plus the existing *Spitzer* photometry are more consistent ( $\chi^2/N = 0.75$ ) with an atmosphere model depleted in  $\text{CO}_2$  and  $\text{H}_2\text{O}$  by a factor of 10 relative to a solar-composition model (Ranjan et al. 2014).

TrES-3's C/O ratio derived here,  $0.29 \pm 0.09$ , also has a small error and is the lowest C/O ratio in the hot Jupiter host stars studied here. The large span in the planet's C/O ratio found by Line et al. (2014) is still too large to draw meaningful conclusions about the formation location and/or growth history of TrES-3b. However, if the degeneracy between CO and  $\text{CO}_2$  absorption in the *Spitzer* 4.5  $\mu\text{m}$  data point is broken by, for instance, observations of the 2.6  $\mu\text{m}$  or 15  $\mu\text{m}$   $\text{CO}_2$  bending band or the 5  $\mu\text{m}$  CO fundamental band by SOFIA/FLITECAM (McLean et al. 2006) or SOFIA/FORCAST (Adams et al. 2010), both the CO and  $\text{CO}_2$  contributions could be better estimated and lead to a tighter C/O ratio constraint for TrES-3b. This system is intriguing and important for further investigation due to both our firmly sub-solar C/O ratio and the relatively metal-poor nature of the host star ( $[\text{Fe}/\text{H}] = -0.21 \pm 0.08$ , the lowest in our sample), which distinguishes TrES-3 from most other hot Jupiter hosts.

#### 5.4.3.4 HD 149026

Observational constraints and extensive theoretical modeling indicate that the exoplanet HD 149026b has between 45-110  $M_{\oplus}$  of heavy elements in its core and surrounding envelope (Sato et al. 2005; Fortney et al. 2006; Ikoma et al. 2006; Broeg

& Wuchterl 2007) , making the core of HD 149026b at least twice as massive as Saturn's, even though its radius is  $\sim 0.86 R_{\text{Saturn}}$  (Triaud et al. 2010) and its mass is  $\sim 1.2 M_{\text{Saturn}}$  (Sato et al. 2005). The massive core of HD 149026b challenges formation by traditional core accretion theory, and many modified formation scenarios have been suggested, including collision with an outer additional giant planet (Sato et al. 2005; Ikoma et al. 2006), accretion of planetesimals or smaller (super-Earth-sized) planets (Ikoma et al. 2006; Broeg & Wuchterl 2007; Anderson & Adams 2012), or core accretion in a disk with  $\times 2$  the heavy element mass in the solar nebula (Dodson-Robinson & Bodenheimer 2009). This latter explanation stems from the metal-rich nature of the star – more massive/metal-rich disks form planets more readily (Ida & Lin 2004ab) and metal-rich planets tend to be associated with metal-rich stars (Guillot et al. 2006; Burrows et al. 2007a; Miller & Fortney 2011). Here we find  $[\text{Fe}/\text{H}] = 0.26 \pm 0.09$  for HD 149026, which is not as high as previous studies ( $[\text{Fe}/\text{H}] = 0.36 \pm 0.05$ ; Sato et al. 2005), but still suggests that, overall, the initial metal abundance in the molecular cloud/disk was enhanced above solar. We measure  $[\text{C}/\text{H}] = 0.26 \pm 0.08$  and  $[\text{O}/\text{H}] = 0.25 \pm 0.04$ , both enhanced above solar, resulting in a C/O ratio of  $0.55 \pm 0.08$ , consistent with solar.

Stevenson et al. (2012) find that the *Spitzer* secondary eclipse observations of HD 149026b (at 3.6, 4.5, 5.8, 8.0, and 16  $\mu\text{m}$ ) can be fit using models with an atmosphere in chemical equilibrium and lacking a temperature inversion, with large amounts of CO and CO<sub>2</sub>, and a metallicity  $\times 30$  solar (Fortney et al. 2006). The retrieval results of Line et al. (2013) also indicate the atmosphere of HD 149026b has more CO and CO<sub>2</sub> than CH<sub>4</sub>, which makes sense given the planet's high temperature ( $\sim 1700$  K) that favors formation of CO over CH<sub>4</sub> at solar abundances. There is also a peak in the Line et al. modeled composition probability distribution of the H<sub>2</sub>O mixing ratio near  $\sim 10^{-5}$ . Given this H<sub>2</sub>O abundance, and the

low abundance of  $\text{CH}_4$ , the C/O ratio of HD 149026b is likely  $<1$ , but it remains poorly constrained (0.55, with a  $\chi^2_{\text{best}}/N=0.23$  fit and a 68% confidence interval of 0.45-1.0; Line et al. 2013). A better estimate of HD 149026b's C/O ratio as compared to the C/O ratio of its host star ( $0.55 \pm 0.08$ ) may shed light on the planet's history and the origin of its massive core. This heavy-cored hot Jupiter system, with the host star carbon and oxygen abundances presented here, is a valuable test-bed for studying how massive planets form.

#### 5.4.3.5 XO-2

The hot Jupiter XO-2b has a host star, XO-2N, with a binary companion, XO-2S, located  $\sim 4600$  AU away and not known to host a hot Jupiter-type planet (Burke et al. 2007). The stars are of similar stellar type, meaning that the non-hosting companion can be used to check for effects of planet formation on the host star, e.g., stellar atmospheric pollution. XO-2b has been observed with HST and *Spitzer* (Machalek et al. 2009; Crouzet et al. 2012) as well as from the ground (Sing et al. 2012 & 2011; Griffith et al. 2014). Griffith et al. (2014) find, with a comprehensive analysis of all existing data, that the water abundance that best matches most of the data is consistent with an atmosphere that has the same metallicity and C/O ratio as the host star in photochemical equilibrium. However there are outlying observations, so additional measurements are needed to understand the cause for the outliers and to investigate the carbon abundance in XO-2b.

Teske et al. (2013b) derived the carbon and oxygen abundances of both binary components, and found  $[\text{C}/\text{H}] = +0.26 \pm 0.11$  in XO-2S versus  $+0.42 \pm 0.12$  in XO-2N, and  $[\text{O}/\text{H}] = +0.18 \pm 0.15$  in XO-2S versus  $+0.34 \pm 0.16$  in XO-2N. The stars are enhanced above solar in C and O, with XO-2N being slightly more carbon- and oxygen-rich. Their relative enhancements result in both having  $\text{C}/\text{O} = 0.65 \pm 0.20$ . (Note that this value is slightly larger than that reported in Teske et al. 2013b be-

cause the  $\log N(\text{O})_{\odot}$  in this work is 8.66 versus 8.69 in Teske et al. 2013b.) Both XO-2N and XO-2S fall exactly on our linear trends with  $[\text{Fe}/\text{H}]$  discussed in §4.1 ( $[\text{Fe}/\text{H}]_{\text{XO-2N}} = 0.39 \pm 0.14$ ,  $[\text{Fe}/\text{H}]_{\text{XO-2S}} = 0.28 \pm 0.14$ ). The elevated-above-solar  $[\text{C}/\text{H}]$  and  $[\text{O}/\text{H}]$  values in the two stars are strong evidence that their parent molecular cloud was elevated in both carbon and oxygen. Given that their C/O ratios are identical, the key to understanding why XO-2N has a planet and XO-2S does not may lie in the exoplanet composition.

#### 5.4.3.6 CoRoT-2

Of the planets around the host stars in our sample, CoRoT-2b is perhaps the most puzzling in terms of its atmospheric structure. Traditional solar composition, equilibrium chemistry models are unable to reproduce the unusual flux ratios from the three *Spitzer* channel observations (it is missing  $5.8 \mu\text{m}$ ) of this very massive hot Jupiter (Alonso et al. 2010; Gillon et al. 2010; Deming et al. 2011; Guillot & Havel 2011). Despite its large mass, the planet has one of the greatest radius anomalies – slower-contraction evolution models that explain the radius anomalies of other inflated planets cannot justify this case (Guillot & Havel 2011). Furthermore, the host star is young (formed within 30-40 million years; Guillot & Havel 2011), chromospherically active and the system has been suggested to be undergoing magnetic star-planet interactions due to the observed stellar spot oscillation period that is  $\sim 10\times$  the synodic period of the planet as seen by the rotating active longitudes (Lanza et al. 2009).

CoRoT-2b's emission data are difficult to interpret, largely because of the anomalously high  $4.5/8.0 \mu\text{m}$  flux ratio. Excess CO mass loss has been suggested to enhance the  $4.5 \mu\text{m}$  flux, as has some unknown absorber acting only below  $\sim 5 \mu\text{m}$  (Deming et al. 2011; Guillot & Havel 2011). Alternatively the low  $8 \mu\text{m}$  flux may be caused by a high C/O ratio through absorption of  $\text{CH}_4$ ,  $\text{HCN}$ , and  $\text{C}_2\text{H}_2$

absorption (Madhusudhan 2012). In addition, the lack of a  $5.8 \mu\text{m}$  measurement leads to a poor constraint on the  $\text{H}_2\text{O}$  abundance, which strongly dictates the resulting C/O ratio. Wilkins et al. (2014) find that no single atmospheric model is able to reproduce all the available CoRoT-2b data, including their new  $1.17 \mu\text{m}$  HST/WFC3 spectra, the optical eclipse observed by *CoRoT* (Alonson et al. 2009; Snellen et al. 2010) and the previously-modeled infrared photometry. More complex models with differing C/O ratios or varying opacity sources do not provide a fit more convincing than a one-component blackbody, which in itself still misses the ground+*Spitzer* eclipse amplitudes by  $\sim 1.8\sigma$  (Wilkins et al. 2014).

Disequilibrium chemistry can significantly affect CoRoT-2b's atmospheric composition. For instance, for a high C/O ratio,  $\text{H}_2\text{O}$  is predicted to be enhanced above  $10^{-2}$  bar by  $\sim$ four orders of magnitude due to both transport-induced quenching and CO photochemistry in the upper atmosphere (Moses et al. 2013). HCN and other  $\text{C}_x\text{H}_x$  compounds may also result from the reaction of the left-over C with N or  $\text{H}_2$  (Moses et al. 2013). Disequilibrium chemistry models with  $0.5\times$ solar metallicity, moderate mixing, and C/O=1.1 yield a significantly better match to the four CoRoT-2b infrared secondary eclipse observations, providing a  $\chi^2/N=1.3$ , versus the solar-composition models, which provide a  $\chi^2/N=7.2$  (Moses et al. 2013).

The host star C/O ratio derived here,  $0.47\pm 0.09$ , is equal to  $\text{C}/\text{O}_{\odot}$  within error, as is the overall metallicity of the host star,  $[\text{Fe}/\text{H}]=0.06\pm 0.08$ . We note that the  $[\text{C}/\text{H}]$  value measured here for CoRoT-2 is based on only 2 carbon lines ( $5380 \text{ \AA}$  and  $7113 \text{ \AA}$ ), and the  $[\text{O}/\text{H}]$  value is based on only the O I triplet at  $\sim 7775 \text{ \AA}$ ; the other potential C and O lines were too weak to be reliably measured in our data. In addition, while the O I triplet NLTE corrections are nominally valid in this case because the  $T_{\text{eff}}$  of CoRoT-2 is  $\geq 5400$ , implementing these corrections results in an

[O/H] that is larger than the LTE case, the opposite direction of the corrections at near solar temperatures. However,  $[\text{O}/\text{H}]_{\text{LTE}}=0.02$ , the same as  $[\text{O}/\text{H}]_{\text{NLTE}}=0.06$  within error (0.07 dex); if we adopt the  $[\text{O}/\text{H}]_{\text{LTE}}$  value, CoRoT-2's C/O ratio increases by only 0.05 dex, also within error.

CoRoT-2b's C/O ratio, while still uncertain, could plausibly be  $>1$ . Several different scenarios could account for  $\text{C}/\text{O}_{\text{planet}} > \text{C}/\text{O}_{\text{star}}$ . CoRoT-2b could have accreted carbon-rich very hot gas from the inner disk regions ( $\lesssim 0.1$  AU). Alternatively, the planet could have accreted the majority of its gas from beyond the  $\text{H}_2\text{O}$  snow line (causing it to be oxygen-depleted), or accreted solid material depleted in oxygen (e.g., from a “tar line” inward of the snow line; Lodders 2004). Interestingly, to explain CoRoT-2b's inflated size and large mass, Guillot & Havel (2011) propose that the CoRoT-2 system previously included multiple giant planets that collided within the last  $\sim 20$  million years to create the currently-observed CoRoT-2b. This scenario could result in a planet that differs significantly in composition from the original states of the impactors, potentially erasing the signatures of where/from what material in the disk the planet formed. CoRoT-2b is another candidate for which additional SOFIA observations at near- ( $2.6\ \mu\text{m}$ ,  $6\ \mu\text{m}$ ) and mid-infrared ( $>20\ \mu\text{m}$ ) wavelengths can help better constrain the exoplanet C/O ratio and thus its formation history.

#### 5.4.3.7 HD 189733

The hot Jupiter HD 189733b is one of the best-studied to date, with data spanning  $\sim 0.3\text{--}24\ \mu\text{m}$  (Barnes et al. 2007; Grillmair et al. 2007; 2008; Tinetti et al. 2007; Knutson et al. 2007; 2009; 2012; Redfield et al. 2008; Charbonneau et al. 2008; Beaulieu et al. 2008; Pont et al. 2008; Désert et al. 2009; Swain et al. 2008 & 2009a; Sing et al. 2009 & 2011; Agol et al. 2010; Gibson et al. 2012; Evans et al. 2013; Birkby et al. 2013). The first complete atmospheric study via statistical analysis with a

systematic, wide parameter grid search (Madhusudhan & Seager 2009) analyzed separately spectroscopic data from 5-14  $\mu\text{m}$  (Grillmair et al. 2008), photometric data at 3.6, 4.5, 5.8, 8, 16, and 24  $\mu\text{m}$  (Charbonneau et al. 2008), and spectrophotometric data from 1.65-2.4  $\mu\text{m}$  (Swain et al. 2009a). Madhusudhan & Seager (2009) place constraints at the  $\xi^2=2$  level (where  $\xi^2$  is a proxy for the reduced  $\chi^2$  using the # of data points as  $N$ ) on HD 189733b's atmospheric mixing ratios of  $\text{H}_2\text{O}$ ,  $\text{CH}_4$ , and  $\text{CO}_2$  using the spectrophotometric data, as it includes features of all of these molecules as well as CO. Their resulting C/O ratio range for HD 189733b is between 0.5 and 1.

Subsequent analysis of all of the available infrared secondary eclipse measurements with the Bayesian optimal estimation retrieval scheme NEMESIS (Irwin et al. 2008) placed constraints on molecular abundances ratios of HD 189733b's atmosphere, resulting in a best-estimate C/O ratio between 0.45 and 1 for  $\xi^2 < 0.5$  and between 0.15 and 1 for  $\xi^2 < 2$  (Lee et al. 2012). However, these authors caution that the current secondary eclipse data are only able to constrain the thermal structure of HD 189733b at some pressure levels, and the mixing ratios of  $\text{H}_2\text{O}$  and  $\text{CO}_2$  with large uncertainties ranging between  $9\text{-}500 \times 10^{-5}$  and  $3\text{-}150 \times 10^{-5}$  for  $\xi^2 < 0.5$ , respectively, due to the model degeneracies. The most significant degeneracy they find is between temperature and  $\text{H}_2\text{O}$  abundance at 300 mbar pressure.

The  $\text{H}_2\text{O}$  abundance has the biggest influence on the overall shape of a hot Jupiter spectrum in thermochemical equilibrium. Moses et al. (2013) focuses on the  $\text{H}_2\text{O}$  mixing ratio constraint of  $\sim 1 \times 10^{-4}$  from Madhusudhan & Seager (2009) in their exploration of disequilibrium chemistry using the combined data sets mentioned above. In both equilibrium and disequilibrium scenarios, for their nominal temperature profile and at solar metallicity, a very narrow range of C/O

ratios around 0.88 provides the  $\text{H}_2\text{O}$  abundance constraint and a good fit to the observations. The recent retrieval analysis of Line et al. (2013), using the same wavelength coverage of data, also finds a best-fit C/O ratio of 0.85 ( $\chi^2_{\text{best}}/N=2.27$  fit, with a 68% confidence interval of 0.47-0.90).

A carbon-enhanced atmosphere for HD 189733b is thus theoretically plausible and consistent with observations. Interestingly, we find the host star has  $\text{C/O}=0.90\pm0.15$ , matching well the best-fit C/O ratios derived for the planet's atmosphere. HD 189733 is the only star within this sample to have  $\text{C/O}>0.8$ ; its C/O ratio spans 0.75-1.05 within  $1\sigma$  errors. Three additional stars in our sample have have  $\text{C/O}>0.8$  within  $1\sigma$  errors.

The derived  $T_{\text{eff}}$  of HD 189733 is  $\leq 5400$  K, therefore the triplet  $[\text{O/H}]_{\text{NLTE avg}}$  (0.125) is not included in the final average  $[\text{O/H}]$  reported here. Instead, the triplet  $[\text{O/H}]_{\text{LTE}}$  ( $0.01\pm0.14$ ) and  $[\text{O/H}]_{6300}$  ( $-0.02\pm0.14$ ) values are averaged. For stars as cool as HD 189733 there is evidence from studies of  $[\text{O/H}]$  in several open clusters that the canonical NLTE corrections are not appropriate –  $[\text{O/H}]_{\text{LTE}}$  increases in lower-temperature stars in the same cluster, the opposite of what is predicted (Schuler et al. 2006). If  $[\text{O/H}]_{\text{NLTE avg}}$  (0.125) is included in the average, the C/O ratio of HD 189733 is reduced to 0.82, and if  $[\text{O/H}]_{\text{NLTE avg}}$  replaces  $[\text{O/H}]_{\text{LTE}}$ , the C/O ratio of HD 189733 is reduced to 0.79. The C/O ratio is reduced to 0.69 if  $[\text{O/H}]_{\text{NLTE avg}}$  is the sole oxygen abundance indicator. Alternatively, one may apply an empirical correction to  $[\text{O/H}]_{\text{LTE}}$  based on the temperature of HD 189733 and the observed cluster  $[\text{O/H}]_{\text{LTE}}$  anomaly (Schuler et al. 2006), which amounts to  $\sim 0.14$  dex. This increases the resulting C/O ratio to 1.20.

HD 189733's  $[\text{C/H}]$  is an outlier as compared to the rest of our sample, while its  $[\text{O/H}]$  is more consistent with the rest of the sample (Figure 5.4). Both mea-



measurements have some of the largest abundance errors of all the targets in our sample. Our reported  $[C/H]=0.22\pm0.13$  for HD 189733 is in fact based on only one carbon line, 5380 Å, from the Keck/HIRES data, though we were able to measure two lines (5380 and 7111 Å) in the Subaru/HDS data, resulting in  $[C/H]=0.24\pm0.15$ . Including the 7113 Å C I line measurement from the Keck/HIRES data or the Subaru/HDS data increases the  $[C/H]$  from 0.22/0.24 to 0.34/0.33, and the reported C/O ratio to 1.16. Thus it appears that the C/O ratio of HD 189733 could be as low as  $\sim 0.75$ , but is very likely  $\gtrsim 0.80$ , as we report here.

In order to match the desired  $H_2O$  mixing ratio, the C/O ratio of the exoplanet HD 189733b's atmosphere must shift to higher values when its metallicity is increased – with an increase of  $3\times$  solar in metallicity the C/O ratio reaches  $\sim 0.96$ , compared to our derived C/O of  $0.90\pm0.15$ . Alternatively, if the metallicity is sub-solar, the required C/O ratio decreases (Moses et al. 2013). Unfortunately with present data the metallicity of HD 189733b's atmosphere is unknown. We find  $[Fe/H]=0.01\pm0.15$  in the host star, providing at least a first-order constraint on the planetary atmospheric metallicity, but not a better constraint on its C/O ratio. However, we note that based on Moses et al. (2013)'s models, a change in the exoplanet's C/O ratio from 0.5 (solar) to 0.88 results in a change in the  $CH_4$  abundance by  $\sim$ an order of magnitude, which should produce observable spectral signatures in the exoplanet's atmosphere.

#### 5.4.3.8 Future of Direct Planet-Star Comparisons

The fact that HD 189733b is one of the most-studied hot Jupiters and yet still has a C/O ratio that can be anywhere from  $\sim 0.5$ -1 indicates the difficulty and uncertainty in deriving exoplanet abundance ratios. Current limitations are due largely to the paucity of data, which gives rise to degenerate solutions for transiting planet spectroscopy (e.g., Griffith 2014). However, as observational efforts

continue to improve the quantity and quality of the measurements more precise C/O ratios will be possible. In addition, studies of transiting planets at high spectral resolution are becoming progressively refined (e.g., Snellen et al. 2010; Birkby et al. 2013; de Kok et al. 2013; Brogi et al. 2013) to the point that C/O ratio constraints are expected in the near future.

Complementary studies of younger, hotter planets are possible with spectroscopy of directly imaged planets. One such system, HR 8799, is particularly promising as it has four directly-imaged planets of similar luminosities, masses, and radii but different orbital distances and, surprisingly, maybe even different compositions (Barman et al. 2011a; Currie et al. 2011; Galicher et al. 2011; Marley et al. 2012; Skemer et al. 2012, 2013; Konopacky et al. 2013). Recent directly-imaged, moderate-resolution ( $R \sim 4000$ ) spectra from  $\sim 1.97$ - $2.38 \mu\text{m}$  of HR 8799c show absorption of CO and H<sub>2</sub>O but little to no CH<sub>4</sub> (mixing ratio  $< 10^{-5}$ ).  $\chi^2$  minimization modeling of these data finds best-fit  $\log N(\text{C})$  and  $\log N(\text{O})$  values of 8.33 and 8.51, respectively, indicating HR 8799c is depleted in both C and O with respect to solar, and resulting in a C/O ratio of  $0.65^{+0.10}_{-0.05}$  (Konopacky et al. 2013). The host star is classified as both  $\gamma$  Doradus and  $\lambda$  Bootis, making stellar abundance analysis challenging, but one previous study of the star derives C/O =  $0.56 \pm 0.21$  (Sadakane 2006). Determining the C/O ratios of the other planetary components in this system, and other multi-planet systems, may provide constraints on how the composition of the host star affects giant planet formation as a function of planet mass and orbital radius.

## 5.5 Summary

The differences between [Fe/H] distributions in hosts versus non-hosts have been the subject of study for over a decade, and a few more recent studies suggest

that refractory element distributions may differ in stars with/without planets, but differences in volatile elements have not been as thoroughly explored. Here we present a uniform stellar parameter and abundance analysis of 16 stars that host transiting hot Jupiter exoplanets. Our study also includes one binary companion that is not known to host planets. This work presents detailed measurements of transiting exoplanet host star carbon and oxygen abundances, derived using multiple indicators of oxygen abundance. The derived host star C/O ratios contribute one component to the direct comparison of stellar and exoplanetary atmospheric compositions.

We compare our results to other studies of C/O vs. [Fe/H] in exoplanet host stars, and find a similar positive slope between these two parameters. This is indicative of Galactic chemical evolution and the increasing importance of the carbon contribution from the death of low- and intermediate-mass stars at more metal-rich times in the Galaxy. A linear fit to our [C/H] versus [Fe/H] data results in a slope  $\sim$ twice that of a linear fit to our [O/H] vs. [Fe/H], with the former relation passing 0.08 dex below solar and the latter passing 0.01 above solar. We derive a linear fit of  $\text{C/O} = 0.53[\text{Fe/H}] + 0.45$  to our data, which falls 0.09 below our adopted  $\text{C/O}_{\odot} = 0.54$ , but corresponds to a 0.08 dex difference in [C/O], similar to the offsets in [C/H] and [O/H] relations. These offsets likely reflect both analysis uncertainties and the real, intrinsic scatter in Galactic disk populations.

There is agreement between the average [C/H], [O/H], and C/O values found here and the results of other studies of radial-velocity-detected planet host stars, supporting previous findings (Ammler von-Eiff et al. 2009) that elemental abundance ratios do not differ significantly between transiting and RV-planet host stars. The mean C/O ratio of the transiting exoplanet host stars in this paper is slightly lower than that found by other studies that consist of non-transiting

host stars,  $0.54 \pm 0.15$  versus  $0.71 \pm 0.07$ . This is more in line with recent suggestions that the prior studies overestimated C/O ratios.

Several cases in which the process of directly comparing the chemistry in specific stars to their planets is already beginning are highlighted – WASP-12, XO-1, TrES-2, TrES-3, HD 149026, XO-2, CoRoT-2, and HD 189733. We encourage follow-up observational and theoretical studies of all of the exoplanets whose host stars are included in this paper. Facilities that are currently available in space and on the ground can be used strategically to obtain estimates of C/O ratios of a large sample of transiting exoplanets, which JWST and several other upcoming space-based missions (e.g., EChO) will be able to better characterize. The more precise abundance analysis that is possible right now for host stars can help infer their exoplanets' formation histories, as well as inform future planet formation theories and models.

Table 5.1. Observing Log

Star	V	Date (UT)	Exposures	$T_{exp}$ (s)	Platform
CoRoT-2	12.57	2013 Aug 30	3	1500	Keck/HIRES
TrES-4	11.59	2013 Aug 30	2	1920, 900	Keck/HIRES
TrES-2	11.25	2013 Aug 30	1	1320	Keck/HIRES
WASP-2	11.98	2013 Aug 30	2	1440	Keck/HIRES
WASP-12	11.57	2012 Feb 10	3	1080 (2), 1800 (1)	Subaru/HDS
		2012 Feb 11	2	1800	Subaru/HDS
XO-2	11.25	2012 Feb 10	2	1800	Subaru/HDS
XO-2B	11.20	2012 Feb 11	2	2100	Subaru/HDS
XO-1	11.25	2012 Feb 10	2	1800	Subaru/HDS
TrES-3	12.40	2012 Feb 10	2	2400	Subaru/HDS
		2012 Feb 11	2	2100	Subaru/HDS
		2008 Jun 12	17	1200 (12), 600 (3), 420, 45	Keck/HIRES archive
HD 189733	7.68	2012 Feb 10	2	120	Subaru/HDS
		2006 Aug 21	3	208, 212, 226	Keck/HIRES archive
HD 149026	8.14	2012 Feb 11	1	480	Subaru/HDS
		2005 Jun 29	3	171,179,176	Keck/HIRES archive
HD 80606	9.00	2012 Feb 11	2	600	Subaru/HDS
HAT-P-7	10.48	2012 Feb 10	1	900	Subaru/HDS
		2012 Feb 11	2	1200	Subaru/HDS
		2007 Aug 24	1	600	Keck/HIRES archive
HAT-P-13	10.42	2012 Feb 11	1	1800	Subaru/HDS
HAT-P-1	10.4	2012 Aug 31	2	500, 630	Keck/HIRES
HAT-P-16	10.91	2012 Aug 31	2	1120, 1043	Keck/HIRES
WASP-32	11.26	2012 Aug 31	2	1500, 1800	Keck/HIRES
Moon		2012 Feb 10	2	1, 5	Subaru/HDS
Vesta		2006 Apr 16	3	216, 232, 241	Keck/HIRES archive

Table 5.2. Observing Platform Details

Platform	slit (and filter, if applicable)	$R$ ( $\frac{\lambda}{\Delta\lambda}$ )	Wavelength Coverage (Å)	S/N of combined frames (at 6300 Å)	Seeing Range
Subaru/HDS	0."6	60,000	~4450-5660; 5860-7100*	~170-230	0."84-1."12; 0."96-1."24 <sup>+</sup>
Keck/HIRES	0."86 (C1 decker) kv370+clear filters	48,000	~3360-8100	~125-150	~0.4-0.6"; ~0.6-0.8" <sup>++</sup>
Keck/HIRES archive					
HAT-P-7	same	same	same	~190	
HD 189733	same	same	same	~250	
HD 149026	same	same	same	~290	
Vesta	same	same	same	~315	
TrES-3	0."57, kv389 filter	72,000	4240-8690	~300	

\*Wavelength coverage across two separate CCDs.

<sup>+</sup>Seeing from Feb. 10; Feb. 11.

<sup>++</sup>Seeing from Aug. 31, 2012; Aug. 30, 2013

Note. — We note that the TrES-3 Keck/HIRES archive observations used a different filter and narrower slit, and thus had slightly different wavelength coverage and higher resolution, but this did not affect our ability to measure the necessary elemental absorption lines.

Table 5.3. Derived Stellar Parameters

Star	$T_{eff}$ K	$\sigma$ K	$\log g$	$\sigma$	$\xi$ $\text{km s}^{-1}$	$\sigma$ $\text{km s}^{-1}$	[Fe I/H]	$N$	$\sigma_{\mu}$	[Fe II/H]	$N$	$\sigma_{\mu}$
CoRot-2	5616	47	4.52	0.14	1.59	0.09	0.063	48	0.007	0.064	7	0.017
TrES-4	6333	44	4.04	0.17	1.74	0.09	0.320	49	0.005	0.322	9	0.025
TrES-2	5823	33	4.45	0.10	1.27	0.07	-0.016	51	0.004	-0.016	9	0.005
WASP-2	5228	60	4.49	0.21	1.07	0.10	0.092	52	0.008	0.091	9	0.021
WASP-12	6166	41	4.05	0.16	1.95	0.13	0.062	40	0.006	0.062	10	0.020
XO-2N	5343	78	4.49	0.25	1.22	0.09	0.386	49	0.011	0.389	8	0.020
XO-2S	5547	59	4.22	0.24	1.24	0.07	0.291	50	0.010	0.295	10	0.048
XO-1	5695	26	4.42	0.12	1.39	0.06	-0.109	36	0.004	-0.110	9	0.008
TrES-3	5534	42	4.56	0.14	1.20	0.10	-0.209	33	0.007	-0.206	8	0.021
HD 189733	5116	76	4.64	0.25	1.27	0.16	0.012	43	0.012	0.011	9	0.041
HD 149026	6093	48	4.30	0.21	1.71	0.09	0.265	51	0.007	0.264	9	0.024
HD 80606	5551	47	4.14	0.17	1.29	0.06	0.274	41	0.008	0.275	8	0.046
HAT-P-7	6474	71	4.33	0.29	2.72	0.37	0.140	40	0.008	0.139	10	0.033
HAT-P-13	5775	57	4.13	0.17	1.44	0.07	0.442	51	0.009	0.445	10	0.035
HAT-P-1	6045	44	4.52	0.12	1.51	0.11	0.172	53	0.006	0.174	8	0.012
HAT-P-16	6236	58	4.49	0.19	1.58	0.15	0.174	54	0.007	0.172	9	0.015
WASP-32	6042	42	4.34	0.20	1.80	0.15	-0.066	53	0.006	-0.069	9	0.023

Table 5.4. Lines Measured, Equivalent Widths, and Abundances

Ion	$\lambda$	$\chi$	$\log gf$	$\text{EW}_{\odot}$	$\log N_{\odot}$	WASP-12			HD 149026		HAT-P-1		
	(Å)	(eV)	(dex)	(mÅ)		EW (mÅ)	$\log N$		EW (mÅ)	$\log N$		EW (mÅ)	$\log N$
C I	5052.17	7.68	-1.304	33.9 <sup>a</sup> , 33.7 <sup>b</sup>	8.46 <sup>a</sup> , 8.45 <sup>b</sup>	62.4 <sup>a</sup>	8.58 <sup>a</sup>	...	...	...	...	43.9 <sup>b</sup>	8.51 <sup>b</sup>
	5380.34	7.68	-1.615	19.4 <sup>a</sup> , 20.7 <sup>b</sup>	8.44 <sup>a</sup> , 8.48 <sup>b</sup>	41.1 <sup>a</sup>	8.57 <sup>a</sup>	...	44.5 <sup>b</sup>	8.76 <sup>b</sup>	...	29.3 <sup>b</sup>	8.56 <sup>b</sup>
	6587.61	8.54	-1.021	12.9 <sup>a</sup> , 15.5 <sup>b</sup>	8.38 <sup>a</sup> , 8.48 <sup>b</sup>	27.0 <sup>a</sup>	8.4 <sup>a</sup>	...	36.4 <sup>b</sup>	8.75 <sup>b</sup>	...	20.2 <sup>b</sup>	8.46 <sup>b</sup>
	7111.47	8.64	-1.074	9.8 <sup>a</sup> , 12.2 <sup>b</sup>	8.38 <sup>a</sup> , 8.50 <sup>b</sup>	21.0 <sup>a</sup>	8.42 <sup>a</sup>	...	26.6 <sup>b</sup>	8.69 <sup>b</sup>	...	16.3 <sup>b</sup>	8.49 <sup>b</sup>
	7113.18	8.65	-0.762	22.8 <sup>a</sup> , 20.9 <sup>b</sup>	8.55 <sup>a</sup> , 8.50 <sup>b</sup>	...	...	...	47.4 <sup>b</sup>	8.79 <sup>b</sup>	...	29.2 <sup>b</sup>	8.53 <sup>b</sup>
[OI]*	6300.30	0.00	-9.717	5.4 <sup>a</sup> , 5.6 <sup>b</sup>	8.68 <sup>a</sup> , 8.67 <sup>b</sup>	7.0 <sup>a</sup>	8.82 <sup>a</sup>	...	8.2 <sup>b</sup>	8.95 <sup>b</sup>	...	4.6 <sup>b</sup>	8.62 <sup>b</sup>
O I	7771.94	9.15	0.37	69.6 <sup>b</sup>	8.83 <sup>b</sup>	...	...	...	119.8 <sup>b</sup>	9.17 <sup>b</sup>	...	89.7 <sup>b</sup>	8.88 <sup>b</sup>
O I	7774.17	9.15	0.22	62.6 <sup>b</sup>	8.86 <sup>b</sup>	...	...	...	108.6 <sup>b</sup>	9.18 <sup>b</sup>	...	...	...
O I	7775.39	9.15	0.00	46.8 <sup>b</sup>	8.81 <sup>b</sup>	...	...	...	82.0 <sup>b</sup>	9.05 <sup>b</sup>	...	61.1 <sup>b</sup>	8.83 <sup>b</sup>

<sup>a</sup>Measured in the Subaru/HDS data.

<sup>b</sup>Measured in the Keck/HIRES data.

\*For [O I], the  $\log N$  values represent those derived from synthesis fitting, as these are the values we use in calculating the final [O/H] for each object. The reported EWs refer to the total EW of the 6300.3 Å blend.

Note. — The full version of this table including all lines and targets is available online.



Table 5.5. Oxygen Abundances Derived from Different Indicators

Star	[O/H] [O I] 6300 Å	[O/H] triplet LTE	[O/H] triplet NLTE, Takeda	[O/H] triplet NLTE, Ramírez	[O/H] triplet NLTE, Fabbian
CoRoT-2*	...	0.02±0.07	0.07	0.06	0.07
TrES-4*	0.22±0.09	0.31±0.07	0.15	0.21	0.08
TrES-2*	-0.02±0.05	0.00±0.05	0.02	0.01	-0.01
WASP-2*	-0.03±0.10	-0.01±0.10	0.08	0.06	0.09
WASP-12	0.14±0.06	...	...	...	...
XO-2N	0.34±0.16	...	...	...	...
XO-2S	0.18±0.15	...	...	...	...
XO-1	-0.09±0.05	...	...	...	...
TrES-3*	-0.04±0.06	...	...	...	...
HD 189733*	-0.02±0.14	0.01±0.14	0.12	0.11	0.14
HD 149026*	0.28±0.03	0.30±0.07	0.21	0.26	0.20
HD 80606	0.20±0.08	...	...	...	...
HAT-P-7*	...	0.22±0.10	0.06	0.11	0.02
HAT-P-13	0.19±0.08	...	...	...	...
HAT-P-1*	-0.05±0.06	0.07±0.06	0.07	0.07	0.02
HAT-P-16*	-0.08±0.10	0.04±0.06	0.03	-0.01	-0.10
WASP-32*	-0.08±0.09	0.08±0.08	0.03	0.00	-0.01

\*Measurements from Keck/HIRES data.

Table 5.6. Elemental Abundances and Ratios

Star	[Fe/H]	[C/H]	[O/H] <sub>avg</sub>	[Ni/H]	C/O <sub>avg</sub>
CoRoT-2	0.06±0.08*	0.01±0.06*	0.06±0.07*	-0.08±0.03*	0.47±0.09*
TrES-4	0.32±0.09*	0.11±0.06*	0.18±0.06*	0.29±0.02*	0.46±0.08*
TrES-2	-0.02±0.05*	-0.12±0.04*	-0.01±0.04*	-0.08±0.02*	0.41±0.05*
WASP-2	0.09±0.12*	-0.01±0.09*	-0.02±0.07*	0.11±0.03*	0.55±0.11*
WASP-12	0.06±0.08	0.09±0.06	0.14±0.06	0.00±0.04	0.48±0.08
XO-2N	0.39±0.14	0.42±0.12	0.34±0.16	0.44±0.04	0.65±0.20
XO-2S	0.28±0.14	0.26±0.11	0.18±0.15	0.38±0.04	0.65±0.19
XO-1	-0.11±0.06	-0.19±0.04	-0.09±0.05	-0.11±0.02	0.43±0.07
TrES-3	-0.21±0.08	-0.31±0.06*	-0.04±0.06*	-0.25±0.04	0.29±0.09*
HD 189733	0.01±0.15	0.22±0.11*	-0.01±0.10*	0.00±0.05	0.90±0.15*
HD 149026	0.26±0.09	0.26±0.08*	0.25±0.04*	0.31±0.03	0.55±0.08*
HD 80606	0.28±0.10	0.29±0.08	0.20±0.08	0.30±0.03	0.66±0.12
HAT-P-7	0.14±0.14	-0.04±0.10*	0.07±0.10*	0.12±0.05	0.42±0.14*
HAT-P-13	0.44±0.09	0.34±0.08	0.19±0.08	0.53±0.04	0.76±0.11
HAT-P-1	0.17±0.06*	0.03±0.05*	0.00±0.04*	0.17±0.03*	0.58±0.06*
HAT-P-16	0.17±0.09*	-0.02±0.06*	-0.05±0.06*	0.13±0.04*	0.58±0.08*
WASP-32	-0.07±0.09*	-0.09±0.07*	-0.04±0.06*	-0.13±0.03*	0.47±0.09*

Note. —  $C/O = 10^{\log N(C)} / 10^{\log N(O)}$ , with  $\log N(C) = \text{derived } [C/H] + \log N_{\odot}(C)$  and  $\log N(O) = \text{derived } [O/H] + \log N_{\odot}(O)$ , where  $\log N_{\odot}(O) = 8.66$  and  $\log N_{\odot}(C) = 8.39$  (solar values from Asplund et al. 2005). The errors on the C/O ratio are represented by the quadratic sum of the errors in [C/H] and [O/H].

\*Measurements include Keck/HIRES data.

Table 5.7. Abundance Sensitivities

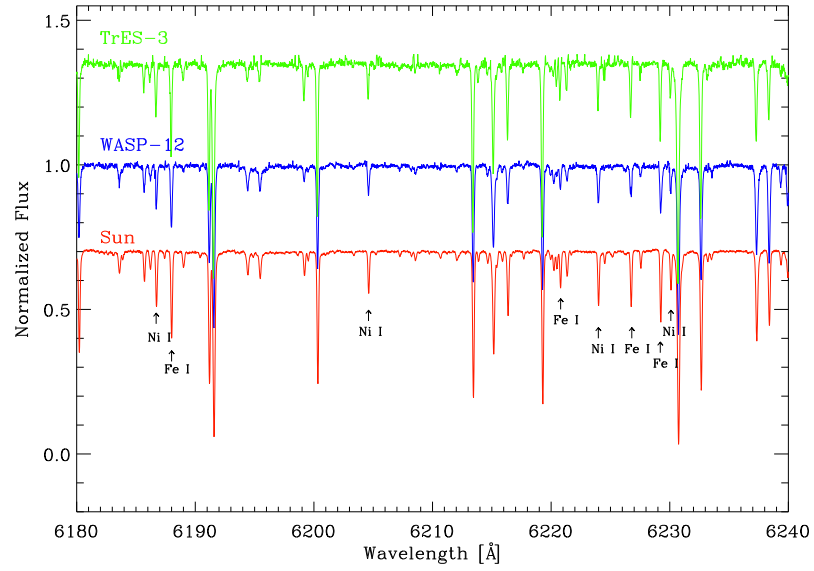
Species	WASP-12			HAT-P-1		
	$\Delta T_{eff}$	$\Delta \log g$	$\Delta \xi$	$\Delta T_{eff}$	$\Delta \log g$	$\Delta \xi$
	( $\pm 150$ K)	( $\pm 0.25$ dex)	( $\pm 0.30$ km s $^{-1}$ )	( $\pm 150$ K)	( $\pm 0.25$ dex)	( $\pm 0.30$ km s $^{-1}$ )
Fe I	$\pm 0.10$	$\pm 0.005$	$\pm 0.03$	$\pm 0.09$	$\pm 0.005$	$\pm 0.03$
Fe II	$\pm 0.02$	$\pm 0.10$	$\pm 0.08$	$\pm 0.05$	$\pm 0.10$	$\pm 0.07$
C I	$\pm 0.08$	$\pm 0.08$	$\pm 0.01$	$\pm 0.10$	$\pm 0.08$	$\pm 0.005$
[OI]*	$\pm 0.06$	$\pm 0.09$	$\pm 0.01$	$\pm 0.11$	$\pm 0.12$	$\pm 0.00$
Ni I	$\pm 0.11$	$\pm 0.02$	$\pm 0.03$	$\pm 0.10$	$\pm 0.005$	$\pm 0.04$
O I triplet (LTE)	...	...	...	$\pm 0.13$	$\pm 0.07$	$\pm 0.03$

\*For [O I], the log  $N$  values represent those derived from synthesis fitting, as these are the values we use in calculating the final [O/H] for each object.

Table 5.8. Comparison of Average C & O Measurements to Previous Work

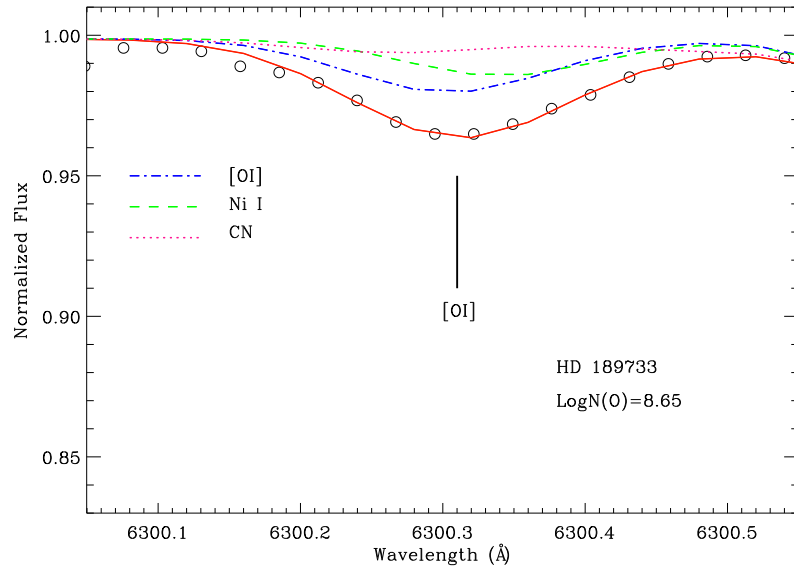
Source	$\overline{[C/H]}_{\text{hosts}}$	$\overline{[C/H]}_{\text{non-hosts}}$	$\overline{[O/H]}_{\text{hosts}}$	$\overline{[O/H]}_{\text{non-hosts}}$	$\overline{C/O}_{\text{hosts}}$	$\overline{C/O}_{\text{non-hosts}}$
Ecuvillon et al. (2004) or (2006)	$0.14 \pm 0.10$	$-0.03 \pm 0.14$	$0.12 \pm 0.11$	$0.07 \pm 0.15$	...	...
Bond et al. (2006) or (2008)	$0.17 \pm 0.11$	$0.01 \pm 0.17$	$0.00 \pm 0.17$	$-0.06 \pm 0.15$	$0.67 \pm 0.23$	$0.67 \pm 0.23$
Delgado Mena et al. (2010)	$0.10 \pm 0.16$	$-0.06 \pm 0.18$	$0.05 \pm 0.17$	$-0.08 \pm 0.17$	$0.76 \pm 0.20$	$0.71 \pm 0.18$
Petigura & Marcy (2011)	$0.17 \pm 0.14$	$0.08 \pm 0.17$	$0.11 \pm 0.12$	$0.05 \pm 0.14$	$0.76 \pm 0.22$	$0.70 \pm 0.22$
Nissen (2013)	$0.11 \pm 0.15$	...	$0.08 \pm 0.10$	...	$0.63 \pm 0.12$	...
this work ( <i>only transiting planets</i> )	$0.06 \pm 0.20$	...	$0.07 \pm 0.13$	...	$0.54 \pm 0.15$	...

Note. — Listed are the means and standard deviations in exoplanet hosts stars and “non-host” stars, for each elemental abundance ratio, given as (mean  $\pm$  standard deviation). Note that the number of objects in each source’s sample is not equal, and that different sources use different solar  $\log N(\text{C})$  and  $\log N(\text{O})$  values.



1

Figure 5.1 Sample spectra of TrES-3 (green), WASP-12 (blue), and the Sun (red) obtained with Subaru/HDS. The spectra have been continuum normalized and are shifted by constant values in flux for ease of viewing. Lines in this order for which EWs were measured are marked with arrows.



2

Figure 5.2 Shown here is the spectrum synthesis fit to the forbidden [OI] line (6300.3 Å) for HD 189733. The data are shown as black open circles. The full synthesis fit is represented by a solid red line, with components shown with blue dash-dotted ([OI]), green dashed (Ni I), and pink dotted (CN) lines.

3

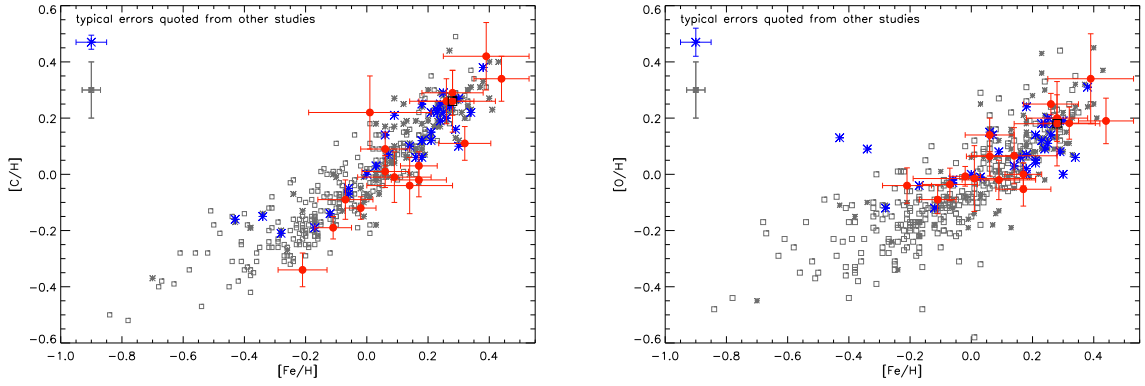


Figure 5.3  $[C/H]$  and  $[O/H]$  versus  $[Fe/H]$  from Delgado Mena et al. (2010) and Nissen (2013) [all Nissen (2013) hosts are in the Delgado Mena et al. (2010) host sample]. Non-host stars from Delgado Mena et al. (2010) are plotted with gray open squares, while host stars from Delgado Mena et al. (2010)/Nissen (2013) are plotted with gray/blue asterisks. Quoted typical error bars are in the upper left. Measurements from this work are plotted as red filled circles, with error bars included (see Table 5.6). In particular, XO-2S is plotted as a red circle enclosed by a black square, to indicate that it does not host a known planet (in the C/O plot, XO-2N overlaps XO-2S).

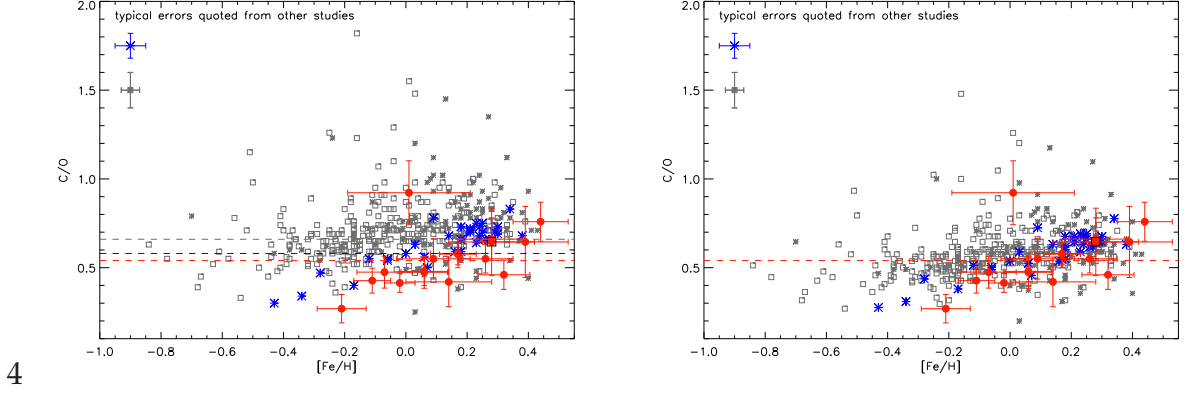


Figure 5.4  $C/O$  versus  $[Fe/H]$  from Delgado Mena et al. (2010) and Nissen (2013) [all Nissen (2013) hosts are in the Delgado Mena et al. (2010) host sample]. Colors and symbols are the same as in Figure 5.3. Left:  $C/O$  ratios as reported in respective sources, using their  $C/O_{\odot}$  (see text for discussion). Dashed lines show the  $C/O_{\odot}$  adopted by each source. Right: All  $C/O$  ratios normalized to the same  $C/O_{\odot}$  adopted in this work,  $C/O_{\odot} = 0.54$  ( $\log N(C)_{\odot} = 8.39$ ,  $\log N(O)_{\odot} = 8.66$ ; Asplund et al. 2005).

5

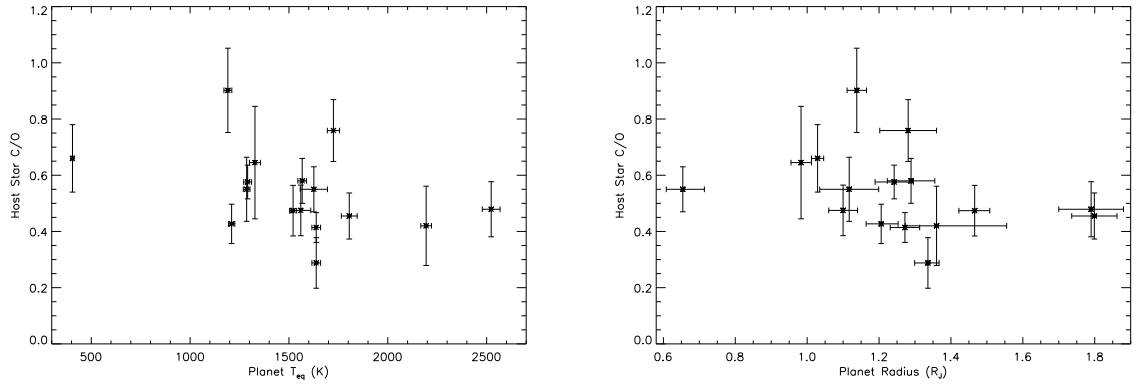


Figure 5.5 Host star  $C/O$  ratio versus planetary equilibrium temperature (left) and radius (right). The planetary parameters are from the NASA Exoplanet Archive, and the host star  $C/O$  ratios are derived in this paper.



## CHAPTER 6

CARBON AND OXYGEN ABUNDANCES IN THE HOT JUPITER EXOPLANET HOST  
STAR XO-2N AND ITS BINARY COMPANION

With the aim of connecting the compositions of stars and planets, we present the abundances of carbon and oxygen, as well as iron and nickel, for the transiting exoplanet host star XO-2N and its wide-separation binary companion XO-2S. Stellar parameters are derived from high-resolution, high-signal-to-noise spectra, and the two stars are found to be similar in their  $T_{\text{eff}}$ ,  $\log g$ , iron ( $[\text{Fe}/\text{H}]$ ), nickel ( $[\text{Ni}/\text{H}]$ ) abundances. Their carbon ( $[\text{C}/\text{H}]$ ) and oxygen ( $[\text{O}/\text{H}]$ ) abundances also overlap within errors, although XO-2N may be slightly more C-rich and O-rich than XO-2S. The C/O ratios of both stars ( $\sim 0.60 \pm 0.20$ ) may also be somewhat larger than solar ( $\text{C}/\text{O} \sim 0.50$ ). The XO-2 system has a transiting hot Jupiter orbiting one binary component but not the other, allowing us to probe the potential effects planet formation might have on the host star composition. Additionally, with multiple observations of its atmosphere the transiting exoplanet XO-2b lends itself to compositional analysis, which can be compared to the natal chemical environment established by our binary star elemental abundances. This work sets the stage for determining how similar/different exoplanet and host star compositions are, and the implications for planet formation, by discussing the C/O ratio measurements in the unique environment of a visual binary system with one star hosting a transiting hot Jupiter. A version of this chapter originally appeared as a published paper in the *Astrophysical Journal* (Teske et al. 2013c). I conducted the observations at the Subaru Telescope, and the analysis, with training from Simon Schuler and Katia Cunha. Katia Cunha performed the synthesis analysis described in this paper, and Verne Smith provided the synthesis figure.

The final text was written by me, with very helpful edits and commentary from my co-authors.

## 6.1 Introduction

Although theory and observations indicate that host-star composition affects planetary evolution, the physical processes responsible are not well understood. Until recently, investigations of the chemical connection between stars and planets were limited to measurements of the host star abundances. One of the most prominent findings is that the (solar-type) host stars of large, closely orbiting (hot Jupiter) exoplanets are more metal-rich than (solar-type) stars without detected gas giant exoplanets (e.g., Gonzalez et al. 1998; Santos et al. 2004; Fischer & Valenti 2005). However, the host star metallicity trend is weaker for Neptune-sized planets (e.g., Ghezzi et al. 2010) and has been found to *not* hold for terrestrial-sized planets (Buchhave et al. 2012), whose host stars show a wide range of metallicities.

With the discovery of transiting exoplanets, planetary atmospheres themselves can be observed, and their compositions determined. Indeed, the *Hubble Space Telescope* and *Spitzer Space Telescope* have been used to detect the most abundant molecules ( $\text{H}_2\text{O}$ ,  $\text{CO}$ ,  $\text{CH}_4$ ,  $\text{CO}_2$ ) in the atmospheres of several of the brightest transiting planets (e.g., Tinetti et al. 2007; Swain et al. 2008; D  sert et al. 2009). Measurements of both stellar and exoplanetary atmospheres combined provide valuable insight into planet formation processes. The ratio of carbon to oxygen is important to interpreting hot Jupiter exoplanet spectra because they are dominated by the main carbon- and oxygen-containing molecules and particularly sensitive to different chemistry induced by different C/O ratios. In thermochemical equilibrium, at the temperatures and pressures characteristic of gas giant at-

mospheres, a high C/O ratio causes differences in the partitioning of C and O among  $\text{H}_2\text{O}$ , CO,  $\text{CH}_4$ ,  $\text{CO}_2$  compared to that expected in solar abundance atmospheres ( $\text{C}/\text{O}_\odot = 0.55 \pm 0.10$ ; Asplund et al. 2009; Caffau et al. 2011) (Kuchner & Seager 2005; Kopparapu et al. 2012; Madhusudhan 2012). This in turn affects the composition and thermal structure, and therefore spectral signatures, of exoplanet atmospheres. Currently a number of teams are working towards establishing the C/O ratios of transiting exoplanets (e.g., Madhusudhan 2012). Observations of the host stars are needed to interpret the exoplanet observations in the context of the elemental composition of each star-planet system.

The C/O ratio of an exoplanet can also give clues as to where in the protoplanetary disk it formed (Stevenson & Lunine 1988; Öberg et al. 2011). Observations indicate that disks are inhomogeneous in physical structure and composition (e.g., Bergin 2011), but that in particular carbon and oxygen in a planet's atmosphere could be indicative of its starting orbital position and evolution (Öberg et al. 2011). Some studies suggest that a planet may also affect the elemental composition of the host star (e.g., Meléndez et al. 2009; Ramírez et al. 2009). It is important to be able to isolate these two potential effects – the effect of the planet on the star's elemental abundances, and the starting (or unperturbed) abundance of the system from which one can study a planet's origin and evolution. Studies of binary star systems, as conducted here, provide a method for decoupling these two potential effects.

Reported in this paper are the C/O<sup>1</sup> ratios of a transiting exoplanet host star and its binary companion. We describe the XO-2 binary system, which consists of the hot Jupiter host XO-2N, and its companion XO-2S, located  $\sim 4600$  AU away and not known to host a Hot Jupiter-type planet (Burke et al. 2007). The hot

---

<sup>1</sup>The C/O ratio – the ratio of carbon atom to oxygen atoms – is calculated in stellar abundance analysis as  $\text{C}/\text{O} = N_{\text{C}}/N_{\text{O}} = 10^{\log N(\text{C})} / 10^{\log N(\text{O})}$  where  $\log(N_{\text{X}}) = \log_{10}(N_{\text{X}}/N_{\text{H}}) + 12$ .

Jupiter XO-2b has an  $M \times \sin i$  of  $0.62 \pm 0.02 M_J^2$  (Narita et al. 2011), a radius of  $0.97 \pm 0.03 R_J$  (Burke et al. 2007), and orbits at  $\sim 0.04$  AU from XO-2N. The exoplanet XO-2b is one of the best characterized bodies outside the solar system, studied extensively with HST and *Spitzer* (e.g., Machalek et al. 2009; Crouzet et al. 2012). We perform a stellar abundance analysis of both binary components to investigate the potential chemical effects of exoplanet formation.

## 6.2 Observations and Data Reduction

Observations of XO-2N and XO-2S were conducted during two half-nights, February 10 and 11 2012 (UT), with the 8.2 m Subaru Telescope using the High Dispersion Spectrograph (HDS; Noguchi et al. 2002). Spectra of the Sun (as reflected moonlight) were taken the first night, and spectra of a telluric standard (HR 6618) were taken on both nights. A  $0.''6$  slit width was used, providing a resolution of  $R = \frac{\lambda}{\Delta\lambda} = 60,000$ , with two-pixel binning in the cross-dispersion direction and no binning in the dispersion direction. Across the two detectors, wavelength coverage of the spectra is  $\sim 4450 \text{ \AA} - 5660 \text{ \AA}$  and  $\sim 5860 \text{ \AA} - 7100 \text{ \AA}$ . The signal-to-noise (S/N) ratios in the combined frames ranged from  $\sim 170 - 230$ . The raw data were reduced using standard techniques within the IRAF<sup>3</sup> software package.

## 6.3 Abundance Analysis and Results

Stellar parameters ( $T_{\text{eff}}$ ,  $\log g$ , microturbulence [ $\xi$ ]) and elemental abundance ratios were derived following the procedures in Schuler et al. (2011a) and Cunha et al. (1998). We used the spectra themselves to determine the parameters by forcing zero correlation between  $[\text{Fe I}/\text{H}]$  and lower excitation potential ( $\chi$ ), and

---

<sup>2</sup> $i = 88.7 \pm 1.3^\circ$ , meaning  $\sin i$  is nearly unity

<sup>3</sup>IRAF is distributed by the National Optical Astronomy Observatory, which is operated by the Association of Universities for Research in Astronomy, Inc., under cooperative agreement with the National Science Foundation.

between  $[\text{Fe I}/\text{H}]$  and reduced equivalent width  $[\log(\text{EW}/\lambda)]$ , as well as ensuring that the  $[\text{Fe}/\text{H}]^4$  abundances derived from Fe I and Fe II lines were equal to within two significant figures. The abundances were determined using an updated version of the local thermodynamic equilibrium (LTE) spectral analysis code MOOG (Sneden 1973), with model atmospheres interpolated from the Kurucz ATLAS9 grids<sup>5</sup>. All abundances were normalized to solar values on a line-by-line basis. Abundances of Fe, Ni, and C were derived directly from equivalent width (EW) measurements of spectral lines in each target (with the “abfind” driver in MOOG). The EW measurements were performed with either the one-dimensional spectrum analysis package SPECTRE (Fitzpatrick & Sneden 1987) or the ‘splot’ task in IRAF.

Specifically, Fe lines were chosen from the Schuler et al. (2011a) line list. We measured 49 Fe I lines in XO-2N and XO-2S, and 8 and 10 Fe II lines in XO-2N and XO-2S, respectively. Lower excitation potentials and transition probabilities ( $\log gf$ ) were taken from the Vienna Atomic Line Database (VALD; Kupka et al. 1999) for Fe, C, and Ni.

Carbon abundances for XO-2N and XO-2S were derived from two C I lines at 5052 Å and 5380 Å, which have been shown to provide reliable abundances in solar-type stars (Takeda & Honda 2005). Oxygen abundances were derived from the forbidden [O I] line at  $\lambda = 6300.3$  Å, which is well-described by LTE (e.g. Takeda 2003); we used the Allende Prieto et al. (2001)  $\log gf$  value of [O I] line. Our analysis of the forbidden oxygen line used the spectrum synthesis method (with the “synth” driver in MOOG; see Figure 6.1) to account for its blending with a Ni I line and a CN line. The free parameters of the synthesis fit were

---

<sup>4</sup>We use the standard bracket notation to indicate abundances relative to solar, e.g.,  $[\text{X}/\text{H}] = \log(N_{\text{X}}) - \log(N_{\text{X}})_{\text{solar}}$

<sup>5</sup>See <http://kurucz.harvard.edu/grids.html>

the continuum normalization, wavelength shift (left/right), line broadening, and oxygen abundance; we used our measured Ni and C abundances for each star, and N scaled from solar based on the measured [Fe/H] of each star (e.g., Cunha et al. 1998). The Ni I line is composed of two isotopic components; the weighted  $\log gf$  values of the two components from Bensby et al. (2004) were used here. We note that the [O I] line in XO-2N (with planet) required more broadening to fit with the synthesis method, suggesting it has a larger  $v \sin i$  than the planet-less XO-2S.

Uncertainties in  $T_{\text{eff}}$  and  $\xi$  were calculated by forcing  $1\sigma$  correlations in the relations between [Fe I/H] and  $\chi$  and between [Fe I/H] and reduced equivalent width [ $\log(\text{EW}/\lambda)$ ], respectively. The change in  $T_{\text{eff}}$  or  $\xi$  required to cause a correlation coefficient  $r$  significant at the  $1\sigma$  level was adopted as the uncertainty in these parameters. The uncertainty in  $\log g$  was calculated differently, through an iterative process described in detail in Baubar & King (2010) and outlined in Schuler et al. (2011a).

There are two components to the uncertainties in the derived elemental abundances – one from stellar parameter errors and one from the dispersion in the abundances derived from different elemental absorption lines. To determine the uncertainty due to the stellar parameters, the sensitivity of the abundance to each parameter was calculated for changes of  $\pm 150$  K in  $T_{\text{eff}}$ ,  $\pm 0.25$  dex in  $\log g$ , and  $\pm 0.30 \text{ km s}^{-1}$  in  $\xi$ . The final uncertainty due to each parameter is then the product of this sensitivity and the corresponding parameter uncertainty (as described above). The second uncertainty component is parameterized with the uncertainty in the mean,  $\sigma_{\mu}$ <sup>6</sup>, for the abundances derived from the averaging of multiple lines. Then the total uncertainty for each abundance ( $\sigma_{\text{tot}}$ ) is the quadratic sum of the

---

<sup>6</sup> $\sigma_{\mu} = \sigma / \sqrt{N - 1}$ , where  $\sigma$  is the standard deviation of the derived abundances and  $N$  is the number of lines used to derive the abundance.

(3) individual parameter uncertainties and  $\sigma_\mu$ .

The equivalent width measurements from our analysis are shown in Table 7.2, along with the wavelength,  $\chi$ ,  $\log gf$ , EWs, and line-by-line abundances for each element for the Sun, XO-2N, and XO-2S. The final derived stellar parameters and their  $1\sigma$  uncertainties, as well as the derived [Fe/H], [C/H], [Ni/H], [O/H], and C/O ratio values and their  $1\sigma$  uncertainties, are shown in Table 7.1. The C/O ratio errors are the errors of [C/H] and [O/H] combined in quadrature. We find [C/H] =  $+0.26 \pm 0.11$  in XO-2S versus  $+0.42 \pm 0.12$  in XO-2N, and [O/H] =  $+0.18 \pm 0.15$  in XO-2S versus  $+0.34 \pm 0.16$  in XO-2N.

In addition to our results, Table 7.1 lists stellar parameters and [Fe/H] of Ammler-von Eiff et al. (2009) and Torres et al. (2012), two studies comparable to this one in their analysis methods and sample. Also listed are results from the exoplanet discovery paper, Burke et al. (2007). Instead of the MOOG+Kurucz models as implemented here, Burke et al. (2007) used the Spectroscopy Made Easy (SME) code (Valenti & Piskunov 1996), which has been demonstrated to be biased by correlations between  $T_{\text{eff}}$ , [Fe/H], and  $\log g$  as compared to a MOOG analysis (Torres et al. 2012). Their results are shown because Ammler-von Eiff et al. (2009) and Torres et al. (2012) do not include XO-2S. Our results for XO-2S differ slightly from those of Burke et al. 2007 (based on SME analysis), but our results for XO-2N are more consistent with those of Burke et al. 2007, and the same within errors as Ammler-von Eiff et al. (2009) and Torres et al. (2012), who found similarly large  $T_{\text{eff}}$  error for XO-2N.

## 6.4 Discussion

XO-2 stands out among transiting exoplanet systems because its host star, XO-2N, is in a wide binary. XO-2S, without a large, close-in planet, can be studied

to determine the composition of the unperturbed environment in which these stars and planet(s) formed. We find that XO-2S and XO-2N are similar in their physical properties (with XO-2S being slightly more massive based on  $T_{\text{eff}}$  and  $\log g$ ), as well as  $[\text{Fe}/\text{H}]$  and  $[\text{Ni}/\text{H}]$ . The errors in  $[\text{C}/\text{H}]$  and  $[\text{O}/\text{H}]$  (both relative to solar) allow for larger differences in the stars' respective carbon and oxygen abundances (see Table 7.1), though within errors they also overlap. Schuler et al. (2011b) conducted a similar analysis (though did not measure O) for another roughly-equal-mass binary with one component hosting a giant planet, 16 Cyg A and B, and found the two stars to be chemically homogeneous (aside from Li and B, attributed to different internal mixing efficiencies). Our results for the XO-2 transiting planet system also indicate that the stars are chemically alike – here we additionally determine the binary stars' C/O ratios and find both to have  $\text{C}/\text{O} \sim 0.60$ .

It is currently unclear whether and how planets affect the composition of the host star (e.g., Meléndez et al. 2009; Ramírez et al. 2009; Chambers 2010; González Hernández et al. 2010; Schuler et al. 2011a & 2011b). Several studies posit that stars with smaller planets are depleted in rock-forming (refractory, e.g. Mg, Si, Ni, Al) elements relative to volatile elements (e.g., C, N, O) due to rock-forming material being “locked up” in the terrestrial planets (e.g., Meléndez et al. 2009; Ramírez et al. 2009). The Sun has been shown to be deficient (by  $\sim 20\%$ ) in refractory elements that have  $T_c \gtrsim 900$  K relative to volatile elements compared to similar stars without detected planets (e.g., Meléndez et al. 2009; Ramírez et al. 2009). However, the details of how an individual star's atmosphere is affected by the local or global composition of the disk during its evolution are uncertain. Also, we do not know whether some or even most stars hosting detected hot Jupiters actually also have small planets that might cause such a signature. The



significance of our detection in both XO-2N and XO-2S of enhanced  $[\text{Fe}/\text{H}]$  and  $[\text{Ni}/\text{H}]$ , the only two refractory abundances measured here, will be better understood when compared to a larger number of refractory elements measured in this system and the abundance trends with  $T_c$  expected based on galactic chemical evolution.

No previous study of which we are aware has uniformly derived  $[\text{C}/\text{H}]$ ,  $[\text{O}/\text{H}]$ , and  $\text{C}/\text{O}$  values for this binary system. Several studies have examined  $\text{C}/\text{O}$  ratios in non-transiting exoplanet host stars versus stars without known exoplanets. [It should be noted that any star designated as a “non-host” has the potential to harbor a smaller (undetected) planet; indeed, it may be the case that most stars have one or more small planets (e.g., Cassan et al. 2012).] Delgado Mena et al. (2010) measured carbon (using high excitation C I lines) and oxygen (using the forbidden  $[\text{OI}]$  6300 Å line) in 100 giant planet host stars from the HARPS planet-search sample, along with 270 non-host stars. They found averaged host-star values of  $[\text{C}/\text{H}] = +0.10 \pm 0.16$ ,  $[\text{O}/\text{H}] = +0.05 \pm 0.17$ , and  $\text{C}/\text{O} = 0.76 \pm 0.20$ , with corresponding “single” star (no known planets) averages of  $[\text{C}/\text{H}] = -0.06 \pm 0.18$ ,  $[\text{O}/\text{H}] = -0.08 \pm 0.17$ , and  $\text{C}/\text{O} = 0.71 \pm 0.18$ . Similar averages, overlapping within  $1\sigma$  errors, were compiled by Bond et al. (2010) and measured by Petigura & Marcy (2011). These studies show no significant difference in  $[\text{C}/\text{H}]$ ,  $[\text{O}/\text{H}]$ , or  $\text{C}/\text{O}$  between stars with/without detected (non-transiting) exoplanets.

Fortney (2012) suggested the  $\text{C}/\text{O}$  ratios of both host- and non-host stars in these studies were overestimated due to errors in the derived  $\text{C}/\text{O}$  ratios and the observed frequency of carbon dwarf stars in large samples of low-mass stars. More recently, Nissen (2013) determined  $\text{C}/\text{O}$  for 33 host stars from the Delgado Mena et al. (2010) sample that had additional ESO 2.2m FEROS spectra covering the O I triplet at 7774 Å (unavailable in our data). Accounting for non-LTE effects

on the [OI] triplet, Nissen (2013) found differences in derived [O/H] as compared to Delgado Mena et al. (2010), resulting in a tighter correlation between [Fe/H] and the C/O ratios derived by Nissen ( $C/O = 0.58 + 0.48[Fe/H]$  with an rms dispersion  $\sigma(C/O) = 0.06$ ). However, the averaged host-star values of Nissen, (2013) overlap those of Delgado Mena et al. (2010) and the other studies listed above ( $[C/H] = +0.11 \pm 0.15$ ,  $[O/H] = +0.08 \pm 0.10$ , and  $C/O = 0.63 \pm 0.12$ ).

The [C/H] values derived here for XO-2S ( $+0.26 \pm 0.11$ ) and XO-2N ( $+0.42 \pm 0.12$ ) are both larger than the averages above, and greater than solar. These stars are also enhanced in [O/H] (see Table 2) and have C/O ratios of 0.60. This is the first measurement of the C/O ratio in a transiting exoplanet host star that is metal-rich. Since XO-2N and XO-2S are physically associated, the elevated [C/H] and [O/H] values in *both* stars are strong evidence that their parent molecular cloud was elevated in both carbon and oxygen. As shown in Figure 7.2, XO-2S and XO-2N follow the broad galactic chemical evolution trends in [C/H], [O/H], and C/O versus [Fe/H] as evidenced by the large sample of Delgado Mena et al. (2010) (and also Nissen 2013). The significance of the C/O ratio derived here is supported by the careful analysis and the fact that we measured this ratio in two separate stars within the same system.

The C/O ratio of a planet does not necessarily reflect the protoplanetary-disk-averaged C/O ratio, and depends on where formation occurs, how much of the atmosphere is accreted from gas versus solids, and how isolated the atmosphere is from the core (Öberg et al. 2011). Carbon-enhanced systems may actually have more solid mass in the inner disk than solar-composition environments, due to a wide zone of C-bearing solids close to the star and a paucity of water ice farther out in the disk (Bond et al. 2010). If planets do form more readily in C-rich environments, this might help explain why there is a giant planet around XO-2N

( $[C/H]=+0.42\pm0.12$ ) and not XO-2S ( $[C/H]=+0.26\pm0.11$ ). However, within uncertainties, the two stars' carbon and oxygen abundances overlap. Furthermore, Delgado Mena et al. (2010) suggest that, based on a lack of trends between C/O ratios and planetary period, semi-major axis, and mass, any effects of an alternative mass distribution due to C-rich material is quickly erased. Thus the key to understanding why XO-2N has a planet and XO-2S does not may lie in the exoplanet composition.

## 6.5 Conclusions

We present an abundance analysis for the transiting exoplanet host star XO-2N and its wide-separation binary companion XO-2S. The two stars are found to be similar in their physical and chemical properties, and both enhanced above solar in carbon and oxygen, with  $C/O\sim0.6$ . Insight into why XO-2N hosts a transiting hot Jupiter, and XO-2S does not, may be revealed by the atmospheric composition and C/O ratio of the planet, which is currently being constrained with observations recorded during the its primary/secondary eclipse (e.g., Machalek et al. 2009; Crouzet et al. 2012). While previous work suggests that refractory element distributions may differ in stars with/without planets, differences in volatile elements have not been as thoroughly explored. Our results motivate further studies of planet formation and evolution with a renewed focus on volatile element distributions (particularly C and O) in both gas giant and terrestrial planets. Additional measurements of binary host star compositions will connect exoplanets and their stars and expand upon the giant planet-metallicity trend to investigate how host star chemical composition (especially C/O) influences planet formation and composition.

Table 6.1. Lines Measured, Equivalent Widths, and Abundances

Ion	$\lambda$	$\chi$	$\log gf$	$EW_{\odot}$	$\log N_{\odot}$	XO-2S		XO-2N	
						EW (mÅ)	$\log N$	EW (Å)	$\log N$
C I	5052.17	7.68	-1.304	27.1	8.31	36.4	8.61	33.0	8.77
	5380.34	7.68	-1.615	18.6	8.41	22.4	8.62	20.5	8.79
O I	6300.30	0.00	-9.717	5.4	8.63	10.7	8.81	11.5	8.97

Note. — This table is available in its entirety in a machine-readable form in the online journal. A portion is shown here for guidance regarding its form and content.

Table 6.2. Derived Stellar Parameters

Parameter <sup>a</sup>	XO-2S		XO-2N			
	this work	Burke et al. 2007	this work	Burke et al. 2007	Ammler-von Eiff et al. 2009	Torres et al. 2012
$T_{\text{eff}}$ (K)	5547±59	5500±32	5343±78	5340±32	5350±72	5450±75
$\log g$ (cgs)	4.22 ±0.24	4.62±0.05	4.49±0.25	4.48±0.05	4.14 ±0.22	4.45 ±0.02
$\xi$ (km s <sup>-1</sup> )	1.24±0.07	...	1.22±0.09	...	1.10±0.08	...
[Fe/H]	0.28±0.14	0.47±0.02	0.39±0.14	0.45±0.02	0.42 ±0.07	0.27±0.11
[C/H]	0.26±0.11	...	0.42±0.12	...	...	...
[Ni/H]	0.38±0.04	0.52±0.02	0.44±0.04	0.50±0.02	...	...
[O/H]	0.18±0.15	...	0.34±0.16	...	...	...
C/O	0.60±0.19	...	0.60±0.20	...	...	...

<sup>a</sup>Adopted solar parameters:  $T_{\text{eff}} = 5777$  K,  $\log g = 4.44$ , and  $\xi = 1.38$  km s<sup>-1</sup>.

Note. — In this table the data listed as Torres et al. 2012 is only that derived from their MOOG-style analysis.

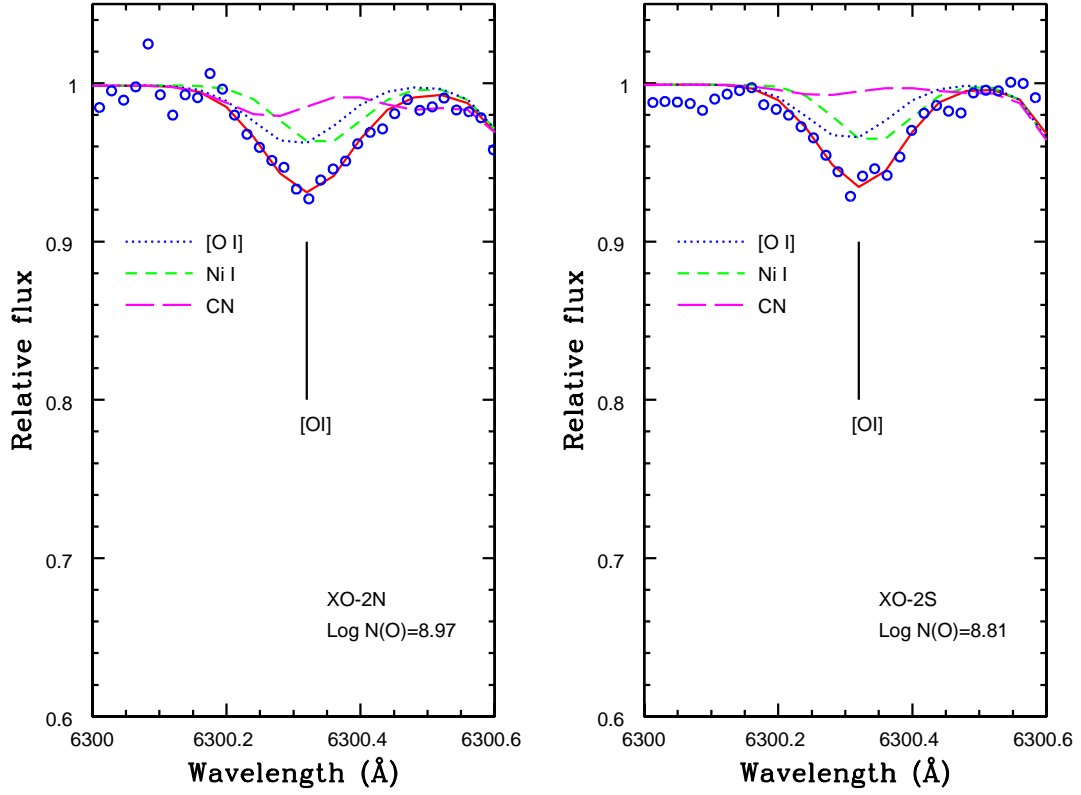


Figure 6.1 Shown are the spectrum synthesis fits to the forbidden [OI] line (6300.3 Å) for XO-2N (left) and XO-2S (right). The data are shown as blue open circles. The full synthesis fit is shown with a solid red line, with components shown with blue dotted ([O I]), green short-dashed (Ni I), and magenta long-dashed (CN) lines. Recall  $\log(N_X) = \log_{10}(N_X/N_H) + 12$ .

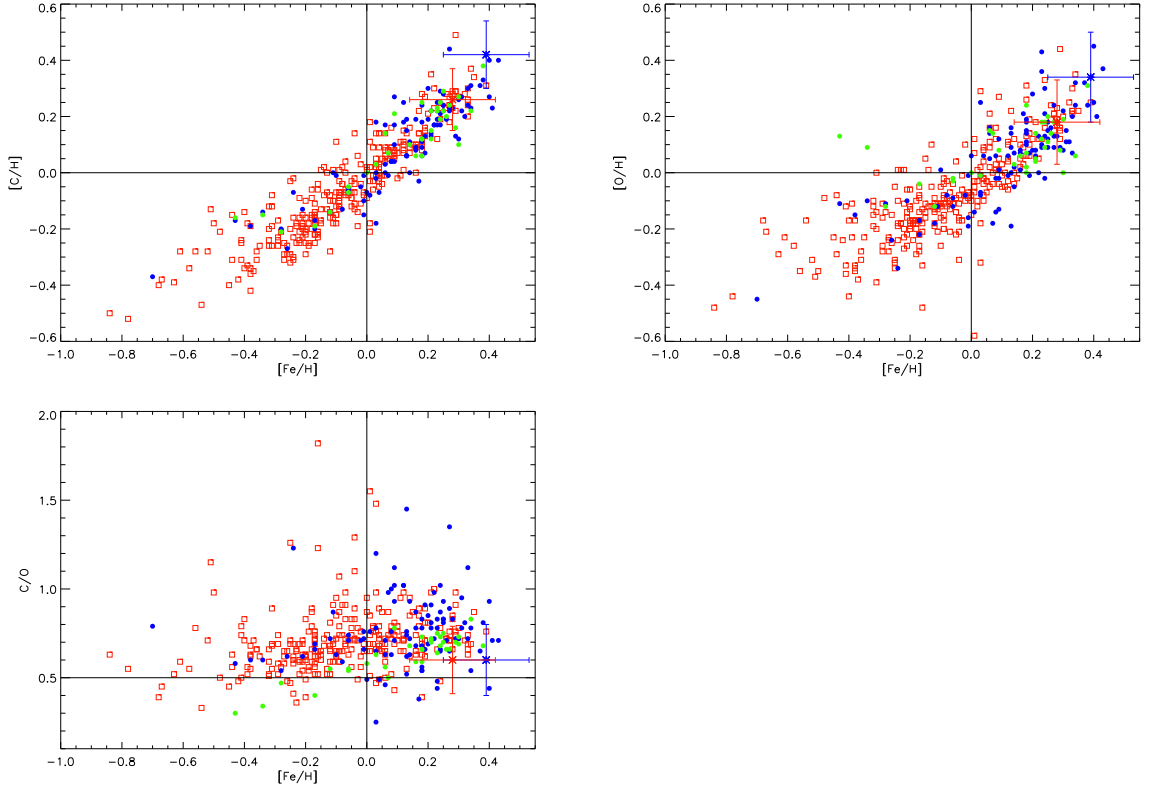


Figure 6.2  $[C/H]$ ,  $[O/H]$ , and  $C/O$  versus  $[Fe/H]$  from Delgado Mena et al. (2010) and Nissen (2013) [all Nissen (2013) hosts are in the Delgado Mena et al. (2010) host sample]. Non-host stars from Delgado Mena et al. (2010) are plotted with red open squares, while host stars from Delgado Mena et al. (2010)/Nissen (2013) are plotted with blue/green circles. Measurements of XO-2N (blue) and XO-2S (red) from this work are plotted as asterisks, with error bars included (see Table 7.1). Black solid lines show the solar values.

## CHAPTER 7

CARBON AND OXYGEN ABUNDANCES IN COOL METAL-RICH EXOPLANET  
HOSTS: A CASE STUDY OF THE C/O RATIO OF 55 CANCRI

The super-Earth exoplanet 55 Cnc e, the smallest member of a five-planet system, has recently been observed to transit its host star. The radius estimates from transit observations, coupled with spectroscopic determinations of mass, provide constraints on its interior composition. The composition of exoplanetary interiors and atmospheres are particularly sensitive to elemental C/O ratio, which to first order can be estimated from the host stars. Results from a recent spectroscopic study analyzing the 6300 Å [O I] line and two C I lines suggest that 55 Cnc has a carbon-rich composition ( $C/O=1.12\pm0.09$ ). However oxygen abundances derived using the 6300 Å [O I] line are highly sensitive to a Ni I blend, particularly in metal-rich stars such as 55 Cnc ( $[Fe/H]=0.34\pm0.18$ ). Here, we further investigate 55 Cnc's composition by deriving the carbon and oxygen abundances from these and additional C and O absorption features. We find that the measured C/O ratio depends on the oxygen lines used. The C/O ratio that we derive based on the 6300 Å [O I] line alone is consistent with the previous value. Yet, our investigation of additional abundance indicators results in a mean C/O ratio of  $0.78\pm0.08$ . The lower C/O ratio of 55 Cnc determined here may place this system at the sensitive boundary between protoplanetary disk compositions giving rise to planets with high ( $>0.8$ ) versus low ( $<0.8$ ) C/O ratios. This study illustrates the caution that must be applied when determining planet host star C/O ratios, particularly in cool, metal-rich stars. A version of this chapter originally appeared as a published paper in the *Astrophysical Journal* (Teske et al. 2013b). I reduced and analyzed the Keck/HIRES archive observations of 55 Cnc, and performed all of

the synthesis analyses myself. I wrote the final text of the paper, with much help in editing from my co-authors.

## 7.1 Introduction

Exoplanet observational surveys reveal a large and diverse population of planets with masses between a few and  $\sim 20$  Earth masses, approaching the size of Solar System terrestrial planets (Lovis et al. 2009; Sumi et al. 2010; Borucki et al. 2011). A member of the five-planet system orbiting a nearby ( $\sim 12.3$  pc) G8V star every 18 hours, 55 Cnc e (e.g., McArthur et al. 2004; Winn et al. 2011) belongs to the small sample of confirmed terrestrial-sized planets that transit their host stars. Observations of 55 Cnc e have provided a well-constrained mass ( $8.37 \pm 0.38 M_{\oplus}$ ; Endl et al. 2012) and radius (e.g.,  $1.990^{+0.084}_{-0.080} R_{\oplus}$  in the visible; Dragomir et al. 2013), yielding the density of the super-Earth exoplanet ( $5.86^{+0.79}_{-0.76} \text{ g cm}^{-3}$ ), which can then be used to constrain its interior composition.

The observed mass and radius of 55 Cnc e place it between the high-density “super-Mercuries”, like CoRoT-7b and Kepler-10b, and the volatile-rich small planets, like Kepler-11b and GJ 1214b. It intersects the threshold mass and radius between interior compositions that necessarily require volatiles and ones that may be rocky (see, for example, Gillon et al. 2012, Figure 5). Hence a massive water envelope ( $\simeq 10\%$ ), which would be super-critical given 55 Cnc e’s irradiation, over an Earth-like interior (33% iron core above 67% silicate mantle with 10% iron by mol), has been suggested to explain the observed mass and radius (Winn et al. 2011; Demory et al. 2011; Gillon et al. 2012).

Recently Madhusudhan et al. (2012) suggest an alternative and carbon-rich composition of 55 Cnc e, garnering the super-Earth popular attention as “the diamond planet.” Measurements of the carbon and oxygen abundances from



two C I lines (5052 Å, 5135 Å) and one forbidden [O I] line (6300 Å) indicate a C/O<sup>1</sup> ratio of  $1.12 \pm 0.19$  (Delgado Mena et al. 2010), i.e., a highly carbon-rich star compared to the solar C/O $\sim 0.50$  (Asplund et al. 2005). If the disk shared the host star's composition, and the host star is carbon-rich, then the planetesimals accreted during the formation of 55 Cnc e were likely Fe- and C-rich (Bond et al. 2010; Madhusudhan et al. 2012). To investigate the composition of the possibly carbon-rich exoplanet, Madhusudhan et al. (2012) consider two families of carbon-rich interior models of 55 Cnc e, consisting of layers, from inner to outer, of Fe-SiC-C and Fe-MgSiO<sub>3</sub>-C. Included in their carbon equation of state (EOS) are the graphite EOS at low pressures, the phase transition to diamond between 10 GPa < P < 1000 GPa, and the Thomas-Fermi-Dirac EOS at high pressures. Madhusudhan et al. (2012) find a wide range of compositions are possible, including extreme combinations like (Fe, SiC, C) = (33%, 0%, 67%), and the best match to 55 Cnc e's observations depends on the adopted radius measurement, and the conditions in the protoplanetary disk, e.g. temperature, at which the building blocks of the planet condense.

The exact composition of 55 Cnc e depends on the primary source of accreted planetesimals, the ratio of gas to solid material accreted, and how isolated the atmosphere was from the interior (e.g., Öberg et al. 2011; Bond et al. 2010). While the C/O ratios of protoplanetary disks likely change with time and distance (Öberg et al. 2011), the assumption that the disk bears roughly the same composition of the host star is a reasonable first-order one for estimating refractory condensates forming rocky planets (Bond et al. 2010; Carter-Bond et al. 2012; Johnson et al. 2012). Thus constraining the elemental abundances of the host star

---

<sup>1</sup>The C/O ratio – the ratio of the number of carbon atoms to oxygen atoms – is calculated in stellar abundance analysis as  $C/O = N_C/N_O = 10^{\log N(C)} / 10^{\log N(O)}$  where  $\log(N_X) = \log_{10}(N_X/N_H) + 12$ .

is a crucial step in determining the composition of 55 Cnc e.

Yet determinations of the stellar C/O ratios can be challenging. The 6300 Å forbidden oxygen line is chosen in many studies, including the previous study of 55 Cnc, because of it has been shown to give reliable abundances in LTE analyses (e.g., Schuler et al. 2011; Cuhna et al. 1998). However, this line is weak and blended with a Ni I line, the treatment of which significantly affects the derived oxygen abundance, particularly at high metallicities. Here we further investigate the C/O ratio of 55 Cnc by determining the nickel abundance from the data and reanalyzing the original line used to study its oxygen content, as well as the same two C I lines. We also determine the oxygen abundance from an additional forbidden [O I] line at 6363 Å and the O I triplet at 7774 Å, and the carbon abundance from two molecular C<sub>2</sub> features. This work aims to determine whether the stellar abundance indicates a diamond-rich composition of 55 Cnc, and to explore the difficulties in deriving the C/O ratios in cool high-metallicity stars.

## 7.2 Observations and Abundance Analysis

### 7.2.1 Data

We analyze Keck/HIRES (Vogt et al. 1994) archive spectra of 55 Cnc (PID H32bH; PI Shkolnik) taken across four nights in January 2006, covering the wavelength range 3360-8100 Å with the kv370 filter. Individual frame exposure times range from 20 to 120 sec and S/N ratios range from  $\sim 170$  to 350 around the 6300 Å [O I] line; the 35 spectra combined yield a S/N of  $\sim 1270$  around the 6300 Å [O I] line. To enable differential abundance determinations relative to the Sun, we also analyze three solar spectra of reflected light from Vesta (PID N014Hr; PI Marcy). These data were taken in April 2006 with the same filter, and with individual frame exposure times  $\sim 230$  sec; combined the spectra yield a S/N ratio  $\sim 315$ .

around the 6300 Å [O I] line. All archive HIRES data were reduced with the MAKEE pipeline<sup>2</sup> using corresponding bias ( $\sim 3$ ), flat ( $\sim 30$ ), ThAr (arc), and trace star frames for each target frame separately. The frames were then combined in IRAF<sup>3</sup>.

### 7.2.2 Stellar Parameters

The stellar parameters ( $T_{\text{eff}}$ ,  $\log g$ , microturbulence [ $\xi$ ]) and metallicity ([Fe/H]<sup>4</sup>) for 55 Cnc were derived following the procedures in Schuler et al. (2011) and Teske et al. (2013). We measured equivalent widths (EWs) of 55 Fe I lines and 9 Fe II lines in 55 Cnc and the Sun (with the one-dimensional spectrum analysis package SPECTRE; Fitzpatrick & Sneden 1987). We fit Gaussian profiles to each absorption line (some weaker lines were fit with a Simpson's Rule integration).

The abundances were determined using an updated version of the LTE spectral analysis code MOOG (Sneden 1973), with model atmospheres interpolated from the Kurucz ATLAS9 grids<sup>5</sup>. To fulfill the requirement of excitation equilibrium, the [Fe/H] values derived from the Fe I lines must not show any correlation with the lower level excitation potential ( $\chi$ ); this was used to determine  $T_{\text{eff}}$ . In addition, the  $\xi$  was determined by requiring [Fe/H] values derived from the Fe I lines to show no correlation with the measured EW values (specifically the reduced equivalent width,  $\log(\text{EW}/\lambda)$ ). Also, the averaged [Fe/H] values derived from the Fe I and Fe II lines must be equal – the requirement of ionization equilibrium; this sets the surface gravity ( $\log g$ ).

Initial values of  $T_{\text{eff}}$ ,  $\log g$ , microturbulence ( $\xi$ ), and [Fe/H] of 55 Cnc from the

---

<sup>2</sup>[www.astro.caltech.edu/~tb/makee/](http://www.astro.caltech.edu/~tb/makee/)

<sup>3</sup>IRAF is distributed by the National Optical Astronomy Observatory, which is operated by the Association of Universities for Research in Astronomy (AURA) under cooperative agreement with the National Science Foundation.

<sup>4</sup> $[X/H] = \log(N_X) - \log(N_X)_{\text{solar}}$

<sup>5</sup>See <http://kurucz.harvard.edu/grids.html>

literature were taken as starting values in the iterative process of determining 55 Cnc's stellar parameters. Prior to this iterative scheme, we ensured that there was no correlation between  $\chi$  and the reduced EWs of the Fe I lines analyzed; unique solutions for  $T_{\text{eff}}$  and  $\xi$  are only possible if there is no such correlation. The measured reduced EWs were used to determine abundances (using the "abfind" task in MOOG), and the stellar parameters were altered and new [Fe/H] abundances determined until the criteria above were met. The  $\log N(\text{Fe})$  values from each line were normalized to solar values on a line-by-line basis. The  $\log N(\text{Fe})$  value for the Sun was determined with our solar spectrum and a solar Kurucz model with  $T_{\text{eff}}=5777$ ,  $\log g=4.44$ , [Fe/H]=0.00, and  $\xi=1.38$ .

#### 7.2.2.1 Uncertainties in $T_{\text{eff}}$ , $\log g$ , and $\xi$

The errors in  $T_{\text{eff}}$  and  $\xi$  were calculated by forcing  $1\sigma$  correlations in the relations between [Fe I/H] and  $\chi$ , and between [Fe I/H] and reduced EW, respectively. The change in  $T_{\text{eff}}$  or  $\xi$  required to cause a correlation coefficient  $r$  significant at the  $1\sigma$  level was adopted as the uncertainty in these parameters. The uncertainty in  $\log g$  was calculated differently, through an iterative process described in detail in Baubar & King (2010). The difference between the Fe I and Fe II abundances is dependent on the  $\log g$  value, so the uncertainty in  $\log g$  is tied to the uncertainties in both [Fe I/H] and [Fe II/H]. To calculate the uncertainty in  $\log g$ , its value is perturbed until the difference between [Fe I/H] and [Fe II/H] is equal to the combined uncertainty in [Fe I/H] and [Fe II/H]. Uncertainties in [Fe I/H] and [Fe II/H] are calculated from the quadratic sum of the individual uncertainties in these abundances due to the derived uncertainties in  $T_{\text{eff}}$  and  $\xi$  as well as the uncertainty in the mean ( $\sigma_{\mu}$ <sup>6</sup>) of each abundance (see §2.3.3). The same procedure

---

<sup>6</sup> $\sigma_{\mu} = \sigma / \sqrt{N - 1}$ , where  $\sigma$  is the standard deviation of the derived abundances and  $N$  is the number of lines used to derive the abundance.

is then repeated, including the first iteration's  $\log g$  uncertainty (the  $\delta \log g$ ) in the calculation of the Fe abundance uncertainties. The final  $\log g$  uncertainty is then the difference between the  $\log g$  value originally derived and that obtained from this second iteration of the error calculation.

Table 7.1 lists the final derived stellar parameters and  $1\sigma$  uncertainties, as well as several literature values for comparison. The errors derived here are larger than those from previous studies, in which 55 Cnc was part of a large ensemble of stars analyzed. We note, however, that using the same stellar parameter analysis and error calculation method on stars with temperatures closer to the Sun than 55 Cnc, we obtain errors on  $T_{\text{eff}}$ ,  $\log g$ , and  $\xi$  that are more similar to typical error values quoted in the literature. Larger errors for cooler stars are also found by Teske et al. (2013), Ammler-von Eiff et al. (2009), and Torres et al. (2012), studies that determine stellar parameters and errors with methods similar to those used in this work. Our conservative stellar parameter errors for 55 Cnc also propagate through the abundance errors, as discussed in §2.3.3.

### 7.2.3 Stellar Abundances

Abundances of iron and nickel ( $[\text{Fe}/\text{H}]$ ,  $[\text{Ni}/\text{H}]$ ) were normalized to solar values on a line-by-line basis, derived directly from EW measurements of spectral lines in 55 Cnc and the Sun with the “abfind” driver in MOOG. Lines lists for Fe and Ni are from Schuler et al. (2011), and lower level excitation potentials ( $\chi$ ) and transition probabilities ( $\log gf$ ) are taken from the Vienna Atomic Line Database (VALD; Kupka et al. 1999), although we note that the  $\log gf$  values do not have a impact on the final abundances due to our strictly differential analysis. The EW measurements (and results of our synthesis analysis, described below) are shown in Table 7.2, along with the wavelength,  $\chi$ ,  $\log gf$ , EWs, and line-by-line abundances for each element for the Sun and 55 Cnc.

### 7.2.3.1 Carbon Abundance

The carbon abundance for 55 Cnc was derived from two C I lines at 5052 Å and 5380 Å and two C<sub>2</sub> molecular features at 5086.3 Å and 5135.6 Å. The two C I lines have been shown to provide reliable abundances in solar-type stars, with negligible NLTE corrections ( $\leq 0.05$  dex; Asplund et al. 2005; Takeda & Honda 2005; Caffau et al. 2010). We derived [C/H] from these lines with our EW measurements, with atomic parameters from Hibbert et al. (1993) (see Table 7.2). The  $\log N(\text{C})_{\odot}$  values we derive with our EW measurements are a good match, with  $\leq 0.02$  dex difference, to the  $\log N(\text{C})_{\odot}$  values derived by Caffau et al. (2010) from these lines using 3D hydrodynamical simulations of the Sun.

The C<sub>2</sub> lines are blends of multiple components of the Swan system, requiring spectral synthesis (matching a set of trial synthetic spectra to the observed spectrum) for abundance derivation. We used the line lists of Schuler et al. (2011) and C<sub>2</sub> molecular data from Lambert & Ries (1981), modified in that paper from theoretical values to fit the Kurucz solar flux atlas assuming a solar abundance of  $\log N(\text{C})_{\odot} = 8.39$  (Asplund et al. 2005). A dissociation energy of 6.297 eV was assumed for C<sub>2</sub> (Urdahl et al. 1991). The synthesized spectra were convolved with a Gaussian profile, based on near-by unblended lines, to represent the instrument PSF, stellar macroturbulence, and rotational broadening; the remaining free parameters were continuum normalization, line broadening, wavelength shift, and carbon abundance. The best fits to the synthesized spectra for the C<sub>2</sub> lines were determined by minimizing the deviations between the observed and synthetic spectra.

As evidenced in Table 7.3, the [C/H] abundance derived from the C I is slightly lower than that derived from the C<sub>2</sub> lines; this is also observed by Asplund et al. (2005) in both 3D hydrodynamical and 1D models of the solar atmosphere.

However, our  $[\text{C}/\text{H}]_{\text{CI}}$  value overlaps with the  $[\text{C}/\text{H}]_{\text{C}_2}$  value within errors.

### 7.2.3.2 Oxygen Abundance

Oxygen abundances were derived from three separate indicators and are listed in Table 7.3. The forbidden  $[\text{O I}]$  line at 6300.3 Å is well-described by LTE (e.g. Takeda 2003). This line is blended with a Ni I line (2 isotopic components) with a strength  $\sim 55\%$  of the  $[\text{O I}]$  line in the Sun (Caffau et al. 2008), requiring spectral synthesis similar to the  $\text{C}_2$  lines. Due to  $[\text{Ni}/\text{Fe}]$  increasing with  $[\text{Fe}/\text{H}]$  (Bensby et al. 2005), the Ni I blend becomes more important at higher metallicities, the regime in which most high-C/O values for exoplanet host stars have been found (Nissen 2013). When determining the oxygen abundance, we used the nickel abundance measured directly from our 55 Cnc spectrum,  $\log N(\text{Ni}) = 6.68$  derived from 14 lines, with  $\log gf(^{60}\text{Ni}) = -2.695$  and  $\log gf(^{58}\text{Ni}) = -2.275$  (Bensby et al. 2004). For the 6300.3 Å line we adopted the Storey & Zeippen (2000)  $\log gf = -9.717$  value, based on their forbidden transition probability calculations including both relativistically-corrected magnetic dipole and electric quadrupole contributions.

The  $[\text{O I}]$  6363.79 Å forbidden line ( $\log gf = -10.185$ , Storey & Zeippen 2000) is weaker than the 6300 Å line, and is also blended with CN lines (6363.776 Å and 6363.846 Å; Asplund et al. 2004). We again determined  $[\text{O}/\text{H}]$  from this line using spectral synthesis, with a line list compiled mostly from Kurucz<sup>7</sup> and supplemented with lines from Asplund et al. (2004). For this analysis, we used the carbon abundance derived here, and a solar-scaled nitrogen abundance.

The O I triplet lines at 7771-7775 Å are unblended and prominent, hence we analyzed them with direct EW measurements (see Table 7.2). Here we did not include the 7774 Å component because the line appears slightly asymmetric, and

---

<sup>7</sup><http://kurucz.harvard.edu>

gives an anomalously high (+0.10 dex) abundance compared to the other two components, 7771.94 Å ( $\chi=9.15$  eV,  $\log gf=0.369$ ; Hibbert et al. 1991) and 7775.4 Å ( $\chi=9.15$  eV,  $\log gf=0.001$ ; Hibbert et al. 1991). This effect is also seen in the coolest stars in Schuler et al. (2006) and Bubar & King (2010); these authors suggest it may be due to a Fe I blend at 7774.00 Å in cool metal-rich stars, but this explanation has yet to be verified.

The triplet lines are strong and form in the higher photospheric layers, and thus suffer from non-LTE (NLTE) effects due to the dilution of each line's source function compared to the Planck function in the line-forming region (Kiselman 2001). The large energy gap between the two lowest energy levels and levels of higher energy prohibits collisional excitation from maintaining LTE, and the upper level of the triplet is underpopulated compared to the lower level (Kiselman 1993). This causes the source function to be smaller than the Planck function, leading to stronger absorption lines (Kiselman 1993; Gratton et al. 1999). Abundances derived from these lines assuming LTE are thus overestimated. The effect increases as the number of electrons in the initial (lower) transition state increases, which can be caused by decreasing gas pressures or increasing temperatures in the line-forming region, and/or an increase in the number of oxygen atoms. Thus the discrepancy between LTE and NLTE calculations and observations is more prominent for hot ( $T_{\text{eff}} \gtrsim 6000$  K) solar-metallicity dwarfs and evolved metal-poor subgiants with decreased surface gravity.

Multiple groups have prescriptions for NLTE corrections, which involve establishing the departure from LTE coefficients ( $n_{\text{NLTE}}/n_{\text{LTE}}$ , the ratios of the populations in NLTE and LTE) from statistical equilibrium calculations for varying stellar parameters. Takeda (2003) constructs a neutral atomic oxygen model with 87 levels and 277 radiative transitions, with atomic data from Kurucz &



Bell (1995). In their atomic model, the neutral hydrogen population is taken from Kurucz LTE model atmospheres, and the photoionizing radiation is computed from the same LTE stellar atmospheres, incorporating the line opacity using Kurucz's (1993) opacity distribution function. The effect of H I collisions is treated according to Steenbock & Holweger's (1984) classical formula, which is derived from Drawin's (1968) application of Thomson's theory for electron-atom encounters to collisions between identical particles. Takeda (2003) finds that for a given  $T_{\text{eff}}$ ,  $\log g$ , and  $\xi$ , the NLTE correction to the oxygen abundances is a nearly monotonic function of EW. They fit the coefficients  $a$  and  $b$  in their relation  $\Delta = a10^{bW_\lambda}$  based on their computed  $\Delta$  values. Here we use this relation and the  $a$  and  $b$  coefficients corresponding to the determined parameters of 55 Cnc to yield  $\Delta$  corrections to our computed LTE oxygen triplet abundances.

Ramírez et al. (2007) compute NLTE corrections using an oxygen model atom with 54 levels and 242 transitions, with atomic data from Allende Prieto et al. (2003) and fixed temperature and electron density structures from the Kurucz LTE models. They allow the H and O level populations to depart from LTE by solving rate equations while recalculating the radiation field with the NLTE stellar atmosphere code TLUSTY (Hubey & Lanz 1995), and do not include H I collisions. Ramírez et al. (2007) construct a grid of NLTE abundances directly from curves of growth corresponding to a range of stellar parameters ( $T_{\text{eff}}$ ,  $\log g$ ,  $[\text{Fe}/\text{H}]$ ) and provide an IDL routine to interpolate within the grid, which we used here.

Fabbian et al. (2009) construct a model atom containing 54 energy levels and 258 radiation transitions, with atomic parameters from the NIST Atomic Spectra Database<sup>8</sup> and radiative and Stark parameters from VALD. They include fine-splitting of energy levels where appropriate (ground state and upper level of O

---

<sup>8</sup><http://physics.nist.gov/PhysRefData/ASD/index.html>

I triplet), and the H I collision approximation of Steenbock & Holweger (1984) scaled by an empirical factor  $S_H$ , either =0 or =1. Fabbian et al. (2009) also include the most recent electron collision cross sections of Barklem (2007) based on quantum mechanical calculations; this gives larger NLTE corrections due to increased intersystem coupling. We obtained their grid of NLTE corrections and IDL interpolation routine, but it does not cover  $[\text{Fe}/\text{H}] > 0$  or  $\log N(\text{O}) > 8.83$ , so we extrapolated to the measurements of 55 Cnc. In order to enable direct comparison, we also interpolated Fabbian et al.'s (2009) NLTE corrections to the same scaling factor as Nissen (2013),  $S_H = 0.85$ , which has been shown to yield the best agreement with observations of O I triplet in the Sun (Pereira et al. 2009).

In Table 7.3 we show the derived LTE  $[\text{O}/\text{H}]$  abundances from the O I triplet, and also apply the NLTE corrections of Takeda (2003), Ramírez et al. (2007), and Fabbian et al. (2009) for comparison. Overall, the NLTE corrections are between 0.06 and 0.1 dex.

### 7.2.3.3 Abundance Uncertainties

There are two components to the uncertainties in derived elemental abundances – one from stellar parameter errors and one from the dispersion in the abundances derived from different absorption lines. To determine the uncertainty due to the stellar parameters, the sensitivity of the abundance to each parameter was calculated for changes of  $\pm 150$  K in  $T_{\text{eff}}$ ,  $\pm 0.25$  dex in  $\log g$ , and  $\pm 0.30$  km s<sup>-1</sup> in  $\xi$ . For the abundances determined through spectral synthesis, models with this range of stellar parameters were compared to the data and the elemental abundance adjusted to determine the best fit. The uncertainty due to each parameter is then the product of this sensitivity and the corresponding parameter uncertainty. The second uncertainty component is the uncertainty in the mean,  $\sigma_\mu$ , for the abundances derived from the averaging of multiple lines. The total uncertainty

for each abundance ( $\sigma_{\text{tot}}$ ) is the quadratic sum of the three individual parameter uncertainties ( $T_{\text{eff}}$ ,  $\log g$ ,  $\xi$ ) and  $\sigma_{\mu}$ .

In the case of the O I triplet, the error on  $[\text{O}/\text{H}]_{\text{NLTE}}$  was calculated separately for each of the NLTE corrections we applied (see Table 7.3). For errors on the Ramírez et al. (2007) and Fabbian et al. (2009) NLTE abundances, we calculated their sensitivity to  $\pm 150$  K  $T_{\text{eff}}$  and  $\pm 0.25$  dex  $\log g$ . We then combined these with  $\sigma_{\mu}$  for the NLTE abundances to determine the NLTE abundance errors. Takeda (2003) NLTE corrections include a dependence on  $\xi$ , so we calculated the sensitivity of these NLTE abundances to  $\xi$  in addition to  $T_{\text{eff}}$  and  $\log g$ , but used changes of  $\pm 1$  km s $^{-1}$ ,  $\pm 500$  K,  $\pm 1.0$  dex, respectively, due to the grid spacing of the Takeda (2003) NLTE corrections. As with the other  $[\text{O}/\text{H}]_{\text{NLTE}}$  errors, we also included the  $\sigma_{\mu}$  for the Takeda (2003) NLTE abundances.

The final derived stellar parameters and their  $1\sigma$  uncertainties, as well as the derived  $[\text{Fe}/\text{H}]$  and  $[\text{Ni}/\text{H}]$  values and their  $1\sigma$  uncertainties, are shown in Table 7.1, along with several literature values for comparison. In Table 7.3 we detail the  $[\text{C}/\text{H}]$  and  $[\text{O}/\text{H}]$  values derived from different abundance indicators. Table 7.4 shows the range in C/O ratios resulting from the different carbon and oxygen abundance indicators. These C/O ratios were calculated with the prescription  $\log N_{55\text{Cnc}}(\text{O}) = \text{derived } [\text{O}/\text{H}]_{55\text{Cnc}} + \log N_{\odot}(\text{O})$  and  $\log N_{55\text{Cnc}}(\text{C}) = \text{derived } [\text{C}/\text{H}]_{55\text{Cnc}} + \log N_{\odot}(\text{C})$ , where  $\log N_{\odot}(\text{O}) = 8.66$  and  $\log N_{\odot}(\text{C}) = 8.39$  (Asplund et al. 2005). The errors on the C/O value are represented by the quadratic sum of the errors in  $[\text{C}/\text{H}]$  and  $[\text{O}/\text{H}]$ .

### 7.3 Results & Discussion

The stellar parameters ( $T_{\text{eff}}$ ,  $\log g$ , and  $[\text{Fe}/\text{H}]$ ) derived here compare well with previous determinations in Table 7.1. The average values from the five literature

sources in Table 7.1 are  $T_{\text{eff}}=5268\pm38\text{K}$ ,  $\log g=4.45\pm0.05$ , and  $[\text{Fe}/\text{H}]=+0.32\pm0.03$ . The differences between the average values in the literature and those derived here are, in the sense of ‘this study - literature’,  $\Delta T_{\text{eff}}=+82\text{K}$ ,  $\Delta \log g=-0.01$  dex, and  $\Delta[\text{Fe}/\text{H}]=+0.02$  dex. These differences are all within the estimated uncertainties presented here and indicate that there are not large systematic differences between this study and those published previously. This result is encouraging, given the challenging nature of characterizing the relatively rare “super-metal rich” stars with their enhanced line absorption (e.g., Cayrel de Strobel et al. 1999; Taylor 2002; Gonzalez & Vanture 1998; Feltzing & Gonzalez 2001). Clearly, 55 Cnc is a well-established metal-rich star that happens to be nearby, hosts a multiple-planet system, and exhibits planetary transits.

Due to its proximity to the Sun and favorable multi-planet geometry, 55 Cnc is an important object in the study of planet formation, and thus it is useful to constrain as many of its fundamental properties as possible. The age of 55 Cnc is uncertain – the  $T_{\text{eff}}$  or color dependencies as a function of isochrone age, even for its known metallicity, render age estimates uncertain by several Gyr’s. Ages from  $\sim 3\text{--}9$  Gyr can fit the position of  $M_V$  versus  $T_{\text{eff}}$ , or  $(V-K)$ , or  $(B-V)$  isochrones (e.g., Fuhrmann, Pfeiffer & Bernkopf 1998). Other indicators tend to result in ages from 2-5 Gyr, such as Eggen’s (1985) identification of 55 Cnc as a member of the Hyades Supercluster with age  $\leq 2$  Gyr. Balinus et al. (1997) use the Ca II K-line activity indicator to estimate an age of 5 Gyr, which is consistent with their measurement of a rotational activity modulation of 42 days. Gonzalez (1999) also uses the Ca II K-line to estimate an age of 5 Gyr for 55 Cnc. Taken together, the slow rotation and Ca II K-line suggest a star perhaps not too different from the Sun in age: almost certainly not younger than 2 Gyr and probably not much older than 6 Gyr.

Given the metal-rich nature of 55 Cnc and the gradual Galactic increase of C/O with [Fe/H] (Nissen 2013), along with the importance of the natal C/O ratio in planetary chemistry (e.g., Kuchner & Seager 2005; Bond et al. 2010), it is important to examine closely the derived C/O ratio in 55 Cnc. Such scrutiny of C/O takes on added importance when considering the recent suggestions that some exoplanet host star C/O ratios in the literature have been overestimated (Fortney 2012; Nissen 2013).

The forbidden, ground-state [O I] 6300.30 Å line, used in previous host star studies (e.g., Delgado Mena et al. 2010; Petigura & Marcy 2011), gives the lowest oxygen abundance, resulting in the largest  $C/O=0.97\pm0.31$  (using the averaged  $\log N(C)$  of the two [C/H] indicators). Previous analysis of 55 Cnc using the [O I] 6300.30 Å line also found a high C/O of  $1.12\pm0.19$  (Delgado Mena et al. 2010). Taken at face value, our 6300.30 Å results would be consistent with this value within errors, though allow for  $0.66 < C/O < 1.27$  within  $1\sigma$  uncertainties.

However, as noted above, this line is blended with Ni and we find that in 55 Cnc, the derived  $[O/H]_{6300}$  is very sensitive to the assumed abundance of nickel when performing synthesis analysis. By changing the Ni abundance within our derived error for [Ni/H] ( $\pm 0.05$ ), the best-fit oxygen abundance  $\log N(O)$  varies by  $\sim 0.20$  (see Figure 7.1, bottom). This results in the C/O ratio varying from  $\sim 0.72$ -1.1, without even considering the  $1\sigma$  C/O errors (and  $\sim 0.42$ -1.4 considering these errors).

The [O I] 6363.78 Å line gives a  $C/O=0.79\pm0.23$ , ranging within error from  $\sim$ solar ( $C/O_{\odot}=0.55\pm0.10$ ; Asplund et al. 2009; Caffau et al. 2011) to 1. This line is a blend with CN, which we find contributes a greater amount to the line strength in the case of 55 Cnc than in the Sun (see Figure 7.1, top). Additionally, it is weaker than the [O I] 6300 Å line, and was found to give higher oxygen abun-

dances in the Sun (e.g.,  $\log N(\text{O})_{6300}=8.69$  vs.  $\log N(\text{O})_{6363}=8.81$ ), 2 dwarf stars, and a sub-giant star (Caffau et al. 2008; Caffau et al. 2013). (We find  $\log N(\text{O})_{\odot,6300}=8.67$  vs.  $\log N(\text{O})_{\odot,6363}=8.84$  in our synthesis analysis of the Sun.) Caffau et al. (2013) suggest that the discrepancy is due to an overestimate in the  $\log gf$  of the Ni I line that is blended with the [O I] 6300.30 Å line. Alternatively, an unknown blend at 6363 Å may affect the spectrum of dwarf stars only, as the 6300-6363 Å discrepancy is not seen in giants (Caffau et al. 2013). Certainly this discussion is still open, and this particular result should be considered as part of a larger effort to determine [O/H] from both [O I] lines in dwarf star spectra. Overall, because [O/H]<sub>6363</sub> for 55 Cnc is larger, the resulting C/O is smaller than for the 6300 Å line.

For the O I triplet at 7771-7775 Å, the LTE [O/H]<sub>LTE</sub> =  $0.19 \pm 0.17$  agrees well with that derived from the [O I] 6363.78 Å,  $0.17 \pm 0.17$ , resulting in a similar C/O =  $0.76 \pm 0.23$ . As noted, these lines have been shown both theoretically and observationally to overestimate oxygen abundances in LTE, most significantly at high temperatures and low gravities. We show in Tables 7.3 and 7.4 that three different NLTE corrections – Takeda (2003), Ramírez et al. (2007), and Fabbian et al. (2009) – give different [O/H] values and C/O ratios for 55 Cnc. The corrections are relatively small and, perhaps surprisingly, similar despite the different atomic models, handling of H atom inelastic collisions, and stellar parameters covered by the corrections. For varying NLTE corrections, C/O<sub>55Cnc</sub> ranges from  $\sim 0.63$ - $0.70$ , with a conservative error of  $\sim 0.2$  based on the LTE abundances (see §2.5).

However, we note that the validity of applying these NLTE corrections to a cool and metal-rich star like 55 Cnc is uncertain. With high-resolution spectroscopy and analysis methods very similar to those used here, Schuler et al. (2004) and (2006) and King & Schuler (2005) find a significant *increase* [O/H]<sub>LTE</sub> values

derived from the O I triplet with *decreasing*  $T_{\text{eff}}$  for dwarfs stars in the Pleiades, M34, Hyades open clusters, and the Ursa Major moving group. Such collections of stars present a unique opportunity for studying the NLTE effects across stellar temperature and thus mass, as the stars are presumably, within a single cluster, chemically homogenous and formed at the same time. This increase in  $[\text{O}/\text{H}]_{\text{LTE}}$  is in direct contrast with all the NLTE calculations presented here, which predict negligible effects (e.g.,  $\leq 0.05$  dex) in dwarfs with  $T_{\text{eff}} \lesssim 5400$  K. These cool cluster dwarf findings are robust, in that the trend remains after re-derivation of temperatures using different (e.g., photometric) scales, across multiple stellar atmosphere models with or without convective treatment and varying the mixing-length parameter, and within all four of these stellar associations.

The physical mechanism responsible for the discrepancy in triplet oxygen abundances between calculations and observations of cool ( $T_{\text{eff}} \lesssim 5400$  K) dwarfs in clusters is not yet certain. By comparing the Hyades cluster (600 Myr;  $[\text{Fe}/\text{H}] = +0.13$ ), Pleiades cluster ( $\sim 100$  Myr,  $[\text{Fe}/\text{H}] = 0$ ), and Ursa Major moving group (600 Myr,  $[\text{Fe}/\text{H}] = -0.09$ ), Schuler et al. (2006) suggest that the similarity in the observed  $[\text{O}/\text{H}]$ - $T_{\text{eff}}$  trend in Hyades and Ursa Major, versus the steeper trend in Pleiades, points towards an age rather than metallicity effect. While the line strengths of the triplet have been shown to increase in a synthetic solar spectrum when a chromosphere is included (Takeda 1995), Schuler et al. (2004) find no correlation between the triplet  $[\text{O}/\text{H}]$  values and  $\text{H}\alpha$  and Ca II triplet chromospheric activity indicators for the Pleiades and M34 stars. This lack of correlation is confirmed by Schuler et al. (2006) between the Hyades stars'  $[\text{O}/\text{H}]$  and Ca II H+K activity indicators, suggesting that a more global chromosphere does not contribute to the observed triplet trends in cool cluster dwarfs. Instead, using simple models including flux contributions to the triplet region from the quiescent star and

both cool and hot spots is, Schuler et al. (2006) are able to reproduce the observed oxygen triplet line strengths in cool Hyades dwarfs. As stellar surface activity is expected to decrease with age, this result is consistent with the suspected age dependence of the cool star O I triplet abundances.

Our derived  $T_{\text{eff}}$  for 55 Cnc ( $5350 \pm 102$  K) places it in the regime ( $T_{\text{eff}} \lesssim 5450$  K) where the O I triplet-temperature trend appears to contradict the canonical NLTE oxygen abundance corrections. Due to the larger oxygen triplet NLTE correction in the Sun versus 55 Cnc, the resulting NLTE-corrected  $[\text{O}/\text{H}]$  values for 55 Cnc are actually larger than  $[\text{O}/\text{H}]_{\text{LTE}}$ , although overlap within errors (see Table 7.3). This behavior is also seen in the cooler stars of Nissen (2013) – NLTE corrections in cool stars (even up to  $\sim 5660$  K) yield an increase in  $[\text{O}/\text{H}]$ . As a result of higher oxygen abundances, the C/O ratios for 55 Cnc derived here using the various  $[\text{O}/\text{H}]_{\text{NLTE}}$  values are smaller, with a mean of  $0.66 \pm 0.07$  using the averaged  $\log N(\text{C})$  of the two  $[\text{C}/\text{H}]$  indicators. However, all of the stellar associations discussed above are much younger than the estimated age of 55 Cnc (2-6 Gyr), so the same mechanism(s) may not apply in this case.

Instead of adopting the canonical NLTE corrections, one could estimate an empirical correction based on the open cluster and moving group data from Schuler et al. (2006). At 5350 K, the  $T_{\text{eff}}$  of 55 Cnc, the typical O I triplet-based abundances are approximately 0.08 dex higher than the mean abundances of the warmer stars in each cluster. Adopting this difference as a first-order correction, the resulting O I triplet abundance of 55 Cnc would be  $[\text{O}/\text{H}] = 0.11$ , a value in good agreement with the  $[\text{O I}]$ -based abundances.

Table 7.4 presents final abundances and respective C/O ratios from the individual C I,  $\text{C}_2$ ,  $[\text{O I}]$ , and O I triplet features. As discussed earlier, at the temperature and metallicity of 55 Cnc, the 6300Å  $[\text{O I}]$  feature is dominated by the Ni I



blend. Inspection of the O-results in Table 7.4 reveals that the 6300Å line yields a lower [O/H] than the other oxygen indicators. A mean of the O I triplet LTE and the 6363Å [O I] line results in  $\log N(\text{O})=8.84\pm0.01$ ; the 6300Å [O I] abundance falls significantly outside of this scatter at  $\log N(\text{O})=8.74$ . The decision here, due to uncertainty caused by significant Ni I blending, is to drop the 6300Å [O I] result from the final C/O calculation. Additionally, the various NLTE corrections to the O I triplet abundance may be unreliable at the temperature and metallicity of 55 Cnc. The O I triplet NLTE  $\log N(\text{O})=8.91\pm0.027$ , different by  $\sim 1.9\sigma$  from the  $\log N(\text{O})=8.84\pm0.01$  calculated from the combined 6363Å [O I] line and O I triplet LTE values. Therefore we also omit the triplet NLTE results from the final C/O calculation. We note, though, that including the triplet NLTE values decreases the mean C/O value only slightly, to  $0.71\pm0.09$ , in agreement with the value we choose to report based on the 6363Å [O I] and O I triplet LTE values. In addition, including the O I triplet LTE values with the empirical correction derived from the cool cluster stars increases the mean C/O value slightly ( $\sim 0.03$  dex) but is completely consistent with the average we choose to report here.

A final mean C/O ratio is calculated for 55 Cnc based on the six values of C/O in Table 7.4, which result from each combination of values from each respective C and O abundance indicator, excluding those based on the 6300Å [O I] line and the O I triplet NLTE corrections. The resulting mean value is  $\text{C/O}=0.78\pm0.08$ . Precise values of C/O are important for constraining the composition of this multiple-planet host star. Several other studies are tackling this issue with larger samples of mostly giant planet host stars (Delgado Mena et al. 2010; Petigura & Marcy 2011; Nissen 2013).

Figure 7.2 shows the values of [C/H], [O/H], and C/O versus [Fe/H] for stars from the samples noted in the previous paragraph, with the results derived here

for 55 Cnc also shown. While the spread is still large, the bottom panel of Figure 7.2 showing C/O versus [Fe/H] indicates that 55 Cnc follows the same trends as defined by the larger samples. With  $C/O=0.78\pm0.08$ , 55 Cnc exhibits a ratio that is significantly larger than solar ( $C/O_{\odot} \sim 0.50$ ), but below  $C/O=1.0$  at the  $2.75\sigma$  level. The value of 0.78 is lower than the value of  $C/O=1.12\pm0.19$  used by Madhusudhan et al. (2012) for their carbon-rich models of the “super-Earth” exoplanet.

#### 7.4 Conclusions

The 55 Cnc system was the first (Wisdom 2005) and remains one of only a few discovered systems with five or more planets. The inner most planet, 55 Cnc e, is one of the most observationally-favorable super-Earth exoplanets for detailed characterization.

While previous analyses indicate the C/O ratio of 55 Cnc to be  $\geq 1$ , our analysis indicates that the picture is not so clear. The C/O ratio of this exoplanet host star is likely closer to  $\sim 0.8$ . This value is lower than the value adopted by Madhusudhan et al. (2012) in their prediction that the small-mass exoplanet 55 Cnc e is carbon-rich, and corresponds to the predicted minimum value,  $\sim 0.8$ , necessary to form abundant carbon-rich condensates, under the assumption of equilibrium (e.g., Bond et al. 2010). Also, possibly the C/O ratio of 55 Cnc’s protoplanetary disk was not uniformly identical to its host star, perhaps causing local carbon enhancements of the gas or grains accreted by 55 Cnc e; carbon-rich planets may still form around oxygen-rich stars (Öberg et al. 2011; Bond et al. 2010). Our study places this system at the theoretically interesting boundary between two diverse planetary types.

Measurements of oxygen are challenging in solar-type stars because the oxy-

gen abundance indicators at optical wavelengths are weak, blended with other atomic or molecular lines, and/or subject to non-LTE effects. Oxygen measurements are even more complicated in cool and high metallicity stars like 55 Cnc, because of the stronger blends with both atomic and molecular lines, and the uncertainty in NLTE corrections that do not accurately predict the behavior of line widths in cool stars. Our case study demonstrates the caution that must be used when determining exoplanet host star (and any star's) C/O ratios, particularly the sensitivity of all three major oxygen abundance indicators to different effects that are not always easy to account for and change based on stellar parameters.

Table 7.1. Derived Stellar Parameters and Elemental Abundances for 55 Cnc

Parameter	this work <sup>a</sup>	Valenti & Fischer 2005 <sup>b</sup>	Butler et al. 2006	Ecuvillon et al. 2004 or 2006	Takeda et al. 2007	Zieliński et al. 2012
$T_{\text{eff}}$ (K)	5350±102	5235±15	5235±44	5279±62	5327±49	5265±15
$\log g$ (cgs)	4.44±0.30	4.45±0.02	4.45±0.06	4.37±0.18	4.48 <sup>-0.01</sup> <sub>+0.05</sub>	4.49±0.05
$\xi$ (km s <sup>-1</sup> )	1.17±0.14	...	...	0.98±0.07	...	...
[Fe/H]	0.34±0.18	0.31±0.01	0.32±0.03	0.33±0.07	0.37±0.04	0.29±0.07
[Ni/H]	0.43±0.05	0.37±0.01	...	0.39 <sup>c</sup>	...	...

<sup>a</sup>Adopted solar parameters:  $T_{\text{eff}} = 5777$  K,  $\log g = 4.44$ , and  $\xi = 1.38$  km s<sup>-1</sup>.

<sup>b</sup>Uncertainties from fitting a single “standard” star, divided by  $\sqrt{n}$ , where  $n = 8$ , the number of observations of 55 Cnc in Valenti & Fischer (2005).

<sup>c</sup>Derived by Delgado Mena et al. (2010) with spectra from the CORALIE survey, using Ecuvillon stellar parameters. Specific errors not provided.

Table 7.2. Lines Measured, Equivalent Widths, and Abundances

Ion	$\lambda$ (Å)	$\chi$ (eV)	$\log gf$	$EW_{\odot}$ (mÅ)	$\log N_{\odot}$	$EW_{55\text{Cnc}}$ (mÅ)	$\log N_{55\text{Cnc}}$
C I	5052.17	7.68	-1.304	33.7	8.45	31.3	8.72
	5380.34	7.68	-1.615	20.7	8.48	20.6	8.78
[O I]	6300.30	0.00	-9.717	5.6	8.67 <sup>a</sup>	7.2	8.75 <sup>a</sup>
	6363.79	0.00	-10.185	1.6	8.84 <sup>a</sup>	3.4	9.01 <sup>a</sup>
O I	7771.94	9.15	0.369	69.6	8.83 <sup>b</sup>	48.9	9.00 <sup>b</sup>
	7775.39	9.15	0.001	46.8	8.81 <sup>b</sup>	33.6	9.01 <sup>b</sup>

<sup>a</sup> Abundance derived through synthesis analysis.

<sup>b</sup> LTE abundance.

Note. — This table is available in its entirety in a machine-readable form in the online journal. A portion is shown here for guidance regarding its form and content.

Table 7.3. 55 Cnc Carbon and Oxygen Abundances from Different Indicators

Abundance Indicator	this work <sup>a</sup>	Ecuivillon et al. 2004 or 2006 <sup>b</sup>	Delgado Mena et al. 2010 <sup>c</sup>	Petigura & Marcy 2011 <sup>d</sup>
[C I/H]	0.29±0.14	0.31±0.10	0.30	0.13±0.06
[C <sub>2</sub> /H]	0.39±0.06	...	...	...
[O/H] <sub>6300</sub>	0.08±0.26	0.13±0.11	0.07	...
[O/H] <sub>6363</sub>	0.17±0.17	...	...	...
[O/H] <sub>7772,7775;LTE</sub>	0.19±0.17	0.21 <sup>avg of all triplet lines no LTE error given</sup>	...	...
[O/H] <sub>7772,7775;NLTE</sub>	0.22±0.08 <sup>Takeda NLTE</sup> 0.25±0.03 <sup>Ramírez NLTE</sup> 0.27±0.03 <sup>Fabbian NLTE</sup>	0.03±0.11 <sup>avg of all triplet lines Ecuivillon NLTE model</sup>	...	...

Note. — The NLTE corrections calculated from Fabbian et al. (2009) have been interpolated to a Drawin formula scaling factor  $S_H = 0.85$ , as in Nissen 2013.

<sup>a</sup> The  $\pm$  errors here = the final combined abundance uncertainties due to both stellar parameters and (if applicable) the dispersion in abundances derived from multiple lines. Errors on  $[O/H]_{7772,7775;NLTE}$  = the uncertainties due to the stellar parameters that factor into in each of the NLTE calculations ( $T_{\text{eff}}$  and  $\log g$  for Ramírez and Fabbian;  $T_{\text{eff}}$ ,  $\log g$ , and  $\xi$  for Takeda) and the dispersion in the derived NLTE abundances.

<sup>b</sup>The  $\pm$  errors here factor in uncertainties in stellar parameters, continuum determination, and (if applicable) the standard deviation of multiple measured lines.

<sup>c</sup>Specific errors not provided.

<sup>d</sup>The  $\pm$  error =15% and 85% confidence limits.

Table 7.4. C/O Ratios of 55 Cnc Based on Different C and O Abundance Indicators

	$\log N(\text{O})$	6300 Å [O I] $\log N(\text{Ni})=6.68$	O I triplet LTE	O I triplet NLTE Takeda (2003)	O I triplet NLTE Ramírez et al. (2007)	O I triplet NLTE Fabbian et al. (2009)	6363 Å [O I]
$\log N(\text{C})$		8.740	8.845	8.875	8.915	8.926	8.830
two blue C I lines	8.675	$0.861 \pm 0.299$	$0.676 \pm 0.217$	$0.631 \pm 0.217$	$0.576 \pm 0.217$	$0.561 \pm 0.217$	$0.700 \pm 0.217$
two C <sub>2</sub> lines	8.775	$1.084 \pm 0.272$	$0.851 \pm 0.178$	$0.794 \pm 0.178$	$0.725 \pm 0.178$	$0.706 \pm 0.178$	$0.881 \pm 0.178$
C I and C <sub>2</sub> averaged	8.725	$0.966 \pm 0.306$	$0.759 \pm 0.226$	$0.707 \pm 0.226$	$0.646 \pm 0.226$	$0.629 \pm 0.226$	$0.785 \pm 0.226$

Note. — The  $\log N(\text{O or C})$  values are calculated as  $[\text{X}/\text{H}] + \log N_{\odot}(\text{X})$ , with  $\log N_{\odot}(\text{O})=8.66$  and  $\log N_{\odot}(\text{C})=8.39$  (Asplund et al. 2005). The  $\pm$  errors here = the final combined abundance uncertainties due to both stellar parameters and (if applicable) the dispersion in abundances derived from multiple lines. We adopted the more conservative (larger)  $[\text{O}/\text{H}]_{\text{LTE}}$  errors for the  $[\text{O}/\text{H}]_{\text{NLTE}}$  values. Serendipitously, the  $[\text{O}/\text{H}]_{\text{LTE}}$  error = the  $[\text{O I}]_{6363}$  error; hence, columns 4-8 have identical errors.

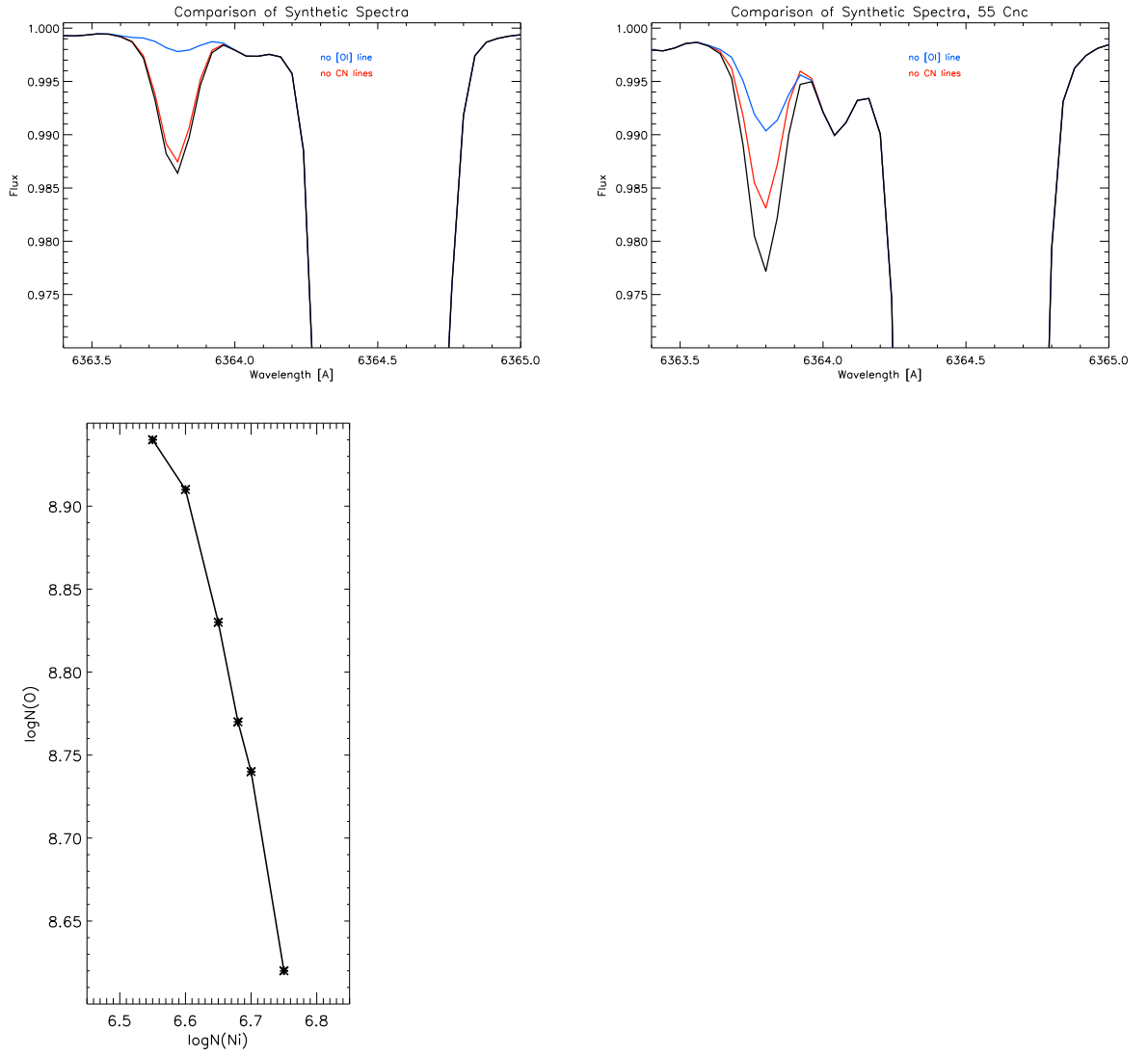


Figure 7.1 **Top row:** The contribution of CN to the blended 6363 Å [O I] line is greater in 55 Cnc than in a solar-type star. The black line shows the model spectrum of (left) the sun and (right) 55 Cnc with our adopted stellar parameters. In red is the stellar model with CN lines removed, showing the contribution of just [O I]. In blue is the stellar model with the [O I] line removed, showing the contribution of just the CN lines. **Bottom:** The measured  $\log N(O)_{55\text{Cnc}}$  changes significantly within the error on the determined  $\log N(Ni)$  abundance ( $\log N(Ni)_{55\text{Cnc}} = 6.68 \pm 0.05$ ).



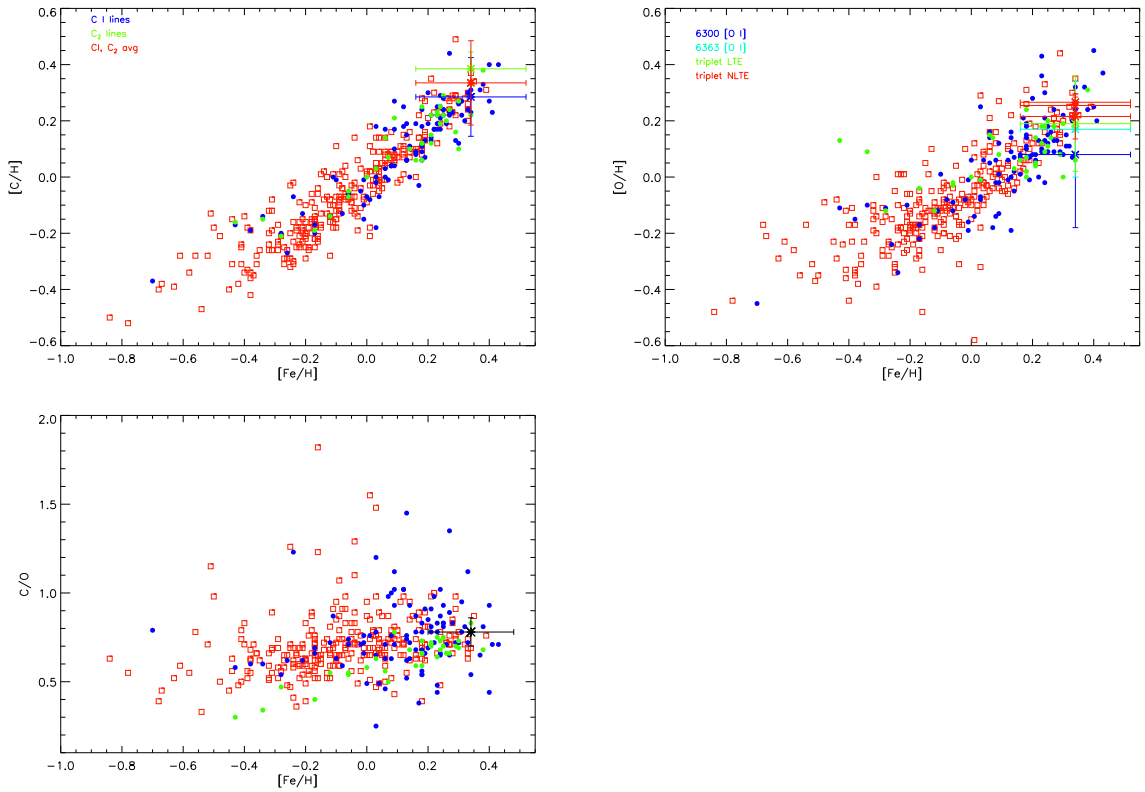


Figure 7.2  $[C/H]$ ,  $[O/H]$ , and  $C/O$  versus  $[Fe/H]$  from Delgado Mena et al. (2010) and Nissen (2013) [all Nissen (2013) hosts are in the Delgado Mena et al. (2010) host sample]. Non-host stars from Delgado Mena et al. (2010) are plotted with red open squares, while host stars from Delgado Mena et al. (2010)/Nissen (2013) are plotted with blue/green circles. Measurements of 55 Cnc from this work are represented by large asterisks in each plot (see Table 7.3). In the upper plots, we designate measurements from different C and O abundance indicators with different colors. Our final mean  $C/O$  value is shown in black in the bottom plot.

## CHAPTER 8

## CONCLUSIONS

## 8.1 Summary

In this thesis I have described work to observationally constrain the compositions of exoplanets and the origin(s) of their chemical diversity. “Exoplanetology” is still a nascent field, and observations of transiting exoplanet atmospheres are still few in number, low in resolution, and high in uncertainty associated both with observational and interpretation (via modeling). However, using multi-wavelength observations of exoplanet primary/secondary eclipses, coupled with observations chemically characterizing what influences/controls planet formation – protoplanetary disks and host stars – we can begin to construct a tentative map of how the compositions of the planets we observe originate and evolve.

Chapter 2 is unpublished, and represents my own brief synopsis of star and planet formation, with an emphasis on how observations of carbon and oxygen, and their molecular carriers, can constrain the timescales and chemical constituents of planet formation.

In Chapter 3 (Teske et al. 2010), I focused on characterizing the inner warm disks of T Tauri stars, the likely region of small planet formation, via *Spitzer*-IRS observations of the 14  $\mu\text{m}$  HCN emission feature. First, I showed that low resolution (SL) observations can recover quantitative trends in molecular emission strength seen in higher resolution (SH) spectroscopic observations. This is important because IRS is no longer in operation, and a much greater number of low versus high resolution observations are available in the archive for further analysis. Second, I found trends between HCN emission strength and stellar accretion rate and X-ray luminosity. The trends indicates that accretion related

processes, e.g., viscous accretion generated by the magnetorotational instability and/or stellar wind interaction with the disk surface, may be an important source of disk atmosphere heating, which could strengthen the HCN emission by increasing the temperature and/or abundance (by increasing the column density) in the disk atmosphere. If H<sub>2</sub>O formation is also enhanced by these processes, and sequesters most available O, this could lead to more available atomic carbon (that is not bound in CO) and in turn more HCN production. Additionally, the HCN abundance is influenced by the availability of nitrogen, which is formed via the dissociation of N<sub>2</sub> by UV radiation; increased UV irradiation could be produced by a higher stellar accretion rate. Interestingly, follow-up work by Carr & Najita (2011) and Najita et al. (2011; 2013) studied how this same HCN emission feature strength varied as compared to H<sub>2</sub>O emission around 17  $\mu$ m, finding that the ratio of HCN/H<sub>2</sub>O emission strength is correlated with disk mass. The authors suggest that this is indicative of more efficient icy solid growth in higher mass disks, which then decreases the water in the inner disk. Thus, the emission strength of HCN, when compared to water or other organic molecules (e.g., C<sub>2</sub>H<sub>2</sub>; Pascucci et al. 2014) may be an indirect probe of planetesimal growth, and also helps characterize how the composition of the inner disk changes with stellar properties and with time.

I described in Chapter 4 (Teske et al. 2013c) small-telescope photometric observations of the most well-known transiting super-Earth exoplanet, GJ 1214b. Using the Kuiper 61" telescope on Mount Bigelow, along with the STELLA-I robotic telescope in Tenerife, my co-authors and I observed nine primary transits in *R*, *V*, and *g'* optical bands in order to determine whether the short-wavelength slope of GJ 1214b's spectrum was consistent with a flat slope, or showed variation from longer wavelengths. Previous studies of *g* and *K<sub>s</sub>* band photometry indicated

possible spectral variation, hinting at an atmosphere *not* dominated by water (having a small scale height/flat spectrum), instead dominated by hydrogen but having spectral features redward of  $\sim 0.5 \mu\text{m}$  muted by some unknown opacity source. While our data was consistent within error with previous observations showing a slight upward slope in  $g'$ -band, they also allowed for a shallower spectral slope, especially when considering the low  $V$  band  $R_p/R_*$  observed value. This work helped keep the door to a water-rich atmospheric composition for GJ 1214b open. The newest GJ 1214b transit observations from HST/WFC3 rule out a cloud-free composition because the spectrum is too flat to be composed of  $\text{H}_2\text{O}$ ,  $\text{CH}_4$ ,  $\text{CO}$ ,  $\text{N}$ , or  $\text{CO}_2$  (Kreidberg et al. 2014). While this means we may never know for sure the dominant constituent of GJ 1214b's atmosphere, it does exemplify the importance of clouds in super-Earth (and possibly larger) exoplanet atmospheres, and gives credence to the possibility of photochemistry in GJ 1214b's atmosphere. Planets in between the sizes of Earth and Neptune appear to be the most prevalent in the Galaxy (e.g., Cassan et al. 2012; Fressin et al. 2013; Petigura et al. 2013), but no examples of this type of planet exist in our Solar System. This makes planets like GJ 1214b crucial to developing an understanding of planet formation overall, and how these super-Earth and mini-Neptune planets form and what they are made of (e.g., are they composed mostly of rock, or do they acquire a large fraction of their mass from volatile ices?).

The last three chapters of my thesis (5-7; published as Teske et al. 2013a, 2013b, and 2014) shift gears to constraining the compositions of exoplanets indirectly via their host star abundances. I measure these host star abundances from high resolution optical spectroscopic observations. Determining exoplanet atmospheric compositions from transit/eclipse observations is difficult, as illustrated in Chapter 4, and even the compositions of targets with many observations can be poorly

constrained because temperature and composition are degenerate in planetary atmosphere models (e.g., the derived abundance of an absorbing species depends on the pressure level, and thus temperature, at which it is absorbing; see Griffith 2014). Alternatively, host star abundances indicate the precursor materials present in the protoplanetary disk and available for incorporation into planets; this is invoked to explain the high metallicities ( $[\text{Fe}/\text{H}]$ ) in close-in giant planet host stars. In models of planet formation (e.g., Bond et al. 2010) and in the modeling of the current compositions of planets (e.g., Madhusudhan et al. 2012), stellar abundance ratios are adopted as the starting chemical conditions for the planet. However, as described in the introduction, observational and theoretical studies of gas and solid material in protoplanetary disks show that planets likely draw from reservoirs of different composition throughout their evolution.

In Chapter 5, I derived carbon and oxygen abundances of the host stars of some of the best studied/observed transiting hot Jupiters. I compared the host star abundances with inferences about the exoplanet's C/O ratios based on observations and both equilibrium and disequilibrium atmospheric models. While I did not find any strong correlations between host star and exoplanet chemical compositions, the latter are still very poorly constrained due to paucity of data. Also, the diversity of the host stars and their hot Jupiters in my sample may cause any such trends to be overwhelmed. Furthermore, *differences* between host star and planet compositions are likely common, and may be used to diagnose from where in the disk and at what stage of evolution the planet accreted or was bombarded by material.

In Chapter 6, I focused on one hot Jupiter system, XO-2, which is actually composed of two stars, one of which hosts the transiting planet XO-2b. The carbon and oxygen abundances of both stars are enhanced above solar, though

the planet hosting star is  $\sim$ twice as abundant in both elements. This results in both stars having the same C/O ratio ( $0.60 \pm 0.20$ ), placing them slightly above the solar C/O ( $\sim 0.50$ ), which is expected based on their enhanced metallicities ( $[\text{Fe}/\text{H}]_{\text{XO-2N}} = 0.39 \pm 0.14$ ,  $[\text{Fe}/\text{H}]_{\text{XO-2S}} = 0.28 \pm 0.14$ ). The elevated C and O in both stars is a strong indication that their parent molecular cloud was also elevated in these elements. My measurements of [C/H] and [O/H] in the two XO-2 stars overlap, so my measurements could be indicative of the effects of planet formation on the host star, and/or help explain why XO-2N hosts a close-in giant planet and XO-2S does not (or at least one has not been detected). However, as discussed in the introduction, the C/O ratio of a planet is not necessarily expected to “match” that of the host star; further observational constraints on the composition of XO-2b (e.g., Griffith et al. 2014, submitted) are necessary to make a host star-planet comparison.

The last chapter of my thesis is another case study comparing the composition of one host star to its exoplanet (Teske et al. 2013a). The planet is a smaller, more dense super-Earth, 55 Cnc e, and the chemical comparison is between planetary bulk composition (versus atmospheric composition) the host star abundances. Madhusudhan et al. (2012) modeled the interior composition of 55 Cnc e, using both the well-measured density of the planet and the previously-measured host star abundances as observational inputs. Specifically, Delgado Mena et al. (2010) published carbon and oxygen abundances of 55 Cnc as part of a larger study of exoplanet host stars, reporting a  $\text{C}/\text{O} \gtrsim 1$ . However, because 55 Cnc is both cool and metal-rich, the derivation of oxygen abundances is more challenging than for a star closer to solar. In Chapter 7 I described a detailed [O/H] determination for 55 Cnc, considering three different oxygen abundance indicators and the NLTE effects and blends that can influence these absorption lines. I also derive the

[C/H] value based on two atomic and two molecular ( $C_2$ ) indicators. My analysis indicates that the C/O ratio is closer to  $\sim 0.8$ , lower than the previously-adopted value but corresponding to the minimum value necessary in theoretical models to form carbon-rich condensates (e.g., Bond et al. 2010). My results demonstrate the caution that is necessary when determining/interpreting stellar abundances as they relate to initial planet formation conditions, especially the sensitivity of all three major oxygen abundance indicators to effects that change based on stellar parameters and are not always easy to calibrate.

## 8.2 Next Steps

One of the great boons, and yet great mysteries, in the study of star and planet formation is the discovery of bodies unlike anything in our Solar System. The first phase of planet detection revealed mostly gas giants orbiting very close to their host stars, tidally locked in orbits of hundredths of an AU with one side constantly exposed to intense stellar radiation. With the advent of *Kepler*, we now know that such hot Jupiters (HJs) are actually not the norm, and instead the most common types of planets have radii of 2-6  $R_{\oplus}$ , dubbed “super- Earths and Neptunes” (SENs) (e.g., Batalha et al. 2013). The differing planet masses and compositions are a function of, among other things, the parent star abundances and stellar mass, initial nebular/disk conditions, and timescale and location in the disk of formation. Given the likely diversity of HJs and SENs and the fact that we have no Solar System analogs, it is important to investigate physical processes that may differentiate them, and allow us to compare their compositions and evolutionary histories to our singular example of a life-bearing solar system. In my near-future work, I will continue to investigate the role that host stars play in the compositions of their orbiting planets.

### 8.2.1 How is Planet Composition Related to Stellar Activity?

Both of these new classes of planets – Hot Jupiters and super-Earths – receive greater UV and X-ray radiation than the planets in our Solar System, which affects their atmospheric structure, temperature, chemistry, circulation patterns, and even stability against evaporation (Lammer et al. 2013). Greater UV and X-ray radiation can photochemically alter HJ atmospheric chemistry down to  $\geq 10$  mbar (Line et al. 2013; Zahnle et al. 2009ab; Moses et al. 2011), potentially causing observable effects in spectra of transiting planets (Moses et al. 2013; Zahnle et al. 2009b). A comprehensive understanding the chemical composition of planets must include observations of the host star's activity.

Growing observational evidence from the *Hubble* and *Spitzer* space telescopes seemed a few years ago to suggest that HJ atmospheres fall into at least two classes, those with and without thermal inversions in their upper atmospheres. Fortney et al. (2008) proposed that the hottest HJs could host gaseous titanium oxide (TiO) and/or vanadium oxide (VO) at high altitudes, causing strong optical absorption and thermal inversions. Knutson et al. (2010) proposed that increased UV flux destroys the high-altitude absorber(s) responsible for HJ temperature inversions, based on the observed correlation between stellar Ca II H & K (3933.7 Å and 3968.5 Å) emission line strengths and the inference from 3.6  $\mu\text{m}$  and 4.5  $\mu\text{m}$  *Spitzer* photometry of thermal inversions in the exoplanet atmospheres. However, this is opposite what we observe in our own Solar System giant planets and their moons, that high-altitude absorbers in the form of haze are produced photochemically by UV radiation (e.g., Vázquez & Hansmeier). Furthermore, Knutson et al. (2010) did not take into account the variability of HJ host star activity, which may affect HJ atmospheres on observable timescales and thus their reported trend. Monitoring campaigns of chromospheric emission from HJ host



stars show in several cases that stellar activity varies by the planet's orbital period rather than the star's rotation (Shkolnik et al. 2003, 2005). Star-planet interaction (SPI) signatures themselves vary, in that they are observed in some observing seasons while in others the chromospheric flux is modulated instead by the usual stellar rotation (Shkolnik et al. 2003, 2005; Poppenhaeger et al. 2011; Scandariato et al. 2013). This on/off nature is predicted due to the complex nature of the multipole fields and dynamic magnetic fields of Sun-like stars interacting with their planets.

Conversely, it is unclear whether heavy TiO and/or VO can even be maintained at high altitude (Spiegel et al. 2009), and the TiO/VO hypothesis is also unable to account for the full range of HJ observations (Swain et al. 2013; Sing et al. 2013; Schlawin et al. 2014). Madhusudhan (2012) introduced an alternative classification scheme incorporating exoplanet incident radiation and C/O ratios in exoplanet atmospheres, which can successfully explain the previously divergent observations of some HJs. In hot gas giant planets the atmospheric carbon-to-oxygen (C/O) ratio significantly affects the molecular composition, and hence the observed spectrum, through thermochemical equilibrium partitioning of carbon in CO, CH<sub>4</sub>, and CO<sub>2</sub> (Lodders & Fegley 1999; Lodders 2004; Kuchner & Seager 2005; Bond et al. 2010).

I will provide the critical link between these two classifications by investigating how exoplanet host star abundances, particularly carbon to oxygen ratios, and host star activities are related. Determining host star abundance ratios and characterizing their activity are two pathways towards understanding the formation and evolution of both HJ and SEN exoplanets. Both require high resolution, high S/N spectroscopy across a wide wavelength range – C and O abundance indicators fall between  $\sim 3000\text{--}8000\text{ \AA}$ , and stellar activity indicators range from

the most-common Ca II H & K lines, to the NIR Ca II triplet at  $\sim 8550$  Å, to H $\alpha$  at  $\sim 6563$  Å, to the He I D<sub>3</sub> line at  $\sim 5876$  Å. I plan to work with Dr. Evgenya Shkolnik of Lowell Observatory, who has a large spectroscopic data set of unprecedented quality, gathered for the purpose of measuring exoplanetary and stellar magnetic fields and rotation periods in HJ systems. Each host star data set consists of spectra taken on each of 4, 5, or 10 consecutive nights, plus matching non-host standard stars. The targets' planets span a wide range of mass (0.07-10.06  $M_J$ ) and semi-major axis (0.02-0.12 AU), while the stellar parameters are kept within a narrow spectral range, ideal for deriving abundances relative to the Sun (as is typically done for high-precision studies). The data span NUV to NIR wavelengths ( $\sim 3900$ -9000 Å), at very high resolution ( $R \sim 50,000$ -80,000), and extremely high S/N ( $\sim 400/800$  per pixel in the blue/red). With these data, I will measure the strength and variation of stellar activity in these host stars and determine their C/O ratios (and other elemental abundances). In fact, I already have C/O ratios measured in two of the targets in Dr. Shkolnik's sample (HD 189733, Chapter 5, and 55 Cnc, Chapter 7). As we begin to analyze these data, we plan to obtain similar data on a sample of smaller planet host stars, focusing on targets in the *Kepler* sample, which have already been surveyed with GALEX in the FUV and NUV regimes. With this study I will help to disentangle the effects that stars and planets have on each other, and answer fundamental questions about hot Jupiter composition and formation history. Our results will also have significant implications for other close-in planets that are smaller and thus potentially habitable.

### 8.2.2 More Transiting Giant Planet Host Stars

The four gas giant planets in our Solar System contain at least 10-15  $M_{\oplus}$  of heavy elements in their interiors, enriching their composition as compared to the Sun

(Fortney & Nettelmann 2010). Is this also the case for some, or many, gas giant exoplanets? The seminal work of Miller & Fortney (2011) showed that a sample of 14 cool ( $\leq 1000$  K), transiting gas giant planets were all over-dense compared to thermal evolution models that match the host star metallicity ( $[\text{Fe}/\text{H}]$ ). By excluding from their sample the greater number of “inflated” HJs that experience an elevated incident flux ( $> 2 \times 10^8 \text{ erg s}^{-1}$ ), the authors avoid having to make assumptions about the poorly understood mechanism that decreases these planets’ densities, in opposition to the effect of adding heavy (metal) elements. Figure 7.1 shows how Miller & Fortney (2011) quantified the trend between host star metallicity and degree of enrichment, where the dotted line represents the flat relation expected at subsolar metallicity if 10-15  $M_{\oplus}$  of heavy elements are needed to trigger planet formation. Now, the number of the systems that fall into the cool, giant, mass-and-radius-measured planet bin has increased to  $\sim 30$ . I will work with Dr. Jonathan Fortney to see whether this relation continues to hold for the larger sample by gathering high resolution optical spectra of the planets’ host stars to measure their chemical abundances.

In addition, Dr. Fortney and I will explore whether there are similar (or different) trends between heavy element enrichment in the planets and other host star abundances of elements that may also contribute to planet formation. For instance, if giant planets formed beyond the water snow line and accreted a large mass of icy solids, we might expect a tighter correlation between stellar  $[\text{O}/\text{H}]$  and planetary enrichment. Alternatively or in addition, if more “rocky” solids – dominated by O, Mg, and Si – form giant planet cores, then we might expect correlations with those elements. As stated in the introduction, doubling Fe, Si, and O in solar protoplanetary disk models increases the solid surface density by 13%, 7.1%, and 58%, respectively (Robinson et al. 2006). Thus, besides Fe, Si and

O are the most significant solid mass contributors – O primarily through  $\text{H}_2\text{O}$  ice accreted beyond the snow line, and Si through silica/silicates in small grains (Brugamyer et al. 2011). Interestingly, Brugamyer et al. (2011) find a difference in  $[\text{Si}/\text{Fe}]$  between host stars and stars “without” planets (likely just stars with yet-undetected planets), controlling for  $[\text{Fe}/\text{H}]$ , but no difference in  $[\text{O}/\text{Fe}]$ . Si and O are both  $\alpha$ -elements, and the Si/O ratio is  $\sim$ constant among metal-rich stars, so  $[\text{Si}/\text{Fe}]$  should trace  $[\text{O}/\text{Fe}]$  (Robinson et al. 2006). Stellar photospheres may instead be tracing species important for grain nucleation (Si) rather than icy mantle growth (O), and refractories like Si may be the limiting reagents for planet formation.

Alternatively, it has been suggested that Jupiter’s heavy element mass may be dominated by carbon instead of water-ice and rocks (Lodders 2004), which has gained support from recent nebular chemistry modeling including local water depletion (Mousis et al. 2012). Carbon is a volatile, like O, but can contribute mass to both grain nuclei – universally up to 20% of C is likely in refractory grains (Henning & Salama 1998) – and to icy mantles – simulations of ice giants Uranus and Neptune show they required solid  $\text{CH}_4$  in their feeding zones to grow to their present sizes (Dodson-Robinson et al. 2010). The atmospheres of the giant planets in our Solar System are enhanced in their  $[\text{C}/\text{H}]$  by factors of  $\sim 3$ -60 compared to the Sun (Wong et al. 2008). As I discussed extensively in the latter chapters of my thesis, there are also hints of carbon-rich gas giant exoplanets. Furthermore, compared to solar-composition, a C-rich system would have an inner zone of refractory C solids and less  $\text{H}_2\text{O}$  ice farther out, concentrating more solid mass in the inner disk (Bond et al. 2010). Perhaps, then, we might expect a tighter correlation between stellar  $[\text{C}/\text{H}]$  and planetary metal-enrichment. The shape and spread of these correlations, and how they differ from element to element,

will provide insight into the composition of the metals inside giant exoplanets.

### 8.2.3 Small Planet Host Stars

Perhaps the most exciting prospect in exoplanet detection and characterization is finding planets that are Earth-like and/or potentially habitable. Of the current  $\sim 3600$  Kepler planet candidates,  $\sim 65\%$  are  $\leq 2.5 R_{\oplus}$  (Figure 7.2) and nearly 300 orbit in/near their host stars' habitable zones ( $180 \text{ K} < T_{\text{eq}} < 320 \text{ K}$ ) (Batalha et al. 2013; NASA Exoplanet Archive). The differing planet masses and compositions – there is a large scatter in radius below  $\sim 10 M_{\oplus}$  (Figure 7.3) – are a function of the parent star abundances and stellar mass, initial nebular/disk conditions, timescale and location of formation, and thermal evolution. I want to help answer the question, what is the chemical “recipe” for making terrestrial planets, and how does it depend on host star (temperature, elemental abundances) or system (number, orientation, size of planets) properties? While there have been many studies of the elemental abundances of giant planet host stars, due to the previously-limited number of terrestrial host stars it is still unknown whether similar relationships exist between small planets and their host star chemistries. As discussed in the introduction, carbon and oxygen are likely important mass contributors to small planets, and the relative abundance of these elements may influence habitability. In addition, a specific trend between elemental abundance and condensation temperature has been suggested as a signature of terrestrial planet formation (Meléndez et al. 2009).

In light of these predictions, I plan to increase the census of small planet host star chemical characterizations for both volatile and refractory elements, to 1) determine how similar these abundance distributions are to larger-planet host stars, 2) constrain the minimum amount of metals required to form a terrestrial planet, 3) determine whether stars with more Si and/or C are more likely to host small

planets, and 4) test the hypothesis that refractory elemental depletion is indicative of terrestrial planets. I have already completed a concept study to prove that, using the exact same data, I am able to reproduce the precise abundance results of Meléndez et al. (2012) (Figure 7.4), meaning that with comparable data I can confidently rule in or out the predicted effect. I will pursue these questions with both public (NASA Keck) observing time and time available through the Carnegie Magellan TAC. In addition, I will work with Paul Butler, Steve Shectman, Pamela Arriagada, Jeff Crane, and Ian Thompson to perform abundance analyses on the host stars of their most promising small planet candidates from the Carnegie Planet Search (RV) Survey. The survey's very high resolution, very high signal-to-noise spectra, which are used as template spectra for detecting planet signatures in stars' radial velocities, are already in hand. Very soon we may be able to distinguish stars that are likely to host Earth-like planets by studying their parameters and atmospheric properties. This is important for planning future telescope (JWST, TESS, *Kepler* 2, EELT, GMT, etc.) targets, and, ultimately, further characterizing planets in the search for life.

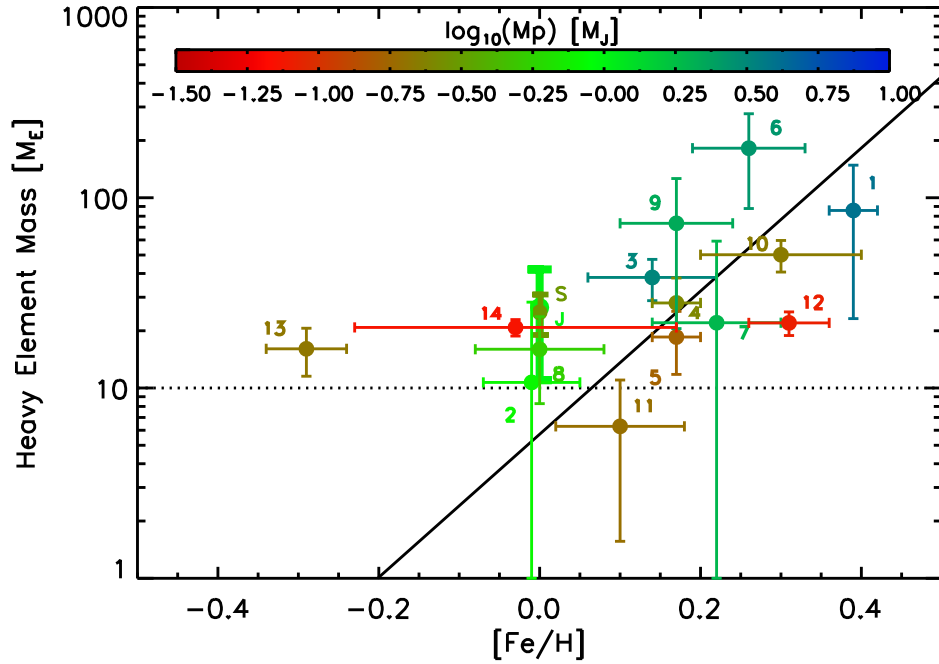


Figure 8.1 Stellar  $[\text{Fe}/\text{H}]$  and inferred planet heavy-element mass (in Earth masses) for the 14 giant exoplanets from Miller & Fortney (2011). On the left side of the figure, the rarity of gas giants around metal-poor stars is apparent. A least-squares fit to the data results in  $\log M_{\oplus} h = (0.82 \pm 0.08) + (3.40 \pm 0.39) [\text{Fe}/\text{H}]$  and a reduced  $\chi^2$  value of 1.95. The fit excludes HAT-P-12b (planet 13) and includes Jupiter and Saturn. The authors suggest from this diagram that planet need at least  $10\text{--}15 M_{\oplus}$  of heavy elements to form, with a stronger enrichment at higher  $[\text{Fe}/\text{H}]$ . This is the type of plot I hope to create with an increased sample size of cool giant planets, and for more stellar abundances like  $[\text{O}/\text{H}]$ ,  $[\text{C}/\text{H}]$ ,  $[\text{Si}/\text{H}]$ , and  $[\text{Mg}/\text{H}]$ .

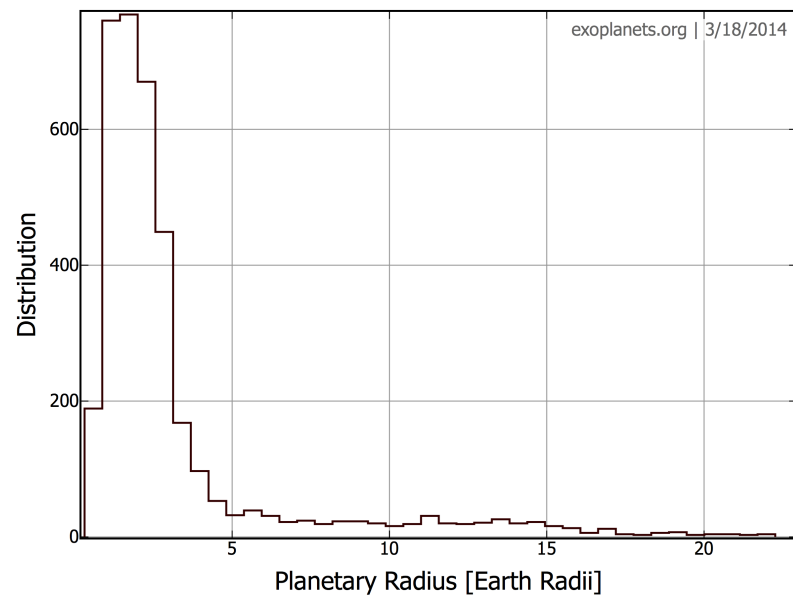


Figure 8.2 Distribution of detected exoplanet radii, showing prominence of planets with  $1.5R_{\oplus} < R < 4R_{\oplus}$ .



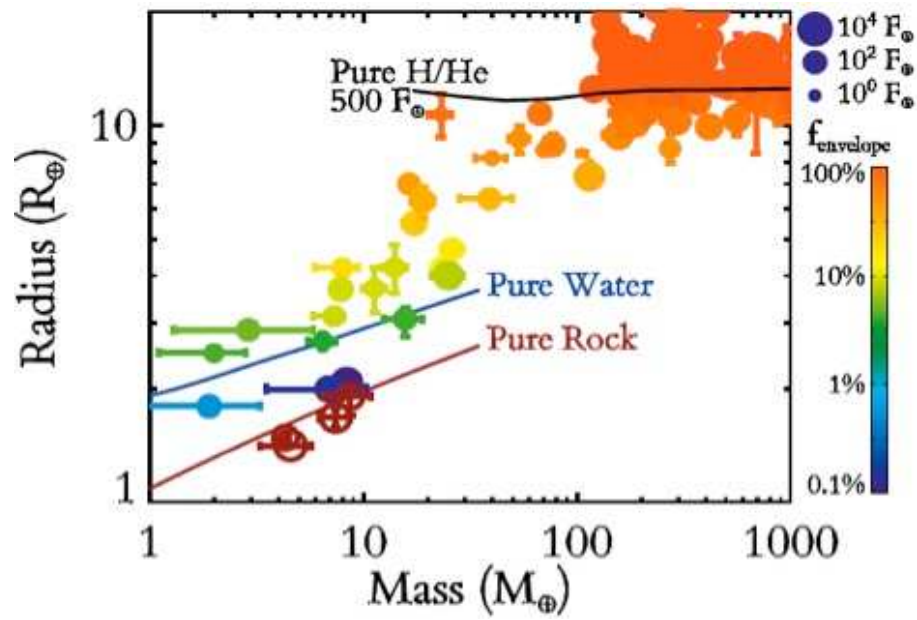


Figure 8.3 From Lopez & Fortney (2013), showing  $R_P$  vs.  $M_P$  for all 200 transiting planets with measured masses. Colors represent fraction of mass in H/He envelope, assuming  $\text{H}_2\text{O}$ -free interior. Sizes represent incident flux received by parent stars, relative to flux Earth receives from Sun ( $F_\oplus$ ).

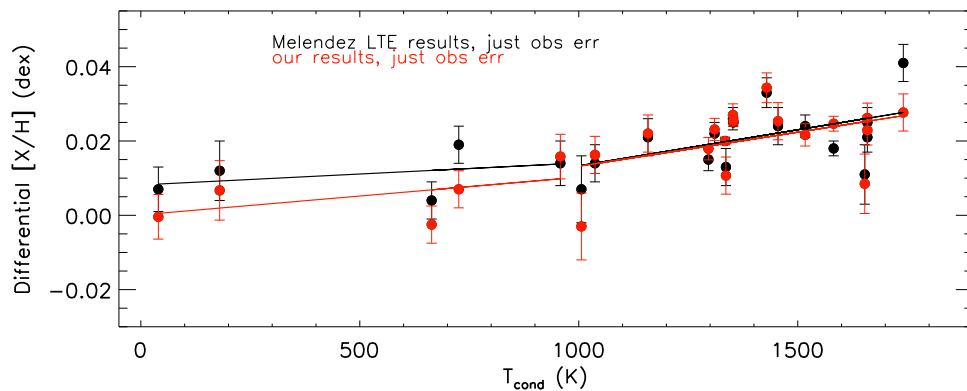


Figure 8.4 A comparison of the (Meléndez et al. (2012)) results detailing the abundance ratios of the solar twin HIP 56948 (in black) to my reanalysis of their equivalent widths (in red), using the methodology adopted by Teske et al. (2013ab; 2014). The solid lines are separate linear fits to the volatile and refractory abundances, with the cut-off at 1000 K. There is excellent agreement between the abundances I derive and those from the original study, indicating that, given similar quality data and using the same methodology as applied in Chapters 5-7, I will have the ability to detect (or refute) a similar trend in other small planet host stars.

## REFERENCES

- Adams, E. R., Seager, S., & Elkins-Tanton, L. 2008, *ApJ*, 673, 1160
- Adams, J. D., Herter, T. L., Gull, G. E., et al. 2010, *Proc. SPIE*, 7735
- Agúndez, M., Cernicharo, J., & Goicoechea, J. R. 2008, *A&A*, 483, 831
- Agol E., Cowan N. B., Knutson H. A., Deming D., Steffen J. H., Henry G. W., Charbonneau D., 2010, *ApJ*, 721, 1861
- Agol, E., Cowan, N. B., Knutson, H. A., et al. 2010, *ApJ*, 721, 1861
- Alencar, S. H. P., & Batalha, C. 2002, *ApJ*, 571, 378
- Alexander, R. D., Clarke, C. J., & Pringle, J. E. 2004, *MNRAS*, 354, 71
- Ali-Dib, M., Mousis, O., Pekmezci, G. S., et al. 2014, *A&A*, 561, A60
- Allende Prieto, C., Hubeny, I., & Lambert, D. L. 2003, *ApJ*, 591, 1192
- Allende Prieto, C., Lambert, D. L., & Asplund, M. 2001, *ApJL*, 556, L63
- Alonso, R., Deeg, H. J., Kabath, P., & Rabus, M. 2010, *AJ*, 139, 1481
- Alonso, R., Guillot, T., Mazeh, T., et al. 2009, *A&A*, 501, L23
- Ammler-von Eiff, M., Santos, N. C., Sousa S. G., Fernandes, J., Guillot, T., Israelian, G., Mayor, M., Melo, C., 2009, *A&A*, 507, 523
- Anderson, K. R., & Adams, F. C. 2012, *PASP*, 124, 809
- Apai, D., & Lauretta, D. S. 2010, *Protoplanetary Dust: Astrophysical and Cosmochemical Perspectives*, 128
- Ardila, D. R., & Basri, G. 2000, *ApJ*, 539, 834
- Asplund, M., Grevesse, N., & Sauval, A. J. 2005, *Cosmic Abundances as Records of Stellar Evolution and Nucleosynthesis*, 33 6, 25
- Asplund, M., Grevesse, N., Sauval, A. J., & Scott, P. 2009, *ARA&A*, 47, 481
- Asplund, M., Grevesse, N., Sauval, A. J., Allende Prieto, C., & Kiselman, D. 2004, *A&A*, 417, 751

- Asplund, M. 2005, *ARA&A*, 43, 481
- Bailey, V., Meshkat, T., Reiter, M., et al. 2014, *ApJL*, 780, L4
- Baliunas, S. L., Henry, G. W., Donahue, R. A., Fekel, F. C., & Soon, W. H. 1997, *ApJL*, 474, L119
- Batalha, N., et al. 2013, *ApJS*, 204, 24
- Barklem, P. S. 2007, *A&A*, 462, 781
- Barman T. S., Macintosh B., Konopacky Q. M., Marois C., 2011a, *ApJ*, 733, 65
- Barman T. S., Macintosh B., Konopacky Q. M., Marois C., 2011b, *ApJ*, 735, L39
- Barnes, J. R., Barman, T. S., Prato, L., et al. 2007, *MNRAS*, 382, 473
- Bean J. L. et al., 2011, *ApJ*, 743, 92
- Bean J. L., Miller-Ricci Kempton E., Homeier D., 2010, *Nature*, 468, 669
- Beaulieu, J. P., Carey, S., Ribas, I., & Tinetti, G. 2008, *ApJ*, 677, 1343
- Beaulieu, J. P., Kipping, D. M., Batista, V., et al. 2010, *MNRAS*, 409, 963
- Bensby, T., Feltzing, S., & Lundström, I. 2004, *A&A*, 415, 155
- Bensby, T., Feltzing, S., Lundström, I., & Ilyin, I. 2005, *A&A*, 433, 185
- Bergfors, C., Brandner, W., Daemgen, S., et al. 2013, *MNRAS*, 428, 182
- Bergfors, C., Brandner, W., Henning, T., & Daemgen, S. 2011, in *IAU Symp.* 276, *The Astrophysics of Planetary Systems: Formation, Structure, and Dynamical Evolution* (Cambridge: Cambridge Univ. Press), Eds. A. Sozzetti, M. G. Lattanzi, & A. P. Boss, 397
- Bergin, E. A. 2013, *arXiv:1309.4729*
- Bergin, E., et al. 2004, *ApJL*, 614, L133
- Bergin, E. A., Aikawa, Y., Blake, G. A., & van Dishoeck, E. F. 2007, *Protostars and Planets V*, 751
- Bergin, E. A. 2011, *Physical Processes in Circumstellar Disks around Young Stars*, 55

- Berta Z. K. et al., 2011, *ApJ*, 736, 12
- Berta Z. K. et al., 2012, *ApJ*, 747, 35
- Berthoud, M. G., Keller, L. D., Herter, T. L., Richter, M. J., & Whelan, D. G. 2007, *ApJ*, 660, 461
- Bertin E., Arnouts S., 1996, *A&AS*, 117, 393
- Birkby, J. L., de Kok, R. J., Brogi, M., et al. 2013, *MNRAS*, 436, L35
- Blake, G. A., & Boogert, A. C. A. 2004, *ApJL*, 606, L73
- Blum, J. & Wurm, G. 2008, *ARA&A*, 46, 21
- Blum, R. D., Barbosa, C. L., Damineli, A., Conti, P. S., & Ridgway, S. 2004, *ApJ*, 617, 1167
- Bond, J. C., Lauretta, D. S., Tinney, C. G., et al. 2008, *ApJ*, 682, 1234
- Bond, J. C., O'Brien, D. P., & Lauretta, D. S. 2010, *ApJ*, 715, 1050
- Bond, J. C., Tinney, C. G., Butler, R. P., et al. 2006, *MNRAS*, 370, 163
- Borucki W. J. et al., 2012, *ApJ*, 745, 120
- Borucki W. J., for the Kepler Team, 2010, arXiv:1006.2799
- Borucki, W. J., Koch, D. G., Basri, G., et al. 2011, *ApJ*, 736, 19
- Brittain, S. D., Simon, T., Najita, J. R., & Rettig, T. W. 2007, *ApJ*, 659, 685
- Broeg C., Wuchterl G., 2007, *MNRAS*, 376, L62
- Brogi, M., Snellen, I. A. G., de Kok, R. J., et al. 2013, *ApJ*, 767, 27
- Brown, D. J. A., Collier Cameron, A., Díaz, R. F., et al. 2012, *ApJ*, 760, 139
- Brugamyer, E., Dodson-Robinson, S. E., Cochran, W. D., & Sneden, C. 2011, *ApJ*, 738, 97
- Bubar, E. J., & King, J. R. 2010, *AJ*, 140, 293
- Buchhave, L. A., Bakos, G. Á., Hartman, J. D., et al. 2010, *ApJ*, 720, 1118
- Buchhave, L. A., et al., 2012, *Nature*, 486, 375
- Burke, C. J., et al., 2007, *ApJ*, 671, 2115

- Burrows A., Hubeny I., Budaj J., Hubbard W. B., 2007a, *ApJ*, 661, 502
- Butler, R. P., Wright, J. T., Marcy, G. W., et al. 2006, *ApJ*, 646, 505
- Caffau, E., Ludwig, H.-G., Bonifacio, P., et al. 2010, *A&AP*, 514, A92
- Caffau, E., Ludwig, H.-G., Malherbe, J.-M., et al. 2013, *A&A*, 554, A126
- Caffau, E., Ludwig, H.-G., Steffen, M., et al. 2008, *A&A*, 488, 1031
- Caffau, E., Ludwig, H.-G., Steffen, M., Freytag, B., & Bonifacio, P. 2011, *Sol. Phys.*, 268, 255
- Carmona, A. 2010, *Earth Moon and Planets*, 106, 71
- Carr, J. 2005, *High Resolution Infrared Spectroscopy in Astronomy*, 203
- Carr, J. S., Mathieu, R. D., & Najita, J. R. 2001, *ApJ*, 551, 454
- Carr, J. S., Tokunaga, A. T., & Najita, J. 2004, *ApJ*, 603, 213
- Carr, J. S., Tokunaga, A. T., Najita, J., Shu, F. H., & Glassgold, A. E. 1993, *ApJL*, 411, L37
- Carr, J.S., & Najita, J.R. 2008, *Science*, 319, 1504
- Carr, J.S., & Najita, J.R. 2011, *ApJ*, submitted
- Carter J. A., Winn J. N., 2009, *ApJ*, 704, 51
- Carter-Bond, J. C., O'Brien, D. P., Delgado Mena, E., et al. 2012, *ApJL*, 747, L2
- Cassan, A., et al. 2012, *Nature*, 481, 167
- Cayrel de Strobel, G., Lebreton, Y., Soubiran, C., & Friel, E. D. 1999, *Ap&SS*, 265, 345
- Chambers, J. E. 2010, *ApJ*, 724, 92
- Chandler, C. J., Carlstrom, J. E., Scoville, N. Z., Dent, W. R. F., & Geballe, T. R. 1993, *ApJL*, 412, L71
- Charbonneau D. et al., 2009, *Nature*, 462, 891
- Charbonneau D., et al., 2005, *ApJ*, 626, 523
- Charbonneau D., Knutson H. A., Barman T., Allen L. E., Mayor M., Megeath

- S. T., Queloz D., Udry S., 2008, *ApJ*, 686, 1341
- Ciesla, F. J., & Cuzzi, J. N. 2006, *Icarus*, 181, 178
- Claret A., Bloemen S., 2011, *VizieR Online Data Catalog*, 352, 99075 Claret & Bloemen (2011)
- Copperwheat, C. M., Wheatley, P. J., Southworth, J., et al. 2013, *MNRAS*, 434, 661
- Croll B., Albert L., Jayawardhana R., Miller-Ricci Kempton E., Fortney J. J., Murray N., Neilson, H., 2011, *ApJ*, 736, 78
- Croll, B., Jayawardhana, R., Fortney, J. J., Lafrenière, D., & Albert, L. 2010b, *ApJ*, 718, 920
- Croll, B., Albert, L., Lafreniere, D., Jayawardhana, R., & Fortney, J. J. 2010a, *ApJ*, 717, 1084
- Crossfield I. J. M., Barman T., Hansen B. M. S., 2011, *ApJ*, 736, 132
- Crossfield, I. J. M., Barman, T., Hansen, B. M. S., Tanaka, I., & Kodama, T. 2012, *ApJ*, 760, 140
- Crouzet, N., McCullough, P. R., Burke, C., & Long, D. 2012, *ApJ*, 761, 7
- Cunha, K., Smith, V. V., & Lambert, D. L. 1998, *ApJ*, 493, 195
- Currie T., et al., 2011, *ApJ*, 729, 128
- Désert J.-M. et al., 2011, *ApJL*, 731, L40
- Désert, J.-M., Lecavelier des Etangs, A., Hébrard, G., Sing, D. K., Ehrenreich, D., Ferlet, R., Vidal-Madjar, A., 2009, *ApJ*, 699, 478
- Davis, S. P. & Phillips, J. G. 1963, *Berkeley Analyses of Molecular Spectra*, Berkeley: University of California Press
- de Kok, R. J., Brogi, M., Snellen, I. A. G., et al. 2013, *A&A*, 554, A82
- Deming, D., Knutson, H., Agol, E., et al. 2011, *ApJ*, 726, 95
- De Mooij E. J. W. et al., 2012, *A&A*, 538, A46

- Delgado Mena, E., Israelian, G., González Hernández, J. I., Bond, J. C., Santos, N. C., Udry, S., Mayor, M., 2010, *ApJ*, 725, 2349
- Demory, B.-O., Gillon, M., Deming, D., et al. 2011, *A&A*, 533, A114
- Dittmann J. A., Close L. M., Green E. M., Fenwick M., 2009b, *ApJ*, 701, 756
- Dittmann J. A., Close L. M., Green E. M., Scuder, L. J., Males J. R., 2009a, *ApJL*, 699, L48
- Dittmann J. A., Close L. M., Scuderi L. J., Morris M. D., 2010, *ApJ*, 717, 235
- Dittmann J. A., Close L. M., Scuderi L. J., Turner J., Stephenson P. C., 2012, , 17, 438
- Dodson-Robinson, S. E., & Bodenheimer, P. 2009, *ApJL*, 695, L159
- Dodson-Robinson, S. E., & Bodenheimer, P. 2010, *Icarus*, 207, 491 Dragomir, D., Matthews, J. M., Winn, J. N., Rowe, J. F., & MOST Science Team 2013, *arXiv:1302.3321*
- Drawin, H.-W. 1968, *Zeitschrift fur Physik*, 211, 404
- Dullemond, C. P., Hollenbach, D., Kamp, I., & D'Alessio, P. 2007, *Protostars and Planets V*, 555
- Dutrey, A., Guilloteau, S., & Ho, P. 2007, *Protostars and Planets V*, 495
- Dutrey, A., Guilloteau, S., Prato, L., Simon, M., Duvert, G., Schuster, K., & Menard, F. 1998, *A&A*, 338, L63
- Ecuivillon, A., Israelian, G., Santos, N. C., et al. 2004, *A&A*, 426, 619
- Ecuivillon, A., Israelian, G., Santos, N. C., Mayor, M., & Gilli, G. 2006, *A&A*, 449, 809
- Eggen, O. J. 1985, *AJ*, 90, 74
- Endl, M., Robertson, P., Cochran, W. D., et al. 2012, *ApJ*, 759, 19
- Ercolano, B., Clarke, C. J., & Drake, J. J. 2009, *ApJ*, 699, 1639
- Ercolano, B., Drake, J. J., Raymond, J. C., & Clarke, C. C. 2008, *ApJ*, 688, 398



- Etzel P. B., 1981, *Photometric and Spectroscopic Binary Systems*, 111
- Evans, T. M., Pont, F., Sing, D. K., et al. 2013, *ApJL*, 772, L16
- Everett, M. E., Howell, S. B., Silva, D. R., & Szkody, P. 2013, *ApJ*, 771, 107
- Fabbian, D., Asplund, M., Barklem, P. S., Carlsson, M., & Kiselman, D. 2009, *A&A*, 500, 1221
- Favre, C., Cleeves, L. I., Bergin, E. A., Qi, C., & Blake, G. A. 2013, *ApJL*, 776, L38
- Fazio, G. G., Hora, J. L., Allen, L. E., et al. 2004, *ApJS*, 154, 10
- Feltzing, S., & Gonzalez, G. 2001, *A&A*, 367, 253
- Fischer, D. A., & Valenti, J. 2005, *ApJ*, 622, 1102
- Fitzpatrick, M. J., & Sneden, C. 1987, *BAAS*, 19, 1129
- Ford E. B., 2006, *ApJ*, 642, 505
- Fortney, J. J. 2012, *ApJL*, 747, L27
- Fortney, J. J., Lodders, K., Marley, M. S., & Freedman, R. S. 2008, *ApJ*, 678, 1419
- Fortney, J. J., & Nettelmann, N. 2010, *Space Science Review*, 152, 423
- Fortney J. J., Saumon D., Marley M. S., Lodders K., Freedman R. S., 2006, *ApJ*, 642, 495
- Fossati, L., Haswell, C. A., Froning, C. S., et al. 2010, *ApJL*, 714, L222
- Fraine J. D., Deming D., Gillon M. et al., 2013, arXiv:1301.6763
- Freedman R. S., Marley M. S., Lodders K., 2008, *ApJS*, 174, 504
- Fressin, F. et al., 2013, *ApJ*, 766, 81
- Fressin, F., Knutson, H. A., Charbonneau, D., et al. 2010, *ApJ*, 711, 374
- Fuhrmann, K., Pfeiffer, M. J., & Bernkopf, J. 1998, *A&A*, 336, 942
- Furlan, E., et al. 2006, *ApJS*, 165, 568
- Güdel, M., et al. 2010, *A&A*, 519, A113
- Gaidos, E., Fischer, D. A., Mann, A. W., & Howard, A. W. 2013, *ApJ*, 771, 18

- Gaidos, E. J. 2000, *Icarus*, 145, 637
- Galicher R., Marois C., Macintosh B., Barman T., Konopacky Q., 2011, *ApJ*, 739, L41
- Gazak J. Z., Johnson J. A., Tonry J., Dragomir D., Eastman J., Mann A. W., Agol E., 2012, *Advances in Astronomy*, 2012
- Gelman A., Rubin D. B., 1992, *Stat. Sci.*, 7, 457
- Ghezzi, L., Cunha, K., Smith, V. V., de Araújo, F. X., Schuler, S. C., de la Reza, R., 2010, *ApJ*, 720, 1290
- Gibson, N. P., Aigrain, S., Pont, F., et al. 2012, *MNRAS*, 422, 753
- Gillon, M., Demory, B.-O., Benneke, B., et al. 2012, *A&A*, 539, A28
- Gillon, M., Lanotte, A. A., Barman, T., et al. 2010, *A&A*, 511, A3
- Glassgold, A. E., Meijerink, R., & Najita, J. R. 2009, *ApJ*, 701, 142
- Glassgold, A. E., Najita, J., & Igea, J. 2004, *ApJ*, 615, 972
- González Hernández, J. I., Delgado-Mena, E., Sousa, S. G., et al. 2013, *A&A*, 552, A6
- González Hernández, J. I., Israelian, G., Santos, N. C., Sousa, S., Delgado-Mena, E., Neves, V., Udry, S., 2010, *ApJ*, 720, 1592
- Gonzalez, G., & Vanture, A. D. 1998, *A&A*, 339, L29
- Gonzalez, G., Laws, C., Tyagi, S., & Reddy, B. E. 2001, *AJ*, 121, 432
- Gonzalez, G. 1998, *A&A*, 334, 221
- Gonzalez, G. 1999, *MNRAS*, 308, 447
- Gorti, U., & Hollenbach, D. 2009, *ApJ*, 690, 1539
- Gratton, R. G., Carretta, E., Eriksson, K., & Gustafsson, B. 1999, *A&A*, 350, 955
- Gray, D. F. 2005, “The Observation and Analysis of Stellar Photospheres”, 3rd Edition, by D.F. Gray. ISBN 0521851866. Cambridge, UK: Cambridge University Press, 2005.

- Griffith, C. A. 2014, *Phil. Trans. R. Soc. A*, 372: 20130086
- Griffith, C. A. et al. 2014, in prep.
- Grillmair C. J., et al., 2008, *Nature*, 456, 767
- Grillmair, C. J., Charbonneau, D., Burrows, A., et al. 2007, *ApJL*, 658, L115
- Guillot, T., & Havel, M. 2011, *A&A*, 527, A20
- Guillot T., Santos N. C., Pont F., Iro N., Melo C., Ribas I., 2006, *A&A*, 453, L21
- Guilloteau, S., & Dutrey, A. 1998, *A&A*, 339, 467
- Gullbring, E., Hartmann, L., Briceno, C., & Calvet, N. 1998, *ApJ*, 492, 323
- Gustafsson, B., Edvardsson, B., Eriksson, K., et al. 2008, *A&A*, 486, 951
- Harpsøe K. B. W. et al., 2013, *A&A*, 549, A10
- Hart, M. H. 1978, *Icarus*, 33, 23
- Hartigan, P., Kenyon, S. J., Hartmann, L., Strom, S. E., Edwards, S., Welty, A. D., & Stauffer, J. 1991, *ApJ*, 382, 617
- Hartigan, P., Strom, K. M., & Strom, S. E. 1994, *ApJ*, 427, 961
- Hartmann, L. 2009, *Accretion Processes in Star Formation: Second Edition*, by Lee Hartmann. ISBN 978-0-521-53199-3. Published by Cambridge University Press, Cambridge, UK, 2009.
- Hartmann, L., Calvet, N., Gullbring, E., & D'Alessio, P. 1998, *ApJ*, 495, 385
- Hebb, L., Collier-Cameron, A., Loeillet, B., et al. 2009, *ApJ*, 693, 1920
- Henning, T., & Meeus, G. 2009, arXiv:0911.1010
- Herczeg, G. J., Linsky, J. L., Valenti, J. A., Johns-Krull, C. M., & Wood, B. E. 2002, *ApJ*, 572, 310
- Herczeg, G. J., Linsky, J. L., Walter, F. M., Gahm, G. F., & Johns-Krull, C. M. 2006, *ApJS*, 165, 256
- Hibbert, A., Biemont, E., Godefroid, M., & Vaeck, N. 1991, *Journal of Physics B Atomic Molecular Physics*, 24, 3943

- Hibbert, A., Biemont, E., Godefroid, M., & Vaeck, N. 1993, *A&AS*, 99, 179
- Houck, J. R., et al. 2004, *ApJS*, 154, 18
- Howard A. W. et al., 2010, *Science*, 330, 653
- Hoyer S., Rojo P., López-Morales M., 2012, *ApJ*, 748, 22
- Hoyer S., Rojo P., López-Morales M., Díaz R. F., Chambers J., Minniti D., 2011, *ApJ*, 733, 53
- Hubeny, I., & Lanz, T. 1995, *ApJ*, 439, 875
- Ida, S., & Lin, D. N. C. 2004a, *ApJ*, 604, 388
- Ida, S., & Lin, D. N. C. 2004b, *ApJ*, 616, 567
- Ikoma M., Guillot T., Genda H., Tanigawa T., Ida S., 2006, *ApJ*, 650, 1150
- Irwin, P. G. J., Teanby, N. A., de Kok, R., et al. 2008, *J. Quant. Spec. Radiat. Transf.*, 109, 1136
- Janson, M., Brandt, T. D., Kuzuhara, M., et al. 2013, *ApJL*, 778, L4
- Johansson, S., Litzén, U., Lundberg, H., & Zhang, Z. 2003, *ApJL*, 584, L107
- Johnson J. A. et al., 2011, *ApJ*, 730, 79
- Johnson, J. A., Aller, K. M., Howard, A. W., & Crepp, J. R. 2010, *PASP*, 122, 905
- Johnson, T. V., Mousis, O., Lunine, J. I., & Madhusudhan, N. 2012, *ApJ*, 757, 192
- Kasting, J. F., Whitmire, D. P., & Reynolds, R. T. 1993, *Icarus*, 101, 108
- Kastner, J. H., Zuckerman, B., Weintraub, D. A., & Forveille, T. 1997, *Science*, 277, 67
- Kenyon, S.J., & Hartmann, L. 1995, *ApJS*, 101, 117
- King, J. R., & Schuler, S. C. 2005, *PASP*, 117, 911
- Kiselman, D. 2001, *NAR*, 45, 559
- Kiselman, D. 1993, *A&A*, 275, 269
- Knutson, H. A., Charbonneau, D., Allen, L. E., Burrows, A., & Megeath, S. T.

2008, ApJ, 673, 526

Knutson, H. A., Charbonneau, D., Allen, L. E., et al. 2007, Nature, 447, 183

Knutson, H. A., Charbonneau, D., Cowan, N. B., et al. 2009, ApJ, 690, 822

Knutson, H. A., Howard, A. W., & Isaacson, H. 2010, ApJ, 720, 1569

Knutson, H. A., Lewis, N., Fortney, J. J., et al. 2012, ApJ, 754, 22

Konopacky, Q. M., Barman, T. S., Macintosh, B. A., & Marois, C. 2013, Science, 339, 1398

Kopparapu, R. k., Kasting, J. F., & Zahnle, K. J. 2012, ApJ, 745, 77

Kuchner, M. J., & Seager, S. 2005, arXiv:astro-ph/0504214

Kundurthy P., Agol E., Becker A. C., Barnes R., Williams B., Mukadam A., 2011, ApJ, 731, 123

Kupka, F., Piskunov, N., Ryabchikova, T. A., Stempels, H. C., & Weiss, W. W. 1999, A&AS, 138, 119

Kurucz, R., & Bell, B. 1995, Atomic Line Data (R.L. Kurucz and B. Bell) Kurucz CD-ROM No. 23. Cambridge, Mass.: Smithsonian Astrophysical Observatory, 1995., 23,

Kurucz, R. 1993, Opacities for Stellar Atmospheres: Abundance Sampler. Kurucz CD-ROM No. 14. Cambridge, Mass.: Smithsonian Astrophysical Observatory, 1993., 14,

Kurucz, R. L. 1992, in IAU Symp. 149, The Stellar Populations of Galaxies, ed. B. Barbuy & A. Renzini (Dordrecht: Kluwer), 225

Kurucz, R. L. 1996, in ASP Conf. Ser. 108, M.A.S.S., Model Atmospheres and Spectrum Synthesis, ed. S. J. Adelman, F. Kupka, & W. W. Weiss (San Francisco, CA: ASP), 2

Lagrange A.-M., et al., 2009, A&A, 493, L21

Lahuis, F., & van Dishoeck, E. F. 2000, A&A, 355, 699

- Lahuis, F., et al. 2006, *ApJL*, 636, L145
- Lambert, D. L., & Ries, L. M. 1981, *ApJ*, 248, 228
- Lammer, H., Erkaev, N. V., Odert, P., et al. 2013, *MNRAS*, 430, 1247
- Lammer, H., Blanc, M., Benz, W., et al. 2013, *Astrobiology*, 13, 793
- Lanza, A. F., Pagano, I., Leto, G., et al. 2009, *A&A*, 493, 193
- Law N. M. et al., 2013, *ApJ*, 145, 58
- Laws, C., & Gonzalez, G. 2001, *ApJ*, 553, 405
- Lee, J.-M., Fletcher, L. N., & Irwin, P. G. J. 2012, *MNRAS*, 420, 170
- Line, M. R., Knutson, H., Wolf, A. S., & Yung, Y. L. 2014, *ApJ*, 783, 70
- Linsky, J. L., Yang, H., France, K., et al. 2010, *ApJ*, 717, 1291
- Lodders, K. 2004, *ApJ*, 611, 587
- Lodders, K. 2010, *Principles and Perspectives in Cosmochemistry*, Springer-Verlag Berlin Heidelberg, Eds. A. Goswami & B. Eswar Reddy, p. 379
- Lopez, E. D., & Fortney, J. J. 2013, arXiv:1311.0329
- Lovis, C., Mayor, M., Bouchy, F., et al. 2009, *IAU Symposium*, 253, 502
- Machalek P., McCullough P. R., Burke C. J., Valenti J. A., Burrows A., Hora J. L., 2008, *ApJ*, 684, 1427
- Machalek P., McCullough P. R., Burrows A., Burke C. J., Hora J. L., Johns-Krull C. M., 2009, *ApJ*, 701, 514
- Madhusudhan, N., & Seager, S. 2009, *ApJ*, 707, 24
- Madhusudhan, N., et al. 2011, *Nature*, 469, 64
- Madhusudhan, N., Lee, K. K. M., & Mousis, O. 2012, *ApJL*, 759, L40
- Madhusudhan, N. 2012, *ApJ*, 758, 36
- Marty, B., Alexander, C. M. O'D., & Raymond, S. N. 2013, *Reviews in Mineralogy and Geochemistry*, 75, 149
- Mandel K., Agol E., 2002, *ApJL*, 580, L171

- Mandell, A. M., Haynes, K., Sinukoff, E., et al. 2013, *ApJ*, 779, 128
- Marley M. S., Saumon D., Cushing M., Ackerman A. S., Fortney J. J., Freedman R., 2012, *ApJ*, 754, 135
- Marois C., Macintosh B., Barman T., Zuckerman B., Song I., Patience J., Lafrenière D., Doyon R., 2008, *Sci*, 322, 1348
- Marois C., Zuckerman B., Konopacky Q. M., Macintosh B., Barman T., 2010, *Nature*, 468, 1080
- Matute I. et al., 2012, *A&A*, 542, A20
- Maxted, P. F. L., Aderson, D. R., Collier Cameron, A., et al. 2010, *PASP*, 122, 1465
- McArthur, B. E., Endl, M., Cochran, W. D., et al. 2004, *ApJL*, 614, L81
- McLean, I. S., Smith, E. C., Aliado, T., et al. 2006, *Proc. SPIE*, 6269
- McCullough P. R., et al., 2006, *ApJ*, 648, 1228
- Meléndez, J., Asplund, M., Gustafsson, B., & Yong, D. 2009, *ApJL*, 704, L66
- Millan-Gabet, R., Malbet, F., Akeson, R., Leinert, C., Monnier, J., & Waters, R. 2007, *Protostars and Planets V*, 539
- Miller-Ricci E., Fortney J. J., 2010, *ApJL*, 716, L74
- Miller-Ricci Kempton E., Zahnle K., Fortney J. J., 2012, *ApJ*, 745, 3
- Miller, N., & Fortney, J. J. 2011, *ApJL*, 736, L29
- Mortier, A., Santos, N. C., Sousa, S. G., et al. 2013, *A&A*, 558, A106
- Morbidelli, A., Lunine, J. I., O'Brien, D. P., Raymond, S. N., & Walsh, K. J. 2012, *Annual Review of Earth and Planetary Sciences*, 40, 251
- Moses, J. I., Visscher, C., Fortney, J. J., et al. 2011, *ApJ*, 737, 15
- Moses, J. I., Madhusudhan, N., Visscher, C., & Freedman, R. S. 2013, *ApJ*, 763, 25
- Mousis, O., Lunine, J.I. , Madhusudhan, N. and Johnson, T. V. 2012, *ApJL*, 751,

L7

Muirhead, P. S. et al., 2012, *ApJ*, 747, 144

Murgas F., Pallé E., Cabrera-Lavers A., Colón K. D., Marín E. L., Parviainen H., 2012, *A&A*, 544, A41

Muzerolle, J., Luhman, K. L., Briceño, C., Hartmann, L., & Calvet, N. 2005, *ApJ*, 625, 906

Najita J. R., Carr J. S., Pontoppidan K. M., Salyk C., van Dishoeck E. F., Blake G. A., 2013, *ApJ*, 766, 134

Najita, J., Carr, J. S., & Mathieu, R. D. 2003, *ApJ*, 589, 931

Najita, J., Carr, J. S., Glassgold, A. E., Shu, F. H., & Tokunaga, A. T. 1996, *ApJ*, 462, 919

Najita, J. R., Carr, J. S., Glassgold, A. E., & Valenti, J. A. 2007a, *Protostars and Planets V*, 507

Najita, J. R., Crockett, N., & Carr, J. S. 2008, *ApJ*, 687, 1168

Najita, J. R., Doppmann, G. W., Carr, J. S., Graham, J. R., & Eisner, J. A. 2009, *ApJ*, 691, 738

Najita, J. R., Edwards, S., Basri, G., & Carr, J. 2000, *Protostars and Planets IV*, 457

Najita, J. R., Strom, S. E., & Muzerolle, J. 2007b, *MNRAS*, 378, 369

Narita N., Nagayama T., Suenaga T. et al., 2012, *arXiv:1210.3169*

Narita, N., Hirano, T., Sato, B., Harakawa, H., Fukui, A., Aoki, W., Tamura, M., 2011, *PASJ*, 63, L67

Natta, A., Testi, L., Calvet, N., Henning, T., Waters, R., & Wilner, D. 2007, *Protostars and Planets V*, 767

Nissen, P. E. 2013, *A&A*, 552, A73

Nissen P. E., Primas F., Asplund M., Lambert D. L., 2002, *A&A*, 390, 235



- Noguchi, K., et al. 2002, PASJ, 54, 855
- Öberg, K. I., Murray-Clay, R., & Bergin, E. A. 2011, ApJL, 743, L16
- O'Donovan, F. T., Charbonneau, D., Bakos, G. Á., et al. 2007, ApJL, 663, L37
- O'Donovan, F. T., Charbonneau, D., Harrington, J., et al. 2010, ApJ, 710, 1551
- O'Donovan, F. T., Charbonneau, D., Mandushev, G., et al. 2006, ApJL, 651, L61
- Owen, J. E., & Wu, Y. 2013, ApJ, 775, 105
- Owen, T., Mahaffy, P., Niemann, H. B., et al. 1999, Nature, 402, 269
- Pascucci, I., Apai, D., Luhman, K., Henning, T., Bouwman, J., Meyer, M. R., Lahuis, F., & Natta, A. 2009, ApJ, 696, 143
- Pereira, T. M. D., Asplund, M., & Kiselman, D. 2009, A&A, 508, 1403
- Petigura, E. A., & Marcy, G. W. 2011, ApJ, 735, 41
- Petigura, E. A., Marcy, G. W., & Howard, A. W. ApJ, 770, 69
- Piskunov, N. E., Kupka, F., Ryabchikova, T. A., Weiss, W. W., & Jeffery, C. S. 1995, A&AS, 112, 525
- Polishook D. et al., 2012, MNRAS, 241, 2094
- Pollack, J. B., Hubickyj, O., Bodenheimer, P., et al. 1996, Icarus, 124, 62
- Poppenhaeger, K., Lenz, L. F., Reiners, A., Schmitt, J. H. M. M., & Shkolnik, E. 2011, A&A, 528, A58
- Pont F., Knutson H., Gilliland R. L., Moutou C., Charbonneau D., 2008, MNRAS, 385, 109
- Pont, F., Hébrard, G., Irwin, J. M., et al. 2009, å, 502, 695
- Pont, F., Knutson, H., Gilliland, R. L., Moutou, C., & Charbonneau, D. 2008, MNRAS, 385, 109
- Pontoppidan, K. M., Blake, G. A., van Dishoeck, E. F., Smette, A., Ireland, M. J., & Brown, J. 2008, ApJ, 684, 1323
- Pontoppidan, K. M., Salyk, C., Blake, G. A., Meijerink, R., Carr, J. S., & Najita,

- J. 2010, arXiv:1006.4189
- Popper D. M., Etzel P. B., 1981, *AJ*, 86, 102
- Preibisch, T., et al. 2005, *ApJS*, 160, 401
- Qi, C., Wilner, D. J., Aikawa, Y., Blake, G. A., & Hogerheijde, M. R. 2008, *ApJ*, 681, 1396
- Ramírez, I., Allende Prieto, C., & Lambert, D. L. 2007, *A&A*, 465, 271
- Ramírez, I., Meléndez, J., & Asplund, M. 2014, *A&A*, 561, A7
- Ramírez, I., Meléndez, J., & Asplund, M. 2009, *A&A*, 508, L17
- Ranjan, S., Charbonneau, D., Désert, J. M., et al. 2014, *ApJ*, 785, 148
- Redfield, S., Endl, M., Cochran, W. D., & Koesterke, L. 2008, *ApJL*, 673, L87
- Robinson, S. E., Laughlin, G., Bodenheimer, P. et al. 2006, *ApJ*, 643, 484
- Rogers L. A., Seager S., 2010, *ApJ*, 716, 1208
- Rogers, L. A., & Seager, S. 2010, *ApJ*, 712, 974
- Ryabchikova T.A., Piskunov N.E., Kupka F., Weiss W.W., 1997, *Baltic Astronomy*, vol. 6, 244-247
- Sada P. V. et al., 2012, *PASP*, 124, 212
- Sadakane, K. 2006, *PASJ*, 58, 1023
- Salyk, C., Blake, G. A., Boogert, A. C. A., & Brown, J. M. 2009, *ApJ*, 699, 330
- Salyk, C., Pontoppidan, K. M., Blake, G. A., Lahuis, F., van Dishoeck, E. F., & Evans, N. J., II 2008, *ApJL*, 676, L49
- Salyk, C., Pontoppidan, K. M., Blake, G. A., Najita, J., & Carr, J. 2011, *ApJ*, accepted
- Santos, N. C., Israelian, G., & Mayor, M. 2004, *A&A*, 415, 1153
- Santos, N. C., Sousa, S. G., Mortier, A., et al. 2013, *A&A*, 556, A150
- Sato B., et al., 2005, *ApJ*, 633, 465
- Scandariato, G., Maggio, A., Lanza, A. F., et al. 2013, *A&A*, 552, A7

- Schuler, S. C., Cunha, K., Smith, V. V., Ghezzi, L., King, J. R., Deliyannis, C. P., Boesgaard, A. M., 2011b, *ApJ*, 737, L32
- Schuler, S. C., Flateau, D., Cunha, K., King, J. R., Ghezzi, L., Smith, V. V., 2011a, *ApJ*, 732, 55
- Schuler, S. C., King, J. R., Hobbs, L. M., & Pinsonneault, M. H. 2004, *ApJL*, 602, L117
- Schuler, S. C., King, J. R., Terndrup, D. M., et al. 2006, *ApJ*, 636, 432
- Scuderi L. J., Dittmann J. A., Males J. R., Green E. M., Close L. M., 2010, *ApJ*, 714, 462
- Shkolnik, E. L. 2013, *ApJ*, 766, 9
- Shkolnik, E., Bohlender, D. A., Walker, G. A. H., & Collier Cameron, A. 2008, *ApJ*, 676, 628
- Shkolnik, E., Walker, G. A. H., & Bohlender, D. A. 2003, *ApJ*, 597, 1092
- Shkolnik, E., Walker, G. A. H., Bohlender, D. A., Gu, P.-G., Kürster, M. 2005, *ApJ*, 622, 1075
- Seager, S. 2010, *Exoplanet Atmospheres: Physical Processes*. By Sara Seager. Princeton University Press, 2010. ISBN: 978-1-4008-3530-0
- Semenov, D., Pavlyuchenkov, Y., Schreyer, K., Henning, T., Dullemond, C., & Bacmann, A. 2005, *ApJ*, 621, 853
- Semenov, D., Wiebe, D., & Henning, T. 2006, *ApJL*, 647, L57
- Sing D. K. et al., 2011, *MNRAS*, 416, 1443
- Sing, D. K., Désert, J.-M., Fortney, J. J., et al. 2011, *A&A*, 527, A73
- Sing, D. K., Désert, J.-M., Lecavelier Des Etangs, A., et al. 2009, *A&A*, 505, 891
- Sing, D. K., Huitson, C. M., Lopez-Morales, M., et al. 2012, *MNRAS*, 426, 1663
- Sing, D. K., Lecavelier des Etangs, A., Fortney, J. J., et al. 2013, *MNRAS*, 436, 2956

- Skemer A. J., et al., 2012, *ApJ*, 753, 14
- Skemer, A. J., Marley, M. S., Hinz, P. M., et al. 2013, arXiv:1311.2085
- Snedden, C., & Lambert, D. L. 1982, *ApJ*, 259, 381
- Snedden, C. 1973, *ApJ*, 184, 839
- Snellen, I. A. G., de Kok, R. J., de Mooij, E. J. W., & Albrecht, S. 2010, *Nature*, 465, 1049
- Sousa S. G., Santos N. C., Israelian G., Mayor M., Monteiro M. J. P. F. G., 2007, *A&A*, 469, 783
- Southworth J., 2008, *MNRAS*, 386, 1644
- Southworth J., Maxted P. F. L., Smalley B., 2004a, *MNRAS*, 349, 547
- Southworth J., Maxted P. F. L., Smalley B., 2004b, *MNRAS*, 351, 1277
- Steenbock, W., & Holweger, H. 1984, *A&A*, 130, 319
- Stelzer, B., & Neuhäuser, R. 2001, *A&A*, 377, 538
- Stevenson K. B., et al., 2012, *ApJ*, 754, 136
- Stevenson, D. J., & Lunine, J. I. 1988, *Icarus*, 75, 146
- Stone, J. M., Gammie, C. F., Balbus, S. A., & Hawley, J. F. 2000, *Protostars and Planets IV*, 589
- Storey, P. J., & Zeippen, C. J. 2000, *MNRAS*, 312, 813
- Strassmeier K. G. et al., 2010, *Advances in Astronomy*, 19
- Sumi, T., Bennett, D. P., Bond, I. A., et al. 2010, *ApJ*, 710, 1641
- Swain, M., Deroo, P., Tinetti, G., et al. 2013, *Icarus*, 225, 432
- Swain, M. R., Tinetti, G., Vasisht, G., et al. 2009b, *ApJ*, 704, 1616
- Swain, M. R., Vasisht, G., & Tinetti, G. 2008, *Nature*, 452, 329
- Swain, M. R., Vasisht, G., Tinetti, G., et al. 2009a, *ApJL*, 690, L114
- Takeda, G., Ford, E. B., Sills, A., et al. 2007, *ApJS*, 168, 297
- Takeda, Y., & Honda, S. 2005, *PASJ*, 57, 65

- Takeda, Y. 1995, PASJ, 47, 463
- Takeda, Y. 2003, A&A, 402, 343
- Taylor, B. J. 2002, MNRAS, 329, 839
- Telleschi, A., Güdel, M., Briggs, K. R., Audard, M., & Palla, F. 2007, A&A, 468, 425
- Teske, J. K., Cunha, K., Schuler, S. C., Griffith, C. A., & Smith, V. V. 2013a, ApJ, 778, 132
- Teske, J. K., Schuler, S. C., Cunha, K., Smith, V. V., & Griffith, C. A. 2013b, ApJL, 768, L12
- Teske, J. K., Turner, J. D., Mueller, M., & Griffith, C. A. 2013c, MNRAS, 431, 1669
- Teske, J. K., Najita, J. R., Carr, J. S., et al. 2011, ApJ, 734, 27
- Thi, W.-F., & Bik, A. 2005, A&A, 438, 557
- Thi, W.-F., van Dalen, B., Bik, A., & Waters, L. B. F. M. 2005, A&A, 430, L61
- Thi, W.-F., van Zadelhoff, G.-J., & van Dishoeck, E. F. 2004, A&A, 425, 955
- Tinetti G., Deroo P., Swain M. R., Griffith C. A., Vasisht G., Brown L. R., Burke C., McCullough P., 2010, ApJ, 712, L139
- Tinetti, G., et al. 2007, Nature, 448, 169
- Torres, G., Fischer, D. A., Sozzetti, A., Buchhave, L. A., Winn, J. N., Holman, M. J., Carter, J. A., 2012, ApJ, 757, 161
- Triaud A. H. M. J., et al., 2010, A&A, 524, A25
- Turner J. D. et al., 2013, MNRAS, 428, 678
- Turner, N. J., Willacy, K., Bryden, G., & Yorke, H. W. 2006, ApJ, 639, 1218
- Vidal-Madjar, A., Désert, J.-M., Lecavelier des Etangs, A., et al. 2004, ApJL, 604, L69
- Vidal-Madjar, A., Huitson, C. M., Bourrier, V., et al. 2013, A&A, 560, A54

- Vidal-Madjar, A., Lecavelier des Etangs, A., Désert, J.-M., et al. 2003, *Nature*, 422, 143
- Vázquez, M., Hanslmeier, A. 2005, *Astrophysics and Space Science Library*, 331
- Valenti, J. A., & Piskunov, N. 1996, *A&AS*, 118, 595
- Valenti, J. A., Johns-Krull, C. M., & Linsky, J. L. 2000, *ApJS*, 129, 399
- van Dishoeck, E. F. 1998, *The Molecular Astrophysics of Stars and Galaxies*, edited by Thomas W. Hartquist and David A. Williams. Clarendon Press, Oxford, 1998., p.53, 4, 53
- Visscher, C. & Moses, J. I. 2011, *ApJ*, 738, 72
- Vogt, S. S., Allen, S. L., Bigelow, B. C., et al. 1994, *Proc. SPIE*, 2198, 362
- Watson, D. M., et al. 2009, *ApJS*, 180, 84
- Wilkins, A. N., Deming, D., Madhusudhan, N., et al. 2014, *ApJ*, 783, 113
- Willacy, K., Langer, W., Allen, M., & Bryden, G. 2006, *ApJ*, 644, 1202
- Winn, J. N., Matthews, J. M., Dawson, R. I., et al. 2011, *ApJL*, 737, L18
- Winston, E., et al. 2010, *AJ*, 140, 266
- Wisdom, J. 2005, *Bulletin of the American Astronomical Society*, 37, 525
- Wong, M., Lunine, J., Atreya, S., Johnson, T., Mahaffy, P., Owen, T., & Encrenaz, T. 2008, *Reviews in Mineralogy and Geochemistry*, 68, 219
- Youdin, A. N., & Kenyon, S. J. 2013, *Planets, Stars and Stellar Systems. Volume 3: Solar and Stellar Planetary Systems*, 1
- Zahnle, K., Marley, M. S., Freedman, R. S., Lodders, K., & Fortney, J. J. 2009a, *ApJL*, 701, L20
- Zahnle, K., Marley, M. S., & Fortney, J. J. 2009b, *arXiv:0911.0728*
- Zieliński, P., Niedzielski, A., Wolszczan, A., Adamów, M., & Nowak, G. 2012, *A&AP*, 547, A91

